



Advanced Monitoring Algorithms for Battery Storage Systems in Electric Vehicles

Seyyed Kamyar Makinejad, M.Sc.

Vollständiger Abdruck der von der Fakultät für Elektrotechnik und Informationstechnik der Technischen Universität München zur Erlangung des akademischen Grades eines
Doktor-Ingenieurs
genehmigten Dissertation.

Vorsitzender: Prof. Dr.-Ing. habil. Dr. h.c. Alexander W. Koch

Prüfer der Dissertation:

1. Prof. Dr.-Ing. Andreas Jossen
2. Prof. Dr.-Ing. Markus Lienkamp

Die Dissertation wurde am 11.04.2019 bei der Technischen Universität München eingereicht und durch die Fakultät für Elektrotechnik und Informationstechnik am 05.09.2019 angenommen.

Declaration of Authorship

I hereby declare that the thesis submitted is my own unaided work. All direct or indirect sources used are acknowledged as references.

I am aware that the thesis in digital form can be examined for the use of unauthorized aid and in order to determine whether the thesis as a whole or parts incorporated in it may be deemed as plagiarism. For the comparison of my work with existing sources I agree that it shall be entered in a database where it shall also remain after examination, to enable comparison with future theses submitted. This work was not previously presented to another examination board and has not been published.

Kamyar Makinejad

Stuttgart, 4. April 2019

Abstract

Internal combustion engine (ICE) vehicles are slowly being replaced by hybrid electric vehicles (HEVs) and pure battery electric vehicles (BEV). By providing sustainable low/zero-emission electricity for pure EVs, a long-term zero-emission solution for transportation can be projected. Energy storage systems such as lithium-ion batteries (LIBs) or fuel cells (FCs) are the key components of EVs; however, key issues of safety, monitoring, and performance need to be addressed.

In all modern EVs and HEVs, a battery management system (BMS) is an integral part of the energy storage system component (battery pack). A BMS includes both hardware and software for monitoring, providing safe operation, and enhancing the performance and lifetime of the cells and the pack. LIBs are currently a top choice for most EVs made by different manufacturers. Similarly, the electric taxi developed at TUM CREATE Singapore "EVA" uses a LIB pack.

This thesis is aimed at developing monitoring algorithms, and models of the battery pack to be used in the BMS. These algorithms enable a BMS to predict cell parameters, perform state detection, provide safety functions, and perform tasks, such as cell balancing, and thermal management, among other functions. Developed models and algorithms can be adapted to other cell technologies regardless of chemistry, format, or size.

To reach these goals, this thesis is organized into seven chapters. After the introduction (Chapter 1), a comprehensive literature research on methods of battery characterization, modeling, and algorithm development (Chapter 2) is provided.

The experimental part (Chapter 3) covers necessary requirements for investigations on battery lifetime and aging mechanisms (cycle life and calendar life). The experiment results have been analyzed for cell parameterization under different operation conditions, such as various temperatures, power demands, and aging conditions.

Battery models in this thesis are so-called electrical and thermal models (Chapter 4). To develop the electrical models, cells have been characterized in both, the time-domain and frequency-domain. This is very useful especially for monitoring the capacity fade and tracking the impedance growth over the lifetime of the cells. Aside from electrical and thermal model parameterization, experimental data have been used for evaluation and verification purposes. Model-coupling and up-scaling techniques are explained in this chapter as well.

Chapter 5 addresses the algorithm development processes. Algorithms in this thesis have been mainly used for parameter prediction and state detection. In this chapter, a wide range of algorithms, from PID controller, learning algorithms, and observers to adaptive algorithms, and real-time model-based filtering techniques have been developed and implemented.

In Chapter 6, based on the performance and robustness of the developed methods, selected methods have been implemented on the battery pack level. The test setup included a hardware in the loop system (HIL) and an in-house developed BMS. For this setup, while the main computer controlled both, the temperature chamber and the battery cyler, models and algorithms have been evaluated in real-time. Finally, models and algorithms have been upscaled to simulate the EVA battery pack (216 cells). Although the battery pack measurements were limited to the pack temperature, current, voltage, and individual cell voltages, it is shown how the models and algorithms predicted individual cell parameters, temperatures (surface and core), and states. These models can be further used to develop other BMS functions, such as power prediction, and cell balancing.

Chapter 7 presents a summary of this thesis and proposes the further steps.

Kurzfassung

Fahrzeuge mit Verbrennungsmotoren (englisch: internal combustion engine, ICE) werden langsam durch Hybrid- (englisch: hybrid electric vehicle, HEV) und rein elektrische Fahrzeuge (englisch: electric vehicle, EV) ersetzt. Speziell EVs stellen eine nachhaltige Lösung für schadstofffreie Mobilität dar. Energiespeichersysteme wie Lithium-Ionen Batterien (LIB) oder Brennstoffzellen sind die Schlüsselkomponente von EV. Es müssen jedoch auch wichtige Themen wie Sicherheit, Monitoring und Leistung betrachtet werden.

In allen modernen EVs ist das Batteriemanagementsystem (BMS) integraler Bestandteil der Energiespeicherkomponente (Batteriepack). Das BMS beinhaltet Hardware und Software für Monitoring, für die Gewährleistung eines sicheren Betriebs und für die Verbesserung der Leistungsfähigkeit und Lebensdauer der Zellen und des Packs. Bei verschiedenen Automobilherstellern sind derzeit LIBs die erste Wahl für die meisten EV. Gleichmaßen wurde bei dem von der TUM CREATE Singapur entwickelten elektrischen Taxi, "EVA", ein LIB Pack verwendet.

Ziel dieser Arbeit ist die Entwicklung von Monitoring Algorithmen sowie von Modellen von Batteriepacks für die Verwendung im BMS. Diese Algorithmen ermöglichen dem BMS neben weiteren Funktionen die Vorhersage von Zellparametern, die Zustandserkennung, die Bereitstellung von Sicherheitsfunktionen, sowie die Durchführung des Zell Balancing und des Temperaturmanagements. Die entwickelten Modelle und Algorithmen können auf andere Zelltechnologien angepasst werden, unabhängig von verwendeter Chemie, Zellformat und Größe.

Um die genannten Ziele zu erreichen, wurde diese Arbeit in sieben Kapitel unterteilt. Nach der Einführung (Kapitel 1) wird eine umfangreiche Literaturrecherche bzgl. Modellen zur Batterie-Charakterisierung, Modellierung und Algorithmen-Entwicklung gegeben (Kapitel 2).

Einen besonders wichtigen Aspekt innerhalb dieser Arbeit stellt der experimentelle Teil (Kapitel 3) dar, welcher die notwendigen Anforderungen hinsichtlich der Untersuchung der Batterielebensdauer sowie Experimente bzgl. Alterungsmechanismen (zyklische und kalendarische Alterung) abdeckt. Die Ergebnisse der Experimente wurden für die Zellparametrierung unter verschiedenen Bedingungen analysiert, wie beispielsweise unter verschiedene Temperaturen, Leistungsbedarfen und Alterungsbedingungen.

Bei den innerhalb dieser Arbeit entwickelten Batteriemodellen handelt es sich um sogenannte elektrische und thermische Modelle (Kapitel 4). Für die Entwicklung der elektrischen Modelle wurden Zellen sowohl im Zeit- als auch im Frequenzbereich charakterisiert. Dies ist insbesondere für die Darstellung des Kapazitätsverlustes und die Verfolgung des Impedanzanstieges über der Batterielebensdauer nützlich. Neben der Parametrierung der elektrischen und thermischen Modelle wurden experimentelle Daten für die Evaluierung und Verifikation verwendet. Des Weiteren werden Modellkopplungen und eine Skalierungsmethode in diesem Kapitel erläutert.

Kapitel 5 beschäftigt sich mit dem Algorithmen-Entwicklungsprozess. Die im Rahmen dieser Arbeit entwickelten Algorithmen werden hauptsächlich verwendet für die Vorhersage von Parametern, Monitoring und Zustandserkennung. Ein breites Spektrum an Algorithmen, beginnend bei PID-Beobachtern, lernenden Algorithmen, nichtlinearen Beobachtern bis hin zu adaptiven Algorithmen und weiteren Echtzeit-Filterungen wurde entwickelt und implementiert.

In Kapitel 6 werden, basierend auf der Performance und der Robustheit der vorhergehend entwickelten Methoden, ausgewählte Modelle und Algorithmen auf einem Hardware in the loop System (HIL) geprüft und bewertet. Für das Monitoring mehrerer Zellen wurde zusätzlich ein in-house BMS entwickelt. Der Testaufbau wurde derart entwickelt, dass alle auf dem HIL System und dem BMS implementierten Modelle und Algorithmen in Echtzeit bewertet werden können, während der Hauptrechner sowohl die Temperatur der Testkammer als auch den sogenannten Batterie-Zyklisierer steuert. Zum Schluss wurden alle Modelle und Algorithmen hochskaliert, um das EVA Batteriepack (216 Zellen) zu simulieren. Obwohl die Messungen auf dem Gesamtstrom des Batteriepacks und den Zellspannungen begrenzt waren, konnte gezeigt werden, wie die Modelle die zellindividuellen Parameter wie Temperaturen (am Gehäuse und in der Zelle) und Zellzustände vorhersagen. Ebenso ist es möglich, weitere notwendige Funktionen wie die Leistungsprädiktion oder den Ladungsausgleich umzusetzen.

Kapitel 7 enthält eine Zusammenfassung der Arbeit und weitere Schritte werden vorgeschlagen.

Acknowledgements

Similarly to life, the behavior of batteries is sometimes difficult to predict. Passion for batteries took me from Hannover to Munich, from Munich to Singapore, from Singapore back to Munich, and, as of today, to Stuttgart.

In November 2011, I came to the Institute for Electrical Energy Storage Technology (EES), Department of Electrical and Computer Engineering at the Technical University of Munich (TUM). However, the joint venture between TUM and Nanyang Technological University (NTU) in Singapore under the TUM CREATE flag brought me to Singapore for more than 4 years. This journey was the biggest turning point of my life, not only for my academic and professional career but also for the great life experience I had during this time. For that, I have written these acknowledgments:

Prof. Andreas Jossen, I would like to express my sincere appreciation to you for giving me the opportunity to work for EES and Research Project 2 (RP2) at TUM CREATE and for your excellent and professional support. You are not only my research advisor but also an incomparable mentor to me. There are no words to thank you enough for encouraging me in the many aspects of my studies, research, career, and life. Working with you has been priceless, and I look forward to many more opportunities to share insights with you for many years to come.

My respect and gratitude expands to Prof. Jürgen Garche for all his advice and support during this time, together with Christian Campestrini for proofreading this work. I would also like to thank my direct colleagues at RP2: Raghavendra Arunachala, Eliud Cabrera-Castillo, Jan Geder, Nora Martiny, Sabine Arnold, Suguna Thanagasundram and Rudy Tjandra for their great support, teamwork, scientific discussions, and their strong friendship. Many other factors were involved in producing the results and creating a whole new level of this work. I sincerely thank Tanja Teutsch, Yani Zhou, Martin Aichriedler, Christian Obermaier, Amin Sakka, Thomas Rauh, and my other colleagues at the EES institute for their valuable input.

Getting through my dissertation required more than academic support. My gratitude and appreciation for their dedicated support and collaboration goes to the members of the battery laboratory team, especially to Lemuel Moraleja, who assisted me in the laboratory, and Han Zhou, who provided me with battery-pack measurement data. I would like to thank everyone in the EES secretary team for their support throughout this journey. I would also sincerely thank the corporate staff in Singapore for their smooth administrative assistance.

Most importantly, none of this could have happened without my family. My sister Nazanin has always been a source of inspiration for me. My parents, every time I got boxed into a corner, you would encourage me. Your support came in many words of motivation that constantly kept me going and looking forward. My fiancé Kerstin, for creating the most beautiful moments and her endless love. This

dissertation is the result of your unconditional love and encouragement.

The presented thesis was financially supported by the Singapore National Research Foundation (NRF) under its Campus for Research Excellence and Technological Enterprise (CREATE) program phase I.

Stuttgart, 4. April 2019

Contents

Acronyms	XI
1 Introduction	1
1.1 Work objective and motivation	1
1.2 The work structure and scope of this thesis	2
2 Technical review of system classification, characterization, modeling, and monitoring	4
2.1 System description	5
2.2 LIB operating conditions	7
2.3 LIB parameters	8
2.4 Battery system modeling	10
2.4.1 Empirical modeling techniques	11
2.4.2 Electrochemical modeling (white-box)	13
2.4.3 Type of equivalent-circuit models	14
2.4.3.1 ECM	14
2.4.3.2 The fundamentals of the time-domain characterization (HPPC-based)	16
2.4.3.3 The fundamentals of the frequency-domain characterization (EIS-based)	21
2.4.4 Thermodynamics and thermal modeling of the cell (TECM)	24
2.4.4.1 The state of the art in thermal modeling of the cell	25
2.4.4.2 Heat generation (production) and heat transfer mechanisms	26
2.5 Battery states definitions	29
2.5.1 SOC definition	29
2.5.2 SOH definition	31
2.6 Control theory and the requirement for state detection	32
2.6.1 State space system	32
2.6.2 Bayesian filtering theory	33
2.6.3 Performance evaluation	36
2.7 State detection techniques	36
2.7.1 Conventional methods	37
2.7.1.1 Voltage-based	37
2.7.1.2 Current-based	38
2.7.1.3 Impedance-based	40
2.7.2 Learning algorithms (self/supervised - data driven)	41
2.7.2.1 Neural networks	42
2.7.2.2 Fuzzy logic	44
2.7.2.3 Other learning algorithms for state detection	44
2.7.3 Adaptive filter algorithms (model-based and non-model-based)	45
2.7.3.1 Kalman filter	45
2.7.3.2 Particle filter	48

2.7.4	Controllers and observers (linear/nonlinear)	49
2.7.4.1	PID controller	49
2.7.4.2	Luenberger observer	50
2.7.4.3	Basics of the sliding mode observer (SMO) design	51
2.7.4.4	Nonlinear observer	51
2.7.4.5	H-infinity observer	52
2.7.5	Combined (hybrid) state detection methods	52
2.7.6	Other state detection methods	52
2.7.6.1	SOC and SOH based on the linear parameter varying method	52
2.7.6.2	SOC and SOH based on mechanical stress	52
2.8	Upscaling and pack-level modeling	53
3	Experimental	55
3.1	DUT	55
3.2	Laboratory setup and cell testing structure	58
3.3	Charging performance and strategies	60
3.4	Aging experiments under different internal and external conditions	62
3.4.1	Aging parameterization	62
3.4.2	Cycle-life: constant current mode vs. drive-cycle	63
3.4.3	Calendar-life	70
4	Model Development for battery storage systems	72
4.1	Electrical modeling part I: Time-domain model development and implementation	72
4.2	Electrical modeling part II: Frequency-domain model development and implementation	75
4.3	An approach to LIB thermal modeling and simulation	77
4.3.1	The proposed TECM	78
5	Algorithm Development for battery storage systems	86
5.1	Big picture of the software architecture	86
5.2	An online filter-based parameter estimator	87
5.3	Sliding mode observer	93
5.4	Kalman filter	96
6	Implementation, Evaluation, Verification, and Upscaling	101
6.1	A scaled BMS development platform	101
6.2	HIL: Real-time battery monitoring	104
6.3	Advanced battery pack simulation	106
6.3.1	Upscaling and battery pack simulation	107
6.3.2	Battery pack modeling under constant current profile	110
6.3.3	Battery pack modeling under dynamic drive-cycle current profile	112
6.3.4	Battery pack state, parameter, and temperature estimation	113
7	Summary, future work, and outlook	118
	Bibliography	122
	List of Figures	152

List of Tables	157
Appendix	159
A.1 Discrete-time approximation	159
A.2 Gaussian (normal) distribution	159
A.3 Matrix-operations	160
A.4 FFT algorithm	161
A.5 Moving average filter (MAF) algorithm	161
B.1 Sliding mode observer Simulink diagram	162
C.1 Lab design and visits	163
C.2 Selected photos of the TUM CREATE battery laboratory, and test setup	164
D.1 DUT datasheet	164
D.2 Cell holder design and construction	172

Acronyms

A

AC	Alternating current
AE	Absolute error
AEKF	Adaptive extended Kalman filter
ANFIS	Adaptive neuro-fuzzy interface system
ANN	Artificial neural network
ANP	Average noise power
ARC	Accelerated rate calorimeter
ASIL	Automotive safety integrity level
ASP	Average signal power
AUKF	Adaptive unscented Kalman filter
AWGN	Added white Gaussian noise
AWNN	Adaptive wavelet neural network

B

BET	Brumauer-Emmett-Teller
BMS	Battery management system
BOL	Beginning of life
BPF	Band-pass filter
BPNN	Backpropagation neural network

C

CAN	Controller area network
CC	Constant-current
CCCV	Constant-current constant-voltage
CDKF	Central difference Kalman filter
CE	Coulombic efficiency
CKF	Cubature Kalman filter
CPE	Constant phase element

D

DA	Differential analysis
DC	Direct current
DE	Differential equation
DEKF	Dual extended Kalman filter
DKF	Dual Kalman filter
DOD	Depth of discharge
DTKF	Dual time-scale Kalman filter
DUT	Device under test

E

ECM	Equivalent circuit model
EC:EMC	Ethylene carbonate (EC):Ethyl methyl carbonate (EMC)
EDLC	Electrochemical double layer capacitor
EIS	Electrochemical impedance spectroscopy
EKF	Extended Kalman filter

ELM	Extreme learning machine
EMF	Electro-motive force
ENN	Elman neural network
EOL	End of life
EV	Electric vehicle
F	
FEM	Finite element methods
FFT	Fast Fourier transform
FL	Fuzzy logic
FTP	Federal test procedure
G	
GA	Genetic algorithm
GEIS	Galvanostatic electrochemical impedance spectroscopy
GUI	Graphical user interface
H	
H_∞	H-infinity observer
HEV	Hybrid electric vehicle
HL	Hazard level
HPF	High-pass filter
HPPC	Hybrid pulse power characterization
I	
IEKF	Improved extended Kalman filter
I/O	Input-output
ITEKF	Iterated extended Kalman filter
K	
KF	Kalman filter
L	
LAB	Lead acid battery
LAN	Local area network
LBO	Luenberger observer
LCO	Lithium-cobalt-oxide
LFP	Lithium-iron-phosphate
Li-ion	Lithium-ion
LIB	Lithium ion battery
LKF	Linear Kalman filter
LMO	Lithium-manganese-oxide
LOLIMOT	Locally linear model tree
LPF	Low-pass filter
LPV	Linear parameter varying
LSSVM	Least square support vector machine
LTO	Lithium titanium oxide
LUT	Look-up-table

M	
MA	Moving average (filter)
MAE	Mean absolute error
MC	Monte Carlo
MCC	Multi-stage constant current
MHE	Moving horizon estimation
MIMO	Multiple-input-multiple-output
MOL	Middle of life
MSE	Mean-square estimation error
N	
NCA	Lithium-nickel-cobalt-aluminium-oxide
NF	Neuro-fuzzy
NiCd	Nickel-cadmium
NiMH	Nickel-metal-hydride
NLO	Nonlinear observer
NMC	Nickel-manganese-cobalt-oxide
NN	Neural networks
O	
OCP	Open circuit potential
OCV	Open circuit voltage
ODE	Ordinary differential equation
OSL	Online self-learning
OTR	Onset of thermal runaway
P	
PDE	Partial differential equation
PDF	Probability density function
PF	Particle filter
PHEV	Plug-in hybrid electric vehicle
PID	Proportional-integral-derivative
PNN	Probabilistic neural network
PRNN	Pipelined recurrent neural network
PV	Photovoltaic
R	
RANN	Recurrent artificial neural network
RBFNN	Radial basis function neural network
RE	Relative error
REKF	Robust extended Kalman filter
RLS	Recursive least square
RMS	Root mean square
RMSE	Root mean square error
RPT	Reference performance tests
RTI	Real-time interface
RUE	Remaining usable energy
RUL	Remaining useful life

S

SMO	Sliding mode observer
SNN	Structured neural network
SNR	Signal-to-noise ratio
SOA	Safety operating area
SOC	State of charge
SOF	State of function
SOH	State of health
SOP	State of power
SOS	State of safety
SPKF	Sigma point Kalman filter
Sqrt-UKFST	Square root spherical unscented Kalman filter
STDC	Singaporean taxi driving cycle
SVM	Support vector machine
SVMR/SVR	Support vector machine for regression

T

TECM	Thermal equivalent circuit model
TEM	Transmission electron microscopy
TGA	Thermogravimetric analysis
TIS	Thermal impedance spectroscopy
TMS	Thermal management system

U

UDDS	Urban dynamometer driving schedule
UKF	Unscented Kalman filter

W

WGN	White Gaussian noise
-----	----------------------

X

XEV	EV/HEV/PHEV
XRD	X-ray diffraction

List of symbols and constants

a_i	activity of species i [$\frac{mol}{m^3}$]
A	surface area [m^2]
C	C-rate, Coulomb: $1C = 2.7778 \times 10^{-4}$ Ah
C_1	capacitance of C_1 in the R_1C_1 element [F]
C_{act}	actual discharge capacity [Ah]
$C_{act,cha}$	actual charge capacity [Ah]
$C_{act,par,dcha}$	actual partial discharge capacity [Ah]
C_{BOL}	beginning of life discharge capacity [Ah]
C_{cha}	charge capacity [Ah]
C_{dcha}	discharge capacity [Ah]
C_N	nominal capacity [Ah]
C_p	practical capacity [Ah]
C_{rel}	released capacity [Ah]
C_{rem}	remainder capacity [Ah]
C_T	theoretical capacity [Ah]
C_{use}	usable capacity [Ah]
c_p	specific heat capacity [$\frac{kJ}{KgK}$]
C_p	heat capacity [$\frac{kJ}{K}$]
e	emissivity, Euler's number: $e = 2.71828$
I	current [A]
I_{R1}	R_1 current [A]
I_{C1}	C_1 current [A]
E	energy [Wh]
E_0	standard potential of the electrode's process [V]
F	Faraday's charge constant $F = 96485 \frac{C}{mol}$
G	Gibbs free energy
h	heat transfer coefficient [$\frac{W}{m^2K}$]
f	frequency [Hz]
k	time step index or sampled data index, thermal conductivity [$\frac{W}{mK}$]
K	constant scaling factor, kelvin
m	mass of the cell [kg]
n	charge number participating in process [\pm]
N	quantity
P	power [W]
$\dot{q}_{conduction}$	conduction heat transfer [W]
$\dot{q}_{convection}$	convection heat transfer [W]
$\dot{q}_{radiation}$	radiation heat transfer [W]
Q	electric charge [As], generated heat [W]
\dot{Q}_{gen}	total heat generation rate [W]
\dot{Q}_{irev}	irreversible joule heat generation rate [W]
\dot{Q}_{rev}	reversible entropic heat generation rate [W]

R	universal gas constant $R = 8.3144598(48) \frac{J}{molK}$
R_1	resistance of R_1 in the R_1C_1 element [Ω]
R_{1kHz}	1 kHz AC impedance [Ω]
R_{act}	actual resistance [Ω]
R_{BOL}	beginning of life resistance [Ω]
R_{ct}	charge transfer resistance [Ω]
R_d	dynamic resistance [Ω]
R_i	ohmic resistance [Ω]
$R_{i,ac}$	ohmic resistance extracted from EIS [Ω]
$R_{i,dc}$	ohmic resistance extracted from HPPC [Ω]
R_s	self-discharge resistance [Ω]
t	time [s]
t_s	sampling time [s]
T	absolute temperature of the reaction [K]
T_{core}	measured temperature in core [$^{\circ}C$]
T_{amb}	ambient temperature [$^{\circ}C$]
T_{surf}	measured temperature at the outer surface [$^{\circ}C$]
u	system input
V	voltage [V]
V_d	estimated dynamic transient voltage [V]
V_{oc}	open circuit voltage [V]
V_{R1}	charge transfer voltage [V]
V_{C1}	double layer capacitance voltage [V]
V_{R1C1}	RC element voltage [V]
V_t	terminal voltage [V]
V_z	dynamic transient voltage [V]
x	system state
y	system output
z	z-direction axial coordinate [m]
Z	impedance [Ω]
Z'	real part of the impedance [Ω]
Z''	imaginary part of the impedance [Ω]

Greek symbols

α	CPE exponent
ΔG	Gibbs free energy
ΔS	reaction entropy
ΔH	reaction enthalpy
η_c	Coulombic efficiency
Φ	electric potential [V]
μ	mean value
ω	angular frequency [$\frac{Rad}{s}$]
σ	standard deviation, Stefan-Boltzmann constant $\sigma = 5.670367(13) \times 10^{-8}$ $\frac{W}{m^2 K^4}$
σ_m	standard deviation of the measurement noise
τ	time constant [s]
θ	charge state of the stoichiometric limits of the negative electrode

Operators

$ A $	matrix determinant
A^{-1}	matrix inverse
\dot{A}	time derivative of quantity A
A^T	matrix transpose
$E\{.\}$	expected value
$var\{.\}$	variance
$Cov\{.\}$	covariance

Kalman filter symbols

A_k	system matrix
B_k	control matrix
C_k	output matrix
D_k	feed-forward matrix
\mathbf{n}_k	measurement noise
\mathbf{p}_k	parameter vector
\mathbf{x}_k	state vector
\mathbf{u}_k	system input
\mathbf{y}_k	system output
\mathbf{v}_k	process noise
\mathbf{K}_k	Kalman gain
\mathbf{L}_k	system matrix for parameter vector
\mathbf{P}_k	covariance of system state estimate error
\mathbf{Q}	covariance of process noise
\mathbf{R}	covariance of measurement noise
$\mathcal{N}(\mu, \sigma^2)$	normal distribution (Gaussian) with mean value μ and variance σ^2

1 Introduction

1.1 Work objective and motivation

Electrical energy storage (EES) systems have shown unique capabilities in various applications, from simple battery-powered devices to EVs, smart grids, and space applications. Among different electrical energy storage systems, LIBs are the most commonly used technology in EVs, hybrid, and plug-in hybrid electric vehicles (PHEVs). At the moment, pure EVs are either based on fuel cell (FC-EV) or LIB technology. Longer driving range can currently be achieved with FC-EVs, as opposed to LIB-EVs, but, in the last several years, the driving range of the LIB-EVs has increased enormously due to the strong increase of LIB energy density. Furthermore, a steep LIB price reduction has been observed within the past few years, and this trend looks promising for a longer run.

Investigations into the LIBs are not only limited to the material level, design, and production process, but have also expanded to the optimal utilization of LIBs during their lifetime. Proper control and utilization of the LIB-packs used in EVs, and other applications that require large EES, leads to improved safety, cost reduction, design simplification, and weight savings, among other benefits.

In EV application, the number of the cells used in the battery-pack may reach a few hundred or even up to a few thousand units. As LIBs are complex nonlinear electrochemical devices, this makes the EV's BMS task complicated. Monitoring algorithms, running on the BMS, must have sufficient accuracy, and contain necessary features, such as accurate monitoring of directly unmeasurable battery states, namely, state of charge (SOC), state of health (SOH), state of function (SOF), state of power (SOP), and state of safety (SOS), among other required states for that specific application.

Due to the various aging mechanisms and the external conditions, such as extreme (very high or low) ambient temperatures or mechanical stresses imposed on the LIB of an EV during operation, the design task of proper monitoring algorithms is complicated and sensitive. Developing these advanced monitoring algorithms is beneficial in various aspects. First of all, BMS provides for safe operation of the battery-pack during the lifetime of the cells. These algorithms operate the LIBs in optimum condition to maximize the lifetime of the cells within acceptable electrical parameters, so the operating depth of discharge (DOD) region can be extended, and, therefore, the useable energy is increased, which reduces the size, cost, and weight of the battery-packs. Furthermore, the BMS provides the users and workshops with all the required information about the EV storage system, which is also important for warranty purposes.

The present dissertation has been involved in the development of the EVA [1], therefore, the same LIBs were used for the investigation, modeling, and algorithm development.

Recently, many attempts have been made to develop reliable and comprehensive monitoring algorithms,

but to date, there is no fully reliable source that solves all the existing problems in terms of safety and reliability. Safety of the battery-pack is the most critical topic to be taken care of, especially with the arrival of new cell chemistries with higher energy density content on the market: A conventional BMS software may not be able to successfully monitor and control the pack.

Apart from the topic of safety, the aging characteristics of the LIBs in the battery-pack due to the usage and environmental impacts have been considered, which required conducting comprehensive testing and data analysis.

1.2 The work structure and scope of this thesis

The goal of this thesis is the development and improvement of the energy storage models, and algorithms inclusive of various monitoring algorithms, and final evaluation and implementation of the models. For these purposes, this thesis contains seven chapters, starting from the introduction in Chapter 1.

Chapter 2 provides comprehensive literature research, general information, and equations required as background for the remaining chapters of the thesis. This chapter includes control theory, modeling techniques, definitions of battery states, and estimation techniques.

Chapter 3 presents the experimental part of this work. This includes design and build-up of the battery-testing laboratory, test preparation for the device under test (DUT), and test structure. Test structure contains reference performance tests, aging tests, and additional tests, used for evaluation, and verification. For aging investigation experiments, tests have been grouped into three types: calendar life, cycle life, and drive-cycle life. The drive-cycle test is designed to investigate the real-world operating conditions on the LIBs. In this chapter, relevant parameters required for the model and algorithm development, were extracted and based on the observations, the evolution/change of the parameters due to the various conditions such as temperature or aging, are explained in detail. The parameterized cell measurements have been used in models and algorithms in the subsequent chapters.

Chapter 4 deals with model development and simulations used throughout this thesis. Cell models have been categorized into electrical models and thermal models. Electrical models were developed based on both, the time-domain and frequency-domain method according to the extracted cell parameters from the Chapter 3. In this chapter, suitable simulation model for each case has been proposed. Additionally, this chapter explains the model coupling, and upscaling for series/parallel cell connections in modules and packs.

Chapter 5 deals with algorithm development for parameter and state estimation. These algorithms have been coupled with the models developed in previous chapters to enhance their precision and accuracy. For hardware implementation, the algorithms have been tuned for optimal performance and robustness. A comprehensive comparison between different algorithms allowed for a short list of the algorithms to be implemented in the hardware in the loop (HIL) system, and in the in-house developed BMS.

Chapter 6 includes the results of the algorithm implementation in the HIL and BMS for cell level. This chapter also introduces the upscaled model and algorithms for the EVA battery-pack only based on the measurements of the total pack current, pack voltage and 108 big-cell (the definition of the big-cell is provided in this chapter) voltages. It is demonstrated how individual cell parameters, voltage, temperatures, SOC, power, and any other required information can be obtained from the battery-pack model.

Chapter 7 presents the summary, future work, and outlook.

2 Technical review of system classification, characterization, modeling, and monitoring

This chapter includes the required definitions, characterization techniques, modeling methods, and development of algorithms used for LIBs. It should be mentioned that this work can be extended to other primary and secondary battery technologies with some necessary changes. This includes lead-acid batteries (LABs), nickel-based cells, such as nickel-metal-hydride batteries (NiMH), nickel-cadmium cells (NiCd), and other LIB technologies. All the developed methods and the results presented in this thesis are reproducible and have been built-up from scratch. These methods can be further extended and utilized.

Compared to other cell technologies, LIBs provide an optimum energy-to-weight ratio with low self-discharge and no memory effect [210]. Among commercially available LIBs, nickel-manganese-cobalt-oxide (NMC), lithium-cobalt-oxide (LCO), lithium-manganese-oxide (LMO), lithium-nickel-cobalt-aluminium-oxide (NCA), and lithium-iron-phosphate (LFP) technologies are the most important ones for the EVs. Currently, the capacity of certain technologies, such as NMC, reaches 240 Ah per cell and beyond.

In this thesis, the cell used for the investigation was a high-power pouch cell (from a Korean manufacturer “Kokam”) with NMC chemistry, a nominal capacity of 63 Ah, and a specific energy of $153 \frac{Wh}{kg}$. Table 3.1 presents more details about this cell. The data sheet of this cell can be found in attachment D.1.

High specific energy, high power, good balance between cost, lifespan, and safety, and the availability in different sizes were the reasons for the selection of the high-power NMC pouch cell for EVA and research studies in this thesis. Figure 2.1 demonstrates the typical specific energy of lithium-, nickel-, and lead-based cells [38, 71, 218]. In this figure, cells with lithium titanium oxide (LTO¹) anode technology have been included for comparison purposes.

Figure 2.2 summarizes the pros and cons of commercially available cells with different technologies. From this comparison, the following results for the cell selection process have been concluded: LMO cells suffer from a short life span and poor performance; LFP cells are very safe and have a good life span, but their lower specific energy and voltage level compared to other lithium-based cells hinders them in most cell selection procedures for EV applications; NCA cells suffer from high costs and lower safety compared to other technologies at the moment; LCO cells suffer from a shorter life span and below-average specific power. For LTO cells, the cost must be lowered and specific energy needs to be improved, as is shown in the specific energy chart.

Cells with NMC and NCA technologies are currently the top candidates for EV applications due to their good overall performance and specific energy. For NMC cells, the mixture of nickel, manganese, and cobalt lowers the cost significantly, the reason is the lower content of cobalt in the cathode material. Nickel provides high specific energy, and, by using manganese, lower internal resistance can be achieved.

¹ $Li_4Ti_5O_{12}$

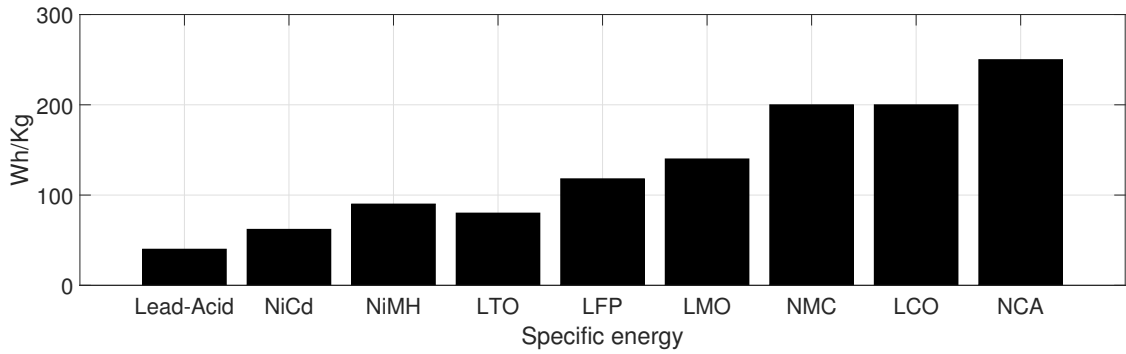


Figure 2.1: Comparison of the specific energy of lead-, nickel-, and lithium-based cells [38].

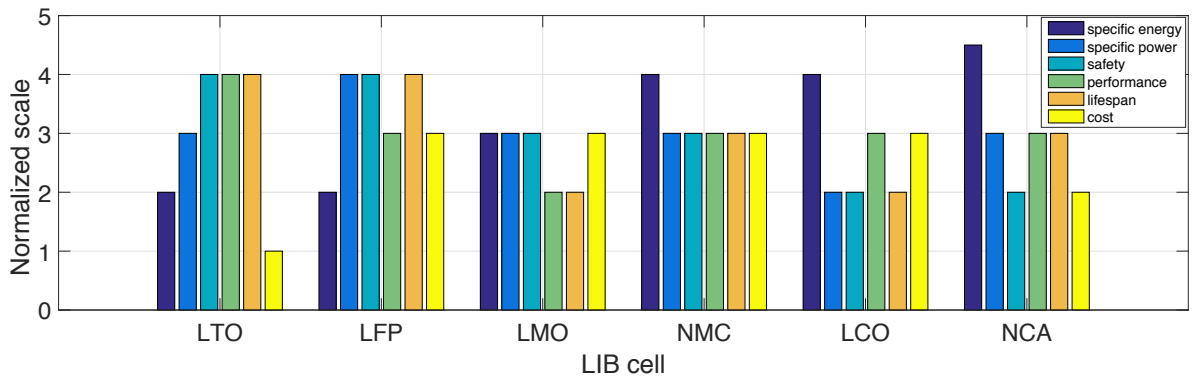


Figure 2.2: Summized details of current commercial LIBs normalized to the scale of 0 to 5, where 5 is the best scenario and 0 is the worst scenario. The figure is based on the data of [38, 71].

Aside from the cost, NMC cells, have better thermal stability compared to NCA cells. For the cell selection process, NMC technology has been considered for the EVA battery pack.

2.1 System description

A cell is the basic single electrochemical unit that converts chemical energy into electrical energy. Series and/or parallel connection of at least two cells forms a battery to achieve higher voltage levels and/or capacity.

In 1868, Maxwell used differential equations (DE) to explain the control system dynamics [279]. Dynamic systems such as LIBs can also be modeled by differential equations. The first step to modeling these complex dynamic systems with differential equations is to define the inputs and outputs of the system.

During the cell testing, sensors enable us to directly measure cell current (I), terminal voltage (V_t), and temperature (T). For a given cell, the terminal voltage and temperatures (surface/core) are the responses to the applied current (loading) at the operating ambient temperature (T_{amb}). Therefore, current and ambient temperature are system inputs, and voltage and cell surface/core temperature are system outputs. However, the LIB system has a few hidden outputs which are not directly measurable, such as SOC. Therefore, the LIB system, we are dealing with, is a multiple-input-multiple-output (MIMO) system, and these inputs and outputs can be expressed by vectors.

Voltage and current are measured directly from the cell terminals. Cell temperature is measured externally by a temperature sensor mounted directly on the cell surface or on the tabs. Cell temperature can be measured internally by specially developed sensors capable of inner cell temperature measurement as well [180]. The center of the cell, terminals, and positions near the terminals are locations of interest for surface temperature measurements.

By possessing knowledge about the system inputs and outputs, one can create and employ differential equations to describe the behavior of these complex nonlinear MIMO systems. Differential equations can be used for checking the response of the system to various inputs under different operational conditions.

Input-output (I/O) models have been widely used for battery systems [86, 133]. To describe the LIB, the relationship between the inputs and outputs of the cell should be considered. Figure 2.3 demonstrates how the device under test (DUT), can be explained with a transfer function (system function) as an input-output system. Laplace representation of the cell can be expressed with $Z(s)$ as a system impedance function (voltage-current ratio), such that $Z(s) = \frac{V_t(s)}{I(s)}$. In this function, $I(s)$ represents input to the system, such as load current, and $V_t(s)$ represents system output, such as response voltage.

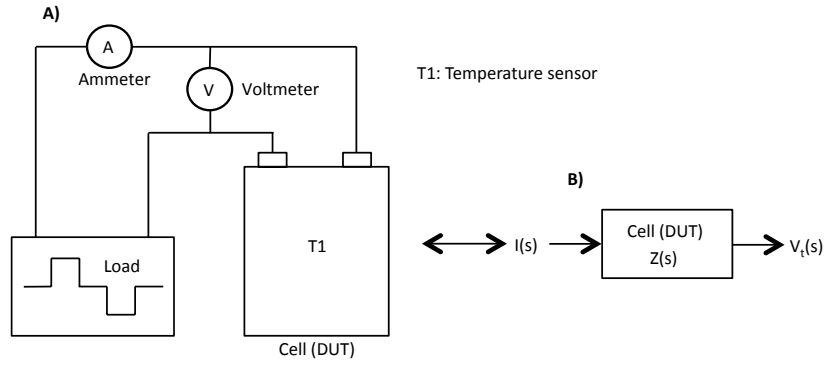


Figure 2.3: A) DUT under load, B) Transfer function representation of the DUT under load

The general system transfer function, which includes the system noise “e”, can be written as the following:

$$a(q)y_k = \frac{b(q)}{f(q)}u_k + \frac{c(q)}{d(q)}e_k \quad (2.1)$$

where:

$$a(q) = 1 + a_1q^{-1} + \dots + a_{n_a}q^{-n_a} \quad (2.2)$$

$$b(q) = b_0 + b_1q^{-1} + \dots + b_{n_b}q^{-n_b} \quad (2.3)$$

$$c(q) = 1 + c_1q^{-1} + \dots + c_{n_c}q^{-n_c} \quad (2.4)$$

$$d(q) = 1 + d_1q^{-1} + \dots + d_{n_d}q^{-n_d} \quad (2.5)$$

$$f(q) = 1 + f_1q^{-1} + \dots + f_{n_f}q^{-n_f} \quad (2.6)$$

Equation 2.1 is a general form of the plant with system input u_k , system output y_k , and the system noise e_k , where “k” is time index (sampled data index) representation [300]. Another nomenclatures in Equations 2.1 to 2.6 is “q”, which is a function of the shift operator, and indicates that the function or filter has a finite set of distinct coefficients relative to the present sample data points ($q.a(k) = a(k+1)$ and more typically: $q^{-n}.a(k) = a(k-n)$). This description corresponds to the polynomial coefficients. These coefficients are parameter sets of the system model. System parameters that are used to describe the dynamics of the plant and error models are:

$$\theta = [a_1, \dots, a_{n_a}, b_0, \dots, b_{n_b}, c_1, \dots, c_{n_c}, d_1, \dots, d_{n_d}, f_1, \dots, f_{n_f}]^T \quad (2.7)$$

In Equation 2.7, θ is the function of the parameter set and indicates that the variable’s values are sensitive to the values of the algorithm’s estimated parameters or actual model parameters.

For EVs or other sensitive applications in which proper system function and safety depends on accurate monitoring, inputs into the monitoring system are limited to voltage, temperature, and current. Normally, current and temperature data are regarded as plant input, and voltage response is considered as plant output.

Besides the limited number of inputs and outputs, cells are more complicated systems than simple transfer functions, as the response or output of the system to the system input will change under several conditions. This means cell characteristics change during normal utilization as well as over time. Operating conditions and stress factors contribute to a cell’s characterization change as well, for example, change in open-circuit voltage (OCV), capacity loss, or impedance growth. LIB operating conditions are described in Section 2.2.

2.2 LIB operating conditions

Lifespan and performance of batteries depend on the operating conditions. Operating conditions are impacted by the user requirements, environmental conditions, and also the manufacturing factors (design, limitations, defects, ...). User requirements include operating temperature, power/energy demand, maximum/minimum current, and voltage range. Other operating conditions such as pressure, and pressure build-up on the cells², could be due to the design limitations.

Operating conditions are both, internal and external. External operating conditions in the realistic driving environment of an EV are driving mode (including the driver behavior), power duty, current fluctuations, changes in ambient temperature, vibration, and shocks [58]. Other external operating conditions are over-discharge, short circuit, and other abusive conditions [90].

Internal operating conditions are the SOC operating window, self-discharge, and internal temperature among other internal operating conditions. By understanding the relation between these operating conditions and investigation of the LIBs aging behavior, the lifespan of the cells can be improved [261]. If there is no constraint imposed on the battery operation, the operating conditions can become abusive. Operation conditions in this thesis are considered as the subset of the safety operating area (SOA), and one should not violate these safety limits. Section 2.3 deals with the LIB characterization

² For instance, cell-to-cell force build-ups due to cell swelling

methods, with defined operating conditions.

2.3 LIB parameters

Energy storage systems should be characterized to investigate their aging, performance, or model development. This can be done by extracting their parameters. In general, characterization tests are performed in-situ and ex-situ, they can be destructive or non-destructive. Based on the area of LIB utilization (EV/PHEV/HEV), main non-destructive characterization tests comprise:

- Hybrid pulse power characterization (HPPC)
- Electrochemical impedance spectroscopy (EIS)

Using the HPPC method, parameters of the cell are time-dependent, while, on the other hand, using the EIS method, cell parameters are frequency-dependent. Models based on the time-domain characterization technique can be directly employed in embedded systems, such as a low-cost target microcontroller and BMS, whereas the EIS method requires additional effort for parameter fitting and approximations.

Comparing both techniques, the EIS method provides deeper insight into the cell and provides more information about the LIBs impedance behavior. These include for instance, the information about the frequencies where the zero-crossing ohmic resistance, and charge transfer resistance take place. With EIS method, the effect of temperature, cycle-life, and calendar-life can be determined as well. The HPPC method is useful for areas where the OCV measurements are necessary, and also pulse power capabilities should be determined. Sections 2.4.3.2 and 2.4.3.3 present the fundamentals of HPPC and EIS characterization techniques. Both techniques are employed in Chapter 3.

Obtained LIB parameters of interest with these methods are discharge capacity, impedance, OCV, and thermal parameters. These parameters have been used for model development and evaluation purposes.

- Discharge capacity and electrical charge:

The amount of electric charge (Q) delivered by a source, such as an electrical energy storage system (cells, batteries, or other energy storage systems) is $Q = \int_0^t I(t)dt$ where “t” is time (s). For batteries, the capacity is expressed in ampere-hours³ (Ah).

Discharge rate and temperature conditions define the available capacity of the LIB. LIBs have a theoretical capacity (C_T) assuming 100% utilization of active materials, that is calculated by use of Faraday’s Law [91]. In practice, a much smaller portion of active material is utilized in a LIB. Rated/Nominal capacity (C_N) is defined by manufacturer under certain specified conditions, that is, the amount of charge delivered from a fully charged LIB under specified temperature and loading conditions. Practical capacity (C_p) can be lower or higher than the nominal capacity; however, the usable capacity (C_{use}) is limited to the operation and electrical parameters of the application. Actual capacity (C_{act}) is the maximum available capacity and is used for calculation of the SOC and SOH. Released capacity (C_{rel}), is the capacity released during the discharge. Remained capacity (C_{rem}), is the available capacity after the discharge, so basically $C_{act} = C_{rem} + C_{rel}$.

Usable capacity is not constant during the cell’s life-time. Different aging mechanisms will lead to

³ 1 Coulomb = 2.7778×10^{-4} Ah

capacity deterioration over time. Capacity deterioration is regarded as either irreversible capacity loss (fade) or reversible capacity loss under some conditions. Charge capacity (C_{cha}), is the capacity measured during charge, from fully discharged state to the fully charged state, under nominal conditions. Finally, discharge capacity (C_{dcha}) is the capacity measured during the discharge of the cell, from full state to the lower cut-off voltage^{4,5}.

- **Impedance, capacitance, and inductance:**

The transfer functions describing the LIB electrical model, is based on the total impedance of the cell. During the EV operation, impedance parameters are estimated by the BMS. Impedance parameters are analyzed for temperature estimation, power prediction, SOH estimation, and remaining useful life (RUL) prediction.

Pure ohmic resistance ($R_{i,dc}$) of the cell, is commonly used for SOC, SOH, aging analysis, power prediction, and heat generation calculation [123]. $R_{i,dc}$ causes the instantaneous voltage drop at the beginning of the current flow. This parameter is current-, temperature-, SOC-, and SOH-dependent. $R_{i,dc}$ can be approximated in real time with the current pulse technique. Due to the physical limitation of the testers and logging devices, it is not possible to accurately measure this parameter with the pulse technique, but it has a good approximation.

Complex impedance, also known as electrochemical impedance, is a complex quantity that is acquired from the cell with EIS measurement. For LIBs, EIS measurements are usually conducted in galvanostatic mode with a DC current as input excitation, superimposed by a sinusoid waveform.

1 kHz impedance (R_{1kHz}) measured by conventional impedance analyzers is usually taken as cell AC impedance, which used in the manufacturer's cell data sheet. The AC impedance parameter is influenced by SOC, operating temperature, and SOH. Another important parameter is $R_{i,ac}$, which is equal to the zero crossing value in the Nyquist diagram (where inductive and capacitive parts are equal and cancel out each others effect).

$R_{i,dc}$ has been calculated in Section 2.4.3.2, showing, slightly different values compared to $R_{i,ac}$, calculated in Section 2.4.3.3. A more detailed study of $R_{i,dc}$ versus $R_{i,ac}$ can be found in [157]. Capacitance usually corresponds with the double-layer capacitance of the cell, and for simplification, is considered current-independent. The inductance is basically caused by the cell design⁶ and wirings, and it can be measured at high frequency ranges in the Nyquist diagram.

- **OCV:**

OCV represents the no-load open-circuit voltage of the electrical energy storage system. OCV is different from the equilibrium voltage, as there are more reactions involved during OCV measurement. The equilibrium state is only reached when there is no further internal process in the energy storage system; however, reaching full equilibrium state might take up to several hours of relaxation time. The sum of the equilibrium potentials of the battery electrodes is know as electromotive force (EMF), and can be measured with the voltage relaxation technique, linear interpolation, or linear extrapolation [192].

OCV has a slow change with relation to the cell's time constant. After a few hours of relaxation during

⁴ Depending on the design requirements, the conditions are selected

⁵ Cut-off voltage is defined as the minimum allowable voltage, that generally defines the "empty" state of the battery

⁶ for example metallic connection between the electrodes and terminals

which, changes over time are small ($\frac{\partial V_{OC}}{\partial t} \rightarrow 0$), OCV is an approximation of EMF. OCV, in general, is a function of SOC, SOH, temperature ($OCV = f(SOC, SOH, T)$). Usually, OCV is measured when the LIB is not under load (zero current) and has rested for several hours. OCV is a complex parameter, depending on the loading direction (charge or discharge), the equilibrium voltage can capture different values. This is known as the hysteresis effect [73]. The average OCV value during charge and discharge is usually considered as the OCV of the cell.

OCV measurement techniques can involve either charging and discharging the cell at an extremely low current ($I < C/100$) and taking the average of the measured voltage, or by charging and discharging the cell stepwise to certain SOC values and giving sufficient rest time to the cell. OCV is defined as:

$$V_{oc} = E_0 + \frac{RT}{nF} \ln \frac{a_o}{a_r} \quad (2.8)$$

where “ E_0 ” is the standard potential of the electrode’s process, “ R ” is the universal gas constant⁷, “ T ” is the temperature of the reaction, “ F ” is the Faraday charge constant ($F = 96485 \text{ C mol}^{-1}$), “ n ” is the charge number participating in the process, and “ a_o/a_r ” are the activity of oxidized/reduced species [94, 300].

2.4 Battery system modeling

LIB modeling is mandatory for BMS operation. Modeling methods are classified into three general categories. These categories include white-box, black-box, gray-box. In a common white-box model, the model is constructed by means of rigorous physical descriptions. For LIBs, the white-box model is widely known as the electrochemical model, and, equivalently, white-box testing means testing electrochemically active cells.

During white-box electrochemical modeling of LIBs, all the reactions in the cell with enhanced fidelity over the full range of the LIB operation are considered; however, the development of a robust and accurate model with improved performance at the system level with this method is critical. For model upscaling from single-scale cells to larger-scale modules or to a LIB pack, this method can not be recommended unless several simplifications are considered. More details are presented in Section 2.4.2. Black-box modeling is the opposite of white-box modeling. These models do not necessarily contain a structure compatible with the underlying reality (no physical explanations of the process). In the black-box modeling case, a preferred general model structure is selected and relevant parameters are obtained from or during the measurements (online, offline). The equivalent-circuit model (ECM), Fuzzy logic controller, neural network, stochastic models, and Shepherd model are an instance of a black box model [248].

For many real-time applications, it is necessary to simulate the LIB performance in order to properly evaluate and design the total system. A more comprehensive and accurate physical model, which includes real physical parameters, which is able to capture the fast dynamics of the cell, is hard to obtain. For that, a combination of a black-box modeling and a white-box modeling approach called gray-box modeling can be utilized. This type of modeling is also known as fractional modeling. Gray-box models can be used to capture the required parameters for dynamic, real-time applications and more efficient aging investigation, and local current/temperature distribution studies can be performed. Similar to

⁷ $R = 8.3144598(48) \frac{J}{molK}$, the two digits in parentheses are the uncertainty (standard deviation) in the last two digits of the value

white-box and black-box modeling, gray-box modeling also varies in complexity. In [181] a dynamic model of the LAB using EIS technique has been presented, which is considered as a gray-box model. Comprehensive gray-box modeling techniques for offline and online approaches can be found in [95]. In this work, the focus of the system modeling has been directed towards LIBs in EV application over a wide range of operation conditions, hence simpler ECM technique was implemented. The goal of system modeling in the field of energy storage systems, specifically LIBs, is to establish methods to accurately monitor the system states, provide safety for the system, and, at the same time, provide a physically meaningful description of the cell.

2.4.1 Empirical modeling techniques

There are popular methods proposed in the literature that can be used to describe the cell or to model the cell voltage. These models are known as empiric- (generic- or analytical-) based models, which are listed under the black-box category. Empiric models are relatively easy to develop. Model parameters can be extracted from battery data sheet. In most cases, only the SOC of the cell is considered as the state variable. These models are based on the equations established according to the battery full-charge and full-discharge curves at various current amplitudes. The following part introduces various empiric methods used to model the cell terminal voltage and OCV.

- Empirical terminal voltage and OCV modeling:

Equation 2.9 presents the famous standard Shepherd equation, which is widely used to model the cell terminal voltage (charge and discharge curves) of the cell with the empirical data [248]. Shepherd equation parameters are found by taking a few voltage reference points (e.g., three reference points) on the cell voltage curve and calculating the coefficients in a backward manner.

Another famous model that is SOC-dependent is the Nernst model (Equation 2.10), which describes the cell voltage as a function of SOC. However, this should not be confused with the Nernst equation, which is used to describe the OCV of the cell. Equation 2.11 is known as the combined model of the simplified Nernst model and other empirical models. For these models, one should consider the following assumptions:

- Discharge/charge of the battery should be under constant current
- Polarization is linear over the range of current densities
- Internal resistance is constant (except for the Shepherd equation, where the resistance is SOC-dependent)
- Temperature is constant

$$\text{Shepherd [248]:} \quad V_t = K_0 - R_i I - K_1 \frac{Q}{Q - It} I + A e^{(-\frac{BIt}{Q})} \quad (2.9)$$

$$\text{Nernst [111]:} \quad V_t = K_0 - R_i I - K_1 \ln(\text{SOC}) + K_2 \ln(1 - \text{SOC}) \quad (2.10)$$

$$\text{Combined model [265]: } V_t = K_0 - R_i I - \frac{K_1}{SOC} - K_2 SOC + K_3 \ln(SOC) + K_4 \ln(1 - SOC) \quad (2.11)$$

where V_t is the cell model terminal voltage, and R_i is the ohmic resistance. Coefficient K_0 is a constant equal to the OCV at 100% SOC. For model fitting, coefficients (K_1 , K_2 , K_3 , and K_4) are chosen in a way that the model matches the experimental measurements. The combined model in Equation 2.11 fits best among others [200].

To enhance the empiric models, because the coefficient does not contain any physical interpretation, but can be related to the operational conditions, such as ambient temperature or current amplitude, these operating conditions should be foreseen through these coefficients. To take these influences into account, all the parameters are considered to be dependent on the temperature and current amplitude, so experimental tests should be repeated for the desired operating conditions, dependent upon the application for which the cells are meant to be used.

Similarly to the empirical modeling of the cell's terminal voltage, OCV can be formulated by fitting functions as well. Modeling of OCV facilitates the aging investigation based on OCV changes over time, and it can also be used to study the temperature effects (e.g., entropy investigation), and the development of monitoring algorithms. In the following equations, OCV is a nonlinear function of SOC; however, the effect of the temperature is not directly reflected, so the temperature effect should be compensated.

In [202], OCV was extracted from the combined model in Equation 2.11, which is shown in Equation 2.12:

$$V_{oc}(SOC) = K_0 - \frac{K_1}{SOC} - K_2 SOC + K_3 \ln(SOC) + K_4 \ln(1 - SOC) \quad (2.12)$$

where OCV is a nonlinear function of the natural logarithm of SOC. In [115], OCV was expressed as:

$$V_{oc}(SOC) = K_0 + K_1 e^{-\alpha_1(1-SOC)} - \frac{K_2}{SOC} \quad (2.13)$$

In [118], a double exponential function for OCV modeling has been suggested, which is shown in Equation 2.14:

$$V_{oc}(SOC) = K_0 + K_1(1 - e^{\alpha_1 SOC}) + K_2(1 - e^{-\frac{\alpha_2}{1-SOC}}) + K_3 SOC \quad (2.14)$$

In [52], OCV is expressed as:

$$V_{oc}(SOC) = K_0 + K_1 e^{-\alpha_1 SOC} + K_2 SOC + K_3 SOC^2 + K_4 SOC^3 \quad (2.15)$$

In [299], OCV has been expressed as a function of pure polynomial form:

$$\begin{aligned} V_{oc}(SOC) = & K_0 + K_1 SOC + K_2 SOC^2 + K_3 SOC^3 \\ & + K_4 SOC^4 + K_5 SOC^5 + K_6 SOC^6 + \dots \end{aligned} \quad (2.16)$$

In [200], OCV has been introduced as a combination of polynomial fit with natural logarithmic terms:

$$V_{oc}(SOC) = K_0 + K_1 SOC + K_2 SOC^2 + K_3 SOC^3 + K_4 / SOC + K_5 \ln(SOC) + K_6 \ln(1 - SOC) \quad (2.17)$$

In these equations, $K_0, K_1 \dots K_6, \alpha_1,$ and α_2 are tunable parameters. These tunable parameters can be calculated at different life cycle stages to represent the OCV under different aging conditions. Many sources introduce various fitting functions (parametric models) to model the cell OCV; however, the equations above mainly differ in complexity and fitting precision. As the cells age or the temperature varies, these functions may not be able to present the accurate OCV of the cells.

Sometimes, an ECM is used to represent the OCV. In [153], a parallel RC circuit has been used to model the OCV for the ECM. In this model, R_s or a self-discharge resistance (in the range of $k\Omega$ for large pouch cells) is used to model the leakage current. From the above OCV models, in this work, a polynomial expression of the OCV has been used.

2.4.2 Electrochemical modeling (white-box)

Electrochemical models are considered the most detailed and comprehensive modeling method for LIBs. First electrochemical models were based on porous electrode and Li-ion transport in the electrolyte by the concentrated solution theory along the thickness dimension of the cell [87, 189]. According to the porous electrode theory, electrode lattice structure is approximated by spherical solid particles that hold Li-ions in the solid phase. Spherical solid particles are immersed in electrolyte. The intercalation process is simulated by Li-ions moving into or out of the spherical solid particles.

Fast processors make the simulation of 2D and 3D electrochemical models more feasible. With 2D and 3D models, inhomogeneity in current and temperature can be studied. These studies will lead to better cell design, that avoids local accelerated aging, performance reduction, and reduced utilization. LIBs model represented by electrochemical methods can be solved with a set of continuum scale governing equations in the form of partial differential equations (PDE). By solving these PDEs, an explanation of the electrochemical kinetics and ion transport processes can be understood. A coupled version of 1D and 2D current collector models results in pseudo-3D (P3D) models.

Table 2.1 presents the major studies on different multiphysics modeling, including 1D, 2D (P2D), 3D (P3D) electrochemical-thermal models available in the existing literature.

Table 2.1: A summary of electrochemical models from literature

Multiphysic models	without thermal	including thermal model
1D	[69, 70, 139, 149, 325]	[330]
2D/P2D	[29, 72, 87, 320]	[17, 258, 317, 319]/[43, 318]
3D/P3D	[286]/[104]	[55, 92, 179, 310, 96]

In this table, 1D models are potential candidates to be examined for possibilities of being employed

for real-time applications. In [149], a 1D electrochemical model-based observer is introduced for more detailed LIB modeling. This model suggests current distribution and SOC estimation within individual electrodes; however, the model was reduced significantly by assuming constant electrolyte concentration and approximations in diffusion equations.

To enable a better study and modeling of LIBs, electrochemical models can better explain the non-uniform distribution of current, voltage, and temperature. However, there is not a simple way to extract the system states, such as SOC or SOH, from the electrochemical models that can be used for BMS. Moreover, it would be difficult to measure the required physical parameters on a cell-by-cell basis in a high-volume consumer product [200].

2.4.3 Type of equivalent-circuit models

In this thesis, to model the electrical and thermal behavior of the cells, two ECMs have been developed. The term “ECM” is dedicated to the electrical equivalent-circuit model, that simulates the cell terminal voltage. The term “TECM” is dedicated to the thermal equivalent-circuit model, that simulates the surface and core temperatures of the cell.

2.4.3.1 ECM

The general model structure including both ECM and TECM is presented in Figure 2.4. For this structure:

- Battery data (sensor measurements) have been captured during testing: current, voltage, and temperatures (ambient temperature and the cell surface temperature)
- Measurement data have been preprocessed, analyzed, and parameters were identified
- Parameters have been fed to the models
- Each model performs certain tasks, and produces certain outputs (for instance, the ECM simulates the cell terminal voltage)
- Models have been coupled with each other and interact during the operation (e.g., exchange of parameters)
- If required, upscaling can be used for pack-level simulation

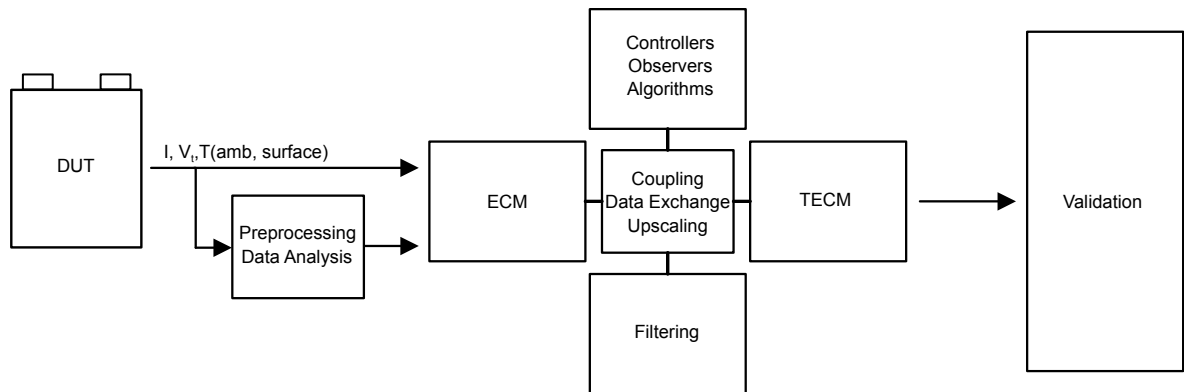


Figure 2.4: Overview of the interaction between the models in this thesis

The ECM can be employed to predict some behaviors of the LIB. With an ECM model, to some extent, the underlying physical processes of LIBs can be explained. While the application of the ECM is limited compared to the electrochemical models, their fast computation time, and acceptable accuracy, makes them the favorable choice for BMS.

In this thesis, for electrical equivalent-circuit model, the term ECM is used. ECM, takes an electrical circuit that includes a series and parallel connections of inductors, capacitors, and resistors. To complete the ECM model, a voltage source that represents the OCV should be added. ECM can be parameterized in the time-domain, where the model parameters are purely resistive, and capacitive elements. Figure 2.5 represent some popular ECMs that fit the LIB behavior in the time-domain. For EV application, an over-simplified model, such as a series connection of a resistor⁸ and a voltage source, may lead to simulation inaccuracies [237], while models with several elements will lead to more complexities. Therefore, an ECM with 1RC, or 2RC elements is a good compromise.

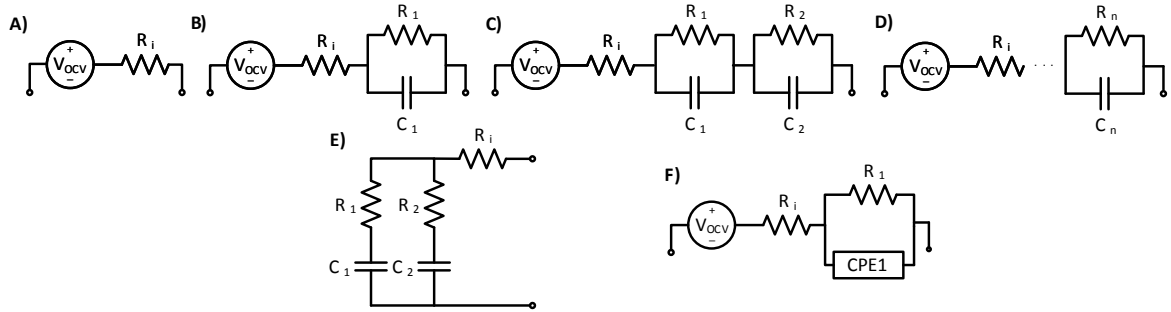


Figure 2.5: A) A simple ECM representing a cell with a resistor, and OCV source, B) ECM with 1RC element to capture the cell dynamics, C) ECM with 2RC elements for a better physical interpretation, D) ECM with three or more RCs (the physical interpretation of the parameters can be challenging), may produce a better fit, E) ECM used for LABs, including surface and bulk capacitor, F) A fractional model (CPE: constant phase element)

ECM can be based on the frequency-domain characterization as well. In this case, the model elements are based on more complex impedance parameters such as ZARC ($R||CPE$) and Warburg impedance (Z_w) [24]. A generalized ECM for EIS measurements is presented in Figure 2.10 A. Based on this generalized model and the observation of the EIS results from Chapter 3, a reduced model was proposed and implemented in Section 4.2. In [121], ten different schemes for EIS-based electrical models have been collected from various research groups. Table 2.2 presents the ECM models with different complexities found in literature.

EIS is sufficient to extract the impedance parameters of the cells at different temperature levels, SOCs, and cell aging conditions. However, to develop a full ECM, based on the EIS technique, a few considerations have to be taken into account. For instance, ZARC and Warburg elements need to be approximated, and also OCV source has to be added in series to these elements to complete the ECM. This is presented in Section 4.2.

Electrical models can be implemented with Matlab/Simulink, among other programming tools. In [124, 125, 150], Matlab/Simulink is used to simulate the cell, particularly with the US federal test procedure (FTP) drive-cycle, which is also known as the Urban Dynamometer Driving Schedule (UDDS), FUDS,

⁸ The series ohmic resistance can be a constant value or a variable depending on the defined operating conditions

Table 2.2: Summary of ECMs used for terminal voltage simulation

Model complexity	EIS	HPPC/Pulse technique
1 CPE/RC	[34, 181]	[198, 88, 120, 295, 269]
2 CPE/RC	[23]	[22, 52, 61, 145, 178, 234, 302, 269]
≥ 3 CPE/RC	[243]	[12, 224, 269]

and LA-4 cycle⁹ [230]. This drive-cycle was used in this work as well. The next two sections present the methods used for ECM parameterization.

2.4.3.2 The fundamentals of the time-domain characterization (HPPC-based)

The main intentions of the HPPC test are characterization of energy storage systems, and determination of the dynamic power capability of the system over its usable capacity and voltage range. The HPPC testing profile includes both discharge and regenerative pulses. For this thesis, during the step discharge, the procedure of discharge and regenerative pulses is repeated for a period of time until the DUT is completely discharged. The duration of the current pulses, rest phases, and other specifications are subject to changes based on the testing condition requirements.

The HPPC test was mainly used as a means of LIB parameter identification. Pure ohmic resistance, charge transfer resistance, double-layer capacitance, diffusion resistance, and OCV values are functions of SOC, temperature, and SOH (mainly the cycle number). These are among the parameters that can be extracted using the HPPC technique. In Table 2.3, the most recent battery test manuals for EVs, PHEVs, and 12 V start/stop vehicles describing the detailed testing procedure for LIBs, are presented. The detailed standard HPPC test is described in these manuals as well.

Table 2.3: Battery testing manuals used for EVs, PHEVs, and 12 V start/stop vehicles

Test manual	reference
PNGV Battery Test Manual	[2]
Battery Test Manual For 12 Volt Start/Stop Vehicles	[25]
Battery Test Manual For Plug-In Hybrid Electric Vehicles	[59]
Battery Test Manual For Electric Vehicles	[60]

To fulfill the requirement of this thesis, the standard HPPC test method was modified to fit the testing requirements. The modified HPPC profile is shown in Figure 2.6. At the beginning of the test, a complete constant-current (CC) discharge and a subsequent complete charge in constant-current constant-voltage (CCCV) were performed on the cells. To calculate the maximum discharge capacity of the cell that can be used for SOC calibration and SOH estimation purposes, from the fully charged

⁹ This cycle should not be confused with the UDDS schedule for heavy-duty vehicles

state, a standard discharge (CC discharge until the cell's lower cut-off voltage, according the manufacturer recommendation for commercial cells) was performed on the cells. The calculated discharge capacity at this step (C_{dcha}) is an important parameter of the LIB, which can be used to the determination of the specific energy¹⁰ [$\frac{Wh}{kg}$]. Volumetric energy density ($[\frac{Wh}{l}]$) is an important parameter of a single cell and a pack as well. These parameters can be calculated as well. After determining the discharge capacity, cells were fully charged to perform the pulse test.

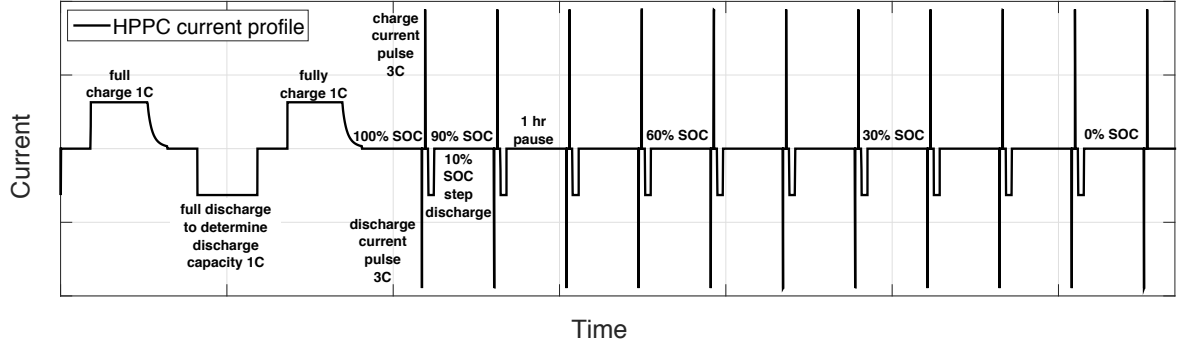


Figure 2.6: Modified HPPC profile used to parameterize the LIB in the time-domain

Battery model parameters were calculated at every 10% ΔSOC steps (SOC = 100%, 90%, ..., 10%, 0%), and at room temperature¹¹ (25°C). Interpolation can be used for parameter approximation between these SOC steps. Discharge and charge current pulses with known amplitude and duration, were given at these 11 SOC steps. Voltage response to the test profile was measured as well. Any type of LIB, regardless of chemistry, size, shape, or format, can be characterized by this technique. With this method, ECM with one, two, or more RC elements can be parameterized as well. Using more RC elements leads to a better model fit to the experimental measurements at the cost of a higher effort. Figure 2.7 demonstrates a typical characterization pulse, and the respective voltage responses. In this figure, three elements required to model the LIB are presented as well. These elements were used as the basis for developing the ECM, and also the transfer function as shown in Figure 2.3.

According to the Figure 2.7 B, the main parameter (first element) that can be extracted from the voltage response, is the no-load behavior or the OCV of the cell. Depending to the cell, OCV depends on SOC, operating ambient temperature, cell temperature, and SOH. Just before the discharge pulse starting at point 1 (P1), as indicated in Figure 2.7 A, the OCV was recorded. This is also presented with Equation 2.18. In this figure, the OCV at P1 is expected be equal to the OCV at P9 (only if sufficient relaxation time is given). This is because that during the charge pulse, the same amount of Ah was charged back to the cell.

$$V_{oc} = V_{P1} \approx V_{P9} \quad (2.18)$$

The OCV values, between the desired SOC steps, can be calculated by interpolation. Accurate OCV measurement is a key to a successful model development. OCV should be measured for a wide range of temperatures. Specially, for very high, and very low SOC, more data points are required.

Another parameter of interest, is the ohmic resistance (R_i) of the cell. This parameter dictates the ohmic behavior of the cell. Right after the pulse, an immediate voltage change occurs. This immedi-

¹⁰ Cell voltage, and total cell weight, should be taken into account as well

¹¹ For scientific work, room temperature is taken to be about 20°C to 25°C with an average of 23°C

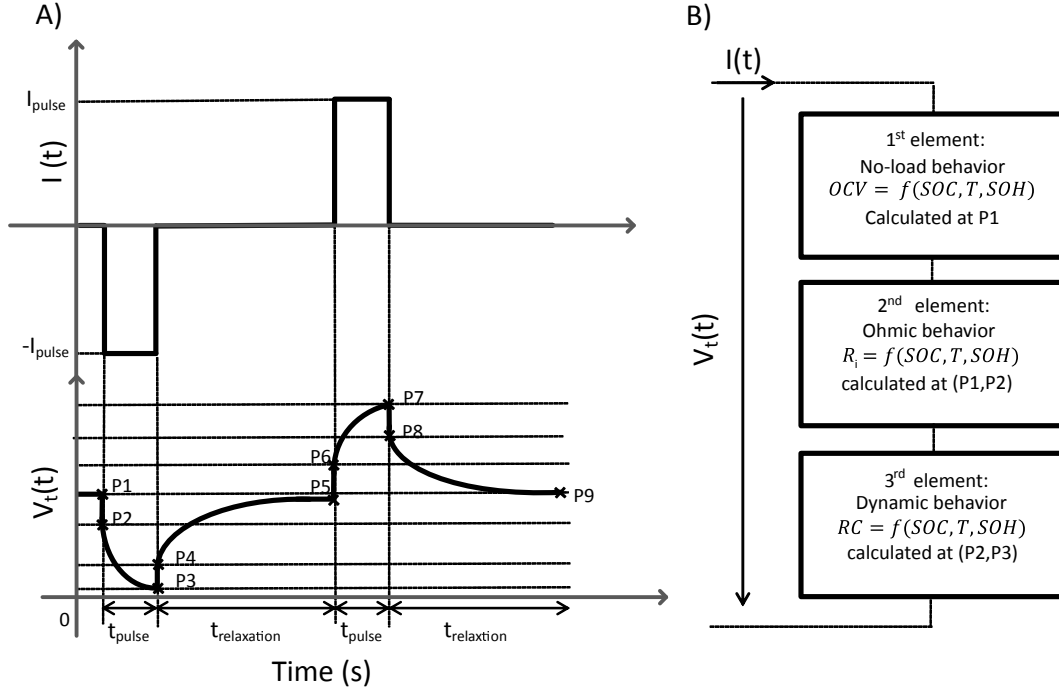


Figure 2.7: A) LIB typical voltage response to the current pulses, respective voltage points are marked (“P”), B) No load, ohmic, and dynamic behavior of the LIB ($I(t)$: load current, and $V_t(t)$: terminal voltage response)

ate voltage change is mainly due to the ohmic resistance. In [233], several methods for determining the ohmic resistance of the LIB are suggested and compared. These include a use of quasi-adiabatic calorimeter, the energy loss method, and switching current method to determine the ohmic resistance. Ohmic resistance can be affected by SOC, operating temperature, pulse amplitude and aging of the LIB. Each of these influences should be considered.

Depending on the accuracy and sampling rate of the data logger, if the voltage change is big enough¹², the ohmic resistance of the cell can be calculated approximately (assuming the negligible wiring resistances). This is shown in Equation 2.19. The reason that the R_i can be only approximated, lies in the fact that the short time constant of the fastest RC elements overlays this measurement, which is because of the physical limitation of the data logger. To accurately calculate this parameter, an infinitely fast voltage change due to the infinitely fast current change needs to be measured, which is practically impossible because of the test equipment limitations.

In general, for each of the 11 SOC points, for charge/discharge pulses, and depending on current switching status (on/off), four R_i values can be calculated. This is shown in Equation 2.19:

$$R_{i1} = \frac{|V_{P1} - V_{P2}|}{|-I_{pulse}|}, R_{i2} = \frac{|V_{P3} - V_{P4}|}{|-I_{pulse}|}, R_{i3} = \frac{|V_{P5} - V_{P6}|}{|I_{pulse}|}, R_{i4} = \frac{|V_{P7} - V_{P8}|}{|I_{pulse}|} \quad (2.19)$$

where R_{i1} is the ohmic resistance at the start of the discharge pulse, R_{i2} is the cell’s ohmic resistance during the discharge pulse switch-off, R_{i3} is the ohmic resistance at the start of the charge pulse, and R_{i4} is the cell’s ohmic resistance during the charge pulse switch-off. The ohmic resistance is important for building the ECM, it is also directly affects the specific power of the cells. This parameter was used to calculate the heat losses and power ability of the LIB. In Section 4.3, the contribution of the

¹² Bigger than the signal-to-noise ratio (SNR), and the data logger resolution accuracy

ohmic resistances in the heat generation is demonstrated. In this thesis, for more simplification, and based on the study in [269], only R_{i1} (denoted as R_i) was used in the ECM.

To model the dynamic behavior of the LIB, RC parameters should be identified (third element of ECM model in Figure 2.7 B). Every RC circuit has a time constant. For charge transfer, and double-layer capacitance, the time constant is relatively small (some 10 ms to a few seconds) [133]. Assuming a short pulse of few seconds, while $R_{1,dcha,pulse}$ and $C_{1,dcha,pulse}$ represent the charge transfer and double-layer capacitance during the discharge pulse, and $R_{1,cha,pulse}$ and $C_{1,cha,pulse}$ representing the charge transfer and double-layer capacitance during the charge pulse, the resistance and capacitance of the RC element in the ECM model can be calculated as follows:

$$R_{1,dcha,pulse} = \frac{|V_{P2} - V_{P3}|}{|-I_{pulse}|} \quad \text{and} \quad R_{1,cha,pulse} = \frac{|V_{P6} - V_{P7}|}{|I_{pulse}|} \quad (2.20)$$

$$C_{1,dcha,pulse} = \frac{\tau_1}{R_{1,dcha,pulse}} \quad \text{and} \quad C_{1,cha,pulse} = \frac{\tau_2}{R_{1,cha,pulse}} \quad (2.21)$$

In equation 2.21, “ τ ” (τ_1 during discharge pulse, and τ_2 during charge pulse) is the system time constant. One time constant (1τ) corresponds to the moment when 63.2% amplitude¹³ of the final voltage (caused either by the pulse step response for charge/discharge directions, or during relaxation) is reached. The cell voltage after “ 5τ ” reaches about 98% of its final voltage amplitude. The RC element can also be measured during the rest phases after the pulses. During current switch-off, $R_{1,dcha,relax} = \frac{|V_{P5} - V_{P4}|}{|-I_{pulse}|}$ and $R_{1,cha,relax} = \frac{|V_{P8} - V_{P9}|}{|I_{pulse}|}$, and, by considering the corresponding time constants, capacitance values can be calculated. According to the study in [269], the ECM is more accurate, when the parameter identification is performed during the short pulses, rather than the relaxation phases. For this reason, the parameter identification was performed during the discharge pulses. Identified parameters have been fed in the form of look-up-table (LUT)¹⁴ to the ECM presented in Figure 2.8:

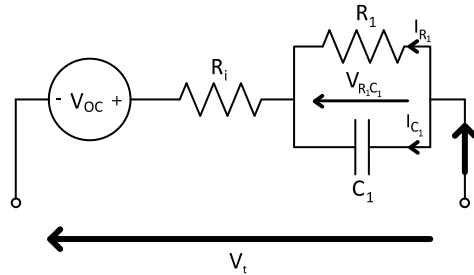


Figure 2.8: Time-domain LIB model (LIB-ECM) used to reproduce the LIB terminal voltage, OCV reproduces the no-load behavior of the cell, which is represented either by analytical, or empiric expressions. All parameters and OCV are a function of SOC, temperature, and SOH

For the LIB-ECM, by considering $I = I_{C_1} + I_{R_1}$ and $I_{C_1} = C_1 \dot{V}_{R_1C_1}$, voltage of the RC circuit ($V_{R_1C_1}$) can be derived:

¹³ τ corresponds to the time, when the system's step response reaches $1 - 1/e \approx 63.2\%$ of its final value, where Euler's number is $e = 2.71828$

¹⁴ LUT is a one-to-one relation obtained in an empirical way

$$\dot{V}_{R_1C_1}(t) = \frac{1}{C_1}I(t) - \frac{1}{R_1C_1}V_{R_1C_1}(t) \quad (2.22)$$

For the ECM, assuming that OCV is superimposed by the dynamic transient voltage (V_z), the terminal voltage of the LIB can be written as:

$$V_t(t) = V_{oc} + V_z \quad (2.23)$$

where V_{oc} represents the open circuit voltage, and is SOC-, temperature-, and SOH-dependent - ($V_{oc}(SOC, T, SOH)$). The dynamic transient voltage is caused by the battery internal parameters ($\theta = [R_i, R_1, C_1]^T$), and can be approximated by the high-pass filtering of the terminal voltage. V_z can be defined as:

$$V_z = R_i I(t) + V_{R_1C_1}(t) \quad (2.24)$$

By substituting Equation 2.24 into Equation 2.23, the general equation for the LIB terminal voltage becomes:

$$V_t(t) = V_{oc} + R_i I(t) + V_{R_1C_1}(t) \quad (2.25)$$

In the above equations, it is assumed that the parameters ($\theta = [R_i, R_1, C_1]^T$) are SOC-, temperature- and SOH-dependent ($\theta = f(SOC, T, SOH)$). These parameters were extracted with Matlab script. The results of the time-domain characterization, over various operating temperatures, and cyclic aging, are presented in Section 3.4.2.

The aging effect could appear in the LIB time constants. When the cell ages, the final amplitude of the voltage drop due to the step pulse response changes, hence the time constant related to the 63.2% of the final voltage drop would change as well. However, detailed investigation on the aging related time constants of the LIB is outside the scope of this thesis. For simplicity, the RC parameters have been identified for the fixed 10 s discharge pulses, over the wide range of SOCs, so not only the charge transfer and double-layer capacitance, but the diffusion effects could partly contribute to this parameter.

Generally, for electrical and electrochemical systems such as energy storage systems, total impedance of the system is equivalent to the transfer function of the system. To obtain the transfer function of the ECM circuit shown in Figure 2.8, the total admittance of the parallel R_1C_1 connection is $Y(j\omega) = \frac{1}{R_1} + j\omega C_1$ where “ ω ” is the angular frequency of the current excitation. For $y(t) = V_t(t) - V_{oc}$ and $u(t) = I(t)$, the transfer function of the total impedance in the Laplace domain ($Z(s)$) becomes (see Figure 2.3):

$$Z(s) = R_i + \frac{1}{\frac{1}{R_1} + C_1 s} = \frac{R_i + R_1 + R_i R_1 C_1 s}{1 + R_1 C_1 s} \quad (2.26)$$

The terminal voltage of the cell can be also described as:

$$V_t(s) = V_{oc} + Z(s)I(s) = V_{oc} + \left(R_i + \frac{1}{\frac{1}{R_1} + C_1 s}\right)I(s) \quad (2.27)$$

where $Z(s)$ represents the dynamic resistance of the LIB. For BMS application, the Laplace transfer

function in Equation 2.26 should be discretized. The discrete-time approximation method is explained in Appendix A.1:

$$s = \frac{2}{t_s} \left(\frac{1 - z^{-1}}{1 + z^{-1}} \right) \quad (2.28)$$

so $Z(z^{-1})$ can be computed. By substituting Equation 2.28 into Equation 2.26 (assumption $t_s = 1$):

$$Z(z^{-1}) = R_i + \frac{R_1}{1 + R_1 C_1 \frac{2}{t_s} \left(\frac{1 - z^{-1}}{1 + z^{-1}} \right)} = R_i + \frac{R_1(1 + z^{-1})}{1 + z^{-1} + 2R_1 C_1 - 2R_1 C_1 z^{-1}} \quad (2.29)$$

solving the right side of the Equation 2.29 gives:

$$Z(z^{-1}) = \frac{R_i + R_i z^{-1} + 2R_i R_1 C_1 - 2R_i R_1 C_1 z^{-1} + R_1 + R_1 z^{-1}}{1 + 2R_1 C_1 + z^{-1} - 2R_1 C_1 z^{-1}} \quad (2.30)$$

rearranging Equation 2.30 gives:

$$Z(z^{-1}) = \frac{R_i + R_1 + 2R_i R_1 C_1 + (R_i + R_1 - 2R_i R_1 C_1) z^{-1}}{1 + 2R_1 C_1 + (1 - 2R_1 C_1) z^{-1}} \quad (2.31)$$

after dividing the right side of Equation 2.31 by $(1 + 2R_1 C_1)$, $H(z^{-1})$ becomes:

$$Z(z^{-1}) = \frac{\frac{R_i + R_1 + 2R_i R_1 C_1}{1 + 2R_1 C_1} + \frac{R_i + R_1 - 2R_i R_1 C_1}{1 + 2R_1 C_1} z^{-1}}{1 + \frac{1 - 2R_1 C_1}{1 + 2R_1 C_1} z^{-1}} \quad (2.32)$$

In this thesis, The ECM was used as the basis for developing more enhanced models, to monitor individual LIBs, and the LIB pack. SOC model and the TECM have been coupled with the ECM to create a comprehensive monitoring system that satisfies the safety, and performance requirements relevant for industry grade products.

2.4.3.3 The fundamentals of the frequency-domain characterization (EIS-based)

Heaviside is known as the father of impedance spectroscopy from the late 19th century [3]. However, Warburg was the first person who extended the concept of impedance spectroscopy to electrochemical and energy storage systems [174]. His name is also well known for the diffusion process occurring at low frequencies in energy storage systems. In the 1940s, the first potentiostats were developed, and, consequently, frequency response analyzers were developed in the 1970s, which led to the development and use of the current EIS meters.

EIS is a powerful tool for ex-situ and in-situ characterization of LIBs and supercapacitors, such as electrochemical double-layer capacitors (EDLC) [7, 151, 282]. With the EIS characterization technique, the transfer function of the cell can be determined in the frequency-domain [7]. Similarly to the time-domain characterization, the cell undergoes EIS measurements at various temperatures, SOC, and aging conditions. EIS technique makes it possible to use the impedance spectra of the cells for diagnostic purposes.

EIS measurements can be performed in the potentiostatic or galvanostatic mode. In battery research and electrodeposition at constant current, EIS measurements are performed under galvanostatic control. In the galvanostatic control mode, experiments are conducted at a fixed DC current with a superimposed sinusoidal current perturbation applied to the cell. The resulting potential response of the cell is measured to determine the complex impedance of the system $Z(f) = \frac{U(f)}{I(f)}$.

LIB's characterization effort in the frequency-domain is much higher and more complex than in the time-domain. Frequency-domain-based models rebuild the effective electrochemical process and provide a better analysis of the dynamic behavior of the cells. EIS is also a non-destructive measurement and has become a standard technique for collecting detailed information over large time scales and amplitudes in the electrochemical system. Common practice for measuring impedance in LIBs involves perturbing a small signal current of a few mA (galvanostatic mode) over the frequency range of 10 kHz down to 0.001 Hz, which corresponds to 1000 s, and measuring the response to this input. The excitation current is sinusoidal and selected in a small range so that the voltage response remains pseudo-linear. The linearity condition implies that the impedance response is independent of the perturbation amplitude. As mentioned in Section 2.1, the system transfer function for the LIB can be determined as the ratio of the output voltage response to the sinusoidal input of the system, which is equal to the total impedance of the system. For the EIS measurement, the excitation current is:

$$I(t) = I_0 e^{(\omega t + \phi_i)} \quad (2.33)$$

As $I(t)$ is a small signal and the system is piecewise linear, the voltage response will be at the same frequency with a phase shift of ϕ_v :

$$V_t(t) = V_0 e^{(\omega t + \phi_v)} \quad (2.34)$$

so for $\phi = \phi_v - \phi_i$ the complex impedance representation becomes:

$$Z(\omega) = \frac{V_0 e^{(\omega t + \phi_v)}}{I_0 e^{(\omega t + \phi_i)}} = |Z_0| e^{j\phi} \quad (2.35)$$

where I_0 is the current excitation amplitude. Figure 2.9 demonstrates that the impedance of the ECM for LIB is dominated by R_i at high frequencies, and the impedance at low frequencies is dominated by $R_i + R_1$.

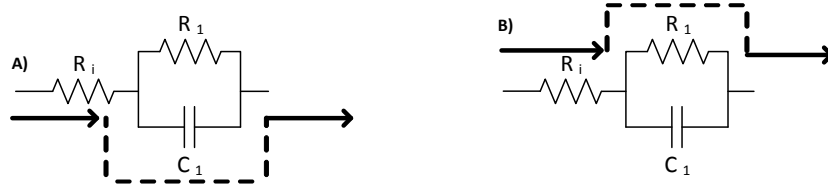


Figure 2.9: A) Impedance path at high frequencies dominated by R_i and current flows through C_1 , B) Impedance path at low frequencies dominated by $R_i + R_1$

This property of the circuit can be used to develop a parameter estimation technique for the LIBs, with filtering¹⁵ the different processes of the cell. A typical Nyquist diagram of the LIB, characterized by the EIS technique, is shown in Figure 2.10. In this figure:

$$\omega_0 = \frac{1}{R_1 C_1} = \frac{1}{\tau} \quad (2.36)$$

In order to characterize the LIB with the EIS method, the proposed ECM should be fitted with the impedance spectra. This can be done with minimization algorithms to find the minimum unconstrained multivariable function of the parameters. The proposed ECM model used to characterize the LIB in the time-domain cannot perfectly represent the frequency-domain, because the RC element in the ECM

¹⁵ Generally, low-pass filter (LPF), high-pass filter (HPF) and a combination of both as a band-pass filter (BPF) can be employed

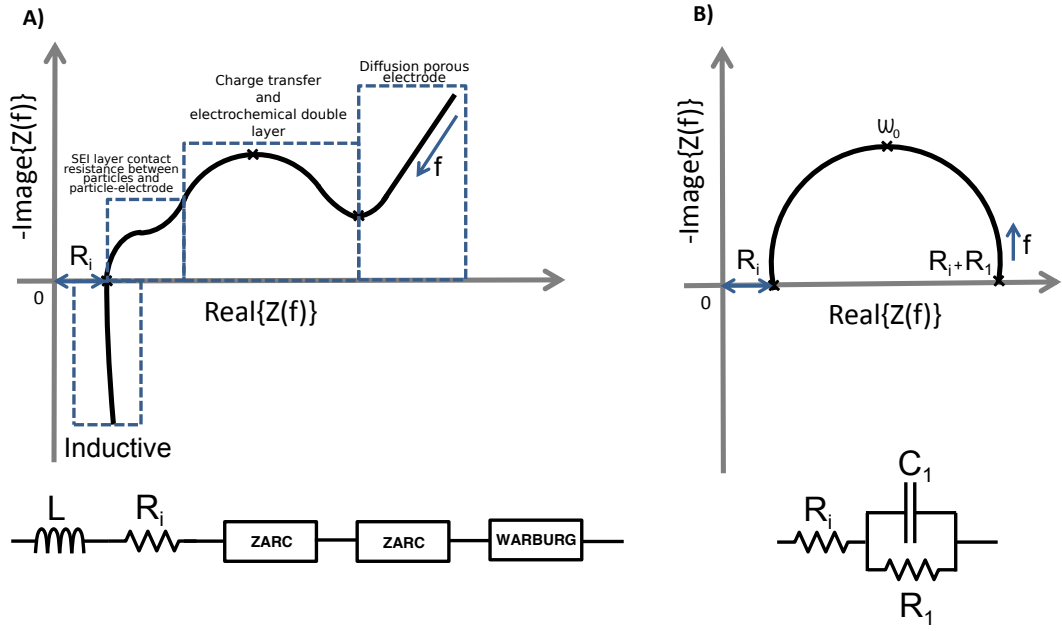


Figure 2.10: A) General Nyquist impedance diagram of a LIB, where the high frequency depressed semicircle represents the SEI layer, and the second depressed semicircle, represents the charge transfer, and electrochemical double-layer. Effects caused by the mass transport are represented by the Warburg impedance, B) A simple RC model represented on the Nyquist diagram

can only model a perfect half circle, as shown in Figure 2.10 B. The simple ECM model is able to represent the shifted perfect half circle rather than the total impedance spectrum of the cell. Hence, capacitance C_1 needs to be replaced with a constant phase element (CPE) to represent the depressed semicircle in the impedance spectra [24].

$$Z_{CPE} = \frac{1}{(j\omega)^\alpha C_{CPE}} \quad (2.37)$$

The impedance spectrum shows that, for the LIB, capacitive behavior is dominant in a wide range of frequency-domain. Frequencies ranging from a few kHz down to a few hundred Hz often reflect the inductive behavior for the high-power, large-format pouch LIBs. Pure ohmic resistance $R_{i,ac}$ occurs at the real axis zero crossing where the inductivity of the LIB is compensated by capacitance properties. For CPE in Equation 2.37, α is less than one. The double-layer capacitor behaves like a CPE and is used to model the depressed semicircles representing the double-layer effect. The local maxima of the second semi circle contains the time constant of the charge transfer resistance and the double-layer capacitance. The parallel connection of the resistance element R_{zarc} and a CPE is known as the ZARC element [79]. ZARC can be formulated as [33]:

$$Z_{ZARC} = \frac{R_{zarc} Z_{CPE}}{R_{zarc} + Z_{CPE}} = \frac{R_{zarc}}{R_{zarc} (j\omega)^\alpha C_{CPE} + 1} \quad (2.38)$$

To model the diffusion effects in electrochemical systems with much higher time constants, the Warburg

element representing the porous electrode diffusion can be used [40]:

$$Z_{warburg} = \sqrt{\frac{R_w}{j\omega C_w}} \coth(\sqrt{j\omega C_w R_w}) \quad (2.39)$$

so the transfer function of the cell characterized by the EIS method can be calculated. By using the general EIS circuit model, as shown in Figure 2.10 A and Equations 2.37 to 2.39:

$$\begin{aligned} Z(\omega) = \frac{U(\omega)}{I(\omega)} = j\omega L + R_{i,ac} + & \frac{R_{zarc1}}{R_{zarc1}(j\omega)^{\alpha_1} C_{CPE1} + 1} \\ & + \frac{R_{zarc2}}{R_{zarc2}(j\omega)^{\alpha_2} C_{CPE2} + 1} \\ & + \sqrt{\frac{R_w}{j\omega C_w}} \coth(\sqrt{\omega C_w R_w}) \end{aligned} \quad (2.40)$$

The EIS characterization technique provides valuable information about the impedance parameters of the cell. Particularly, aging, and temperature effects can be clearly seen on these parameters, which relate to different processes in the LIB. However, OCV cannot be measured with this technique. Also, recording the impedance data with this technique is often performed using the single-sine wave method, which results in lengthy measurements; this makes the application at the moment unsuitable for real-time applications. In this thesis, the effect of inductance was neglected, and only one ZARC element was used for parameter fitting. The next section presents the TECM for the LIB used in this thesis.

2.4.4 Thermodynamics and thermal modeling of the cell (TECM)

Temperature affects the safety and performance of the LIBs. Safety must not be compromised during the operation of the LIBs in EVs. Onset of thermal runaway (OTR) may cause catastrophic incidents, such as damage to life and property loss. The cell thermal runaway is sensitive to cell aging, SOC, and operating temperature, as described in [176].

Thermal gradients have a great effect on the performance of LIBs. Measuring the internal temperature of the cells during the operation provides essential information about the cells' working conditions, and can be used to provide the required information to the thermal management system¹⁶ (TMS). This critical information could help to avoid the OTR temperatures [276], and provides optimum operating conditions, which will greatly enhance the life time of the cells [274]. Measuring the internal temperature of LIBs is a crucial task, and, to date, no LIB has been made commercially available with built-in temperature sensors.

In Section 3.4, experimental studies and aging investigations on the performance of the LIBs supports the fact that LIBs are extremely temperature-sensitive. Extreme low temperatures affect the kinetics of the cells such that the performance decreases, or accelerated aging occurs. High cell temperatures accelerate the aging during the charging process or may even trigger thermal runaway [82]. To provide a completely safe operation environment, and to enhance the lifetime and performance of the cells, the temperature of the cells should be controlled and monitored during the operation. Therefore, internal and external temperatures of the cells should be known.

The aim of thermal modeling is to estimate the external and internal temperatures of the cells with or without the presence of temperature sensors (for reliability reasons). External cell temperature refers

¹⁶ In most cases TMS is an integrated part of the BMS

to the cell surface temperature, and internal cell temperature refers to the cell core temperature. The next section, presents an overview of different thermal modeling techniques available in literature, and Section 2.4.4.2 introduces the heat generation and heat transfer mechanisms. Finally, in Section 4.3, a thermal model (TECM) was developed, and used for the battery pack model.

2.4.4.1 The state of the art in thermal modeling of the cell

Thermal models mainly fall into two major groups:

- Lumped-model-based (Lumped 0D, 1D models)
- Multi-dimension coupled electrochemical-thermal models (Local 2D, 3D models)

Those that are model-based (0D, 1D) are known as lumped-element thermal models. Multi-dimension electrochemical thermal models (2D, 3D) are known as local models due to their ability to locally calculate heat generation and heat transport within LIBs.

Nowadays, multi-dimension electrochemical thermal models are solved based on the finite element methods and represent a more detailed model of heat generation and temperature distribution during the charging [147], and discharging [319] of the cell. Additionally, the heat generation rate and the energy balance of the cell proposed by Rao and Newman can be found in [211]. Multi-dimension electrochemical thermal models are currently not popular for implementation in the BMS hardware due to the complexity of the models. These models are useful for fundamental studies, cell, and pack design.

Lumped thermal models are aimed at being implemented in the TMS for better cooling or heating of the system to provide optimum homogenous temperature distribution inside the battery module for a uniform and slowed-down aging for all the cells.

Unlike cylindrical cells, pouch-bag and prismatic cell thermal modeling has not been given enough attention in the existing literature. In Table 2.4, a summary of developed thermal models based on different modeling techniques, cell types, and chemistry is presented.

In the existing literature, limited lumped-thermal models are available for pouch cells, particularly for the high energy NMC pouch cell. Authors in [232] studied the thermal behavior, and electrochemical heat generation in a commercial 40 Ah NMC pouch LIB.

In this thesis, to calculate the heat capacity of the DUT, tests were conducted under quasi-isothermal and adiabatic conditions in an accelerated rate calorimeter (ARC). To develop a thermal model of the LIB, aside from heat generation, heat transfers and thermodynamics of the cell should be known. Reversible and irreversible heat can be used to calculate the heat generation. A thermal model for pouch LIB based on the concepts explained in the next section was developed. This model was able to estimate the internal and external temperatures of the cell, without using temperature sensors. Two main parts of the TECM are heat generation (production) and heat transfer mechanisms, these mechanisms are explained in the next section.

Table 2.4: A summary of a thermal LIB modeling, sorted based on the modeling technique, cell type, and cell chemistry

Thermal model/cell type	Cylindrical	Pouch/Prismatic
Chemistry: LFP		
Lumped-models	[84, 170, 209, 217]	[226]/[50, 66, 67, 194, 324]
Coupled electrochemical-thermal models	[147, 320, 319](2D)[179](3D)	[317](2D)/[310](3D)
Chemistry: LCO+NCA/NiCd		
Lumped-models	[209]	[231]/[188](NiCd)
Coupled electrochemical-thermal models	[128](2D)[312]3D	-/-
Chemistry: LMO/NMC		
Lumped-models	[330]	-/-
Coupled electrochemical-thermal models	[287](2D)	-/[321](NMC)

2.4.4.2 Heat generation (production) and heat transfer mechanisms

Development of the internal temperature of the cell is caused by the increase of thermal energy generated inside the cell. Different parts of the LIB are responsible for thermal energy generation. Internal parameters contributing to the thermal energy generation are electrolyte resistance, and additional forms of resistance caused by the current collector are known as ohmic resistance and charge-transfer resistance, which cause over-potential together with entropy change at both electrodes.

Heat generation of LIB due to the side reactions are neglected. This is because side reactions are mainly aging reactions, and their slow heat generation process can be neglected. Electrolytes at the operating potentials might be unstable, which should result in side reactions. Side reactions take place on the electrode surfaces, which could eventually lead to the solid electrolyte interphase (SEI) formation [307]. The sum of the mixing effect on heat generation¹⁷ is zero and can be neglected as well [50, 271]. In order to develop a lumped thermal model in this thesis, it is assumed that the temperature distribution from the cell's core to its surface is homogeneous.

In this thesis, two sources of heat generation have been considered: reversible entropy heat generation

¹⁷ Heat generation from mixing effects is negative during the gradient concentration creation, and is positive when the gradients disappear

rate (\dot{Q}_{rev}) and irreversible electric Joule heat generation rate (\dot{Q}_{irev}). Therefore, the average total heat generation is:

$$\dot{Q}_{gen} = \dot{Q}_{rev} + \dot{Q}_{irev} \quad (2.41)$$

The total generated heat is partially stored in the cell and the rest is transferred to the environment.

- **Reversible entropy heat generation (\dot{Q}_{rev}):**

Electrode structural changes during charging or discharging release or absorb energy, which results in reversible heat generation. Because the reversible heat generation rate has been found to be a significant portion of the total heat generation, this part should not be neglected.

Gibbs free energy (G) is the thermodynamic potential minimized at equilibrium at constant pressure and temperature in a cell [91]. Reaction entropy (ΔS) and reaction enthalpy (ΔH) changes may lead to reversible changes in Gibbs free energy. Entropy change also depends on the cell chemistry. LCO-graphite cells demonstrate much larger entropy change compared to NMC-graphite or LPF-graphite cells [278]. In the case of constant pressure and constant temperature, changes in Gibbs free energy can be calculated as [20]:

$$\Delta G = \Delta H - T\Delta S \quad (2.42)$$

In an ideal system, Gibbs free energy change can be converted into the work in the form of electricity [267]:

$$\Delta G = -nFV_{oc} \quad (2.43)$$

where n is the number of electrons passed in the reaction and F is Faraday's constant. This indicates how the incremental addition of lithium atoms affects the ordering of lithium on the host lattice [270]. Taking a derivative from Equation 2.42:

$$\Delta S = -\frac{\partial \Delta G}{\partial T} \quad (2.44)$$

ΔS can be obtained from OCV measurements. This is shown in Equation 2.45:

$$\Delta S = nF \frac{\partial V_{oc}}{\partial T} \quad (2.45)$$

Entropy change (ΔS) leads to the heating and cooling of the system, which depends on the direction of the reaction and can be measured by using an electrochemical thermodynamic measurement system (ETMS) [278], or by measuring the OCV at different temperature steps. After measuring ΔS , entropic reversible generated heat rate \dot{Q}_{rev} can be calculated:

$$\dot{Q}_{rev} = I \frac{\Delta S}{nF} T_{core} \quad (2.46)$$

Substituting ΔS from Equation 2.45 in Equation 2.46:

$$\dot{Q}_{rev} = I \frac{\partial V_{oc}}{\partial T} T_{core} \quad (2.47)$$

where T_{core} , is the core temperature of the cell.

- **Irreversible Joule heat generation** (\dot{Q}_{irev}):

The respective resistive cell's circuit parameters contributing to Joule heating loss are ohmic resistance, charge transfer resistance, and the resistances with a longer time constant. These losses are due to the movement of charged particles and contact resistances.

In this thesis, R_1 has been calculated for a 10 s pulse, which includes the charge transfer term as well. It should be noted that, this equation fits to a typical drive-cycle containing dynamic and short pulses with high amplitudes. The irreversible heat generation rate is formulated as:

$$\dot{Q}_{irev} = R_i I^2 + \frac{V_{R_1 C_1}^2}{R_1} \quad (2.48)$$

The ECM has been used to calculate heat generation due to irreversible losses. Considering both entropic heat and electrical heat loss from Equation 2.47 and 2.48, the final equation for the total heat generation in this thesis becomes:

$$\dot{Q}_{gen} = \dot{Q}_{rev} + \dot{Q}_{irev} = R_i I^2 + \frac{V_{R_1 C_1}^2}{R_1} + I \frac{\partial V_{oc}}{\partial T} T_{core} \quad (2.49)$$

When the load current is zero, heat generation accordingly becomes zero [165].

- **Heat transfer mechanisms** ($\dot{q}_{transfer}$):

The generated heat is partially transferred to the environment. Heat transfer mechanisms for a LIB can be described by the following equations [28, 183]:

$$conduction : \dot{q}_{conduction} = \frac{kA}{d} (T_{core} - T_{surf}) \quad (2.50)$$

Heat transfer by conduction is the heat exchanged between two neighboring elements through a layer of material. In this equation, “k” is the material thermal conductivity, “A” is the area normal to the heat flow direction, and “d” is the thickness of the layer. The heat transfer is directly proportional to the temperature difference between the core and the surface (T_{surf}) of the cell.

$$convection : \dot{q}_{convection} = hA(T_{surf} - T_{amb}) \quad (2.51)$$

The convective heat transfer mechanism is governed by the Newton's law of cooling (independent of the cell shape). This heat transfer is correlated with the energy transfer by convection between two bodies by means of fluid motion. The convective heat transfer is directly proportional to the temperature difference between the cell surface and the surrounding (for instance coolant). In equation 2.51, “h” is the heat transfer coefficient. The convective heat transfer coefficient can be estimated from the heat losses for a battery module.

$$radiation : \dot{q}_{radiation} = e\sigma A(T_{surf}^4 - T_{amb}^4) \quad (2.52)$$

Heat transfer by radiation is governed by the Stefan-Boltzmann law. In this equation, the radiation is directly proportional to the difference of the forth powers of body temperatures. In this equation, “ σ ”

is the radiation coefficient (Stefan-Boltzmann constant¹⁸) that depends on the configuration properties and emissivity ($e = 1$ for ideal radiator) of interacting bodies. The total transferred heat then becomes:

$$\dot{q}_{transferred} = \dot{q}_{conduction} + \dot{q}_{convection} + \dot{q}_{radiation} \quad (2.53)$$

Heat transfer by radiation is neglected in this thesis.

- Heat capacity (C_p) and heat balance:

The generated heat is partially stored in the cell. This is because of the heat capacity of the cell. Heat capacity of the LIB can be calculated using the product of the specific heat capacity (c_p) of the cell and the mass “m” of the cell, as shown in Equation 2.54:

$$C_p = mc_p \quad (2.54)$$

In order to identify the specific heat capacity, the battery should be packed with insulating material and be heated with defined rest intervals in an adiabatic environment, such as an ARC device. The stored heat in the cell is:

$$\dot{q}_{stored} = mc_p \frac{\partial T_{core}}{\partial t} \quad (2.55)$$

From equations 2.49, 2.53, and 2.55, the energy balance description of the thermal cell model from the combination of heat sources and heat sinks becomes:

$$\dot{Q}_{gen} = \dot{q}_{stored} + \dot{q}_{transferred} \quad (2.56)$$

Possessing knowledge about heat generation mechanisms in the cell, and the heat transfer mechanism can lead to the design and verification of a thermal model of the cell. The advantage of this type of modeling lies in the suitability for control design, and implementation in the battery pack BMS. Thermal abuse modeling is neglected in this thesis.

2.5 Battery states definitions

2.5.1 SOC definition

SOC does not have a universal definition. For different applications, different definitions are used. A classic definition of SOC for LIBs can be found in [227], where Sauer et al. defined the SOC based on the cell capacity.

Taking a deeper look into the cell’s negative electrode quantities, the SOC of the cell can be explained based on the concentration of lithium in the solid particles of the electrodes, so the bulk SOC is the average utilization of the entire electrode [48, 155, 156]. Based on this definition, SOC can be expressed as:

$$SOC = \frac{\frac{c_{s,ave}(t)}{c_{s,max}} - \theta_{min}}{\theta_{max} - \theta_{min}} \quad (2.57)$$

¹⁸ $\sigma = 5.670367(13) \times 10^{-8} \frac{W}{m^2 K^4}$

where $c_{s,ave}(t)$ is known as the average concentration of lithium in the solid particles of the negative electrode. $c_{s,max}$ is a physical parameter of the cell, and defines the maximum value of the concentration of lithium in the solid particles of the negative electrode. θ_{min} is the fully discharged state, and θ_{max} is the fully charged state of the stoichiometric limits of the negative electrode. As can be seen in Equation 2.57, realization of the non-dimensional SOC quantity based on this equation requires in-situ measurements, which makes it impractical for online applications.

In most of the existing literature, the approaches to define the SOC are based on the actual electric charge of the cell or pack with relation to the total electric charge that the cell or pack can store at that specific temperature and SOH. This definition has recently become more generalized [27].

For EV applications, the SOC definition can be established based on the power requirements (both charging and discharging power) as long as no voltage limit is violated [132]. To provide a clearer description, SOC_{min} and SOC_{max} are clarified first. SOC_{min} is the minimum allowable SOC to fulfill the specified power requirements for all given discharge current profiles (usually constant current pulse powers) as long as lower cut-off voltage is not violated. Based on the application requirement, pulse power current profiles usually come in the form of the current pulses with various amplitudes and durations such as 1 s, 2 s, 5 s, 10 s, 30 s, 60 s or even 1000 s pulses. SOC_{max} or the maximum allowable SOC can be defined when the specific power requirements for the application with the desired charge powers (for instance fast charging) are fulfilled. However, fast-charging impacts the lithium-plating [45, 93].

The most notable reviews on SOC detection methods are presented in Table 2.5.

Table 2.5: Reviews of SOC detection techniques available in the literature

Review	reference
Reviews on SOC detection techniques	[27, 46, 63, 68, 129, 137, 199, 207, 215, 227, 290, 296, 315]

According to the reviews in Table 2.5, SOC estimation techniques are categorized in various ways. In [215], Rezvanizani et al. categorized SOC detection techniques based on direct (e.g., acid density in lead-acid batteries) and indirect methods. Indirect methods are also divided into online and offline methods. In [315], Yanhui et al. categorized the SOC detection techniques according to voltage-based techniques (discharge model, OCV model, load voltage), current-based techniques (Ah model, Peukert model), resistance-based techniques, and adaptive-algorithms (Kalman filter, artificial neural network (ANN), fuzzy logic, hybrid algorithm).

In [63], Cuma et al. compared various SOC detection techniques for NiMH, lead-acid, lithium-polymer, and LIBs presented in the literature with regard to the percentage of estimation error. However, as all these methods are not evaluated under the same conditions, a comparison between SOC detection errors of different methods without reference measurements might be misleading.

All available reviews of SOC detection techniques, however, agree that hybrid methods are more reliable. Hybrid method means a combination of two or more detection methods.

To conclude this section: a simple definition, from engineering point of view, can be proposed for understanding the SOC of the energy storage system, particularly for the LIB or LIB pack. Therefore, the SOC, under nominal operating conditions (manufacturer allowed charging, discharging, and recommended usage temperature), is a value between 0% (totally empty) and 100% (totally full) that indicates the relative level of charge (or residuum capacity) held by the battery system at the time “t”.

2.5.2 SOH definition

The aging mechanisms of LIBs are complicated, also the aging occurring at the anode and cathode are different from each other [26]. In the anode side, the dominant aging mechanism comes from the solid electrolyte interface (SEI) formation, which leads to a significant increase of the cell impedance and loss of recyclable Li-ions.

The aging of the cells is usually linked to the capacity fading, impedance growth, or both factors. This depends on the application the cells are used for. For applications with high power demands, impedance monitoring (SOH_R) is preferred, and for applications where the duration or range of EVs is more of concern, capacity tracking (SOH_C) is required. A combination of both, impedance and capacity estimation, is also used.

Figure 2.11 graphically explains the aging related terms for a LIB. BOL is known as the cell's beginning of life when the normalized capacity ratio ($\frac{C_{act}}{C_{BOL}}$), or resistance ratio ($\frac{R_{BOL}}{R_{act}}$) of the cell are ideally equivalent or greater than one. " C_{BOL} " is the battery discharge/charge capacity that can be measured by a complete discharge/charge of the cell from a fully charged/discharged state under nominal conditions. " R_{BOL} " is the cell's resistance at the BOL, and " R_{act} " is the actual resistance of the cell. Due to the production spread, the normalized values can be slightly more or less than one. These parameters can be defined with the HPPC test.

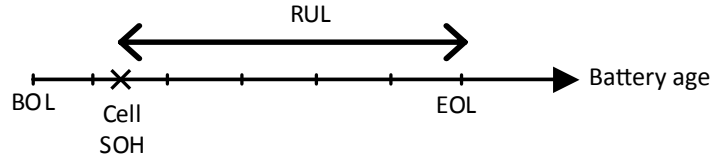


Figure 2.11: Schematic explanation of BOL, EOL, SOH, and RUL

In Figure 2.11, RUL is a measure reflecting the cell's predicted lifetime, and it is defined as the difference between the current state and its end of life (EOL). This is the reason that having information regarding the cell's history is important.

For EVs, the EOL criterion can be based on the service life (for instance, 10 years), or based on the cell's capability of providing the required power or energy. A generic SOH equation based on the capacity is defined as:

$$SOH = \frac{C_{act}}{C_{BOL}} \quad (2.58)$$

In this equation, C_{BOL} is a fixed value. However, in both, SOH and SOC (see equation 2.70) equations, C_{act} changes over the time (due to capacity fade, or temperature effects). For BMS implementation, while C_{BOL} has been already defined in the algorithm (in most cases a value measured during a standard charge), it is recommended that the C_{act} should be also calculated during the charging process ($C_{act,cha}$). However, it is possible to estimate the SOH during the discharge of the cells, while the EV is in operation. SOH is equal to 0% at the cell EOL, however, Equation 2.58 is not suitable for implementation. As rule of thumb, the cell has reached the EOL ($SOH = 0\%$), when the actual discharge capacity falls below 80% of the BOL discharge capacity under nominal conditions ($C_{act} = 0.8 C_{BOL}$) [229]. This is shown in Equation 2.59:

$$SOH_C = \frac{5C_{act}}{C_{BOL}} - 4 \quad (2.59)$$

For SOH_R , the resistance of the cells should be monitored. In this thesis, SOH_R is considered 0% when the cell's resistance is doubled due to the aging effects [18]. However, this factor mainly depends on the application requirements, in some EVs, the increase of the internal resistance (or ohmic resistance) should be limited to 30%. Equation 2.60 presents the SOH_R with this method:

$$SOH_R = 2 - \frac{R_{act}}{R_{BOL}} \quad (2.60)$$

In this work, aging experiments have been designed in a way to figure out the main aging factors of the cells. Such investigations are necessary because LIBs have a finite lifetime, and their lifetime should be maximized by providing optimal working conditions.

In this thesis, to determine the SOH, relevant cell parameters, such as discharge capacity and ohmic resistance, were extracted from the HPPC test results. A schematic of the test procedure is shown in Figure 2.12:

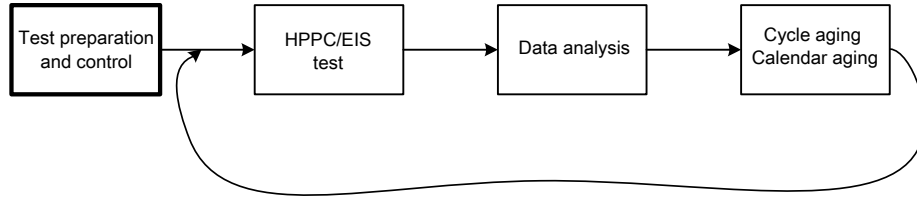


Figure 2.12: Chart showing the schematic of the test procedure used to periodically extract the cell parameters

The next chapter introduces the control theory requirements used for state detection algorithms.

2.6 Control theory and the requirement for state detection

A state refers to the present and future condition of the battery. In most cases, battery states cannot be measured or sensed directly using physical sensors. However, many attempts have been made to estimate the SOC from the actual current flow from the cell tabs, or by measuring the terminal voltage of the cell.

LIB states can be estimated by an estimator (also known as the state detection algorithm). An estimator uses past and present data to perform a projection of the future observation of the target parameter. State detection algorithms for SOC estimation are more widespread compared to other states (e.g., SOH or SOP); however, the basics of algorithms to estimate other states remain the same.

2.6.1 State space system

To design an estimator, a description of the system based on the discrete state-space model is beneficial [152]. To create a state-space model of a dynamic system, developing a mathematically based model of the system is required.

A schematic of a discrete-time state-space model is presented in Figure 2.13. In this figure, “ \mathbf{u} ” is the system input (current and temperature sensor measurements), and “ \mathbf{y} ” is the dynamic system output (voltage and temperature). “ \mathbf{x} ” is the system state vector, and variables “ \mathbf{v} ” and “ \mathbf{w} ” are random variables representing measurement noise and the process noise.

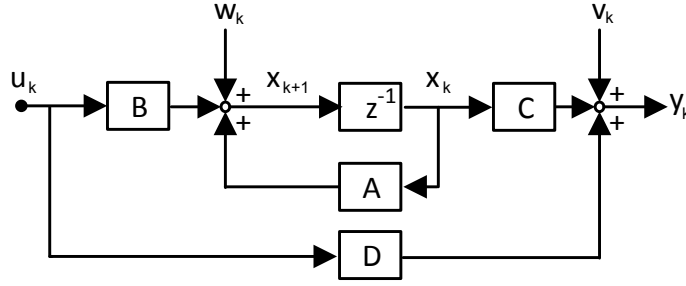


Figure 2.13: Dynamic process represented by discrete state-space model [201]

$A \in \mathbb{R}^{n \times n}$ is the system matrix, $B \in \mathbb{R}^{n \times p}$ is the control matrix, $C \in \mathbb{R}^{m \times n}$ is the output matrix and $D \in \mathbb{R}^{m \times p}$ is the feed-forward matrix. The state-space model represents the dynamics of the system, which are also time varying. In this thesis, discrete state-space representation has been used to develop the adaptive state detection algorithms (see Section 2.7.3).

2.6.2 Bayesian filtering theory

Bayesian filtering is optimal and useful in applications where memory usage and computational complexity are the limiting factors. For practical, nonlinear filtering applications, approximate solutions are required. Recursive Bayesian estimation can be used to determine the probability density function of the state vector of the nonlinear systems conditioned by the available measurements. The posterior density function provides the most complete description of an estimate of the systems [56, 154]. The Bayesian filtering application in algorithms such as the Kalman filter simplifies the problem because all the calculations are based on the matrix calculations. Aside from the simplification, nonlinear filtering problems can be solved by assuming the optimal conditional densities that can be approximated using Gaussian distribution.

To develop a Bayesian filter for LIBs, a few assumptions should be taken into account:

- LIB states ($\mathbf{x}(t) = [SOC, SOH, SOP, SOF, SOS, \dots]$) are not directly measurable or observable
- Current state ($\mathbf{x}(t)$) depends on previous state $\mathbf{x}(t-1)$ but not older states (known as the Markov process of the first order)
- Probability density functions are used to represent the state vectors

Algorithms developed based on Bayesian theory are in the form of conditional probability density, which represents the state estimate. The state-space described in continuous-time is:

$$\dot{\mathbf{x}}(t) = \phi(\mathbf{x}(t), u(t), \mathbf{w}(t)) \quad (2.61)$$

Considering the state space model representation in Figure 2.13 and the sequential Bayesian interface presentation in Figure 2.14:

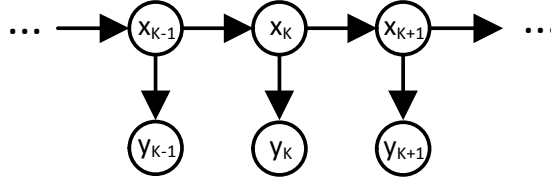


Figure 2.14: Graphical illustration of the sequential Bayesian interface

the discrete model representation can be derived. From Equation 2.61, $\dot{\mathbf{x}}(t)$ is the system state derivative in continuous-time and is equivalent to x_{k+1} in discrete-time. For realization and implementation in a target microcontroller, Equation 2.61 should be discretized. Realization is shown in Equation 2.62:

$$\mathbf{x}_{k+1} = \mathbf{F}(\mathbf{x}_k, u_k) + \mathbf{w}_k \quad (2.62)$$

where $\mathbf{F}(\cdot)$ is the nonlinear system transition function, u_k is the deterministic system input vector, and \mathbf{w}_k is stochastic modeling uncertainties (the subscript “k” is the discrete-time index). Given the sampling time $t_s = t_k - t_{k-1}$, the discretized system state vector \mathbf{x}_k can be calculated at a discrete-time index ($k = 0, 1, \dots, n - 1, n$). The probability density function $P(x_k|y_k)$ is used for estimation of the state x_k with the set of all measurements. Measurement data is used to gather information about \mathbf{x}_k , and discrete-time observation output (\mathbf{y}_k) can be modeled in the form:

$$\mathbf{y}_k = \mathbf{H}(\mathbf{x}_k, u_k) + \mathbf{v}_k \quad (2.63)$$

where $\mathbf{H}(\cdot)$ is the nonlinear measurement function, and \mathbf{v}_k is the measurement noise. To simplify the Bayesian algorithm, and to consider the typical uncertainties of the system, external noises (\mathbf{w}_k and \mathbf{v}_k) were added to the system. Measurement noise, and process noise are assumed to have white Gaussian distribution with a zero mean. Measurement noise is responsible for external disturbances, and process noise is responsible for modeling uncertainties. These noises (modeled with probability density functions) are assumed to be independent.

In Equation 2.62, a sequence of given sensor measurements ($\mathbf{u}_{1:m} = \mathbf{u}_0, \dots, \mathbf{u}_m$) or the history of measurements up to discrete time step “k” can be used to estimate \mathbf{x}_k [205].

Based on the difference between the measurement time step and the algorithm sampling, there exist three different estimation problems [222]. This is shown in Figure 2.15.

- if $m > k$, the problem is known as “smoothing”
- if $m = k$, the problem is known as “filtering” (the case for Bayesian filtering)
- if $m < k$, the problem is known as “prediction”

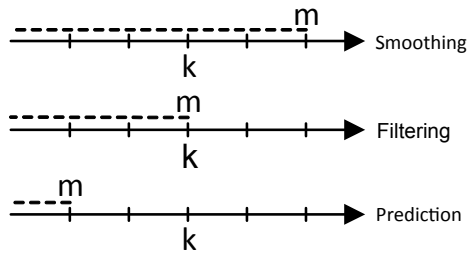


Figure 2.15: Schematic illustration of various estimation problems; dashed lines represent the available measurements up to the time “m”

As depicted in Figure 2.15, smoothing is typically performed offline, while filtering and prediction can be performed online. Because, in LIB system, \mathbf{x}_k is only dependent on \mathbf{x}_{k-1} , and with the assumption of white Gaussian distribution for process noise and measurement noise, and with prior knowledge of the system state’s initial value (\mathbf{x}_0), the algorithm developed based on the Bayesian filtering theory is capable of recursively estimating \mathbf{x}_k . For instance, with the Bayesian filtering problem, linear Gaussian state-space models can be solved with the Kalman filter [127].

The state-space model presented in Figure 2.13 is an open-loop model representation. Open-loop models (without any feedback) are prone to modeling errors. Adding a controller (for example, a proportional-integral-derivative (PID) type controller) is a simple way to minimize the modeling error. Figure 2.16 represents the concept of closed-loop state filtering by including an adaption block such as a PID controller or a more sophisticated adaptive algorithm.

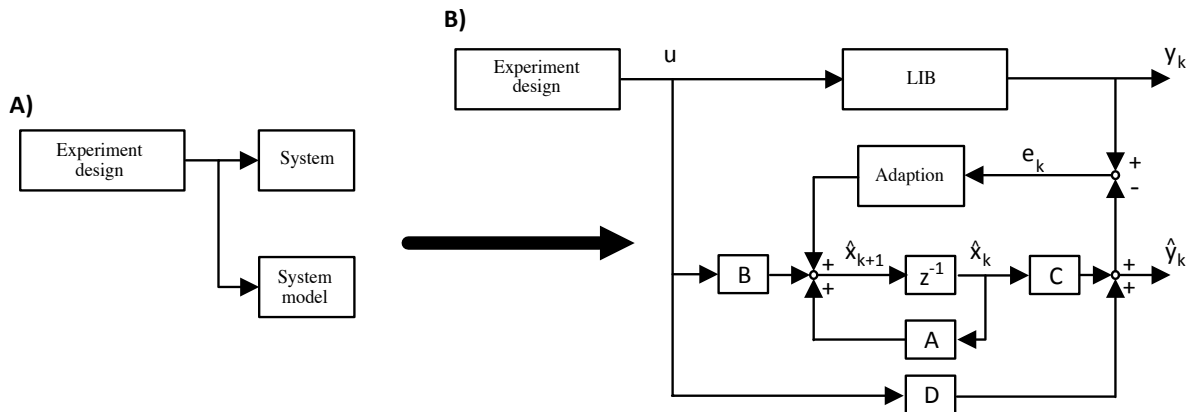


Figure 2.16: A) A representation of a dynamic system and its open-loop model, B) Closed-loop system model for state filtering including adaption scheme (for signal descriptions see Section 2.7.3.1). The adaption part can be a PID controller (see Figure 2.19, how SOC (x_k) as a state gets corrected, and Figure 2.20 the PID controller for the adaption part)

The adaption block has a closed-loop model correction role, which uses the weighted error to correct the system model. The correction term is the modeling error multiplied by an adaption gain. If the algorithm is adaptive, such as the Kalman filter, correction gain is not constant and is updated at each time step. The next part presents the model and filter error, and performance evaluation techniques.

2.6.3 Performance evaluation

In order to quantify the filtering performance and the estimator accuracy or to evaluate the modeling performance, the following error evaluation methods can be used:

- Absolute error (AE)
- Root mean square error (RMSE)
- Mean absolute error (MAE)
- Relative error (RE)

If “ e_k ” (see figure 2.16) is the absolute error between the true value \mathbf{y}_k , and the estimated value $\hat{\mathbf{y}}_k$:

$$AE = \mathbf{e}_k = \mathbf{y}_k - \hat{\mathbf{y}}_k \quad (2.64)$$

The RMSE can be defined as:

$$RMSE = \sqrt{\frac{1}{N} \sum_{k=1}^N e_k^2} \quad (2.65)$$

and mean absolute error is defined by:

$$MAE = \frac{1}{N} \sum_{k=1}^N |e_k| \quad (2.66)$$

Relative error (RE) gives an indication of how good a measurement is relative to the size of the reference being measured. RE is in percent and given by:

$$RE = \frac{e_k}{\mathbf{y}_k} \quad (2.67)$$

To have an ideal model or algorithm, the modeling error should be minimized. Minimization is normally performed with optimization algorithms, by functions, or by updating the correction weight ($w_{adaption}$) of the adaption block (Figure 2.16 B):

$$w_{adaption} = K_{adaption} e_k \quad (2.68)$$

Almost all available SOC detection strategies are covered in following section, and, in Chapter 5, some selected methods were used for the cell and pack state detection.

2.7 State detection techniques

The following part is dedicated to the various state detection techniques, particularly, the SOC detection techniques. SOC and SOH are both dimensionless measures, and in this thesis, they are scaled from 0 to 100%. Table 2.6, presents a categorized SOC detection techniques extracted from major literature reviews presented in Table 2.5.

The SOC detection is one of the current key issues of the BMS, and the control strategies are essentially dependent on it. The focus of this work is mainly on the SOC estimation techniques that can fulfill the EV requirements. This signifies the importance of searching for the most efficient and suitable algorithms to accomplish this task.

Table 2.6: State detection categorizes

State detection techniques
Conventional methods (see 2.7.1)
Learning algorithms “self/supervised - data driven” (see 2.7.2)
Adaptive filter algorithms “model-based and non-model-based” (see 2.7.3)
Controllers and observers “linear/nonlinear” (see 2.7.4)
Combined (hybrid) methods (see 2.7.5)
Other state detection methods (see 2.7.6)

2.7.1 Conventional methods

The first class of state detection techniques is summarized as conventional methods. Table 2.7, presents these methods gathered from a variety of literature reviews on state detection methods (see Table 2.5).

Table 2.7: SOC detection techniques based on the conventional methods

Category	Submethod
Voltage-based	terminal-voltage-based, OCV-based
Current-based	Ampere-hour counting (Coulomb-counting)
Impedance-based	ohmic-resistance-based, EIS-based methods
Physical properties	acid density measurement

State detection based on the physical properties is not so common for the LIBs. However, based on this method, the measured variables are directly translated into SOC or SOH through a LUT, or a predefined function.

In this section, a brief description for the most common conventional methods is provided.

2.7.1.1 Voltage-based

The voltage-based method refers to the use of terminal voltage of the LIB to calculate the SOC. This method is widely used as a SOC indicator for devices such as laptops, cellular phones, and other similar applications. The most simple and straightforward, however, inaccurate method for SOC detection is the use of terminal voltage values. A simple voltage monitoring method establishes a linear relationship between cell SOC and terminal voltage. This is shown in the following equation:

$$SOC = \frac{V_t - V_{min}}{V_{max} - V_{min}} \quad (2.69)$$

In Equation 2.69, 100% SOC is associated to the upper cell voltage limit (V_{max}), when the terminal voltage (V_t) is equal to the upper cell voltage limit ($V_t = V_{max}$), and $SOC = 0\%$ is associated with

the lower cut-off voltage (V_{min}) in the application. The SOC-voltage relation in Equation 2.69 is not accurate and is limited, because this relation is not always linear and does not consider operating conditions such as operating temperature and cell aging.

Beside the terminal voltage method, OCV is measured for a desired set of SOC values, then a LUT similar to Figure 2.17 can be created. Based on this method, OCV is measured, and a SOC value per point on a pre-measured curve is reported [148]. Table 2.8 presents the advantages and disadvantages of voltage-based techniques for state detection.

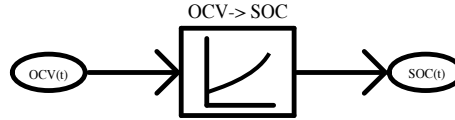


Figure 2.17: Voltage based method SOC estimation

Table 2.8: Advantages and disadvantages of SOC detection methods based on the voltage-based methods

Advantages	Disadvantages
Online and offline	Hysteresis effect even after long rest time
Simple implementation	Low dynamics [129]
Fast and stable	Extensive lab experiment \rightarrow large LUTs
Acceptable accuracy (for limited applications)	OCV is difficult to be estimated under load
Most battery technologies (except LFP) [137]	Temperature sensitive [197], influenced by aging [206]
Integrity	Long rest times

As there is no linear relationship between the OCV of the cell to the SOC, this method requires extensive data collection and laboratory experiments. Additionally, OCV is sensitive to temperature, so the OCV-based method is usually combined with other techniques to achieve more accurate results [15]. This technique can be used for SOC initialization required in the state detection algorithms, as in Chapter 4. Further publications on using of OCV, and terminal voltage for SOC detection for lead-acid and LIBs, in consideration of different discharge C-rates, are reported in [62, 182].

2.7.1.2 Current-based

Ampere-hour counting¹⁹ (Ah-counting) is the most commonly used technique for SOC estimation. This method is based on the current measurement and discrete integration of measured current over time as a direct indicator of SOC. Under controlled experimental laboratory conditions, this method is considered as the reference method for evaluation of other SOC algorithms. This method is widely used for SOC calculation in most EVs, and HEVs, as a complete charge is often reached, and SOC recalibration becomes possible.

¹⁹ Also known as Coulomb-counting methode. “Ah-counting” term is used throughout this dissertation

A key factor for this method is precise battery current measurement. By integrating the measured current over time and with prior knowledge of the initial available charge, SOC can be accurately measured over the operation time. Being open-loop²⁰ and the need for recalibration over time are the drawbacks of this method. Additionally, capacity fade directly influences the accuracy of this technique (reflected in the C_{act}), so it should be considered as well. The required assumptions for this technique are having perfect knowledge of the modeled physical system, perfect knowledge of the initial conditions and no additional constraint on the input. Table 2.9 presents some noteworthy advantages and disadvantages of the Ah-counting technique for SOC calculation.

Table 2.9: Advantages and disadvantages of SOC detection methods based on the current-based methods

Advantages	Disadvantages
Generic (all type of battery technologies)	Poor standalone performance
Integrity	Requires recalibration
Simple implementation and robust	Open-loop
Flexibility in combination with other methods	SOH dependant
Online	Limited functionalities
Low computation requirement and fast	Sensitive to the sensor accuracy and noise

Considering the fact that C_{act} is SOH dependant, and changes over time, and assuming $C_{act} = C_{rem} + C_{rel}$, the generic formulation of SOC and DOD are:

$$SOC = \frac{C_{rem}}{C_{act}} \quad (2.70)$$

$$DOD = \frac{C_{rel}}{C_{act}} \quad (2.71)$$

Ah-counting formula for SOC calculation based on the equation 2.70 is:

$$SOC(t) = SOC_0 + \int_0^t \frac{\eta_c I(\tau)}{C_{act}} d\tau = 1 - DOD(t) \quad (2.72)$$

where “ $\eta_c = \frac{C_{dcha}}{C_{cha}}$ ” is the Coulombic efficiency (CE) and is mainly dependent on undesired reactions, operating temperature (during charge and discharge), and current rate (in this thesis, it is assumed that $\eta_c = 1$). If during “ $(t - t_0)$ ”, current stays constant, then ΔSOC can be formulated as:

$$\Delta SOC = I(t - t_0) \frac{1}{C_{act}} \quad (2.73)$$

The derivative of Equation 2.72 becomes:

$$\dot{SOC}(t) = \frac{1}{C_{act}} I(t) \quad (2.74)$$

²⁰ From control theory perspective, if the estimation error is accumulated over time, the system is referred to as open-loop

To initialize the algorithm (SOC_0), using a LUT can be beneficial. The algorithm can be initialized around its real start value, based on the last information before the application interruption. This means that, when the EV is no longer in operation, in the next run (key on), models and algorithms can be initialized based on the last saved data.

An efficient way to auto-initialize is to use the OCV-LUT, or the estimated OCV from a model. The schematic representation for this method is shown in Figure 2.18.

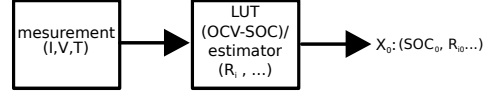


Figure 2.18: Parameter/state initialization scheme

In Equations 2.72 and 2.73, for discharge current direction, a negative sign is considered. The Simulink implementation of Equation 2.72 with the additional feedback loop from the PI controller is shown in Figure 2.19. By using this configuration, together with the ECM shown in Figure 2.8, an enhanced ECM has been obtained (see Chapter 5). This configuration can be used for implementation²¹ in the BMS.

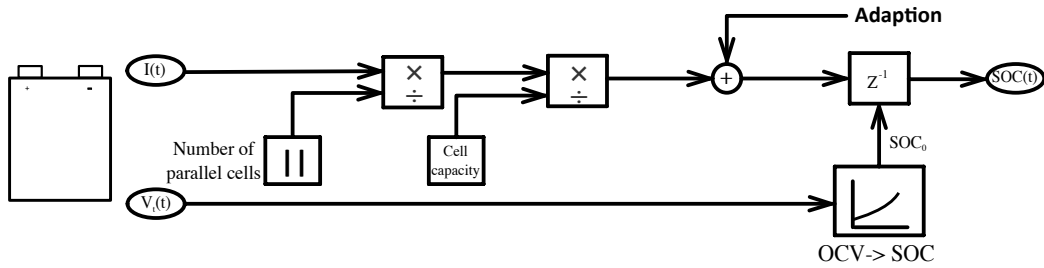


Figure 2.19: Implementation of the enhanced SOC estimator based on the Ah-counting method (Equation 2.72), combined with the OCV-based SOC detection technique used for algorithm initialization. The adaption part is a PI controller as shown in Figure 2.20

In this figure, to enhance the accuracy, a feedback loop that contains information about the simulation error (difference between the measured voltage, and the modeled voltage) has been introduced. The Ah-counting method has great flexibility of being mixed or combined with other SOC detection methods, especially with the voltage-based methods [15], the PI controller [22], and adaptive state estimators such as the extended Kalman filter (EKF). Other noticeable works on the SOC definition and Ah-counting method can be found in [190, 228].

2.7.1.3 Impedance-based

Battery impedance can be used for SOC detection. In the literature, EIS is proposed to be used for state detection [68, 123, 220]. Generally, EIS measurement of the cell over the desired frequency range, helps the understanding of cell's impedance behavior. EIS measurement is normally performed under various operating conditions. SOC, SOH, and temperature conditions, define the operating conditions used for the EIS measurement.

To monitor the SOC in the desired frequency range, where at least one impedance parameter ($Z_p \in$

²¹ For programming purposes, a factor of 3600, which converts seconds to hours, and a factor of 100 to represent the SOC in percent should be included

$\{Re(Z), Im(Z), |Z|, \phi\}$ is sensitive to SOC, this parameter should be mapped to the SOC ($Z_p \rightarrow Z_p(SOC)$). In this way, the SOC can be monitored.

Using EIS measurement for SOC estimation in a standalone manner can be challenging. Conventional real-time SOC estimators use ECM parameterized in the time-domain, whereas, for EIS-based SOC estimation, the time-domain ECM should be replaced with a model parameterized with EIS measurements in the frequency-domain. In [166], Li et al. measured the EIS at eleven SOC data points (between 6 to 100%) for 41 frequencies. They used cubic spline interpolation to fit the OCV at these SOC data points, and by using EKF for SOC estimation, a SOC estimation accuracy of better than 3% error was reported.

Table 2.10 presents the advantages and disadvantages of SOC detection methods based on impedance measurement technique.

Table 2.10: Advantages and disadvantages of SOC detection methods based on the impedance-based methods

Advantages	Disadvantages
Generic (all type of battery technologies)	Online estimation is critical
SOC and SOH detection	SOC sensitive for most chemistries
Acceptable accuracy	Extensive lab experiment
Faulty cell detection	Parameters vary with the type of the battery
Simple	Temperature sensitive

In [121], several typical circuit models used to interpret EIS impedance are presented. The main drawback of the EIS-based SOC estimation method is the limited number of EIS measurements over the SOC and the effort of finding impedances that are sensitive to SOC but not sensitive to temperature and SOH. Another drawback of the method is the time the EIS measurement takes, and the effort required for circuit parameterization, especially at low frequencies, where diffusion is occurring, that makes the EIS method inoperable in practical application. Advantages of EIS-based SOC estimation are that this technique is implementable for all types of battery systems and the impedance parameters can be evaluated for SOH estimation as well. Sensitivity to frequency and temperature is another drawback of this method.

2.7.2 Learning algorithms (self/supervised - data driven)

Learning algorithms, also known as data-based or data-driven algorithms, are used to model and predict the system plants in various engineering fields. Table 2.11 presents the different learning algorithms in six categories. Different algorithm methods in this table are expressed by their abbreviations (see Abbreviations list).

If the system has a distinguishable pattern and the required data and inputs are available, then it can be modeled with these types of learning algorithms. For LIB state estimation, these methods can be suitable candidates. The main difference between data-based methods and model-based methods is that, unlike model-based methods, in data-based methods, there is no exclusive mathematical expres-

Table 2.11: Learning algorithms used for battery state detection

Learning algorithm	subcategory
Neural network family	ANFIS, ANN, AWNN, BPNN, ENN, NN, PRNN, RANN, RBFNN, SNN
Fuzzy logic	FL
Neuro-fuzzy family	NF, ANFIS
Support vector machine family	LSSVM, SVM, SVR
Genetic algorithm	GA
Online self-learning	OSL

sion to describe the connections between LIB voltage, current, temperature, SOC, or other parameters of the cell. The next part, briefly describes two main learning algorithm methods.

2.7.2.1 Neural networks

Neural network and Kalman filter are considered the state-of-the-art methods in estimation of battery states and parameters. Various types of neural networks have been developed to improve the performance and enhance the functionality of the standard approach. Besides the standard approach, which is well defined in [221], other neural-network-based approaches, which are mostly used for state detection, are presented in Table 2.12.

Table 2.12: Available literature on different neural network methods used for battery state detection

Neural network method	Reference
Adaptive neuro-fuzzy interface system (ANFIS)	[6, 42, 80, 303]
Adaptive wavelet neural network (AWNN)	[332]
Artificial neural network (ANN)	[5, 16, 30, 57, 77, 109, 272, 297]
Backpropagation neural network (BPNN)	[130, 223, 262]
Extreme learning machine (ELM)	[74]
Elman neural network (ENN)	[246, 250]
Probabilistic Neural Network (PNN)	[169]
Pipelined recurrent neural network (PRNN)	[35]
Recurrent artificial neural network (RANN)	[76]
Radial basis function neural network (RBFNN)	[47, 138, 171, 241]
Structured neural network (SNN)	[8]

A neural network is considered a data driven method used to describe nonlinear models. Similar to the model-based methods, neural network inputs are cell current, voltage, and temperature. For instance, in the SNN case, the system structure can be reduced, and, by taking advantage of predefined functions, faster computation can be achieved. If issues other than computational speed come into play and ANN is unable to access the internal parameters of the cell, a possible solution can be SNN. While different ANN-based approaches are mentioned here, detailed investigation of each method is outside of the scope of this work.

In an energy storage field, a member of NN is usually used for SOC and SOH estimation and, in rare cases, for other battery states. The performance of ANN is highly dependent on how good the collected data is or how well the algorithm is trained. In [130], different training functions are examined to train BPNN. Experiment results show that the performances of neural networks trained by different training functions differ in estimation accuracy and even training speed. It has to be taken into account that

the ANN works with the given amount of data and demonstrates generalized behavior. In [272], it is reported that charge pulses are used to collect training data for LIBs. However, Xu et al. in [309], used FTP drive-cycles for training data collection.

In general, neural network methods can be implemented in a real-time HIL system, but their application in embedded systems such as BMS can be limited due to the processing computation and the increased effort. Some advantages and drawbacks of NN techniques are listed in Table 2.13.

Table 2.13: Advantages and disadvantages of neural network algorithms for state, and parameter estimation gathered from the literature presented in Table 2.12

Advantages
SOC and SOH detection
Detailed investigation of the cell's internal chemistries is not required
Online
Good accuracy, when combined with other techniques
Disadvantages
Large effort in collecting the training data, and training procedure
Should be redesigned once input variables are changed
Computations limits
Higher modeling errors compared to the adaptive algorithms techniques
Limited functionalities

The achievable performance (error range) for the neural network model reported in [272] is 3.8% in SOC estimation; however, methods based on neural networks can be combined with other methods for improvement. The Kalman filter is a popular method that is combined with NN to further reduce the estimation error. In [109], authors used ANN in combination with UKF. They concluded that at 25 °C using FTP-72, the solo NN had an RMS error of 2.6% and a maximum error of 16%. With a combined usage of ANN and UKF, the RMS error decreased to 1.4% and the maximum error decreased to 1.9%. Compared to static neural network, RNN is a dynamic neural network that is also able to reproduce LIB terminal voltage and SOC [35].

In Table 2.14, some references concerning combined ANN and fuzzy logic method (known as “neuro-fuzzy”) are presented.

Table 2.14: Available literature on the neuro-fuzzy combined method used for battery state detection

Method	Reference
Neuro-fuzzy	[49, 64, 81, 161, 263, 303, 309]

2.7.2.2 Fuzzy logic

Fuzzy logic application has also been used and investigated by several researchers for battery state detection. Similarly to the electrical-model-based technique, fuzzy-logic-based methods can be developed by the data obtained from reference performance tests. Generally speaking, data can be categorized into crisp or fuzzy sets. The fuzzy logic method makes use of crisp data that have certainty (real-value data) as the inputs and outputs of the algorithm [26].

A complete fuzzy interface system includes a fuzzifier, which receives both, the input analogue signals and output analogue signals, as feedback to the systems, and a rule processor, which receives the fuzzifier outputs. A rule processor includes a rule base, which describes the relationship between the input variables and output variables and is typically developed based on expert knowledge. The fuzzy logic algorithm also includes a knowledge-data-based section. Finally, a defuzzifier part is required to transform fuzzy output sets into the crisp output.

Application of fuzzy-logic-based methods for LIB state estimation is more practical for SOH detection because the membership functions used to define the border conditions are limited and the fast changes of SOC are hard to capture. For instance, EIS measurement can be used for SOH detection based on fuzzy logic technique [225, 256, 322]. EIS measurements as input data to the fuzzy logic algorithm should be pre-processed (for example, by observing the significant impedance growth at low frequencies and determining possible monotonic changes over the desired SOC/temperature range). For that, EIS data are mapped to the black-box model (Matlab fuzzy logic toolbox, for instance).

Table 2.15 gathers most of the noticeable works developed with the fuzzy logic technique for SOC, SOH, and combined detection.

Table 2.15: Available literature on the fuzzy logic method used for battery state detection

State	Reference
SOC	[41, 99, 101, 159, 161, 167, 177, 213, 255, 313]
SOH	[49, 240, 241, 253, 254]
Combined SOC-SOH	[225, 252, 322, 323]

The drawbacks of using the fuzzy logic method for state detection is, first, that it is a time consuming procedure (because of the effort of collecting EIS data or defining membership functions) and, second, the temperature dependency, which is mostly neglected. Another issue is the relatively higher estimation errors. In [252], and [291], SOC estimation error is reported to be around 5%, which is more than double the error in comparison with other adaptive algorithms. The development of the fuzzy logic algorithm has been neglected for this thesis.

2.7.2.3 Other learning algorithms for state detection

Other learning algorithms used for state detection or parameter prediction found in the literature are listed in Table 2.16.

The genetic algorithm (GA) has been found to be suitable for optimization and parameter prediction. In [32], authors used GA for automatic parameter extraction. Even cell balancing can be performed with genetic algorithm optimization that is integrated with the neural network algorithm or fuzzy logic control.

The support Vector Machine (SVM) algorithm has been developed in statistical learning theory. This

type of algorithm is widely used for a domain of nonlinear classification, for approximation of the functions, and even in pattern recognition [327]. For the battery field, SVM methods are used for battery modeling and state detection in particular SOC. In [83], the development process of this algorithm is explained. The major drawback of SVM is its higher computational burden for the constrained optimization programming. For that LSSVM (least square support vector machine), which solves linear equations instead of a quadratic programming problem can be used. LSSVM is especially preferred for large-scale problems [288].

Table 2.16: Available literature on other learning algorithm techniques used for battery state detection

Method	Reference
Genetic algorithm (GA)	[32, 328]
Locally linear model tree (LOLIMOT)	[219]
Least square support vector machine (LS-SVM)	[19, 54, 160]
Online self-learning (OSL)	[314]
Support vector machine (SVM)	[10, 11, 97, 102, 136, 185, 327]
Support vector machine for regression (SVMR/SVR)	[9, 103, 249, 298]

2.7.3 Adaptive filter algorithms (model-based and non-model-based)

The algorithms based on the adaptive filtering are accurate methods for state detection. These algorithms are iterative, and the model predictions can be compared with the experimental data in each iteration. This helps the prediction converges to the true state over the time. High current fluctuations in the input current profile allow the gathering of more information about the battery dynamics, whereas a constant current profile contains much less information for adaptive model development, as no dynamics of the cell are excited. Adaptive filter algorithms can be categorized as listed below:

- Kalman filter family
- Particle filter family (PF, UPF, RPF, GRPF)
- Moving horizon estimation (MHE) ([244])
- Recursive least squares (RLS)

The adaptive monitoring algorithms are often based on the battery ECM or based on differential equations. This is in accordance with the equations, that describe the ECM [281], or state space model of the system [202, 204]. In Table 2.17, different algorithms based on the basic Kalman filter are presented, and, in Section 2.7.3.1, linear and nonlinear Kalman filter algorithms are explained.

2.7.3.1 Kalman filter

In 1960, Kalman developed an optimal state estimation algorithm given noisy observations. Kalman filter is an optimal recursive estimator that can be developed based on the Bayesian theorem in an efficient manner under certain assumptions [132, 105]. Depending on the application and requirements, Kalman filter theory can be used to develop other methods belonging to the Kalman filter family listed in Table 2.17.

Table 2.17: Available literature on the variation of Kalman filter methods used for battery state detection

Kalman filter method	reference
Linear Kalman filter (LKF)	[200, 259, 316]
Extended Kalman filter (EKF)	[8, 74, 114, 155, 162, 158, 203, 295]
Improved extended Kalman filter (IEKF)	[239]
Adaptive extended Kalman filter (AEKF)	[74, 108, 135, 238, 305]
Dual extended Kalman filter (DEKF)	[144, 283]
Robust extended Kalman filter (REKF)	[81, 117]
Cubature Kalman filter (CKF)	[293]
Central difference Kalman filter (CDKF)	[164]
Iterated extended Kalman filter (ITEKF)	[78]
Unscented Kalman filter (UKF)	[9, 74, 107, 109, 110, 134]
Adaptive unscented Kalman filter (AUKF)	[74, 196, 264, 329]
Sigma point Kalman filter (SPKF)	[111, 112, 162, 185, 204, 326]
Square root spherical unscented Kalman filter (Sqrt-UKFST)	[14]
Dual time-scale Kalman filter (DKF)	[65, 114, 306]

In [74], a comparative study of different Kalman filter algorithms (EKF, AEKF, UKF, AUKF) is presented.

- **Linear Kalman filter LKF:**

LKF is the basic form of the Kalman filter. The objective of the estimator is to extract as much information as possible contained in the observations about the states ($\mathbf{y}_k \rightarrow \mathbf{x}_k$). According to the state-space model of the system (see Figure 2.13), and assuming the Equations 2.62 and 2.63, the description of the linear discrete system becomes:

$$\mathbf{x}_{k+1} = \mathbf{A}_k \mathbf{x}_k + \mathbf{B}_k \mathbf{u}_k + \mathbf{w}_k, \quad (2.75)$$

$$\mathbf{y}_k = \mathbf{C}_k \mathbf{x}_k + \mathbf{D}_k \mathbf{u}_k + \mathbf{v}_k, \quad (2.76)$$

The matrices “ \mathbf{A}_k ”, “ \mathbf{B}_k ”, “ \mathbf{C}_k ”, and “ \mathbf{D}_k ” describe the behavior of the linear system (see Section 2.6). In order to avoid notation and indexing confusion, below the variations are described briefly:

- $\mathbf{x}(t)$ is the true continuous state of the dynamic system
- \mathbf{x}_k is the discrete-time state vector of the dynamic system
- $\hat{\mathbf{x}}_k$ is the system model estimated state vector
- $\hat{\mathbf{x}}_k^-$ is the system model predicted state
- $\hat{\mathbf{x}}_k^+$ is the system model updated estimate of the state
- $\hat{\mathbf{x}}_k$ is the dynamics of the state estimated error

The initialization of the algorithm for $k = 0$ is shown in Equation 2.77 (see the explanation of the expected value in Appendix A.2):

$$\hat{\mathbf{x}}_0^+ = \mathbb{E}\{\mathbf{x}_0\} \quad (2.77)$$

The covariance matrix of the state estimation error is:

$$\mathbf{P}_0^+ = \mathbb{E}\{(\mathbf{x}_0 - \hat{\mathbf{x}}_0^+)(\mathbf{x}_0 - \hat{\mathbf{x}}_0^+)^T\} \quad (2.78)$$

During the time update (prediction), initial (previous) LIB states, and the error covariances are predicted. When the new measurement comes, these predictions are corrected; this is also known as estimation.

During the prediction step, the predicted model state $\hat{\mathbf{x}}_k^-$, and the covariance matrix of the system state estimate error \mathbf{P}_k^- are predicted [205]:

$$\hat{\mathbf{x}}_k^- = \mathbf{A}_{k-1}\hat{\mathbf{x}}_{k-1}^+ + \mathbf{B}_{k-1}u_{k-1} \quad (2.79)$$

$$\mathbf{P}_k^- = \mathbf{A}_{k-1}\mathbf{P}_{k-1}^+\mathbf{A}_{k-1}^T + \mathbf{Q} \quad (2.80)$$

After the prediction step, LKF gain (\mathbf{K}_k) can be calculated:

$$\mathbf{K}_k = \mathbf{P}_k^- \mathbf{C}_k^T (\mathbf{C}_k \mathbf{P}_k^- \mathbf{C}_k^T + \mathbf{R})^{-1} \quad (2.81)$$

where $\mathbf{Q} = E[ww^T]$ and $\mathbf{R} = E[vv^T]$ are tunable parameters. Kalman gain as a metric that shows how informative the measurement is (representative of the measurement to the noisiness of the state). The larger the variance in measurement (the more measurement deviation, and uncertainties, or less informative measurement), the less trust in the measurement, hence, the smaller Kalman gain. In other words, the Kalman gain takes the measurement as the reliable source of an estimation update. If the model uncertainties are high, then the Kalman gain will be high. The larger the state prediction covariance, the more we trust the measurement, and thus the larger the Kalman gain. A high Kalman gain will lead to a high correction of the state estimate during the update step. The updated state estimate is calculated by weighing the error, between the measured voltage, and the model output ($\tilde{\mathbf{e}}_k = \mathbf{y}_k - \hat{\mathbf{y}}_k^-$) with the Kalman gain. The covariance matrix of the system state is also updated with a term weighted by the Kalman gain:

$$\hat{\mathbf{x}}_k^+ = \hat{\mathbf{x}}_k^- + \mathbf{K}_k(\mathbf{y}_k - \hat{\mathbf{y}}_k^-) \quad (2.82)$$

$$\mathbf{P}_k^+ = (\mathbf{I} - \mathbf{K}_k \mathbf{C}_k) \mathbf{P}_k^- \quad (2.83)$$

The LKF calculated voltage output is written as [205]:

$$\hat{\mathbf{y}}_k = \mathbf{C}_k \hat{\mathbf{x}}_k^- + \mathbf{D}_k u_k \quad (2.84)$$

- **Extended Kalman filter** *EKF*:

If the model is nonlinear, EKF can be utilized instead of LKF. EKF can be implemented by linearization of the nonlinear process. Linearization can be done via first order Taylor series expansion [122] at each step time. In most situations, EKF provides good performance, but, if local observability fails, the filter may become unstable [186]. To formulate the EKF, the Jacobian matrix of the partial derivatives of nonlinear state transitions functions “ \mathbf{F} ” and “ \mathbf{H} ” in Equations 2.62 and 2.63, become [201]:

$$\begin{aligned}\mathbf{F}(\mathbf{x}_k, u_k) &\approx \mathbf{F}(\hat{\mathbf{x}}_k, u_k) + \frac{\partial \mathbf{F}(\mathbf{x}_k, u_k)}{\partial \mathbf{x}_k} \Big|_{\mathbf{x}_k = \hat{\mathbf{x}}_k} (\mathbf{x}_k - \hat{\mathbf{x}}_k) \\ \mathbf{H}(\mathbf{x}_k, u_k) &\approx \mathbf{H}(\hat{\mathbf{x}}_k, u_k) + \frac{\partial \mathbf{H}(\mathbf{x}_k, u_k)}{\partial \mathbf{x}_k} \Big|_{\mathbf{x}_k = \hat{\mathbf{x}}_k} (\mathbf{x}_k - \hat{\mathbf{x}}_k)\end{aligned}\tag{2.85}$$

where $\frac{\partial \mathbf{F}(\mathbf{x}_k, u_k)}{\partial \mathbf{x}_k} \Big|_{\mathbf{x}_k = \hat{\mathbf{x}}_k} = \hat{\mathbf{A}}_k$, and $\frac{\partial \mathbf{H}(\mathbf{x}_k, u_k)}{\partial \mathbf{x}_k} \Big|_{\mathbf{x}_k = \hat{\mathbf{x}}_k} = \hat{\mathbf{C}}_k$

In EKF, noise processes are assumed to be Gaussian white noise with a zero mean. This assumption is a good approximation for the model mismatch, as the order of sensor noise is far below compared to the model mismatch.

The resting period is usually the determining factor for filter initialization. In this thesis, SOC has been always initialized from the initial voltage measurement. For real-world applications, SOC initialization within 5% of the true SOC value is considered reasonable. In [260], also is shown that the EKF convergence speed with false initialization is quick and the EKF is robust to the initialization errors. In [115], robustness of the EKF under varying loading profiles and temperatures is evaluated, and the estimation errors in validation datasets were found to be around 1%.

2.7.3.2 Particle filter

An alternative branch for solving nonlinear estimation problems, aside from the EKF, is the discretization of the state-space as in grid filters, and particle filters. EKF, particle filter, and approximate grid-based methods comprise three approximate nonlinear Bayesian filters. Theoretically, these estimation techniques allow one to approach the true statistics of the state with arbitrary accuracy. As the computational complexity grows with the dimension of the state-space system [13], the applications are limited to the low-dimensional problems. For a given sequence of observations, both, Kalman filter and particle filter algorithms, recursively update the estimates of the state variables. However, the main difference between the two is that the Kalman filter algorithm performs this task with linear projections and the particle filter algorithm with the sequential Monte Carlo (MC) method.

As with Kalman filter, particle filter can be used to recursively update the posterior distribution using sequential importance sampling (SIS) and resampling. A set of weighted particles is used to approximate the posterior without any explicit assumption [89]. Using Monte Carlo resampling techniques for particle filter makes it possible to deal with any kind of distribution by approximating the respective probability density function (PDF) with a set of particles or samples. The computational effort of a particle filter increases with the number of particles and the resampling algorithm [113]. In order to utilize the particle filter method for microcontroller implementation, employing a reasonable number of particles and states can be beneficial; however, to have an accurate online estimation, particle filter seems to be the most difficult method [26]. Table 2.18 gathers the available literature based on the particle filter method.

Table 2.18: Available literature on the particle filter technique used for battery state detection

State	Reference
SOC	[4, 89, 110, 242, 275, 294]
SOH	[187, 285]
Combined SOC-SOH	[235, 236]

In [195], it is shown that an EKF-based approximation of the nonlinear dynamic system is generally the more suitable selection than UKF and particle filter. Particle filter usage is justifiable when the system is corrupted with non-Gaussian noise, which leads to much higher simulation complexities and less accuracy for the test case, and its practical applicability would be difficult to justify.

2.7.4 Controllers and observers (linear/nonlinear)

Observers and controllers can be also employed for battery state detection and parameter prediction. In the mid 1960s, Luenberger introduced the theory of observers: “Any system driven by the output of the given system can serve as an observer for that system.”

Advanced state observers, including the PID controller, sliding-mode observers, Luenberger observer, and nonlinear observer are now commonly used for various applications [292]. Generally, the observer design is based on the mathematical model of the plant (e.g., state-space system representation); therefore, system nonlinearities, uncertainties, and disturbance could affect the design in the practical applications. Table 2.19 summarizes the available literature on different observer algorithms used for state detection and parameter prediction.

Table 2.19: Available literature on observer algorithm techniques used for battery state detection

Observer algorithms	reference
PID	[22, 247, 268, 308]
Luenberger observer	[116, 162, 208, 277]
Sliding mode observer	[53, 75, 142, 143, 146, 173, 191, 331]
Nonlinear observer	[193, 304]
H-infinity observer	[106, 168, 277, 311]

The following section introduces the most commonly used observers/controllers for the battery system state detection problem.

2.7.4.1 PID controller

The PID controller is the industry’s most common type of controller. Common variations of the PID controller are P, PI, PD, and PID. In this thesis, types P and PI have been used for regulating the estimated SOC, and parameters based on the model error (see Equations 2.88 to 2.90). If “e” is the error signal the controller receives and “y” is the controller output, the PID controller formulation in continuous-time is:

$$y(t) = k_p e(t) + k_i \int_0^t e(\tau) d\tau + k_d e'(t) \quad (2.86)$$

that has a Laplace form of:

$$C(s) = \frac{Y(s)}{E(s)} = k_p + \frac{k_i}{s} + k_d s \quad (2.87)$$

The simulation error can be used as the input of the PID controller. The error signal can be of three types; the error of OCV, the error of the terminal voltage, and the error of the filtered voltage signal.

$$e_{OCV} = OCV_{measurement} - OCV_{model} \quad (2.88)$$

$$e_V = V_t - V_{t,model} \quad (2.89)$$

$$e_{V_z} = V_{t,z} - V_{model,z} \quad (2.90)$$

In this thesis, the error of the ECM terminal voltage (e_V) was used to correct the SOC. By using the terminal voltage measurement, the modeling error can be calculated in real time and passed to the algorithms for correction purposes. Figure 2.20 shows the PI controller implementation in Simulink. By setting $k_i = 0$, the PI controller becomes a P controller.

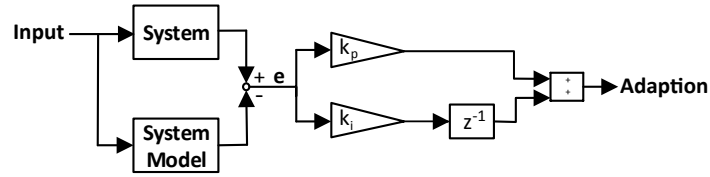


Figure 2.20: PI controller Simulink schematic

The PI controller was used to regulate the estimated SOC for the Ah-counting method. The SOC equation by Ah-counting method is presented in Equation 2.72. The conventional Ah-counting formula is then being corrected by including the modeling voltage error term into Equation 2.72:

$$SOC(t) = SOC_0 + \int_0^t \left(\frac{\eta_c I}{C_{act}} + (k_p + k_i z^{-1}) e_V \right) dt \quad (2.91)$$

In this equation, k_p and k_i are the PI controller tuning factors which can be adjusted manually to regulate the calculated SOC. The regulated SOC was used to update the parameters of the ECM's LUTs. With this method, the error of ECM voltage can be reduced significantly. This technique has been used throughout this thesis.

2.7.4.2 Luenberger observer

The Luenberger observer (LO) has simple implementation and tuning; therefore, in industry applications, it is used mostly for linear deterministic systems. The LO corrects the estimation equation with

feedback from the estimation error. The observer design is as follows [162]:

$$\hat{\mathbf{x}}_{k+1} = \mathbf{A}_k \hat{\mathbf{x}}_k + \mathbf{B}_k \mathbf{u}_k + L(\mathbf{y}_k - C_k \hat{\mathbf{x}}_k - D_k u_k) \quad (2.92)$$

The dynamics of the state estimation error $\mathbf{e}_k = \tilde{\mathbf{x}}_k = \mathbf{x}_k - \hat{\mathbf{x}}_k$ (for simplification $D_k = 0$) is:

$$\tilde{\mathbf{x}}_{k+1} = \mathbf{A}_k \mathbf{x}_k + \mathbf{B}_k \mathbf{u}_k - \mathbf{A}_k \hat{\mathbf{x}}_k - \mathbf{B}_k \mathbf{u}_k - L(\mathbf{y}_k - C_k \hat{\mathbf{x}}_k) = (\mathbf{A}_k - LC_k) \tilde{\mathbf{x}}_k \quad (2.93)$$

2.7.4.3 Basics of the sliding mode observer (SMO) design

The detailed description of the SMO algorithm for state detection is presented in Section 5.3. The system equations are:

$$\dot{\mathbf{x}} = \mathbf{A}\mathbf{x} + \mathbf{B}\mathbf{u} + \mathbf{\Gamma}\zeta(x, u) \quad (2.94)$$

$$\mathbf{y} = \mathbf{C}(\hat{\mathbf{x}}) + \mathbf{D}\mathbf{u} \quad (2.95)$$

In Equation 2.94, $\mathbf{\Gamma}$ and ζ are the bounded disturbance input. In Equation 2.95, \mathbf{y} is the output. So, based on system Equations 2.94 and 2.95, the sliding mode general observer design equation can be presented as follows:

$$\dot{\hat{\mathbf{x}}} = \mathbf{A}\hat{\mathbf{x}} + \mathbf{B}\mathbf{u} + \mathbf{H}(\mathbf{y} - \hat{\mathbf{y}}) + \rho\mathbf{\Gamma}sgn(\mathbf{y} - \hat{\mathbf{y}}) \quad (2.96)$$

$$\hat{\mathbf{y}} = \mathbf{C}\hat{\mathbf{x}} + \mathbf{D}\mathbf{u} \quad (2.97)$$

In Equation 2.96, “ \mathbf{H} ” is the gain matrix and “ ρ ” is the switching gain. These two gains should be chosen in such a way (usually manually) that the stability of the observer system is ensured. The error of the observer is defined as $\mathbf{e} = \mathbf{x} - \hat{\mathbf{x}}$, and it can be calculated by subtracting the Equation 2.94 from the Equation 2.96, so \mathbf{e} becomes [142]:

$$\dot{\mathbf{e}} = (\mathbf{A} - \mathbf{H}\mathbf{C})\mathbf{e} + \mathbf{\Gamma}\zeta(x, u) - \rho\mathbf{\Gamma}sgn(\mathbf{y} - \hat{\mathbf{y}}) \quad (2.98)$$

2.7.4.4 Nonlinear observer

A nonlinear observer (NLO) is proposed with the following observer design [304]:

$$\hat{\mathbf{x}}_{k+1} = \mathbf{A}_k \hat{\mathbf{x}}_k + \mathbf{B}_k \mathbf{u}_k + K \dot{h}^T(\hat{\mathbf{x}}_k)(\mathbf{y}_k - \hat{\mathbf{y}}_k) \quad (2.99)$$

$$\hat{\mathbf{y}}_k = \mathbf{H}(\hat{\mathbf{x}}_k) + \mathbf{D}_k \mathbf{u}_k \quad (2.100)$$

Since “ $\mathbf{H}(\hat{\mathbf{x}})$ ” is a function of system states (SOC), this observer design is nonlinear. By using the Lyapunov equation observer gain, and by using the state estimate error equation ($e = \mathbf{x} - \hat{\mathbf{x}}$), the system matrices can be built. Similar to the sliding mode observer, the observer stability can be proven by choosing a candidate Lyapunov function.

In [304], NLO is compared with SMO and EKF, and it is shown that the performance of this observer

is less accurate for SOC detection (NLO with the error bound of 5% compared to 2.5% for SMO the observer and 1% for EKF).

2.7.4.5 H-infinity observer

the H-infinity (H_∞) observer has been used to solve the state estimation problems in linear and nonlinear systems. Compared with the Kalman filter, the H-infinity observer does not depend on the exact model structure, measurement errors, or system noise. But, similarly to Kalman filter, it is insensitive to the measurement noise and the model uncertainties [106]. Table 2.19 summarizes the available literature for various observers introduced in this part.

2.7.5 Combined (hybrid) state detection methods

Combined or hybrid models have been developed to obtain both advantages from the different methods. As explaining the work accomplished in the literature is an intense task, Table 2.20 presents the research literature on the available combined methods for SOC detection (e.g., Kalman filter in combination with other methods).

Table 2.20: Literatures on hybrid techniques (a combination of the Kalman filter with other techniques) used for SOC detection

SOC	SVM	Ah	NN	Fuzzy Logic	Neuro-fuzzy
Kalman filter	[185]	[289]	[8, 74, 109]	[41]	[64, 309]

In [289], Wang et al. proposed a SOC estimation method, denoted as the KalmanAh method, which uses the Kalman filter method to correct for the initial value used in the Ah-counting method. Other combinations of algorithms, such as learning algorithms with impedance- and voltage-based methods in [76], or with observers are reported in [22, 246].

2.7.6 Other state detection methods

2.7.6.1 SOC and SOH based on the linear parameter varying method

Linear parameter varying (LPV) is based on the linearization of the non-linear systems operating in one or a few distinct operation points. The LPV framework can be developed by deriving a linear description of the system at its operation points. In the LPV framework, linear system dynamics depend on the so-called scheduling parameter [273]. In [119], authors proposed the SOC estimation method for automotive application based on the LPV technique, and, in [214], an on-board SOH monitoring of LIBs with this technique is proposed. LPV has a medium complexity for the model implementation.

2.7.6.2 SOC and SOH based on mechanical stress

In [44], a method for SOC and SOH calculation is proposed based on the observation of stack stress on cells during their cycle-life with different cycling parameters. Cannarella et al. claimed that this method could be more advantageous than conventional voltage-based SOC detection, as stress measurement is more sensitive to SOC than voltage, and it also has the ability to measure SOC in the

presence of self-discharge. For experimental purposes, Uniaxial stress as a result of electrode expansion against a constraint (0.05 MPa force fixture) in the direction normal to the plane of the electrodes was used. In [45], it is shown that light stack pressure can be beneficial for long-term performance by preventing layer delamination. The stress-based method could be more suitable for SOH detection and should be measured carefully at high and low SOCs during cycle-life to find a corresponding fit.

2.8 Upscaling and pack-level modeling

Modeling of the LIB for pack-level has not been given enough attention in the existing literature. Unlike deep level modeling of LIBs, which results in detailed parameters and high accuracy, modeling of the LIB pack is at a high-level, meaning that fewer parameters are estimated. Monitoring algorithms for a single LIB has to be upscaled to expand the usage of developed algorithms to the pack-level. For that, a general review of the pack-level models is presented in [85]. The battery pack includes a series and/or parallel connection of the cells. On the one hand, the cell with the lowest capacity limits the capacity of the entire pack due to the serial connection of all cells, and, on the other hand, the cell with the highest resistance limits the upper usable SOC because the cell voltage limits, restrict the charge power as well as the cut-off voltage limits. The lower usable SOC is limited by the increase in the sum of all cell resistances in the pack because the system voltage limit is reached prior to the cell voltage limit during discharge.

Individual cell models and algorithms, including the electrical model, thermal model, and state detection algorithms, can be upscaled to represent the whole pack. As testing the whole pack is an expensive effort and requires a lot of resources, most tests were performed at the cell-level, and the models developed at the cell-level have been verified and upscaled.

The first step towards developing the pack model is to create series and parallel connection of the ECM by using the verified cell-level models. Figures 2.21 and 2.22 demonstrate series and parallel connection of two cells. Equations 2.101 to 2.104 formulate the series and parallel connections of the cells.

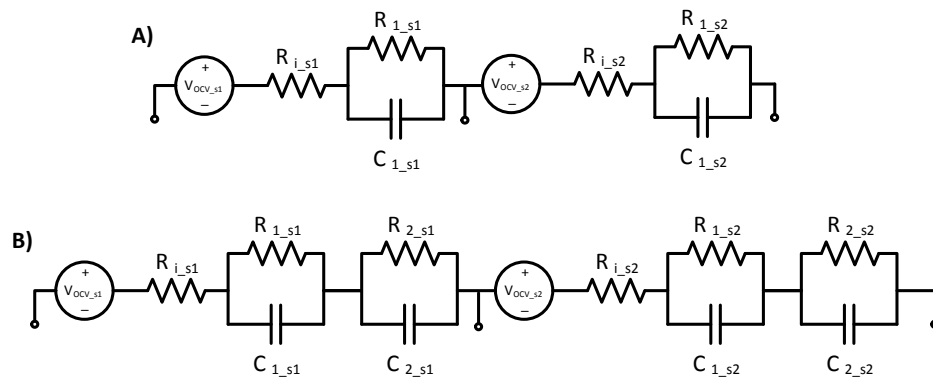


Figure 2.21: Series connection of two LIB-ECMs: A) 1RC, B) 2RC

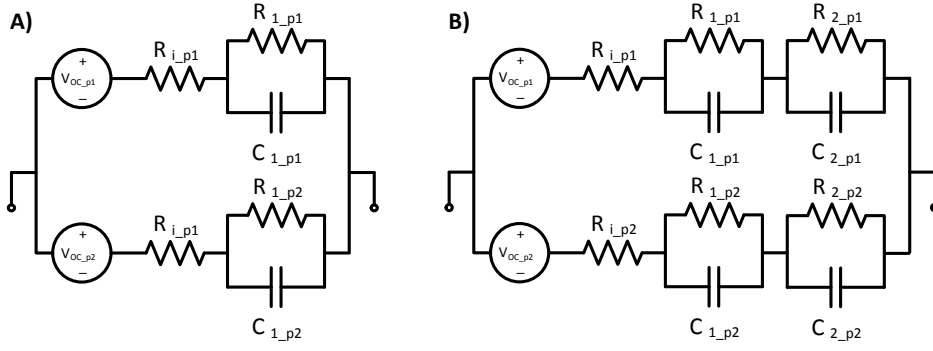


Figure 2.22: Parallel connection of two LIB-ECMs: A) 1RC, B) 2RC

Adding an additional RC element to the LIB-ECM significantly increases the parameterization effort, and calculation of the whole pack increases accordingly. Impedance of 1RC element can be calculated as:

$$Z_{R_n C_n} = \frac{1}{\frac{1}{R_n} + j\omega C_n} = \frac{R_n}{1 + j\omega R_n C_n} \quad (2.101)$$

Total impedance and voltage of the series-connected ECMs with 1RC can be calculated as:

$$Z_{series} = \sum_{n=1}^m R_{i-sn} + \sum_{n=1}^m \frac{R_{1-sn}}{1 + j\omega R_{1-sn} C_{1-sn}} \quad (2.102)$$

$$V_{series} = V_{oc-series} + I Z_{series} \quad \text{where} \quad V_{oc-series} = \sum_{n=1}^m V_{OCV-sn} \quad (2.103)$$

If all cells in the series string assumed to be identical, Equation 2.102 is simplified to:

$$Z_{series} = m \left(\frac{R_i + R_1 + j\omega R_i R_1 C_1}{1 + j\omega R_1 C_1} \right) \quad \text{and} \quad V_{OCV-series} = m V_{oc} \quad (2.104)$$

where “m” is the number of series ECMs.

Similarly, for a parallel connection of two LIB models, each with 1RC:

$$Y_{parallel} = \sum_{n=1}^p \frac{1 + j\omega R_{1-pn} C_{1-pn}}{R_{i-pn} + R_{1-pn} + j\omega R_{i-pn} R_{1-pn} C_{1-pn}} \quad \text{and} \quad Z_{parallel} = \frac{1}{Y_{parallel}} \quad (2.105)$$

If all the cells are identical, Equation 2.105 becomes:

$$Y_{parallel} = p \left(\frac{1 + j\omega R_1 C_1}{R_i + R_1 + j\omega R_i R_1 C_1} \right) \quad (2.106)$$

Where “p” is the number of parallel ECM connections. Modeling the series connection of the cells is straightforward, however, to model the parallel cells, a big-cell configuration is introduced in Section 6.3.1.

3 Experimental

To provide deeper insights into LIB, laboratory experiments make both, in-situ and ex-situ measurements and studies, possible. For that, a well equipped laboratory has been designed, commissioned, and brought into operation. The design and building-up of the laboratory, and the equipping process are briefly described in Appendix C.1.

In this thesis, non-destructive ex-situ tests were conducted on the DUT to systematically produce the required data, used for model and algorithm development. For that, all the cells were initially conditioned (by performing a few standard charge/discharge cycles). After a few conditioning cycles, a series of periodic experiments were performed on the cells to collect the required data for extracting the aging parameters. This includes, cycle-life tests (including drive-cycle-based tests), reference performance tests (RPT), EIS test, and evaluation tests (drive-cycles, mixed profiles). RPT tests are considered as HPPC tests in this thesis. A temperature range of $0^{\circ}\text{C} \leq T \leq 60^{\circ}\text{C}$ was selected for the cycle-life characterization studies of the cells (this range covers beyond the Singapore climatic temperatures). Three fresh cells were used for each temperature to provide statistically reliable data. Standard accelerated cycle-life tests followed the reference performance tests after every 100 cycles, and this process were repeated until the cells' EOL. The structure of this chapter is as follows:

The DUT is introduced in Section 3.1, laboratory setup and cell testing structure is introduced in Section 3.2. This chapter continues with charging strategies in Section 3.3. In Section 3.4, the results of the aging studies (cycle-life and calendar-life) are presented.

3.1 DUT

The investigation has mainly been conducted on one cell type: a high-power NMC pouch cell with a nominal capacity of 63 Ah designed for automotive applications. Table 3.1 provides an overview of the important cell parameters.

Table 3.1: The DUT specification (manufactured by Kokam). Cell data sheet can be found in Appendix D.1

Characteristic	Value
Dimensions ($L \times W \times T$)	262 mm x 257 mm x 10.6 mm
Weight	1.52 kg
Nominal voltage	3.7 V
Lower voltage limit	2.7 V
Upper voltage limit	4.2 V
Rated capacity	63 Ah

Figure 3.1, presents a typical DUT used in the experimental.

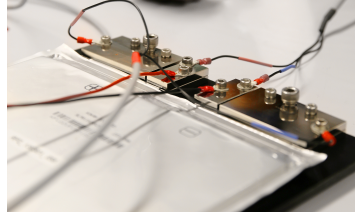
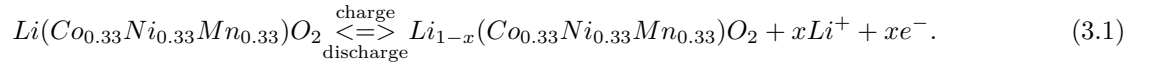


Figure 3.1: DUT mounted on the in-house custom-made cell holder

Little information about the exact chemistry was available for this cell, and it was assumed that the cathode material was $LiCo_{0.33}Ni_{0.33}Mn_{0.33}O_2$ (NMC111). The anode material was graphite (C), which was found by X-Ray Diffraction (XRD) analysis. Graphite is popular for its more safety and aging properties. The electrolyte solvent is EC:EMC with $LiPF_6$ salt. More information about this electrolyte was presented by Botte et al. in terms of thermal stability by means of a differential scanning calorimeter (DSC) [36].

Cell-to-cell parameters vary, even if the cells are from the same batch. There may be small impurities or manufacturing variations or faults that may lead to the sudden failure of the cells or cause behaviors different from that of the rest. To address this issue, for each experiment set, three cells have been used in order to obtain statistically reliable results.

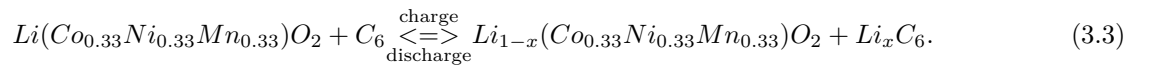
In total, 40 Kokam cells were used for the experiment. Assuming an equally distributed compound of nickel, manganese, and cobalt for the cathode and the graphite anode, the reactions on the cathode side can be written as:



The reaction in the anode side is described by:



The simplified overall reaction (neglecting the electrode balance) is:



LIBs are temperature sensitive, and for this reason, tests were designed and conducted at different temperatures. This is shown in the testing flowchart in Figure 3.4.

Table 3.2 presents the cells' ID¹ used for the calendar-aging experiments. The cells were stored at 10°C, 25°C and 60°C at a SOC of 100%, and the cells stored at 40°C were adjusted to a SOC of 50%. The cells listed in the Table 3.3 underwent an accelerated cycle-life test with a current of 1C for charging and 1C for discharging. Kok-023, Kok-024, and Kok-025 were used to repeat the same accelerated cycle-life tests performed on the Kok-017, Kok-018, and Kok-019, which were tested at 15°C. The reason for this was that the first 3 cells demonstrated highly unexpected behavior and non-uniform results.

Aging investigations of the cell performance over the different charging currents (1C and 2C) and the fast charging (3C) current was conducted by another colleague; however, the detailed studies on finding

¹ Cells were tagged with the ID, in a format of Kok-XXX, for instance, Kok-520 was used for the calendar-life test. This cell was stored (fully charged) at 10°C for 32 weeks

an optimum charging protocol to enhance the lifetime of the cells has not been investigated and is outside the scope of this thesis.

Table 3.2: An overview of the cells used for the calendar-aging experiment

Storage temperature	10°C	25°C	40°C	60°C
SOC level	100%	100%	50%	100%
Cell ID (Kok-XXX)	520	038	516	524
	522	039	517	525
	523	040	518	526
Storage (weeks)	32	20	8	20

Table 3.3: An overview of the cells used for the cycle-life experiments based on the accelerated aging profile with the SOC range of 0%-100%

Accelerated cycling temperature	15°C	15°C	25°C	40°C	60°C
Cell ID (Kok-XXX)	017	023	014	002	020
	018	024	015	003	021
	019	025	016	004	022
Cycles carried out	1000	1000	2500	2000	500

Table 3.4 lists the cells' ID used for the cycle-life experiments, designed according to the FTP drive-cycle load profile (1000 cycles with 1C CCCV charge, and FTP discharge) to prove the eligibility of the models for EV applications developed in this work.

Table 3.4: Overview of the cells used for cycle-life experiments based on the FTP drive-cycle in order to simulate a real case scenario with the SOC range of 0%-100%

FTP cycling Temperature	25°C	40°C
Cell ID (Kok-XXX)	502	527
	504	528
	505	529
Cycles carried out	1000	1000

Among all the cells, Kok-511 was specifically dedicated to the real-time HIL testing with the dSPACE simulator (see Section 6.2).

The next section deals with the testing structure, and introduces the test setup used in this work.

3.2 Laboratory setup and cell testing structure

Table 3.5 presents an overview of the laboratory equipment. Main equipment include: battery cyclers, climate chambers, HIL system, and data loggers. Figure 3.2 presents a schematic of the complete test setup used in the experimental.

Table 3.5: Testing equipment

Cyclers: BaSyTec (CTS, XCTS, GSM), Digatron (MCT-200, MCT-300)
Climate chambers : Memmert (256L, Incubators), Espec
Data logger: Dewetron (20 kHz)
HIL: dSPACE

To study the temperature impact on the performance and lifetime, cells were placed inside the climate chamber and tested at the controlled temperatures, while the humidity effect was neglected. The experiments were carried out based on the manufacturer recommendation, provided in the DUT data sheet. Mechanical investigations, such as shock, vibration, and external pressure have not been investigated.

The cells were cycled by the battery cycler, while the climate chamber was controlled by the battery cycler computer through local area network (LAN) communication. Both the HIL system, and the BMS setup were directly connected to the DUT, and used to evaluate the models and state detection algorithms. This was a real-time process.

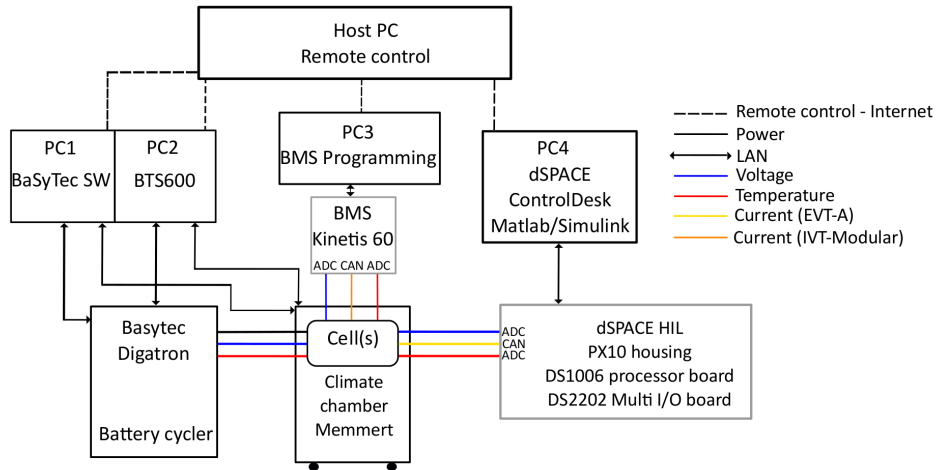


Figure 3.2: Complete test setup used in this work. Cell models and state detection algorithms were implemented in the HIL system and the BMS for evaluation purposes

To operate the batteries safely and to produce accurate, and reliable results, proper external connections to the battery terminals were necessary. Custom-designed general purpose cell holders were built in-house (see Figure 3.3). These cell holders were designed in such a way as to accommodate various cells, regardless of their size or geometries². Acrylic polymer material (cast acrylic ISO 7823-1) was used to build the cell holders. This material is lightweight with good dielectric properties. It also has

² From coin cells (all types) and cylindrical cells (18650, 26650, and 32113) up to the large-format pouch bag cells

exceptional weatherproof durability, mechanical strength, heat strength, and impact strength. Basically, acrylic demonstrates superior properties compared to other plastic materials for this purpose. A laser-cutting machine (Epilog Legend 36EXT 75W) was used to cut the acrylic material into the desired sizes. For more accurate measurement, four-wire³ measuring technique was used in all the experiments.

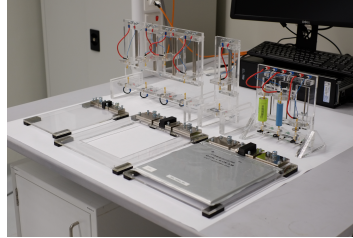


Figure 3.3: Various in-house custom-made cell holders with gold-plated Kelvin probes and nickel-plated copper bars providing a four-wire measurement capability

Cells listed in Tables 3.2, 3.3, and 3.4 underwent a testing structure as shown in the flowchart in Figure 3.4.

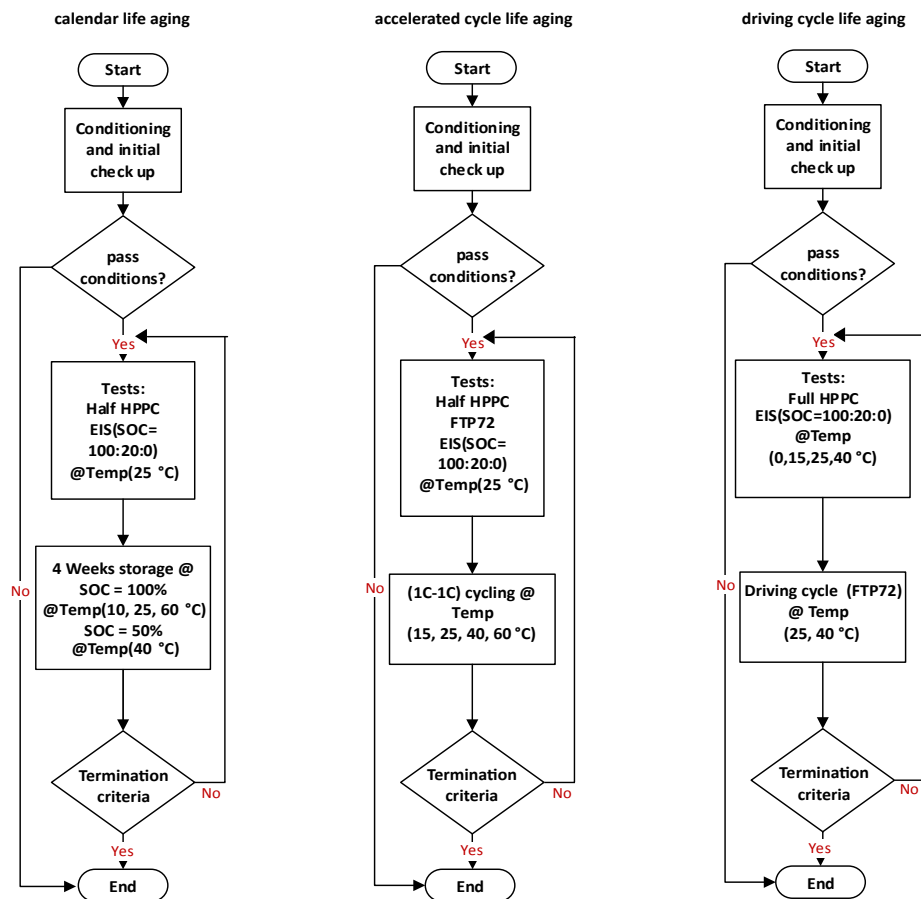


Figure 3.4: Testing flowcharts containing calendar-life and cycle-life aging experiments

³ This technique uses separate wire pairs for current-carrying and voltage-sensing electrodes

This flowchart has a few stages. The first stage was dedicated to the initial checkup, and conditioning. At first, the new cells were visually checked for any mechanical damages, or abnormalities, then the cells were conditioned. Before conducting any test on the LIBs for the first time, they should be cycled a few times inside the temperature chamber controlled at room temperature. The reason for doing it is to stabilize the discharge capacity of the cells [100]. In order to condition the cells, two complete cycles were conducted on the cells. After that, basic electrical checks such as 1 kHz AC impedance measurement (with HIOKI HiTESTER BT3562), and discharge capacity test were used to check if the cells were electrically suitable for the aging experiments. The results from this stage were used to sort the cells with regard to their discharge capacity.

In this flowchart, the pass condition stage was used to check if the cells fulfill the requirements. The next stage, was dedicated to the performance HPPC test⁴, drive-cycle, and EIS measurements. After this stage, cycle-life and calendar-life tests were performed, then the cells were checked for test termination criteria. The whole process is describe in more details in this chapter. The next section shortly presents the charging performance of the DUT.

3.3 Charging performance and strategies

The charging of the LIBs means intercalation of Li-ions into the anode and deintercalation from the cathode. Charging can be performed using different techniques. The conventional charging technique is conducted with direct current (DC) charging with CCCV mode (widely used in commercial chargers) or CC mode. For a new cell, this is shown in Figure 3.5.

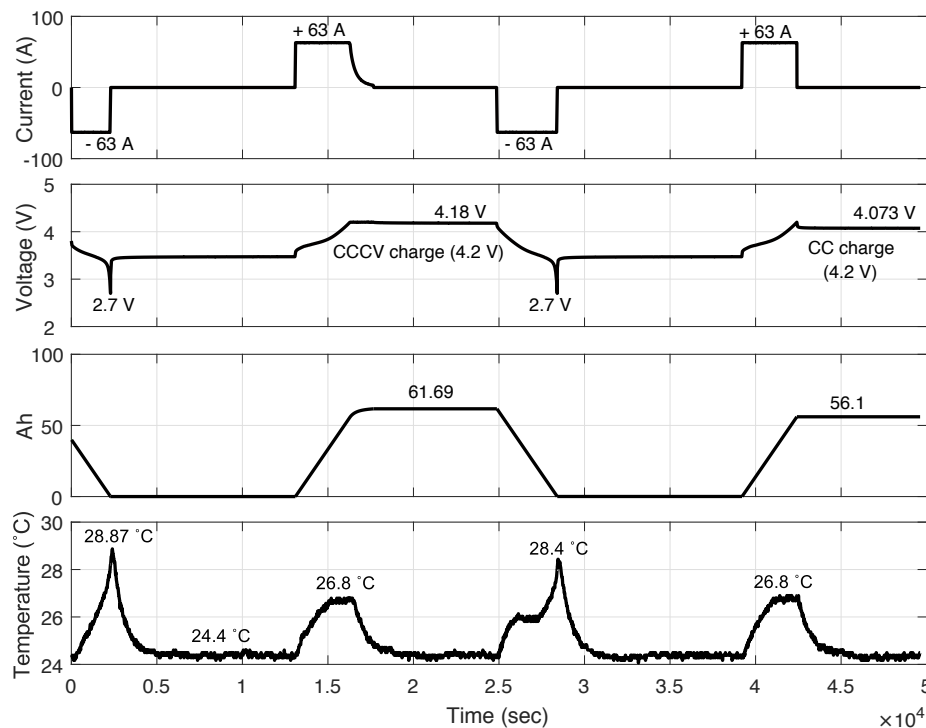


Figure 3.5: Comparison of CCCV vs. CC charging of a new cell

In this figure, a comparison between CCCV charging and CC charging for a new cell (cell 511) is

⁴ Half HPPC test in the flowchart: pulse tests performed only for discharge direction

presented. With the CCCV charging technique, the LIB is initially charged with constant current. During this stage, the voltage of the cell follows the OCV curve superimposed by overpotential [140] until it reaches the upper charge voltage limit, which is 4.2 V. At this moment, the CV stage starts, and the voltage is maintained at 4.2 V until the charging current reaches the cut-off current (0.05C, as a rule of thumb). At this moment, the charging process is terminated.

In EV application, the LIB pack is often not charged with the CCCV technique, and the charging is limited to a SOC of about 90%. For this reason, the new and the aged cells were charged with both the CCCV and the CC techniques to have a comparison between the charging time, temperature, and amount of charge that can be stored in the cells.

Table 3.6 presents the comparison between the CCCV and CC charging modes with 1C current for both new and cycle-aged cells at 25°C.

Table 3.6: 1C (63 A) CCCV vs. CC charging comparison between a new cell and an aged cell at 25°C (for both charge protocols, the same cell was used)

Charging condition single cell	CCCV			CC		
	OCV (V)	SOC (%)	Time (hr)	OCV (V)	SOC (%)	Time (hr)
New Cell (SOH = 100%)	4.18	100	01:15	4.073	90.9	00:53
Aged Cell (SOH = 11.90%: 82.5% of the BOL capacity)	4.15	100	01:25	3.94	80.1	00:38

In this table, OCV represents relaxed cell voltage after the cut-off of the charging current, and the SOH is scaled from 0 % (80% of C_{BOL}) to 100 %. For a new cell, an additional 22 minutes was required for the CV phase, which increased the cell capacity by less than 10%. Compared to the new cells, aged cells took more time to be fully charged with the CCCV mode, however they reached the upper voltage limit faster in the CC mode. For the new cell, a SOC of 100% corresponded to the total charge amount of 61.69 Ah, whereas for the aged cell, the capacity was measured at 50.82 Ah. According to Equation 2.59, because of this capacity loss, the SOH was about 11.90%. From the comparisons above, it can be concluded that charging the cells used in an EV with the CCCV mode will take much more time for new cells compared to the CC mode (1C charging in both cases). However, for the aged cells, the CC charging method was able to charge the cells to only about 80% SOC compared to 90% for the new cells in the CC mode, for EV application. Table 3.7 shows the CCCV and the CC charging for two new paralleled cells with a mean charging current of 126 A.

For two parallel cells, during the CCCV charging mode, the CC stage elapsed time was 54:45 (MM:SS) with a mean current of 126 A. The charged Ah with the CC charge protocol was 114.9 Ah, which corresponds to a SOC of 89.7%. For the parallel cells, the CV phase took 37.1% of the total charging time, which is higher in comparison with the total charging time of a single cell in the CV phase, that took about 29% of the total charging time in a new cell. It is assumed, that this effect is caused by the additional resistance in the cell-cell connector.

In the existing literature, it has been recently reported that the standard CCCV technique for charging the cells is not the most optimal method [251]. The most important and noticeable issues are anode lithium-plating and electrolyte oxidation. In [245], different methods for the charging of LIBs have

Table 3.7: 1C (126 A) CCCV vs. CC charging comparison of two new parallel cells at 25°C

Charging condition parallel cells	CCCV			CC		
	OCV (V)	SOC (%)	Time (hr)	OCV (V)	SOC (%)	Time (hr)
New Cells (25°C)	4.18	100	01:27	4.069	89.701	00:55

been discussed. To enhance the lifetime of the cells with a proper charging method, in [280], it has been shown that a multi-stage constant current (MCC) charging method is considered to have advantages for a long cycle-life of the cells, and, in [284], Waldmann et al. showed how proper charging strategies can lead to avoidance of lithium deposition, which leads to extension of the cycle-life and total charge throughput in LIBs.

The cycle-life of the LIBs is more influenced by the high charging currents (particularly at low temperatures) than by high discharging currents. However, in [141], it has been shown that high-power NMC cells can withstand high charging pulses and peak voltages without deteriorating the cycle-life and that it is a suitable method for charging these cells.

For this thesis, the charging protocol was only based on the CCCV mode. However, an optimized charging protocol should be designed for a shorter charging time, while, at the same time maintaining an expected cycle-life. The next section presents the aging experiments under various operating conditions.

3.4 Aging experiments under different internal and external conditions

3.4.1 Aging parameterization

Both, HPPC and EIS, have been used for characterization of the LIBs; the fundamentals of these methods are explained in Sections 2.4.3.2 and 2.4.3.3. As shown in Figure C.3, a test setup with a four-wire measurement was built inside the temperature chamber for the experiments. The experimental results are presented in this section.

HPPC

In this thesis, the HPPC test was conducted at a controlled ambient temperature of 25°C. However, it is recommended to conduct the HPPC at different temperatures as well. There were some changes made to the current profile of the standard HPPC test plan (see Section 2.4.3.2). The main parameters that have been extracted with this method were OCV, ohmic resistance (R_i), and the R_1C_1 circuit parameters contributing to a 10 s pulse. These parameters were extracted at every 10% SOC steps.

EIS

Similarly to the HPPC test, three cells were used for each set of EIS tests. The cells were tested with a Digatron EIS-meter in galvanostatic operation mode covering the resistance range of 0.3-3000 mΩ,

and a frequency range of 1 mHz to 6.5 kHz. The impedance amplitude measurement accuracy of the device was $\pm 1\%$. For every 20% SOC steps, the EIS measurements were conducted between 700 Hz and 0.1 Hz at 40 frequency points. For the EIS measurements, the climate chamber was set to 0°C, 15°C, 25°C, and 40°C. All the cells had the same known history, and any differences between them could be a result of the manufacturing spread. The averaged test results of the cells were then taken into account. The aim of the experimental chapter is only to investigate cell parameters' variation due to cycle-life and calendar-life. A detailed aging analysis is not included. This part presents the experimental results of the cycle-life and calendar-life aging investigation.

3.4.2 Cycle-life: constant current mode vs. drive-cycle

LIBs experience different rates of aging during their service life. In this thesis, cells underwent accelerated cycle-life experiments at various operating conditions to accelerate real-life aging. Eighteen cells with a CC discharge and a CCCV charge profile were continuously tested at five different temperatures (for 15°C, 6 cells were used). To present a truer-to-life scenario, a second batch of cells (six cells at 25°C and 40°C) was aimed to suit the EV applications. For that, cycle-life tests based on the drive-cycle discharge, and CCCV charge have been designed. However, cycle-life based on drive-cycle method provides no clear identification of the C-rate. Driving cycles were employed to evaluate the cell performances under dynamic conditions. A drive-cycle current profile has been down-scaled from pack-level to cell-level. Various standard drive-cycles [21] are used by manufacturers to test the vehicle emission and for other purposes. In this thesis, two different drive-cycles were used for cycle-life tests and verification purposes. The FTP drive-cycle profile was used for the cycle-life tests, and the Sg taxi drive-cycle (STDC) was additionally employed for further verification. The STDC was a drive-cycle developed in-house at TUM CREATE, based on the Singaporean taxi GPS traces. By comparing both of the drive-cycles, the maximum and an average velocities for the STDC were found to be smaller than the FTP. Figure 3.6 shows a typical FTP drive-cycle profile:

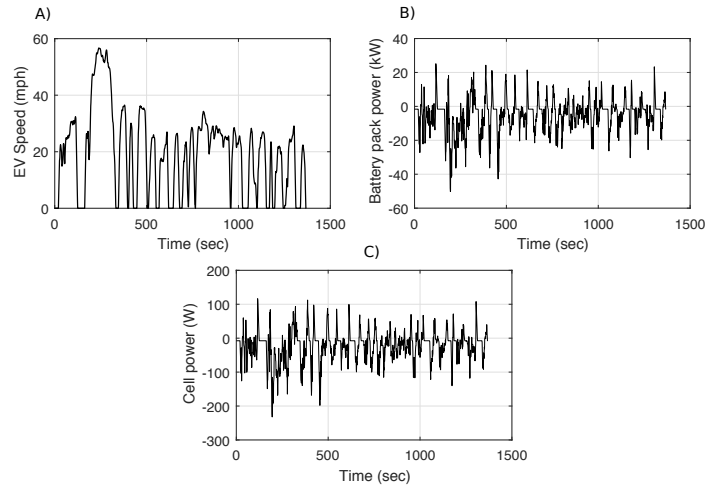


Figure 3.6: A) US EPA urban dynamometer driving schedule “UDDS” (also known as FTP), B) EV battery pack power output, C) Cell-level power data used for drive-cycle implementation

The EV speed and the respective pack power can be measured directly. The power required for the single cell was recalculated. The cell power data was used in the battery cycler test program to implement the drive-cycle profile at the cell-level.

A parametrization script was developed for parameter extraction. Figure 3.7 presents the normalized usable capacity as the result of the cycle-life experiment with the 1C charge/discharge current profile at four different temperatures. The cells tested at 15°C, 25°C, and 40°C show an increase in the discharge capacity for the first few hundreds of cycles. After about 1000 cycles, the usable capacity was reduced to approximately 95% for the cells tested at 15°C. Kok-023 showed malfunctions and therefore its results have been neglected. The test at 25°C showed that all three cells had more homogenized behavior compared to other conditions, and, after 2500 cycles, the capacity degradation was about 15% of the initial discharge capacity. For the cells tested at 40°C the discharge capacity increased for the first 300 cycles, afterwards, capacity loss was so fast, that after 2000 cycles, the cells reached 82% BOL capacity. Cells tested at 60°C only lasted about 300 cycles before the discharge capacity reduced to about 80%; however, the test was continued for 500 cycles to monitor the parameters further. Apparently, the reason for the capacity increase in the first 300 cycles was the increase in the conductivity of the active material in the electrolyte during the initial cycle period [143]. The anode overhang [301] can also result in some temporary storage of lithium, which could explain this initial capacity increase. In the beginning of the cycling, all cells gave a higher capacity than the nominal 63 Ah given by the manufacturer. This is especially apparent in the cells discharged at higher temperatures, which improves the performance by enhancing the reaction kinetics. However, all the side reactions were accelerated as well, resulting in faster performance degradation [126].

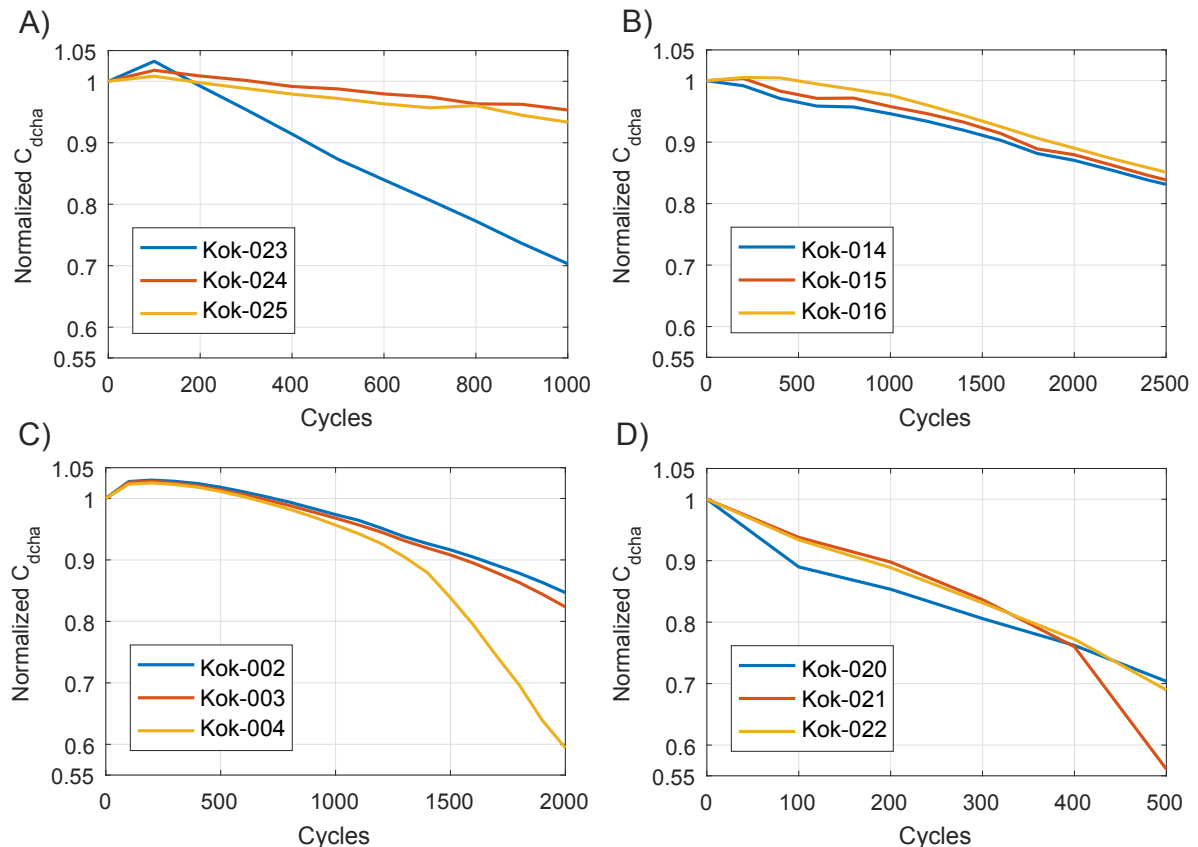


Figure 3.7: Usable capacity evolution over the cycle number: A) at 15°C, B) at 25°C, C) at 40°C, and D) at 60°C

Figure 3.8 presents the ohmic resistance parameters extracted from the cycle-life experiments. The 3D

graph demonstrates the dependence of R_i on the cycle number, SOC, and temperature. The general observable trend for all the graphs at different temperatures shows a direct influence of the cycle number and the SOC on the ohmic resistance values. The cycle number also imposed constant growth of ohmic resistance. For all cases, higher SOC values resulted in a bit lower ohmic resistances. After the initial capacity increase during the cycle-life tests, the decrease of discharge capacity accompanied the increase of ohmic resistance for all four cases.

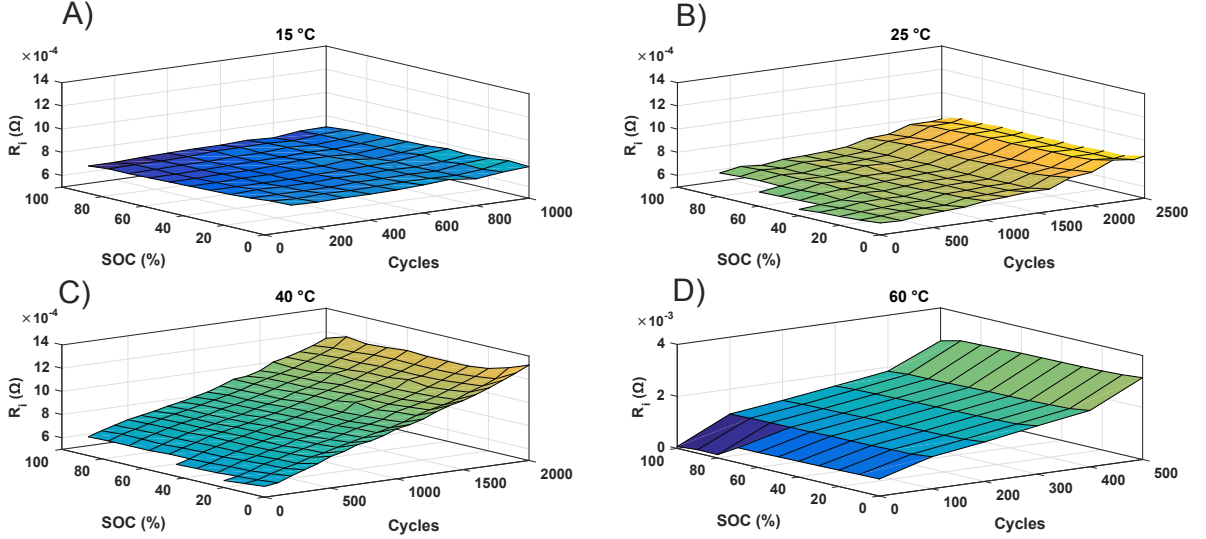


Figure 3.8: Averaged R_i during cycle-life aging at A) 15°C, B) 25°C, C) 40°C, and D) 60°C

The second parameter is regarded as the 10 s resistance and labeled as “ R_1 ”. Figure 3.9 illustrates this parameter. It was extracted from the modified HPPC test results. For all test temperatures, the result shows an almost similar trend of increasing resistance values at lower SOCs and higher cycle number.

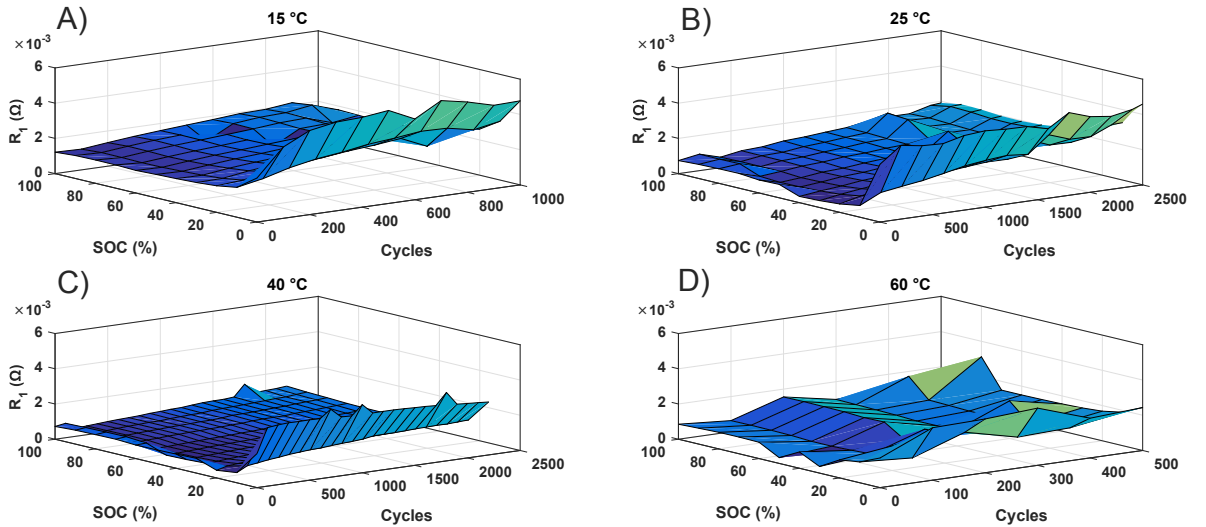


Figure 3.9: Averaged R_1 during cycle-life aging at A) 15°C, B) 25°C, C) 40°C, and D) 60°C

Figure 3.10 illustrates the RC branch capacitance, labeled as “ C_1 ”. The results showed that the

capacitance decreased at lower SOC's as well as during cycle-life aging.

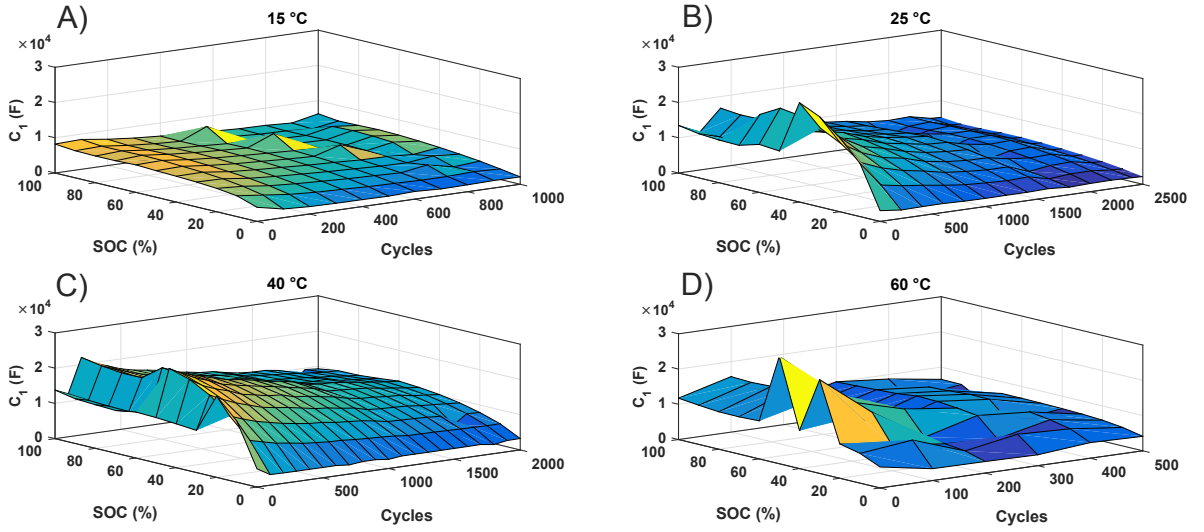


Figure 3.10: Averaged C_1 during cycle-life aging at A) 15°C, B) 25°C, C) 40°C, and D) 60°C

Figure 3.11 shows the evolution of the OCV depending on the number of cycles performed at different SOC's. The OCV is one of the most important cell parameters. On one hand, the trend of using the OCV for SOC estimation is going down; however, the OCV can be successfully used for the initialization of the SOC for SOC estimators. On the other hand, the use of the OCV for SOH estimation is becoming more and more popular. In particular, by having access to open-circuit potential (OCP) of both, the anode and cathode, a method can be developed for SOH estimation by mapping the individual OCPs of each electrode. This method can only be developed if the cell manufacturer provides the OCP of both electrodes when the cell is new. In Figure 3.11, the OCV at about 4.2 V, corresponds to the SOC of 100%. Over the first 1000 cycles, the OCV shows almost no changes for all SOC values; however, an overall decreasing trend can be observed. At 0% SOC, the OCV showed deviant behavior. At this SOC value, due to the extreme nonlinearity, cell parameterization is most critical. No apparent temperature influence was observed on the OCV of the cells.

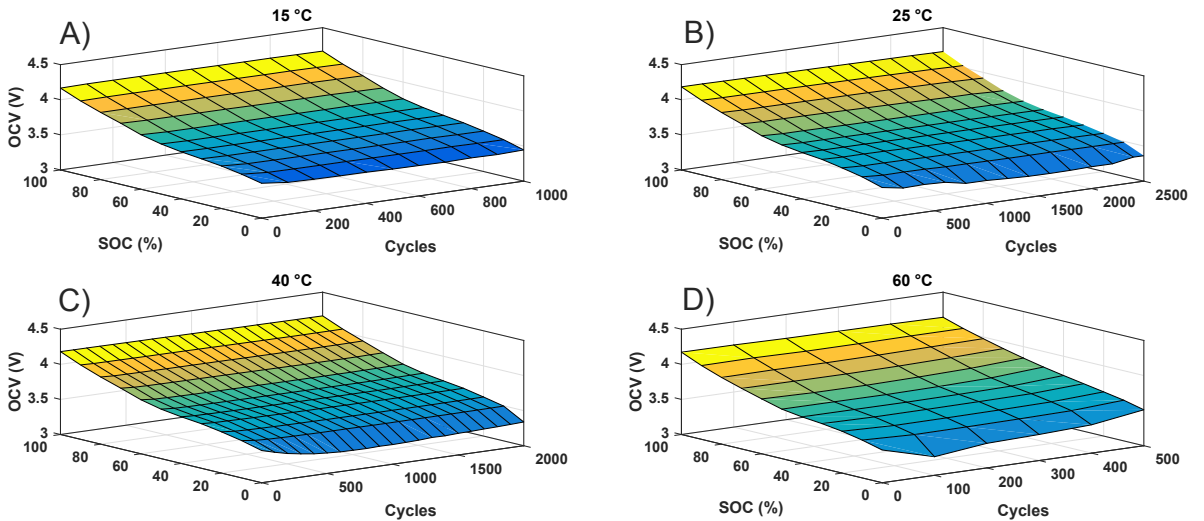


Figure 3.11: Averaged OCV measured at 25°C for cycle-life aging at A)15°C, B) 25°C, C) 40°C, D) 60°C

In total, six cells were used for cycle-life investigation based on FTP load profile at 25°C and 40°C. Figure 3.12 A presents the evolution of the normalized usable capacity for the first three cells cycled at 25°C controlled temperature. Similarly to the previous case, some cells showed an increase in usable capacity within the first 200 cycles. Kok-504's normalized usable capacity increased the most in this period and showed less decay compared to the other two cells. Kok-502 and Kok-505 showed more similar results, and, after 1000 cycles, the average normalized discharge capacity was about 97% for all the cells. As shown in Figure 3.12 B, the drive-cycle experiment showed a bit more nonlinearity at 40°C, and Kok-527's discharge capacity reached 80% of its BOL capacity only after 600 cycles. The other two cells showed similar behavior until 600 cycles, and, after that, Kok-529 started to show a faster capacity decay and reached 80% BOL capacity after 750 cycles.

By comparing the FTP-based cycle-life results to the standard accelerated cycle-life, the cells exposed to the drive-cycle, showed faster capacity decay. For both test cases, the operating temperature had a strong impact on the cell performance and created a critical situation in the cells used in one system. This greatly affects the battery pack aging performance, so a proper cooling system should be considered.

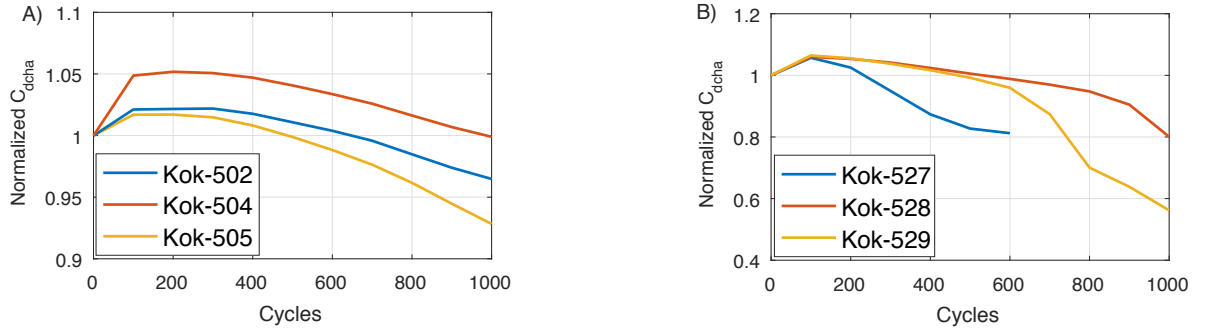


Figure 3.12: Cycle-life aging (FTP-based) investigation of the cell's usable capacity at A) 25°C and B) 40°C

To investigate the influence of temperature and SOC on the cells in more detail, comprehensive EIS measurement experiments were carried out. During the cycle-life tests based on the drive-cycle, after each 100 cycle, the cells' impedances were tested with the EIS-meter at six different SOCs (0%, 20%, 40%, 60%, 80%, and 100%) and four different temperatures (0°C, 15°C, 25°C, and 40°C).

Some selected results for Kok-505 are presented in Figure 3.13. This figure presents the temperature, and cycle-life effect on the EIS results. Four different temperatures at a 60% SOC at BOL, 200, 400, and 600 drive-cycles are shown. At lower temperatures, higher impedances were observed for all cycles. Using the cells at higher temperatures showed less impedance increase, but at the cost of faster capacity decay. These results showed that, for real-world EV operation, regulation of operating temperature is critical, and effective thermal management is a must. The desired operating temperature of the EVA was set to 28°C; however, internal heating of the cell during operation should not be neglected. The raw EIS measurements have been analyzed, and presented in Figures 3.14 to 3.16.

Figure 3.14 contains four figures. Figure A, presents the Kok-505 ohmic resistance (R_i), extracted from the all four plots of Figure 3.13. Figure B, contains the R_i values for Kok-529. Figure C, presents the normalized averaged R_i values for all the cells aged at 25°C during FTP drive-cycle (Kok-502, Kok-504, and Kok-505). Similarly, Figure D, contains the information for the normalized averaged R_i values for all the cells aged at 40°C during FTP drive-cycle (Kok-527, Kok-528, and Kok-529).

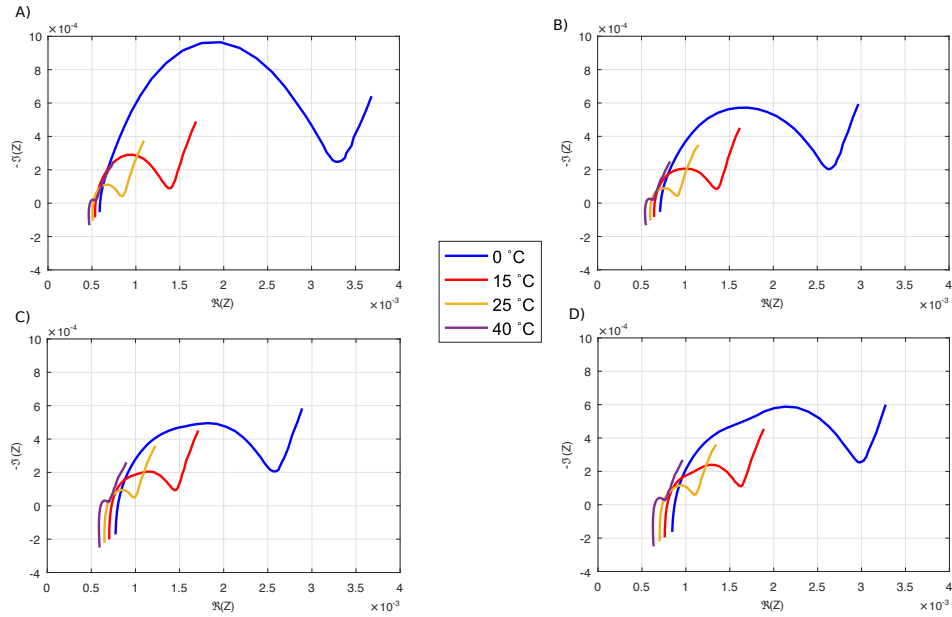


Figure 3.13: Temperature effect on the EIS measurements, results for Kok-505 at 60% SOC: A) BOL, B) After 200 FTP cycles, C) After 400 FTP cycles, and D) After 600 FTP cycles

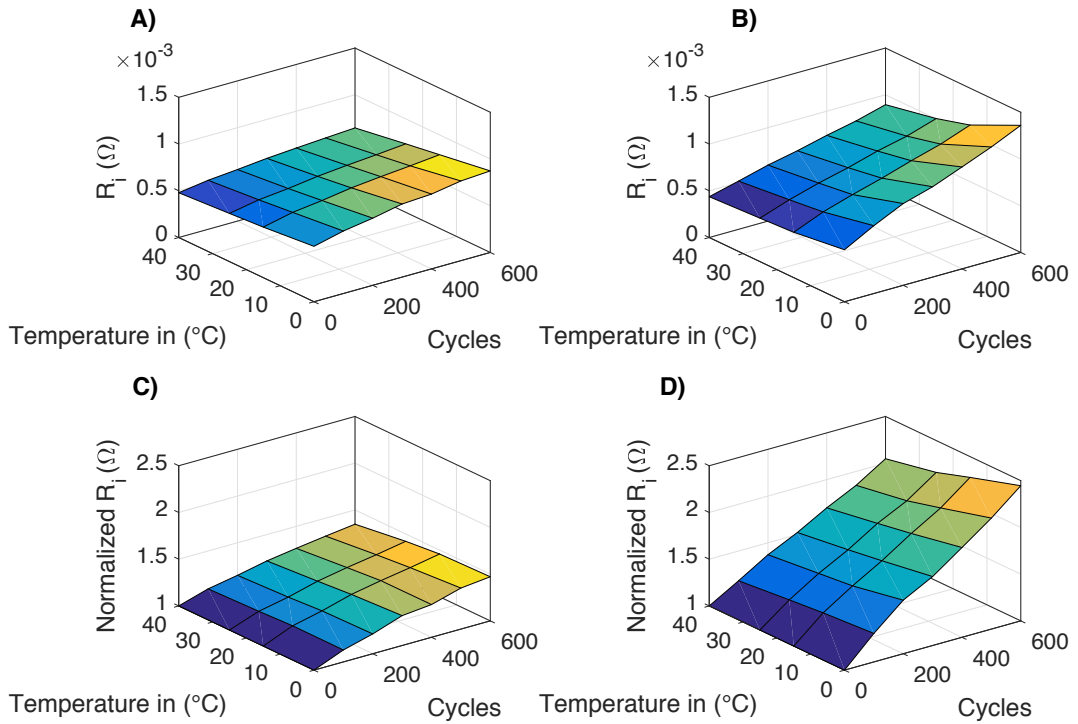


Figure 3.14: A) R_i from EIS measurement of the Kok-505 (FTP cycle at 25°C) and 60% SOC, B) R_i from EIS measurement of the Kok-529 (FTP cycle at 40°C) and 60% SOC, C) Normalized averaged R_i (Kok-502, Kok-504, Kok-505) from EIS measurement (FTP cycle at 25°C) and 60% SOC, D) Normalized averaged R_i (Kok-527, Kok-528, Kok-529) from EIS measurement (FTP cycle at 40°C) and 60% SOC

To present more comprehensive analyzed data, Figure 3.15 contains the information for the extracted

charge transfer resistance (R_{ct}). Figure A presents the R_{ct} values extracted for Kok-505, and Figure B presents the R_{ct} values extracted for Kok-529 at 60% SOC. This figure shows, that R_{ct} was extremely temperature dependent. R_{ct} increased rapidly at lower temperatures. However, R_{ct} was not affected much by the cycle-life for the first 600 FTP drive-cycle for both test cases.

To have an idea about the frequency ranges, that R_i and R_{ct} were determined, Figure 3.16 is presented. Figures A, and B demonstrate the frequencies, where R_i and R_{ct} for Kok-505 have been extracted (FTP drive-cycle at 25°C). Figures C, and D demonstrate the frequencies, where R_i and R_{ct} for Kok-529 have been extracted (FTP drive-cycle at 40°C).

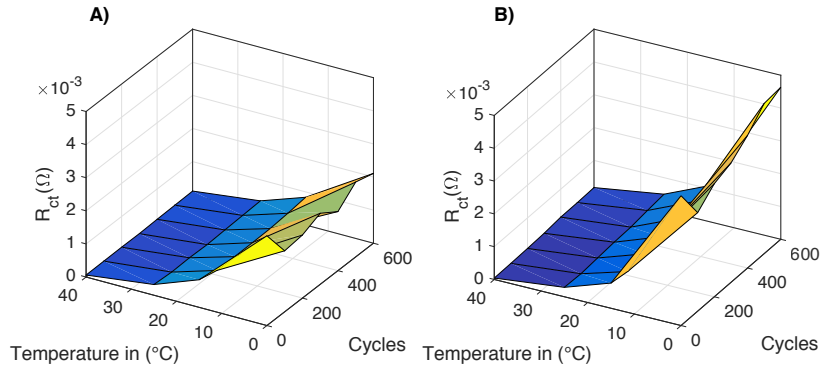


Figure 3.15: A) R_{ct} from EIS measurements of the Kok-505 (FTP cycle at 25°C) and 60% SOC, B) R_{ct} from EIS measurements of the Kok-529 (FTP cycle at 40°C) and 60% SOC

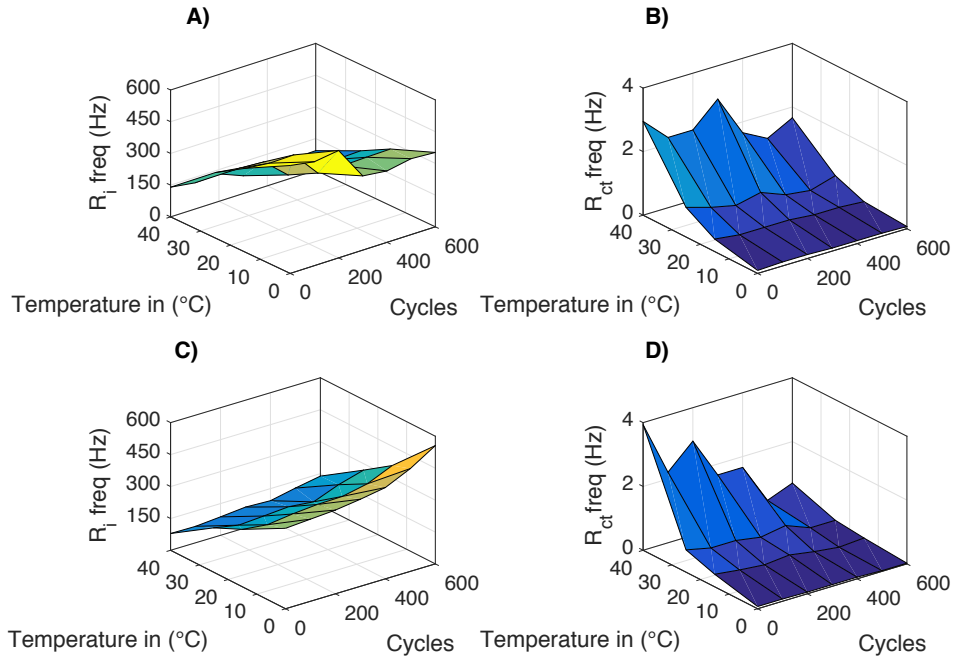


Figure 3.16: A) Kok-505 R_i frequencies, B) Kok-505 R_{ct} frequencies, C) Kok-529 R_i frequencies, D) Kok-529 R_{ct} frequencies

Based on these results, at lower temperatures, the zero crossing frequencies have been increased. At the same time, at these low temperatures, charge transfer resistance frequencies became much smaller. At higher temperatures, charge transfer resistance frequencies, clearly increased from some mHz (0.04)

range to the order of few Hz (<4 Hz). Cycle-life had not a big influence on the charge transfer resistance frequency.

3.4.3 Calendar-life

Calendar-life investigations have been performed at the selected temperatures (60°C, 40°C, 25°C, and 10°C) based on the test flow chart presented in Figure 3.4. The reason for storing the cells in a fully charged state was, that the EV drivers tend to keep the EVs nearly charged on most occasions. At elevated storage temperatures, the charged cathode materials in most LIB technologies (except LFP) are unstable and decompose [131]. For this reason, the effect of high temperature storage on the calendar-life has been investigated as well.

Before conducting the calendar-life experiments, important parameters of the cells have been evaluated by the HPPC test (see the test procedure in Section 2.4.3.2). Nine cells were adjusted to 100% SOC, and stored at stabilized temperatures at 10°C, 25°C, and 60°C (three cells for each conditions) for a period of 30 weeks. These three temperatures were selected to examine the cell characteristics at low-to-high storage temperatures (representing beyond Singapore climatic temperatures). To study the SOC's impact on the cell's calendar-life, three half-charged cells (50% SOC) underwent calendar-life experiments at 40°C.

Every four weeks, LIBs were removed from the chambers and allowed to cool down to room temperature. After the HPPC test, the cells were adjusted to the test-level SOC and were returned to the temperature chamber.

Figure 3.17 presents the processed calendar-aging results. The cells stored at 10°C showed slight increase of 2 to 4% of capacity during storage, but the internal resistance increased more than 10%. The reason that the capacity of cells have been increased during the storage time, is in the overhang areas of the anode [98]. Although for the cells stored at 25°C, capacity fade was about 10%, but the ohmic resistance increased by a factor of 2, meaning that even storing at an ambient temperature at high SOC levels could significantly influence the cells' SOH_R . The storage temperature of 60°C, highly affected the cells during the storage period, such that the capacity fade was more than 50% after 15 weeks. In a nutshell, the higher temperatures led to a greater capacity loss and resistance increase over time.

Finding the optimum storage temperature and SOC level requires a careful examination to aid the minimization of the calendar-life aging on the cells. This section indicated the significant impact of calendar-life on the capacity and resistance. Both, cycle-life and calendar-life, impact the cell's SOH_C and SOH_R . For EV's BMS, SOH detection algorithm should include both SOH_C , and SOH_R .

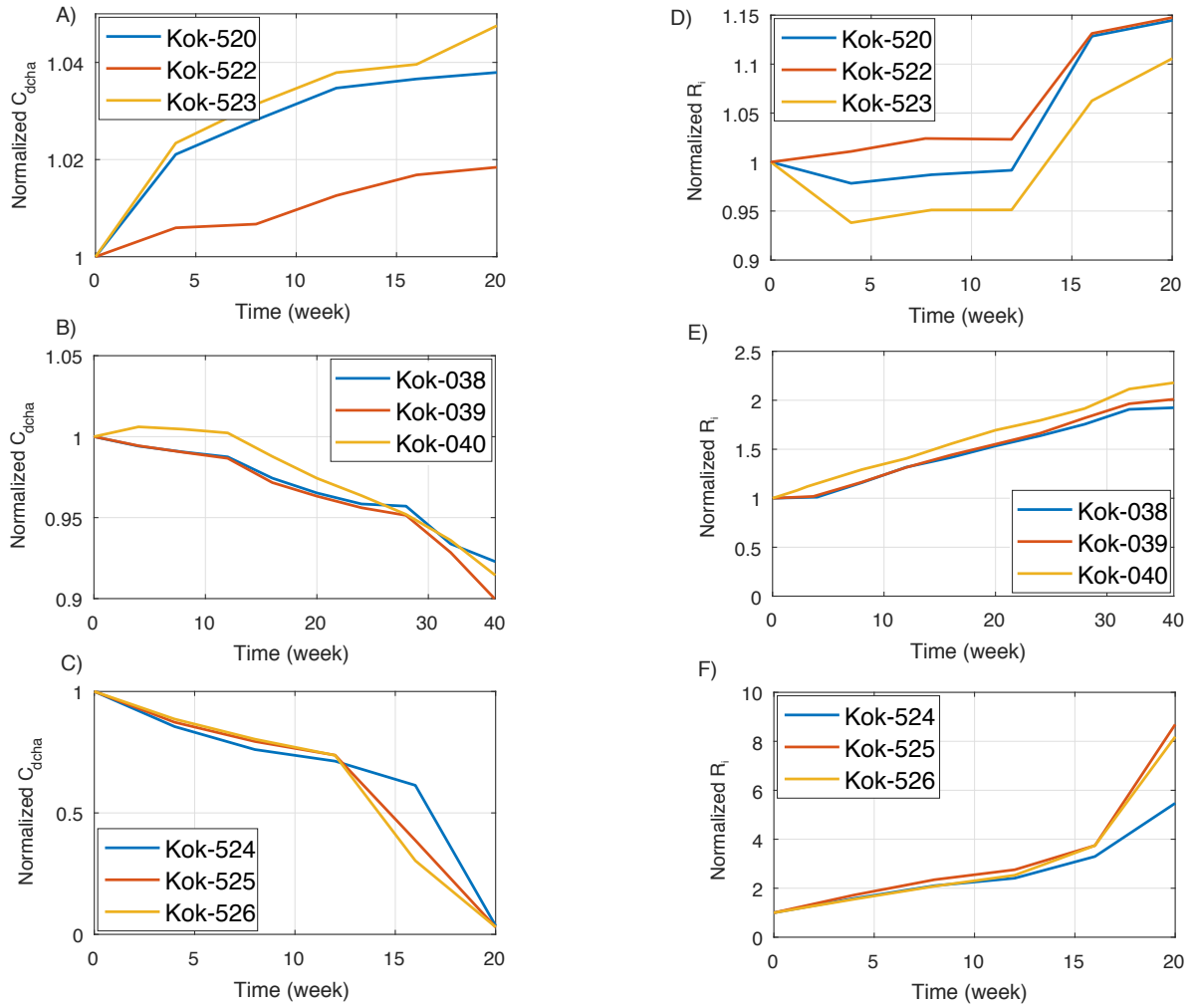


Figure 3.17: Normalized discharge capacity during calendar-aging at A) 10°C, B) 25°C, and C) 60°C. Normalized ohmic resistance at 60% SOC during calendar-aging at D) 10°C, E) 25°C, and F) 60°C

4 Model Development for battery storage systems

The use of the models in the industry is common because they are operational and can be utilized based on the product requirements. The models introduced in this chapter have industry relevance and can be used in the BMS of a wide range of products, such as 12 V, 24 V, 48 V, hybrid, and pure EV systems (400/800 V) based on Li-ion technology.

In this thesis, it is assumed that the system dynamics are a function of time and the model parameters are ordinary lumped parameters. This chapter presents the models developed for the high-power 63 Ah Kokam LIB used in the 400 V pack. These models include, but are not limited, to the cell and pack ECM voltage model, TECM (for internal and external temperature estimation), parameter estimators, and state detection models. These models are mainly coupled and upscaled, and can be used as the basis for further BMS function development.

4.1 Electrical modeling part I: Time-domain model development and implementation

In this thesis, an ECM with 1RC (as shown again in Figure 4.1) was used to represent the time-domain voltage model of the DUT. This model can be used to develop various functions for a BMS. These functions include safety monitoring, parameter estimation, power prediction, or state detection.

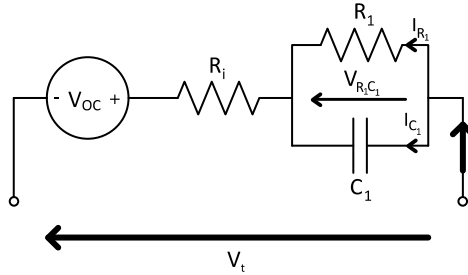


Figure 4.1: Time-domain representation of the cell voltage model with 1RC, used as LIB model (LIB-ECM) in this thesis

In EV applications, the capacity of the battery pack is relatively large. For the EVA pack, it was about 126 Ah (two cells in a parallel connection). In a real-scenario operation, the electric motor draws equal or less than 1C (126 A for the EVA pack), hence, the variation of the SOC within few seconds is negligible (for one second 1C discharge: $\frac{\partial SOC}{\partial t} = -\frac{126}{126 \times 3600} \frac{1}{s} = -2.7 \times 10^{-4} \frac{1}{s}$). By considering the OCV models introduced in Equations 2.12 to 2.17 and $\frac{\partial SOC}{\partial t} \approx 0$, the OCV variation in one second is also negligible¹ ($\frac{\partial V_{oc}}{\partial t} \approx 0$). The OCV of the cell was measured using the HPPC test at 11 SOC data

¹ According to the Equations 2.12 to 2.17, the $\frac{\partial V_{oc}}{\partial t}$ either results in 0 or ∞ , however the rate of the OCV change in one second is approximately close to zero

points (for every 10% SOC). As this method introduces large inaccuracies at critical SOC ranges (e.g., no information for $SOC < 10\%$), calculating more OCV-SOC data points is necessary. To overcome this issue, 41 data points have been considered for the ECM's SOC-OCV LUT. Additionally, OCV was estimated from discharging the cell at a small current ($0.01C$). Figure 4.2 presents a comparison between these methods.

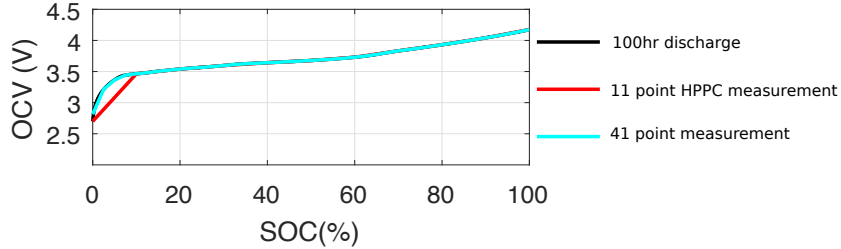


Figure 4.2: 100 hr discharge with $0.01 C$ to approximate the OCV vs. 11 points OCV measurement vs. 41 points OCV measurement

In Figure 4.3, the OCV ($0.01C$ discharge) plot, and the derivative of the OCV over the SOC are shown. Since the OCV is a nonlinear function of the SOC, the first derivative of the OCV with regard to the SOC ($\frac{\partial V_{oc}}{\partial SOC}$) was calculated to be used later for the EKF development. To represent the OCV in the voltage model, these results have been stored in the respective ECM's LUTs.

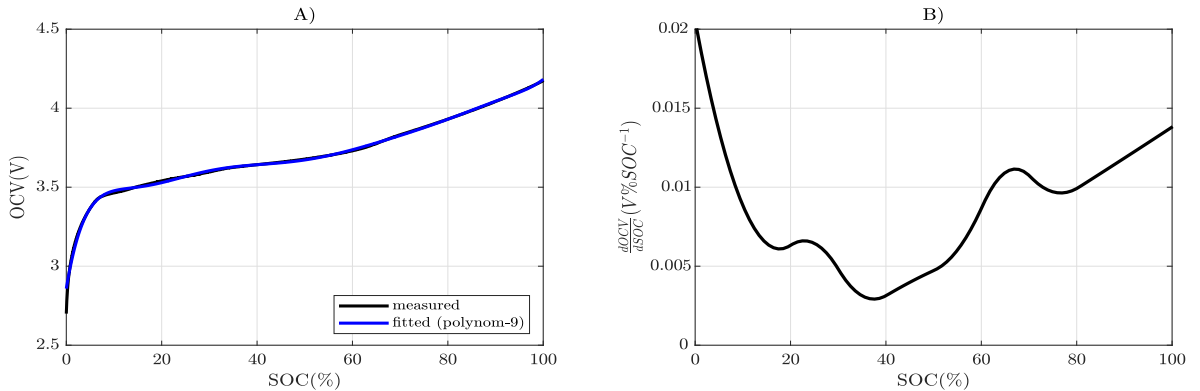


Figure 4.3: A) OCV curve over the full range of SOC vs. the OCV-fit via polynomial function (9^{th} order, B) First derivative of the OCV with respect to SOC

The Simulink implementation of a 1RC network is shown in Figure 4.4. In this figure, both parameters R_1 and C_1 are SOC-, temperature-, and aging-dependent (cyclic aging at defined temperatures). By setting the cycle number in the algorithm LUT, the respective aging data to that cycle have been selected for the simulation. SOH detection can be implemented with two different methods. Either all the aging parameters have been identified, and stored in the respective LUTs, or the these parameters were estimated in real-time. Both methods have been implemented.

Similarly, as shown in Figure 4.5, the ohmic resistance (R_i) and OCV are dependent on the SOC, temperature, and aging. In this figure, the circuit parameters were modeled by using function blocks to achieve higher simulation speeds (these parameters have been modeled with the respective physical components² as well). This is a practical method for developing the voltage model of the single cell,

² By using Simulink-Simscape toolbox for physical systems simulation

which can be used for voltage simulation, power prediction, calculation of the heat generated, and SOH detection. Additionally, this model can be easily upscaled to the module or pack for higher system voltages according to the application requirements.

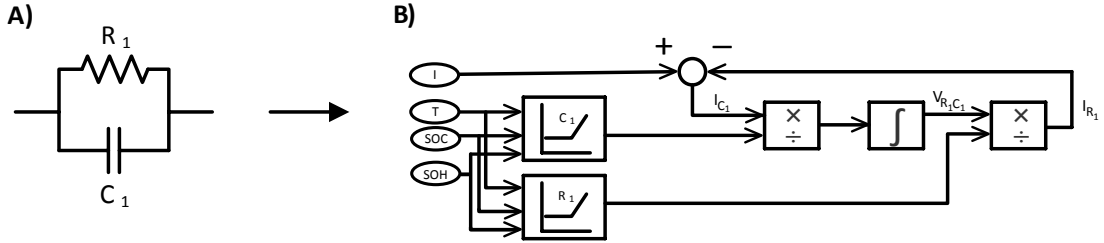


Figure 4.4: A) A parallel RC circuit, B) Simulink implementation of a parallel RC circuit

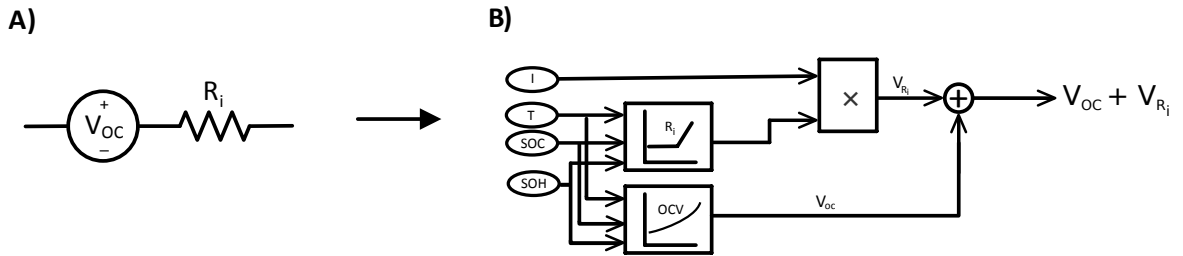


Figure 4.5: A) OCV in series with the cell's ohmic resistance B) Simulink implementation of OCV in series with the cell's ohmic resistance

The parameterized open-loop voltage model (see figures: 4.1, 4.4, and 4.5) based on the time-domain HPPC parameter identification was evaluated with a current profile as shown in Figure 4.6 A. The simulated voltage showed a relative error of less than 1% for $10\% < SOC < 100\%$. The SOC was calculated with Ah-counting method. At SOC's lower than 10%, the model error increased to 4.5%. Due to the high nonlinearities in the voltage response, for more accurate simulation, the cell identification should be conducted for more data points, rather than only 10% steps. The ECM at this stage did not include any control loop. To enhance the model accuracy, PID controller (see figure 2.20) was added to the ECM. This enhanced ECM was used for evaluation of the other algorithms in this thesis. The next section presents a cell model based on the impedance identification in the frequency-domain.

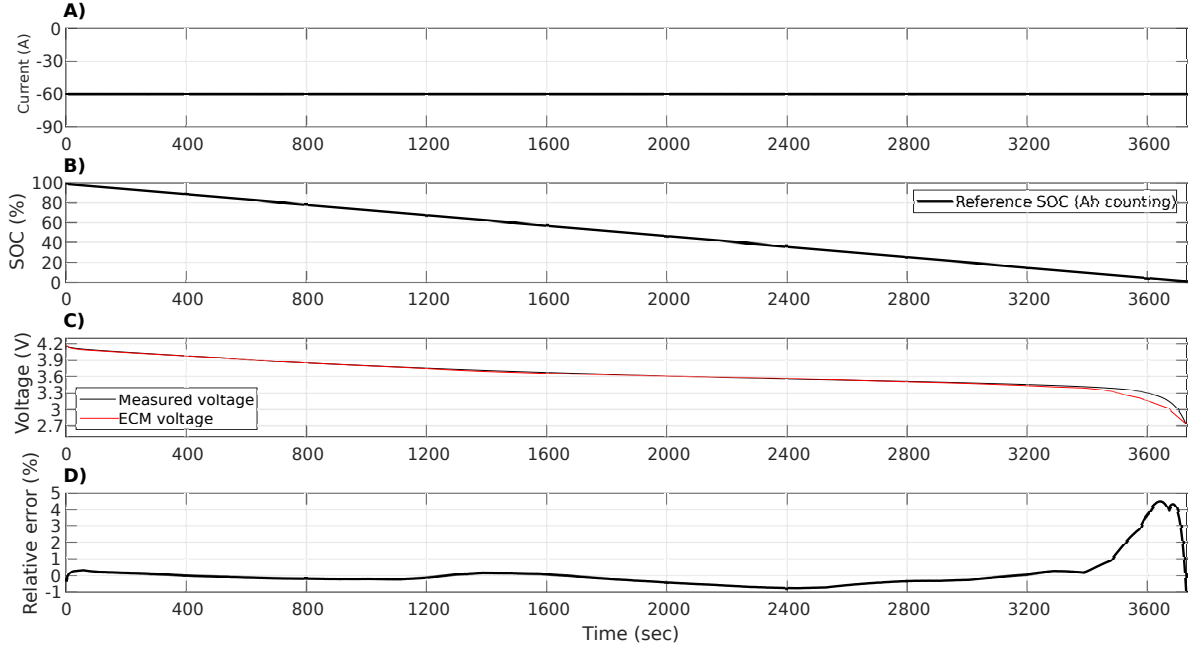


Figure 4.6: A) 1C discharge current implemented on the fresh cell at the controlled temperature of 25°C, B) SOC calculated with Ah-counting method (open-loop), C) Comparison between the measured terminal voltage, and the open-loop ECM voltage (no model correction), D) The relative error of the ECM voltage

4.2 Electrical modeling part II: Frequency-domain model development and implementation

Besides the 1RC ECM, a more complex frequency-domain model was also developed in this research. The frequency-domain model is based on the EIS measurements and impedance parameter, which requires more modeling effort compared to the time-domain model. A general circuit to fit the EIS measurement is shown in Figure 2.10.

EIS data were analyzed at different SOCs, temperatures, and the aging stages. By fitting EIS Nyquist plots, cell parameters have been extracted. All these parameters may not be interpretable with basic elements such as resistors, inductors, or capacitors. Due to this fact, the parameters have to be approximated to make the simulation and modeling development possible.

As shown in Equation 2.38: $Z_{ZARC} = \frac{R_{zarc}Z_{CPE}}{R_{zarc} + Z_{CPE}} = \frac{R_{zarc}}{R_{zarc}(j\omega)^\alpha C_{zarc} + 1} = \frac{R_{zarc}C_{zarc}^{-1}(j\omega)^{-\alpha}}{R_{zarc} + C_{zarc}^{-1}(j\omega)^{-\alpha}}$, with the CPE exponent range of $0 < \alpha \leq 1$. For $0.6 \leq \alpha < 0.85$, one can approximate the ZARC element with at least 3RC ladders. An exception is that, with no obvious deformation in the semicircle impedance spectra of the cell, $\alpha = 1$ can be used to model 1RC circuit. In [39], it is proven how a ZARC element can be accurately fitted with an uneven number of RC elements. In this work, as shown in Figure 4.7, the ZARC element has been approximated with 3RC elements:

$$R_a = R_b = R_c \quad (4.1)$$

and

$$C_a = \frac{C_b}{\zeta}, C_c = C_b\zeta \quad (4.2)$$

with ζ as an optimization factor, that depends on the α . With this method, with a suitable range for

alpha, the ZARC element has been approximated:

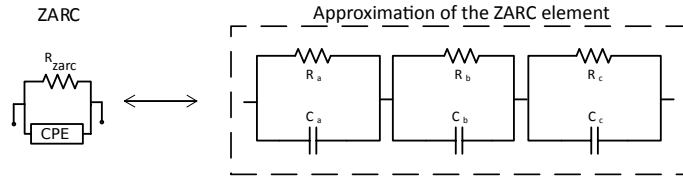


Figure 4.7: 3RC Ladder to approximate the ZARC element (approximation of the depressed semicircle in the EIS Nyquist diagram)

Warburg impedance can be interpreted as a serial connection of an infinite number of RC circuits [181]. The model in Figure 4.8 has been used to approximate the Warburg impedance. Warburg impedance, and the mathematical model’s parameters are presented in [39].

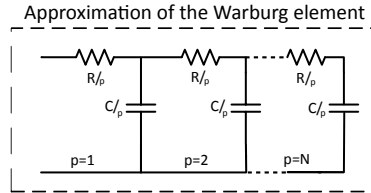


Figure 4.8: Approximation of the Warburg element with N ladders of RC circuits

In this thesis, in order to build up the voltage model parameterized in the frequency-domain, a series connection of an open-circuit voltage source, ZARC element approximation, and a Warburg element approximation have been used³ (frequency-domain ECM). The complete model is shown in Figure 4.9.

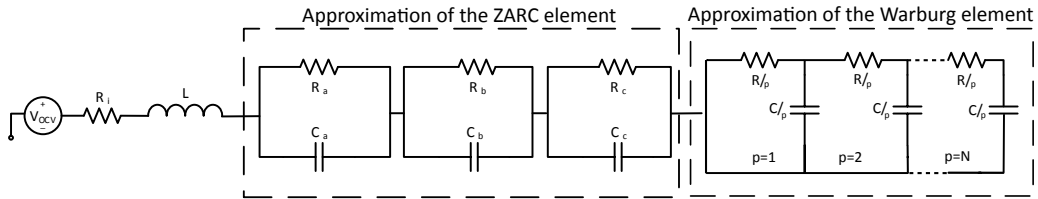


Figure 4.9: Voltage model of the cell based on the EIS measurement (for simulation, inductor “L” was neglected)

To model the voltage of the cell based on the simplified circuit shown in Figure 4.9, one ZARC element was used.

To verify the model, Kok-014 was measured at the BOL with the Sg taxi drive-cycle, and at the EOL with the FTP drive-cycle. The simulation results based on the frequency-domain modeling are shown in Figure 4.10. During normal EV operation, when the cell voltages are not allowed to reach values less than 3 V, the simulation error was below 6 mV. The battery cycler (Digatron MCT-300) measurement accuracy was 0.1% in full scale (0-6 V), which was equivalent to 6 mV.

³ The proposed model is able to capture the dynamics of the cell both for the new and aged cells

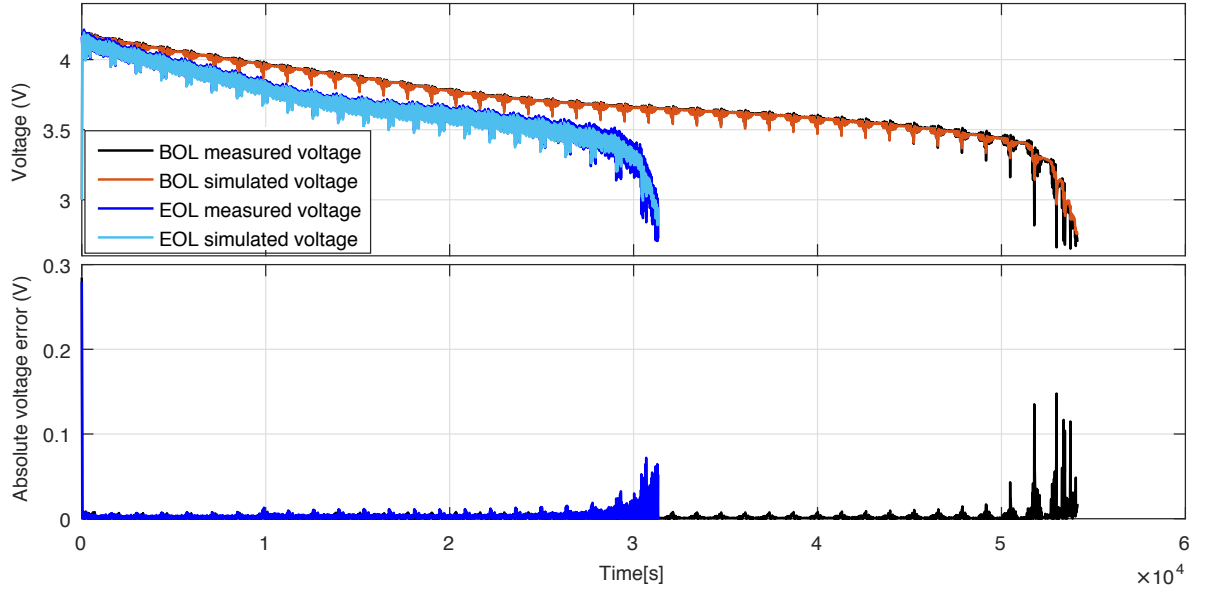


Figure 4.10: Kok-014 measurement and simulation from the Sg taxi drive-cycle at the BOL, and the FTP at the EOL. Frequency-domain model was parameterized from the EIS data. The model used Ah-counting method for SOC estimation and a P-controller

This section revealed that the modeling, based on the EIS parameterization, would provide accurate results; however, this technique had some drawbacks as well. EIS measurement is sensitive to the relaxation time; it also requires larger effort to collect the aging data. The required effort to fit the measurement data, was much higher compared to the time-domain method as well.

To have a clearer comparison between the two methods, Table 4.1 evaluates the different aspects of both techniques. In this table, integrity as an indication of how well the model can be coupled with other models is also shown. By comparing both techniques according to Table 4.1, the method based on the time-domain has been chosen for further use for the battery pack model.

Table 4.1: A comparison between the time-domain, and frequency-domain voltage modeling techniques

Test method	Accuracy	testing	parameterization	cost	computational	integrity
Time-Domain	+	+	++	+	++	++
Frequency-Domain	++	-	+	-	+	+

The next sections introduce the TECM used for the single LIBs and the LIB pack.

4.3 An approach to LIB thermal modeling and simulation

This section introduces an approach to thermal modeling of the cell. The TECM considers the heat mechanisms in the cell. Both, heat generation and heat transfer, have been calculated, and used for thermal modeling. The TECM outputs are the cell’s surface and core temperatures. Thanks to the temperature sensors mounted on the cell, the model surface temperature has been verified; however, no reference measurements were available for verification of the core temperature. To verify the core temperature, temperature sensors inside the cell are required. Internal temperature sensors are not commercialized at the moment. Recently, some research has been done with the focus on placing the

temperature sensor inside the cell [257].

In this section, a one-dimensional mathematical model with lumped parameters has been presented to simulate the temperatures of the cell. Figure 4.11 shows a simple charge and discharge current profile implemented in a new cell (Kok-502) to observe the temperature evolution during CCCV charging at 1C, and CC discharging at 0.5C, 1C, 2C, and 3C. There was no significant temperature change during 0.5C, and 1C discharge/charge. The maximum cell temperature reached 36°C during 2C discharge, and 43°C at 3C constant discharge. In EV applications, when the car accelerates, or climbs a hill, the load current can be on the extreme side.

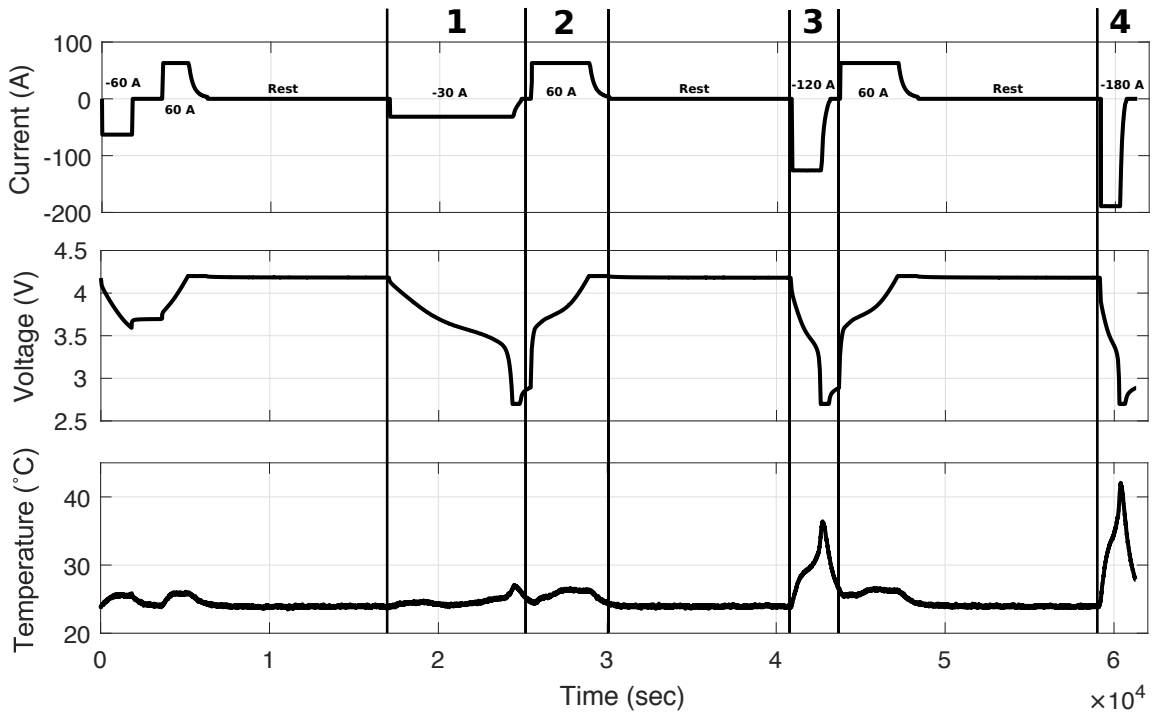


Figure 4.11: Temperature development of a new cell at different discharge currents of 0.5C, 1C (For 1C full charge and discharge temperature development, refer to figure 3.5), 2C, and 3C

The temperature effect on the cell’s performance, and aging have been discussed in Chapter 3. In real scenarios, without thermal management, the cell’s temperature variation can be more extreme than what is shown in Figure 4.11. In this section, the thermal model was verified for discharge pulses of up to 15C, and the drive-cycle profiles.

4.3.1 The proposed TECM

Temperature measurement for all the cells is costly; therefore, in commercially available BMSs, only some selected locations in the battery pack (usually for the cells in the middle of the pack, and other likely hotspot locations) are monitored [216, 324]. Thermal models can be used to monitor the temperature development of the individual cells in the pack. To develop the TECM of the cell, heat generation sources, heat transfer, and heat balance equations, as explained in Section 2.4.4.2 should be considered.

As mentioned before, TECM has been developed for the EVA pack. TECM inputs, such as the required parameters to calculate heat generation, were generated by the ECM; therefore, the TECM and ECM models have been coupled, this is shown in Figure 4.12. Based on this figure, at each step time, the ECM model calculates the required parameters at the given SOC. The ECM model passes the required parameters into the TECM. Heat transfer mechanisms are calculated directly by the TECM. The output of the TECM model is the estimated core and surface cell temperature. The estimated temperature values are passed to the ECM model for more accurate parameter estimation.

Figure 4.13 presents the proposed TECM. With this model, instead of approximating the heat transfer with simple thermal resistance, both heat transfer mechanisms (conduction and convection) have been modeled (radiation was neglected).

To create the test profile required for TECM parameterization, the requirements for a real EV scenario have to be considered. The EV's battery pack temperature mainly depends on the load power, ambient temperature, and pack casing.

During acceleration (high current pulses), and hill climbing, high currents would increase the battery temperature considerably. To simulate this, a specific test profile was designed containing several high current pulses to observe the temperature build up in the cells. The designed load profile associated with this test is shown in Figure 4.14. The load profile contained three charge and discharge cycles to check the quality of the ECM voltage model, and 20 pulses, each with a duration of 10 s, and an amplitude of 600 A. Such pulses could result in highly nonlinear behavior of the LIB and considerable temperature increase in the cell. The improved ECM was used to calculate heat generation by estimating the resistive parameters of the cell and other required inputs. In the combined ECM-TECM model, the estimated temperatures were fed-back to the ECM to include the temperature effect in the parameters.

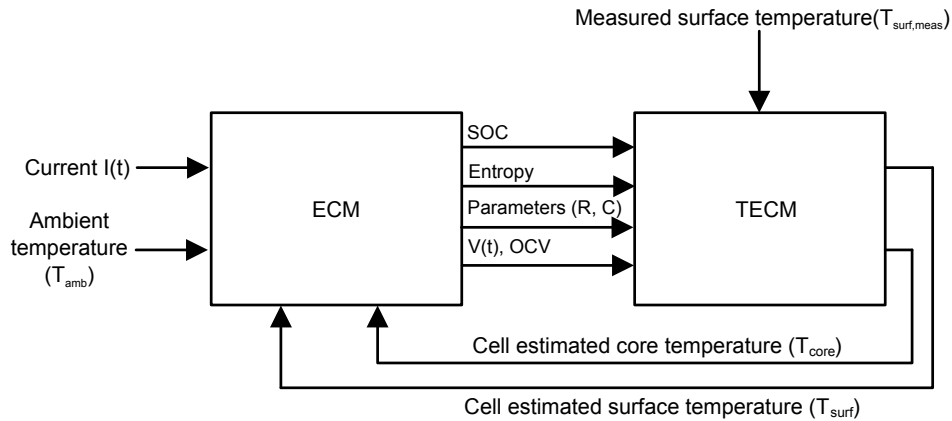


Figure 4.12: Interaction between the ECM, and the TECM

In Figure 4.14, the ECM was verified by comparing the simulated voltage with the measured voltage of the LIB, and the voltage error of the ECM during current pulses was in an acceptable range. Therefore, the ECM parameters can provide a good estimate for the calculation of generated heat Q (see equation 2.41).

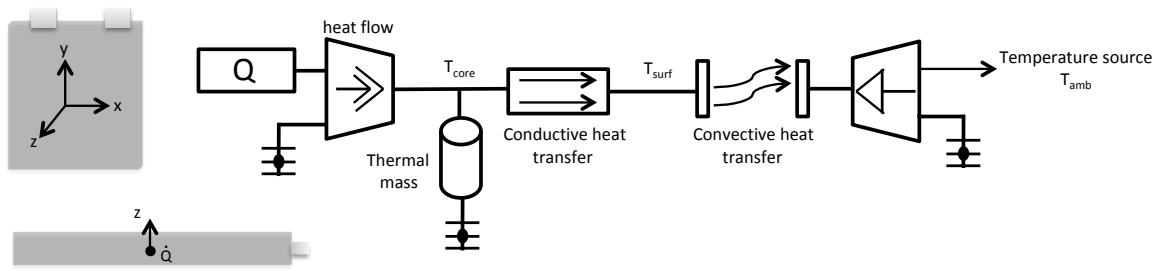


Figure 4.13: 1D TECM used to estimate the cell's core and surface temperature in the z coordinate

The internal resistance is the key value for determining battery heat loss during the operation. Figure 4.15 A presents the cell's ohmic impedance, and Figure 4.15 B represents the 10 s resistance, resulting from the load current profile in Figure 4.14 A. For both graphs, R_i and R_1 are temperature dependant, meaning the change of temperature affects the resistances.

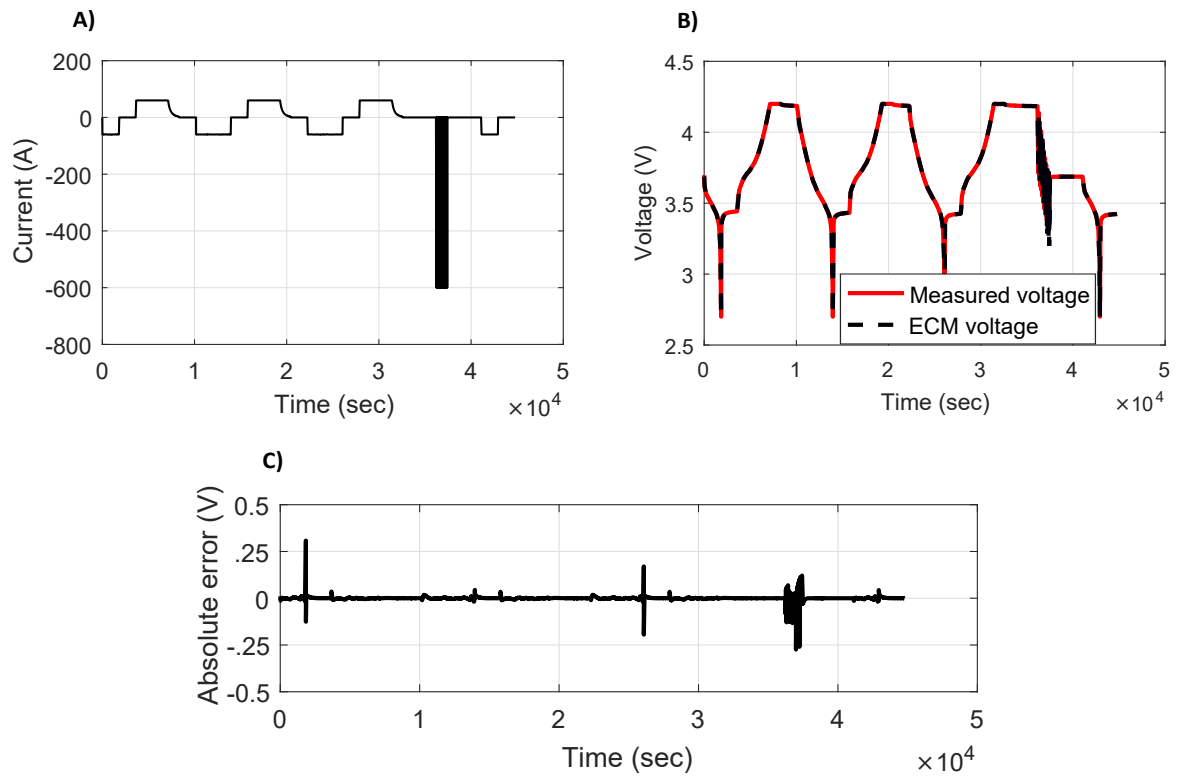


Figure 4.14: A) Test current profile including 20 pulses each 600A discharge for 10 s, B) Verification of the enhanced ECM voltage with the measurement, C) Absolute error of the ECM voltage

The heat capacity (C_p) of the cell was measured using the calorimetry technique with ARC. To measure the heat capacity, DUT underwent an increasing temperature from 30°C to 55°C in five intervals of 5°C each. About 11.5 g of heat mat, and 6.4 g of wire and glass tape, together with other insulating materials, were used for this experiment. Specific heat capacity (c_p) was then measured between a minimum value of 0.9389 and a maximum of 1.1297 $\frac{kJ}{kgK}$.

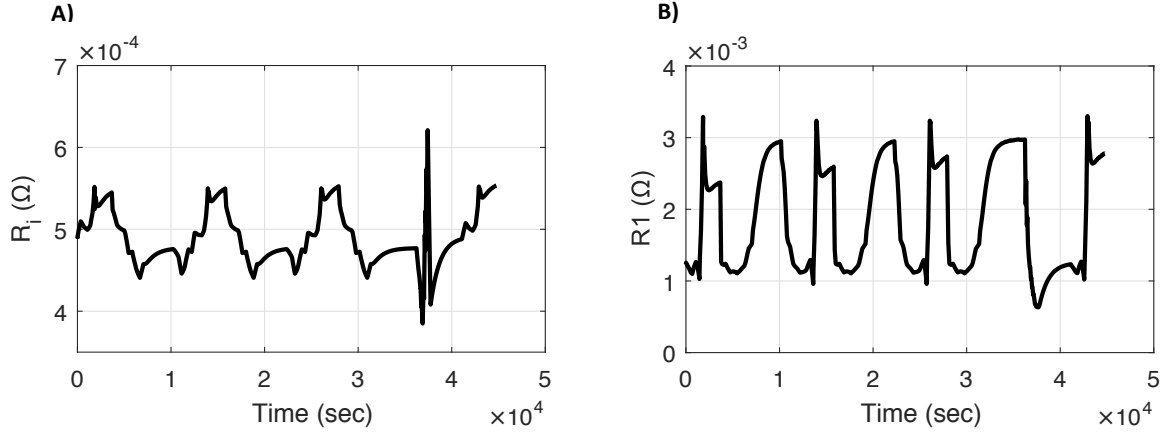


Figure 4.15: A) ECM ohmic resistance as a function of SOC B) ECM 10 s resistance as a function of SOC

The final c_p value and other thermal coefficients are presented in Table 4.2. In most practical applications, the heat capacity of a battery module does not change substantially during operation [28] or with aging. The physical parameters of the DUT, such as dimensions and weight are presented in Table 4.3. Other parameter coefficients, such as heat transfer and heat thermal conductivity were found experimentally.

Table 4.2: DUT thermal parameters

Thermal-Parameter	Thermal conductivity	Convective heat-transfer coefficient	Specific heat capacity
Unit	$k \left(\frac{W}{mK} \right)$	$h \left(\frac{W}{m^2K} \right)$	$c_p \left(\frac{kJ}{kgK} \right)$
Value	0.3627	38.9532	1.1044

The entropy can be measured by varying the temperature of the cell and recording the open-circuit voltage as a function of temperature. Based on Equation 2.47, developed in Chapter 2, an entropy test was performed in the laboratory, the cell temperature was increased at intervals of 5°C, and the respective OCV was recorded. The entropy data over the full range of SOC as shown Figure 4.16 A was stored in a LUT. For this test, the results of the simulated entropy is shown in Figure 4.16 B .

Table 4.3: DUT physical parameters

Physical Parameter	Mass	Cross section area	Thickness
Unit	m (kg)	A (m ²)	d (m)
Value	1.52	0.262*0.257	0.0053

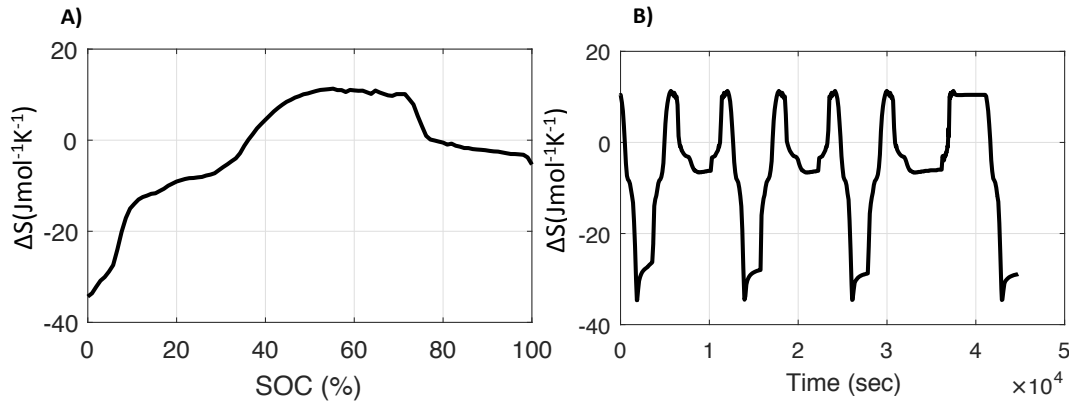


Figure 4.16: A) Entropy change measurement as a function of SOC, B) Cell entropy change under the load profile shown in Figure 4.14 A

Ohmic irreversible heat loss and entropic reversible heat loss are shown in Figure 4.17, the results demonstrating that entropic heat was responsible for over 10% of the heat generation rate.

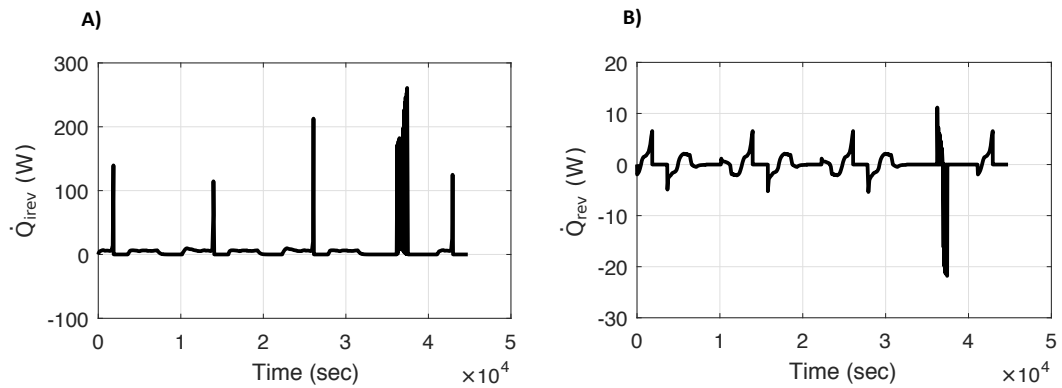


Figure 4.17: A) Ohmic irreversible heat loss, B) Entropic reversible heat loss

Figure 4.18 A presents the results for the estimated core and surface temperatures from the TECM. To enhance the TECM, the model parameters have been optimized with the RLS optimization routine⁴. An RLS optimization routine calculates a weight factor by comparing the estimated temperature to the sensor measurements, this weight factor was also used to correct the estimated core temperature. Both reversible and irreversible heat were dependent on the estimated resistances and the OCV. Thermal

⁴ For simplicity called as RLS method

parameters were assumed to be constant for this model; however, heat transfer is dependant on the ambient temperature. With the TECM method, the simulation error (i.e., temperature error between the measurement and the model) was in the range of ± 0.5 K during the test, and the RLS method simulation error was within ± 0.1 K, as shown in Figure 4.18 B.

As insertion of thermocouples into the pouch cell was not possible at the time due to the manufacturing limitations and laboratory facilities, an approximate of the internal temperature in the center of the cell was used for core cell temperature estimation.

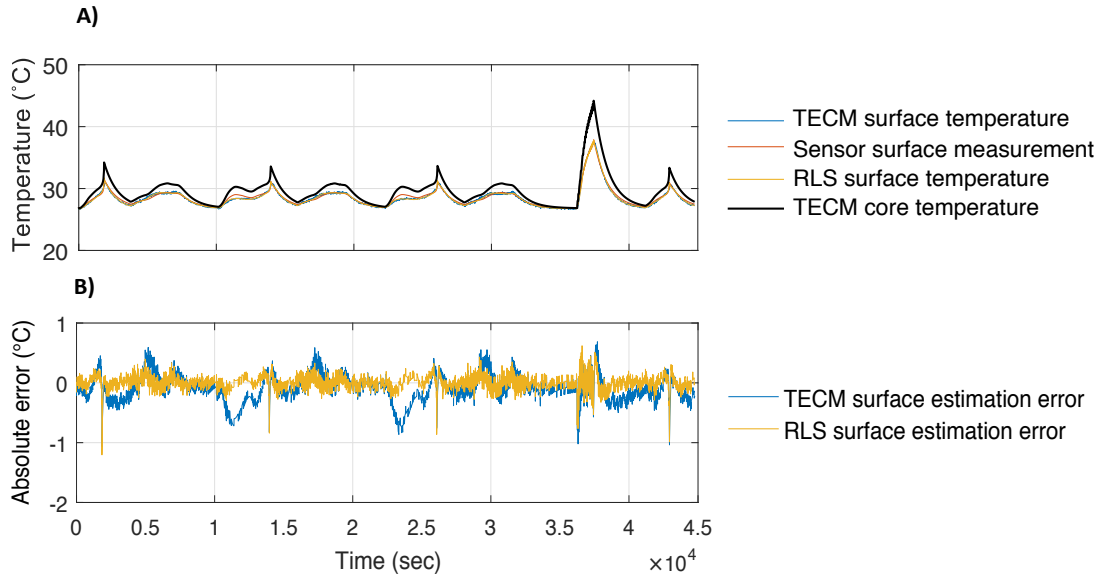


Figure 4.18: A) Measurement and simulation results for both core and surface temperature estimations using TECM and RLS methods, B) Error of TECM and RLS temperature estimation

The TECM introduced here is implementable in embedded systems, and was implemented in the HIL system as well as in a small BMS development platform. Flexibility of being coupled with an electrical model, being computationally effective, and the option to be employed for online applications are among the advantages of this model.

Figure 4.19 shows the temperature difference between the cell surface and its core. During normal operation such as typical drive-cycles or 1C/2C charge/discharge cycles, there is no significant temperature difference between the core and surface of the cell. In cases where high power is required, for instance, during the climb or high acceleration, the LIB temperature can increase significantly. To consider this effect, short-duration high-current pulses have been used for verification of the TECM. This current profile is shown in Figure 4.20 A.

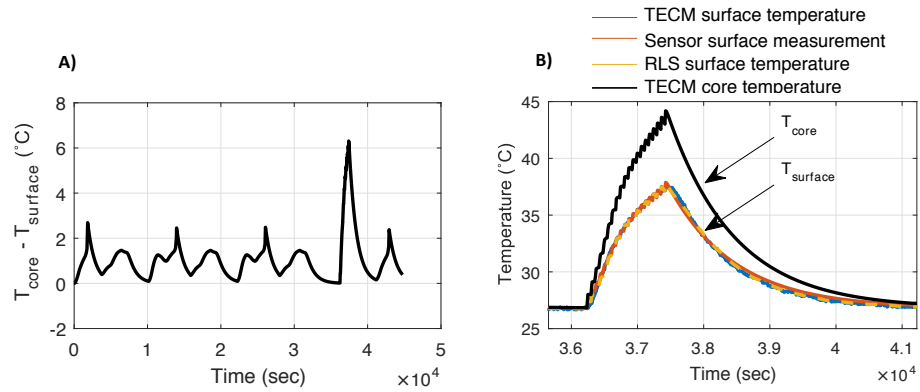


Figure 4.19: A) TECM temperature difference between the cell's simulated core temperature, and the cell's surface temperature, B) Temperature rise, partially zoomed from Figure 4.18 A

In this test, DUT was kept inside the temperature chamber at a controlled temperature of 25°C. As a part of this current profile, it can be concluded that a drive-cycle dynamic load profile with a relatively low average power, does not lead to a high temperature build-up in the DUT. This test profile was used to verify the TECM with 20 subsequent high-current pulses, each with an amplitude of 15C (900 A) and a duration of 10 s.

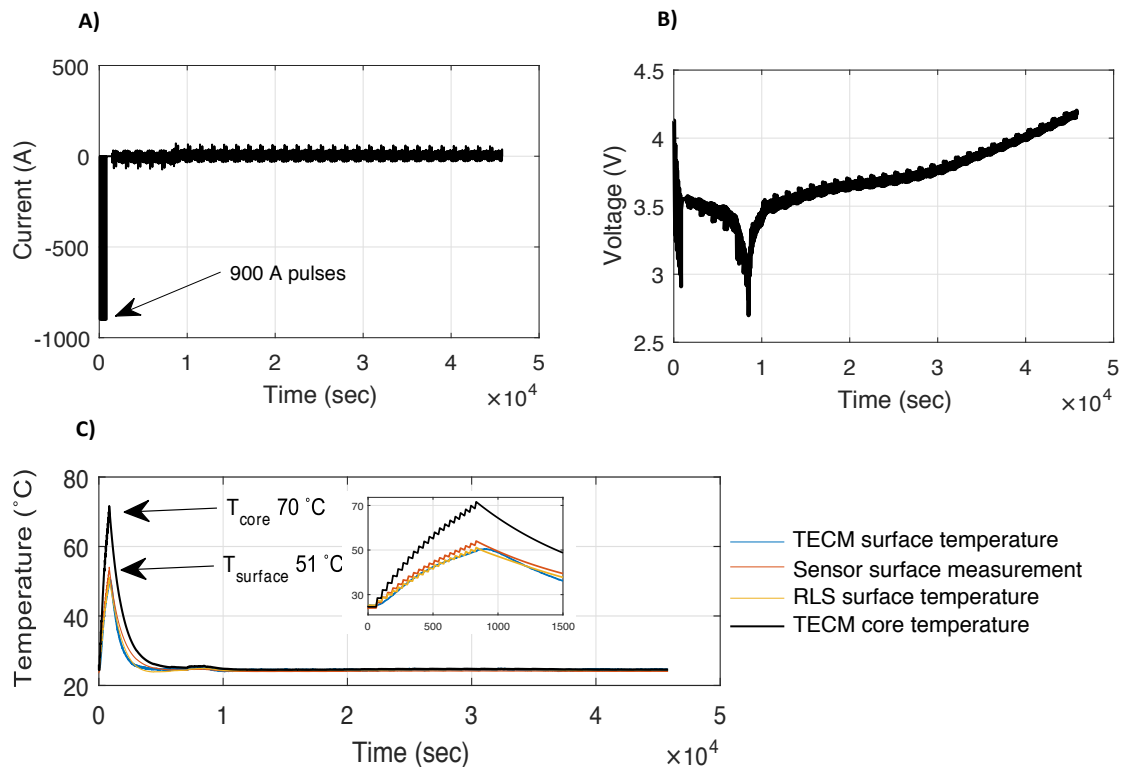


Figure 4.20: A) Current profile containing 15C discharge pulses, FTP drive-cycle, and the reversed FTP drive-cycle profile for charging of the cell, B) Voltage response of the cell, C) Measured and simulated temperature, RLS optimization was used to enhance the TECM accuracy

Fifty seconds rest was given between each pulse. After the pulses, the FTP drive-cycle was used to discharge the remaining Ah, and then the DUT was fully charged by using a reversed FTP drive-cycle profile. The current profile and voltage response are presented in Figure 4.20. The measured temperature of the cell rapidly reached 51°C at the end of the pulses, and the TECM estimated the surface temperature with less than 0.5K absolute error during the estimation. At this point, the core temperature was estimated to be around 70°C.

This chapter presented two most popular LIB models. The first model was the conventional ECM. ECM is mainly used to model the terminal voltage of the cell. Additionally, in this chapter, some techniques to enhance the accuracy of the ECM have been suggested and evaluated as well. The second model was the TECM. TECM was used to model the cell's temperatures. Both ECM and TECM have been coupled to each other. Some of the required TECM parameters have been calculated from the ECM, in return, the calculated temperature was reported back from the TECM to the ECM. An RLS optimization was introduced, this method was used to enhance the accuracy of the TECM.

The next chapter introduces the algorithms used for the LIB parameter and state detection. For the LIB and the LIB pack, these algorithms have been used in parallel with the two introduced models in this chapter.

5 Algorithm Development for battery storage systems

This chapter is dedicated to the development of the algorithms that can be used for state and parameter estimation. Section 5.1 presents the big picture of the cell-level software architecture. The developed software was upscaled, and used for the pack-level simulation as shown in section 6.3. Section 5.2, describes a novel online filter-based parameter estimation technique. This method is based on the implementation of the monitoring functions on the filtered current and voltage of the cell. By filtering, the dynamic part of signals have been extracted. By passing the dynamic part of the signals to a state observer, certain parameters have been estimated. Section 5.3 presents the development of the sliding mode observer, and the development and implementation of the extended Kalman filter is described in Section 5.4. To evaluate the aforementioned methods, algorithms have been verified under controlled laboratory conditions, such as controlled testing temperatures, while aging history of the cells were available.

5.1 Big picture of the software architecture

The coupled ECM and TECM has been presented in Figure 4.12. To provide a general overview of the overall software architecture, Figure 5.1 is presented.

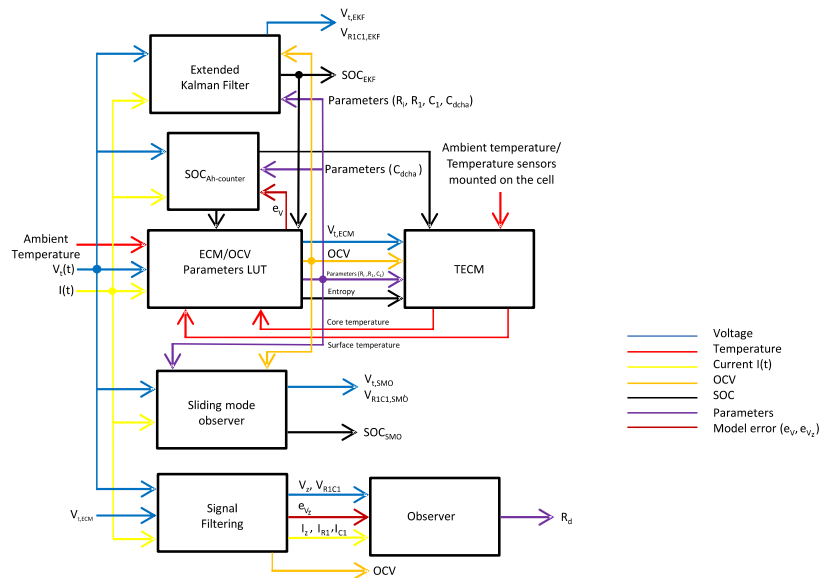


Figure 5.1: Software architecture of the combined cell models and algorithms

The cell software architecture includes a combination of different models and algorithms. To model

the cell voltage and temperatures, ECM and TECM have been introduced. This big picture presents how the coupled ECM-TECM have been coupled to the rest of the algorithms. In the next section, a filter-based technique to estimate the dynamic resistance of the cell is introduced.

5.2 An online filter-based parameter estimator

This section introduces a filter-based parameter estimator developed for online parameter estimation based on the digital filtering technique. This method contains two main parts; the first part includes the filtering of the measurement signals, such as current and voltages (see Figure 5.2), and the second part uses these filtered signals for observing the dynamic resistance (R_d) of the cell. To evaluate this technique, the results of this method have been compared to the ECM technique.

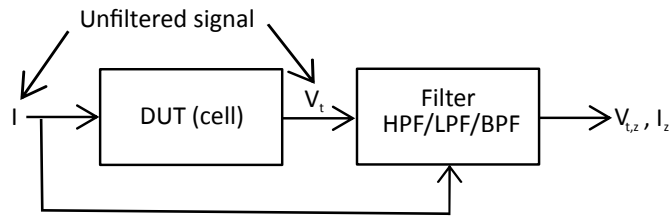


Figure 5.2: Principle of digital signal filtering, the filter can be a HPF, a LPF or a BPF

According to the Equation 2.23, the cell terminal voltage contains two parts; OCV and the dynamic transient voltage (V_z). The dynamic transient voltage contains high frequency components, that can be approximately extracted from the DC component. To reconstruct the V_z from the terminal voltage, a HPF can be used. HPF transfer function is:

$$HPF(z^{-1}) = \frac{1}{1 + \omega z^{-1}} = \frac{y}{u} \quad (5.1)$$

where $\omega = \frac{1}{\tau}$. By solving equation 5.1, we have:

$$- \int \frac{y}{\tau_{HPF}} + u = y \quad (5.2)$$

Using the Equation 5.2, and assuming $\frac{y}{u} = \frac{\text{output}}{\text{input}}$, the HPF can be developed. The LPF can be developed in a similar way. Figure 5.3 presents the Simulink implementation of the HPF and LPF.

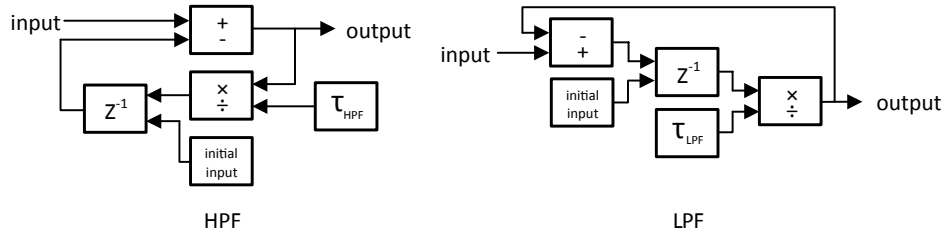


Figure 5.3: The principle of HPF and LPF Simulink implementation. With the initial input, each filter can be initialized independently, and the time constant defines the corner frequency

By connecting the output of the HPF to the input of the LPF, a BPF can be produced as well. The

filtering frequency can be varied by changing the time constant of the filter.

By setting the desired initial input, each filter can be initialized accordingly. The HPF have a slop of 20 dB/Decade (-20 dB/Decade for the LPF). To double the roll-off gain, two filters can be connected to each other.

As shown in Figure 5.4, FTP drive-cycle current profile have been implemented on the cell at 25°C. The cell was at the BOL. The response voltage to this current profile is shown in Figure 5.5 A.

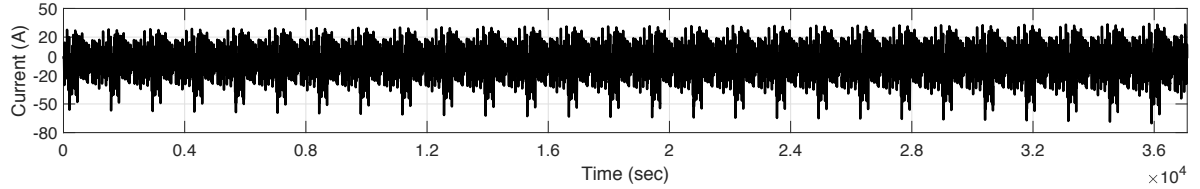


Figure 5.4: The FTP drive-cycle implemented on the cell at 25°C and at BOL

To extract the dynamic transient voltage V_z (see equation 2.24), the time constant of the HPF was set to 30 s. This corresponds to a high-pass filtering with a corner frequency of 0.0053 Hz ($\tau = \frac{1}{\omega} = \frac{1}{2\pi f}$). The dynamic part of the terminal voltage is shown in Figure 5.5 B.

If the time constant of the HPF, is selected to be equal to the time constant of the ECM (see Figure 4.1), then I_{C_1} and I_{R_1} can be extracted by filtering the current profile. By high-pass filtering the load current (see Figure 5.4), the current flowing into the RC-branch capacitor (I_{C_1}) can be extracted.

Figure 5.6 suggests how the current flowing into the RC-branch resistor (I_{R_1}) can be extracted accordingly.

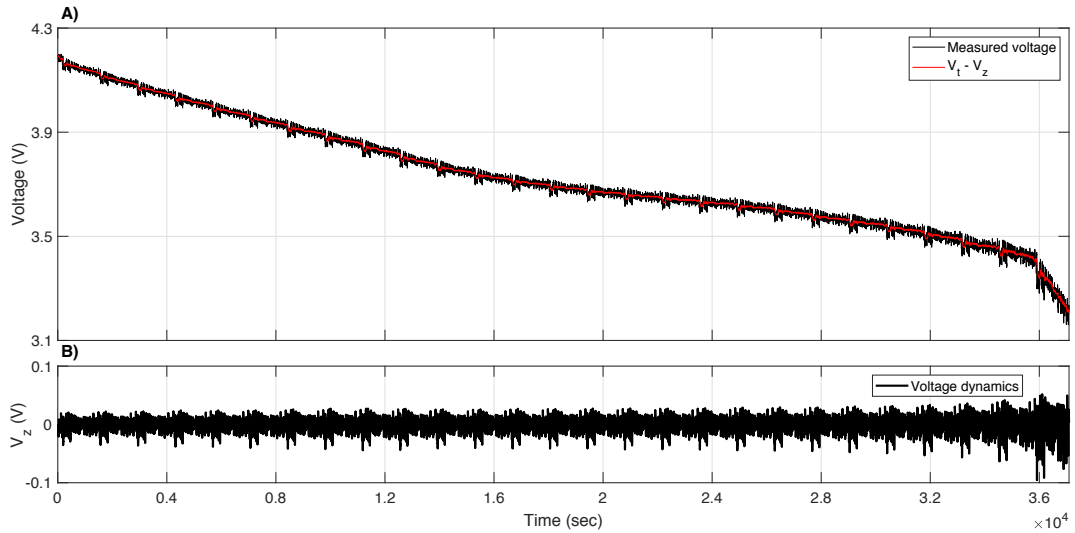


Figure 5.5: A) The voltage response of the cell to the FTP drive-cycle, B) Dynamic part of the voltage response (V_z)

As shown in Chapter 3, the RC-branch parameters have been extracted during 10 s HPPC pulses. By setting the HPF time constant (τ_{HPF}) to 10 s, with good accuracy, I_{C_1} and I_{R_1} have been estimated. This is shown in Figure 5.7.

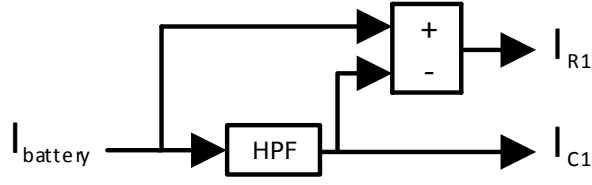


Figure 5.6: Block diagram of the proposed method to extract the current flowing into the RC-branch. For that, the HPF time constant should be equal to the time constant of the ECM model (10 s)

To estimate the OCV, with using a LPF, the terminal voltage has been filtered. The LPF time constant was set to 120 s. To evaluate the estimated OCV, Figure 5.8 presents the comparison between the OCV calculated from the enhanced ECM, and the OCV from the filter-based method. The OCV of the ECM model was obtained from aging experiments, and was SOC-, temperature-, and SOH-dependent. The advantage of the filter-based technique is that the estimated parameters are independent of SOC, temperature, and aging.

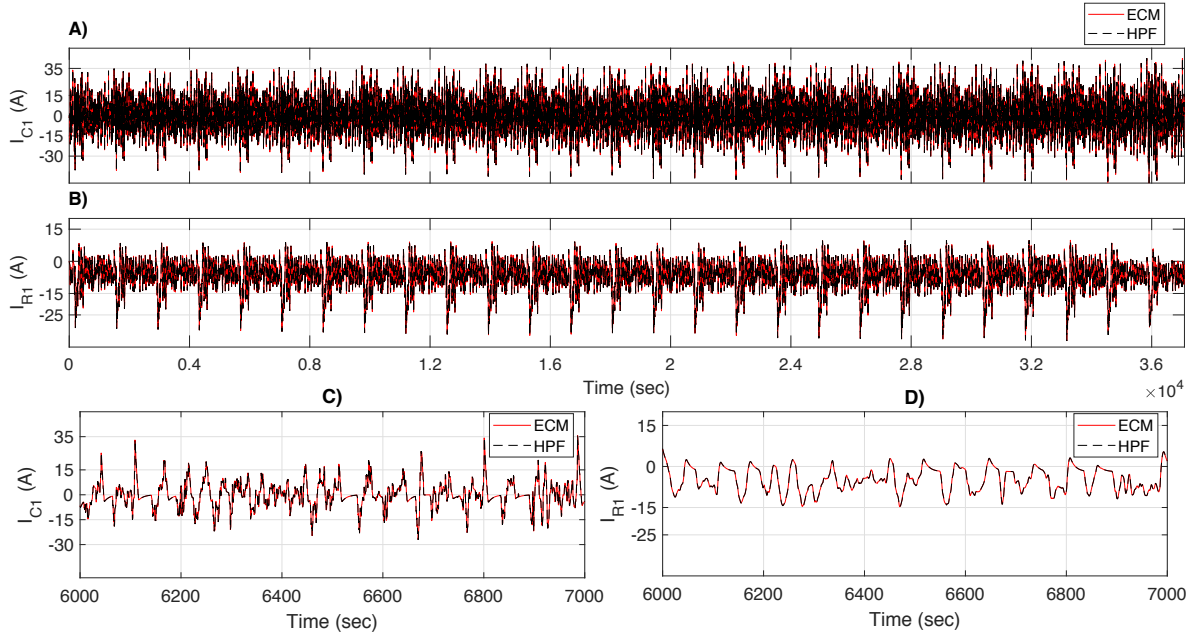


Figure 5.7: A) ECM- I_{C1} vs. I_{C1} extracted from the filter-based method, B) ECM- I_{R1} vs. I_{R1} extracted from the filter-based method, C) I_{C1} zoomed for 1000 s for a better visualization of I_{C1} , D) I_{R1} zoomed for 1000 for a better visualization of I_{R1}

The Nyquist plot of an EIS measurement can be represented in two parts: kinetic control and mass-transfer control. The kinetic-control part occurs at high frequencies, which can be characterized by ohmic resistance, charge-transfer resistance, and double-layer capacitance. The mass-transfer control occurs at low frequencies, which includes the behavior of the cell during the diffusion process. As the Nyquist plot, at the location of the local minima of the impedance spectrum, visualizes the sum of these resistances ($R_i + R_1$), the frequency of this region is of great interest. This frequency is usually located before the diffusion process.

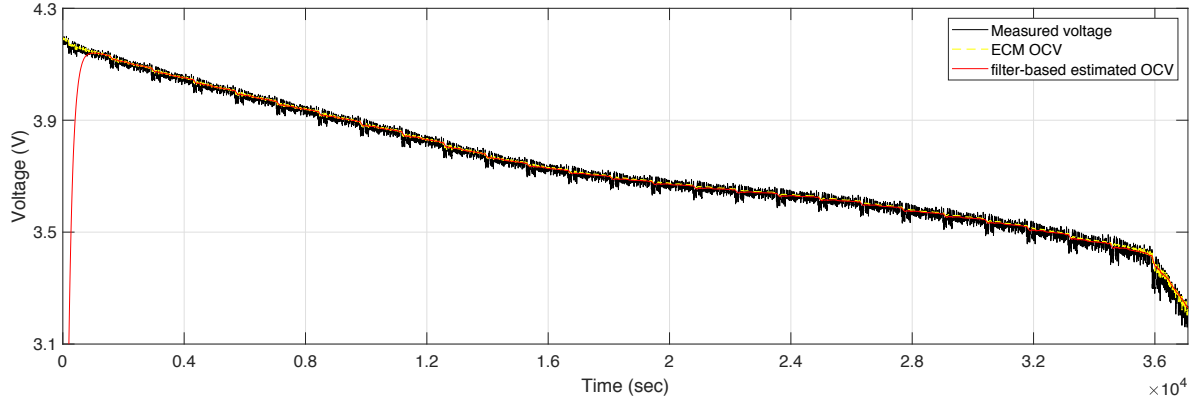


Figure 5.8: A) OCV estimated from the low-pass filtering of the terminal voltage (see Figure 5.3 for the LPF design), OCV estimated from the filter-based method was evaluated with the OCV calculated by the ECM

The R-observer is a part of the general filter-based method as shown in Figure 5.9. In this figure, V_t is the cell terminal voltage response to the input load current.

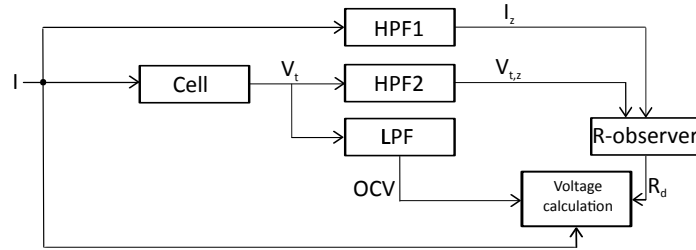


Figure 5.9: Schematic of the filter-based method; including the filters, and R-observer. Time constant of HPF1, and HPF2 were set to 30 s. Time constant of the LPF was set to 120 s

To estimate the dynamic resistance “ R_d ” of the cell, the filtered signals have been passed through an R-observer. Both current, and voltage have been high-pass filtered with the similar filters, and time constants. The design of the R-observer is presented in Figure 5.10. In this figure, the filtered current (I_z), and voltage ($V_{t,z}$) have been used to estimate the LIB dynamic resistance. e_{V_z} (see Equation 2.90) represents the error of the estimation, and was used to correct the estimated dynamic resistance:

$$R_{d,k+1} = R_{d,k} + Ke_{V_z}I_z \quad (5.3)$$

Where “K” is the adaption gain and is adjusted manually. By evaluating the results, the dynamic resistance calculated from the filter-based method, was approximately equal to the total resistance of the ECM ($R_i + R_1$). This is shown in Figure 5.11.

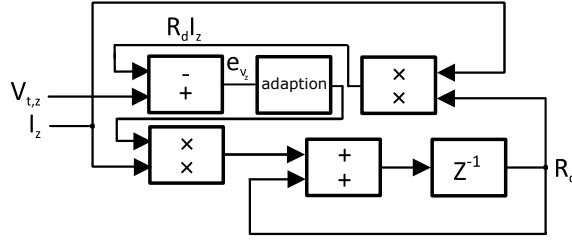


Figure 5.10: Schematic of the R-observer design

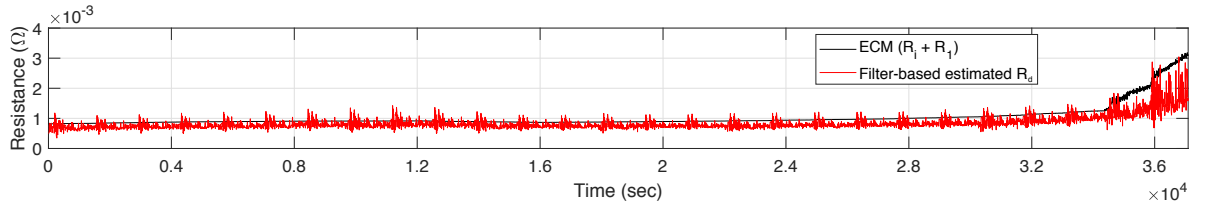
To evaluate the overall performance of this method, terminal voltage of the battery has been reconstructed. To do this, the OCV estimated from the LPF (OCV_{LPF}) was added to the estimated dynamic transient voltage (V_d). The estimated dynamic transient voltage is:

$$V_d = R_d I \quad (5.4)$$

and the total estimated voltage with this method is:

$$V_{t,d} = V_d + OCV_{LPF} = R_d I + OCV_{LPF} \quad (5.5)$$

This process is shown in the voltage calculation block in Figure 5.9. Figure 5.12 shows the comparison between the measured voltage, and the total estimated voltage with the filter-based method. The relative error of estimation was less than 1% for most of the SOC range. The exception was at low SOC, where the estimation relative error reached 2%.


 Figure 5.11: The comparison between the dynamic resistance estimated from the filter-based method, and the total resistance ($R_i + R_1$) calculated from the ECM

For final evaluation, a current profile containing a non-dynamic CCCV charge was added to the FTP drive-cycle. The aging history of the cell was available. The cell at this stage has been used for 2000 FTP cycles. Figure 5.13 A shows the current profile of this test. For this test, the DUT was placed in a temperature chamber set to 23°C. Figure 5.13 B presents the estimated dynamic resistance of the cell. Obviously, this method is insufficient during relaxation time, and the constant load phases. However, the estimation of the dynamic resistance during the dynamic current profile was in good agreement with the enhanced ECM results. As the cell resistance, at this stage, has been doubled compared to the previous test case, it was concluded that the cell was at EOL.

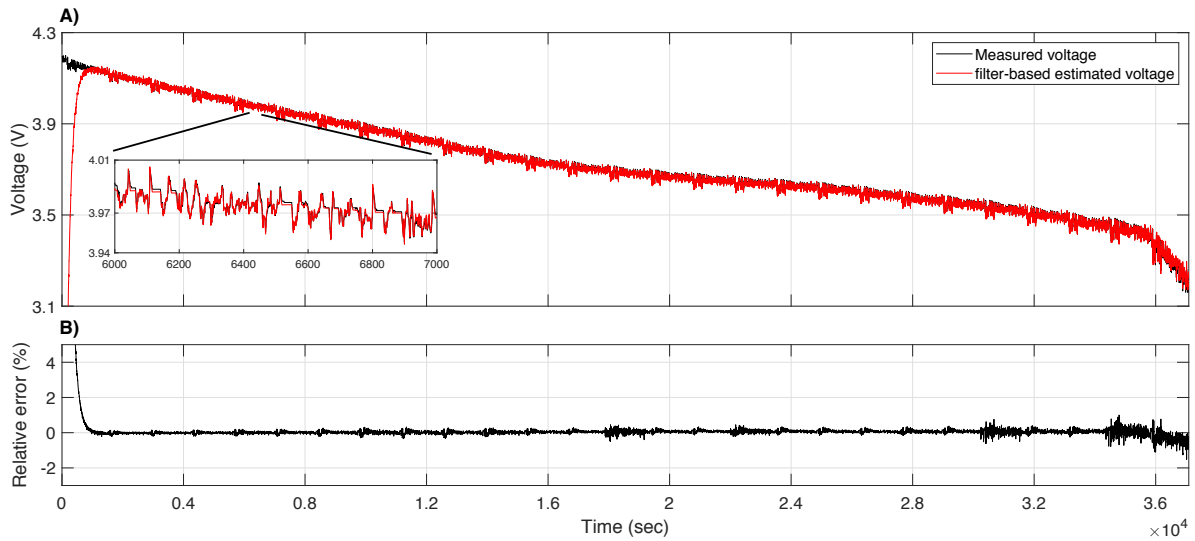


Figure 5.12: A) Measured voltage vs. estimated voltage based on the filter-based method, B) The relative error of estimated voltage based on the filter-based method

Figure 5.13 C presents a comparison between the total estimated voltage with the filter-based method to the measurement. During the CC charge phase, the resistance was over estimated so the model voltage was above the measurement; whereas during the CV phase, the estimated resistance was about zero, and the modeled voltage followed the estimated OCV path. During the dynamic drive-cycle, the model estimation was in good agreement with the measured voltage and the error of modeling was about 2%.

The presented method in this section, had a good performance during the dynamic current phases, however, not reliable results were obtained during the non-dynamic phases. Therefore, this method is unsuitable for standalone usage, and should be coupled to other methods to ensure reliable results.

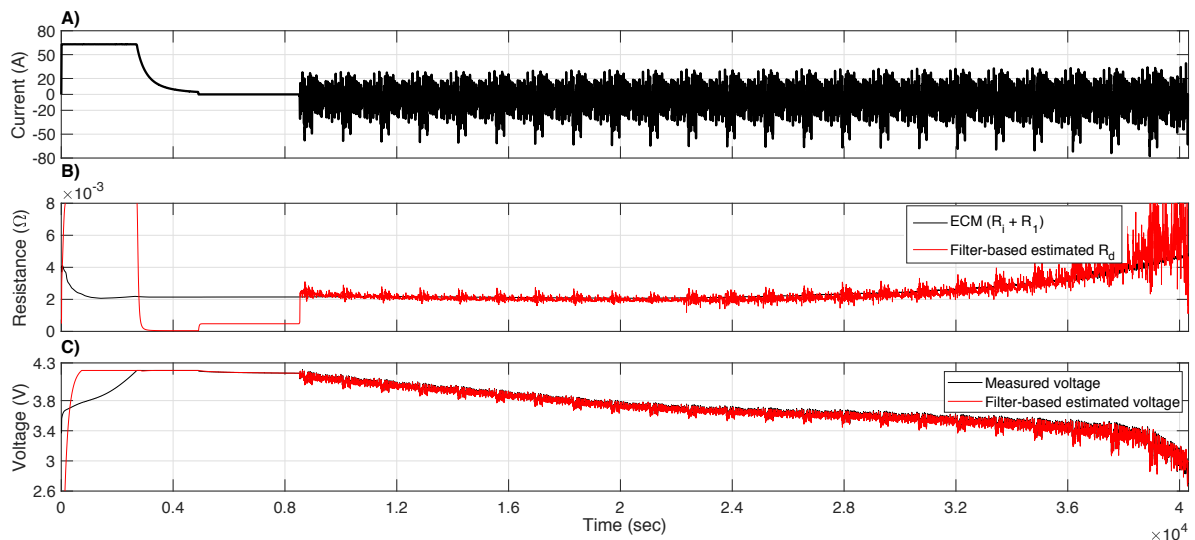


Figure 5.13: A) The current profile containing CCCV charge, and the FTP drive-cycle for aged cell (2000 cycle), B) A comparison between the estimated total resistance between the ECM model and the filter-based method, C) Filter-based estimated voltage in comparison with the measured voltage

Among most of the LIB models and algorithms suggested in literature, model-based methods, such as Kalman filters, sliding mode observer, and neural networks are the most promising methods. The next sections presents the development of the extended Kalman filter, and the sliding mode observer.

5.3 Sliding mode observer

To formulate the SMO algorithm, for ECM with 1RC-branch as shown in Figure 2.8, we have:

$$V_t = V_{oc}(SOC) + IR_i + V_{R_1C_1} \quad (5.6)$$

where “ V_t ” is the battery terminal voltage, “ $V_{oc}(SOC)$ ” is the SOC-dependent open-circuit voltage, “ R_i ” is the ohmic resistance, and $V_{R_1C_1}$ is the voltage of the RC element. All the parameters, such as $V_{oc}(SOC)$, R_i , and $V_{R_1C_1}$ are a function of SOC, temperature, and SOH. Taking derivative of the terminal voltage in Equation 5.6, results in:

$$\dot{V}_t = \dot{V}_{oc}(SOC) + \frac{d}{dt}(IR_i) + \dot{V}_{R_1C_1} \quad (5.7)$$

In Equation 5.7, the first term of the right side of the equation is the derivative of the OCV over the time. As the SOC-OCV relationship is nonlinear, there exists a piecewise linear relationship between them. By assuming this piecewise relationship, the relation between SOC and OCV using the piecewise linearization method becomes $V_{oc}(SOC) = kSOC + d$ with constant values for “ k ” and “ d ”. Assuming this, the derivative of the OCV is formulated as follows [53]:

$$\dot{V}_{oc}(SOC) = k\dot{SOC} = k\frac{I}{C_{act}} \quad (5.8)$$

For the second term of the terminal voltage derivative ($\frac{d}{dt}(IR_i)$), due to the fast sampling intervals, the rate of the current change (δI) during charging and discharging has been neglected.

For the 63 Ah Kokam cell, the current of 1C (63 A) during charge or discharge and with the sampling time of 1 s led to a small change of the SOC ($\dot{SOC} = \pm \frac{63}{63 \times 3600} = \pm 0.000277 \frac{1}{s}$). In a real-time scenario, the sampling time is faster than 1 s (now more commonly, 200 ms), so it can be concluded that $\dot{SOC} \approx 0$, which means that the current during 1 s or less has an insignificant impact on SOC. For this reason, the change of current is assumed to be constant zero in each sampling period ($\frac{dI}{dt} \approx 0$). The terminal voltage derivative can be written as:

$$\dot{V}_t = k\frac{I}{C_N} - \frac{1}{R_1C_1}V_{R_1C_1} + \frac{I}{C_1} = k\frac{I}{C_{act}} - \frac{1}{R_1C_1}(V_t - V_{oc}(SOC) - IR_i) + \frac{I}{C_1} \quad (5.9)$$

Modeling error in the observer design can be present. To consider these modeling errors, uncertainties (Δf) are added in the system equations. Considering the piecewise SOC-OCV linearization uncertainties in Equation 5.7, Equation 5.9 becomes:

$$\dot{V}_t = \alpha_1(V_{oc}(SOC) - V_t) + \beta_1 I + \Delta f_1 \quad (5.10)$$

By substituting “ I ” from Equation 5.6 into 2.74, we can write [143]:

$$\dot{SOC} = \alpha_2(V_t - V_{oc}(SOC) - V_{R_1C_1}) + \Delta f_2 \quad (5.11)$$

“ Δf_2 ” is the uncertainty that is caused by the unknown actual capacity “ C_{act} ” term [191]. $\dot{V}_{R_1C_1}$ (see Equation 2.22) is reformulated as:

$$\dot{V}_{R_1C_1} = \frac{I}{C_1} - \frac{1}{R_1C_1}V_{R_1C_1} + \Delta f_3 = -\alpha_1 V_{R_1C_1} + \beta_2 I + \Delta f_3 \quad (5.12)$$

“ Δf_3 ” is the uncertainty due to the unknown nonlinear polarization term [142]. According to the equations above, the coefficients of the SMO are collated in Table 5.1.

Table 5.1: The SMO coefficients calculation taken from Equations 5.10 to 5.12

SM coefficients	α_1	α_2	β_1	β_2
equivalent	$\frac{1}{R_1C_1}$	$\frac{1}{R_iC_{act}}$	$\frac{k}{C_{act}} + \frac{1}{C_1} + \frac{R_i}{R_1C_1}$	$\frac{1}{C_1}$

The controllability and observability matrices are introduced in Appendix A.3. The system is observable and controllable, because these matrices are full rank. The system stability with one RC-branch for convergence of the error equation can be proven by the Lyapunov stability check method [75, 143]. The output equation of the SMO can be derived from Equation 2.96.

$$\dot{\hat{V}}_t = -\alpha_1 \hat{V}_t + \alpha_1 V_{oc}(S\hat{O}C) + \beta_1 I + L_1 \text{sgn}(V_t - \hat{V}_t) \quad (5.13)$$

From the Equation 5.13, \hat{V}_t and $V_{oc}(S\hat{O}C)$ are the estimates of terminal voltage and the OCV. L_1 is the terminal voltage observer feedback gain, which is an observer tuning coefficient. in Equation 5.13, $\text{sgn}(x)$ is the sign function. The voltage estimation error ($e_v = V_t - \hat{V}_t$) is:

$$\dot{e}_v = -\alpha_2 e_v + \alpha_2 (V_{oc}(SOC) - V_{oc}(S\hat{O}C)) + \Delta f_1 - L_1 \text{sgn}(e_v) \quad (5.14)$$

The Lyapunov candidate function of $V_v = \frac{1}{2}e_v^2$ can be used to prove the zero convergence of the terminal voltage error equation as time tends to infinity ($\lim_{t \rightarrow \infty} e_v = 0$):

$$L_1 > |\Delta f_1 + \alpha_2 (V_{oc}(SOC) - V_{oc}(S\hat{O}C))| \quad (5.15)$$

SOC equation for the SMO design can be written as:

$$\dot{S\hat{O}C} = \alpha_2 (\hat{V}_t - V_{oc}(S\hat{O}C) - \hat{V}_{R_1C_1}) + L_2 \text{sgn}(SOC - S\hat{O}C) \quad (5.16)$$

and to have a complete equation set for the SMO design, the voltage of the RC element can be written as:

$$\dot{\hat{V}}_{R_1C_1} = -\alpha_1 \hat{V}_{R_1C_1} + \beta_2 I + L_3 \text{sgn}(V_{R_1C_1} - \hat{V}_{R_1C_1}) \quad (5.17)$$

In a similar manner in proving the convergence of terminal voltage error, a suitable Lyapunov candidate function for SOC, and the RC-branch voltage can be used to prove the zero convergence of the error equations. The simulation model implemented for the SMO contains three main subsystems. The first subsystem block computes the discretized cell’s terminal voltage ($V_{t,k}$) and requires the battery current, OCV, α_1 , β_1 , e_v and the previous iteration of the estimated voltage ($V_{t,k-1}$) as inputs. The second subsystem estimates the SOC, and the inputs into this subsystem are the estimated voltage from first subsystem, α_2 , e_Z and the estimated $V_{R_1C_1}$ from the third block. The last block estimates

the RC voltage ($V_{R_1C_1}$). This block requires the input current, α_1 , β_2 , $e_{V_{R_1C_1}}$, and $V_{R_1C_1,k-1}$ as inputs. The coefficients of the SMO can be computed with the mathematical operations on the ECM parameters. The SMO observer design schematic is presented in the Annex B.1 figure.

Figure 5.14 presents the estimation result of the cell terminal voltage by the SMO as well as the absolute error of the estimation. For the SMO, the voltage estimation error is better than 40 mV over the large SOC range, except for low SOC.

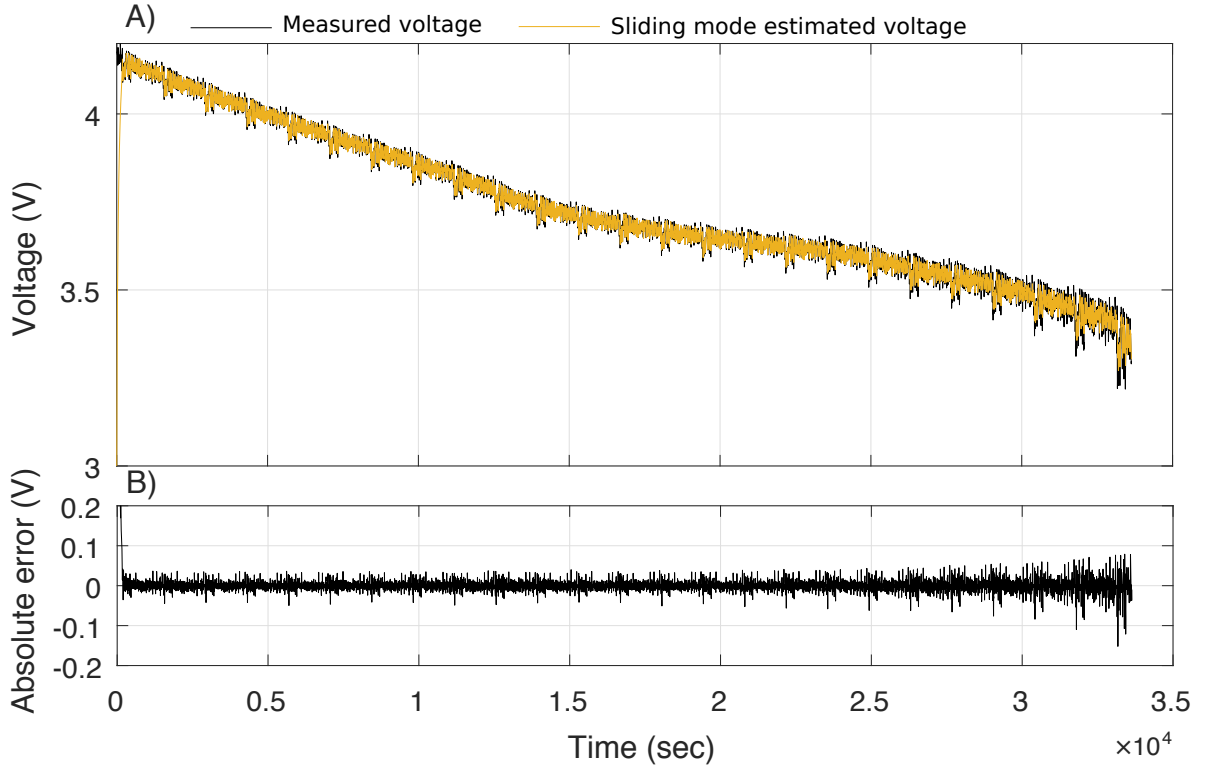


Figure 5.14: A) Estimated cell terminal voltage by SMO, B) Absolute error of the estimated terminal voltage by SMO

The next figure evaluates the observer in comparison with the calibrated reference SOC based on controlled laboratory conditions (Ah-counting). To make the comparison more challenging, an enhanced ECM model controlled with a PI controller was involved (see Equation 2.91). The SOC estimation based on a combined ECM and PI controller method requires fine tuning of the controller; however the tuning should be manually performed. The last parameter that was estimated by the SMO was the RC element voltage. This is shown in Figure 5.16.

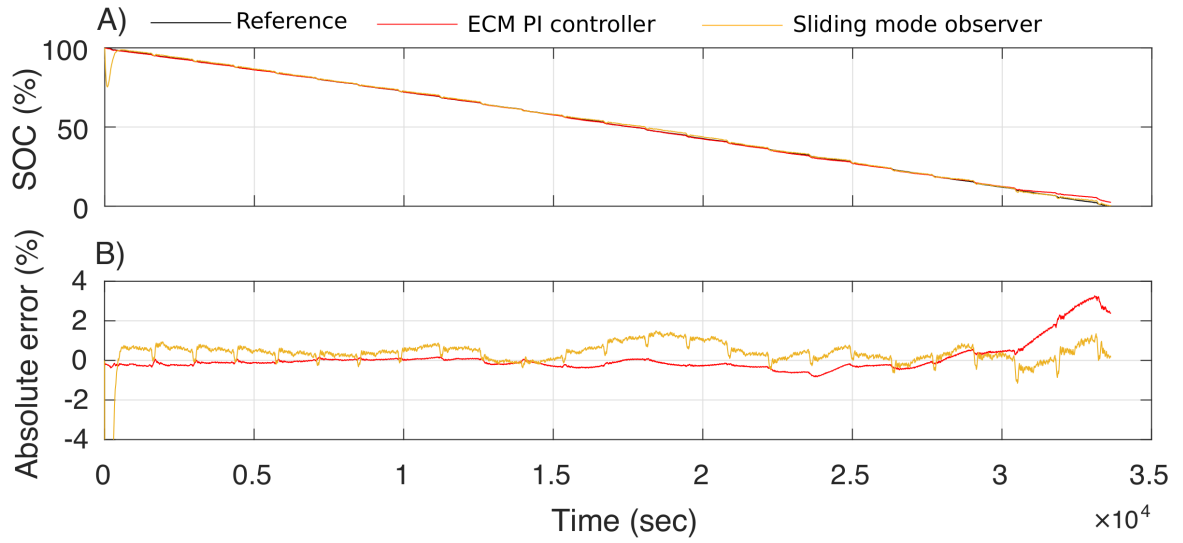


Figure 5.15: A) Cell SOC estimation performance: a comparison between the combined ECM-PI controller, the SMO vs. the reference SOC, B) SOC estimation error

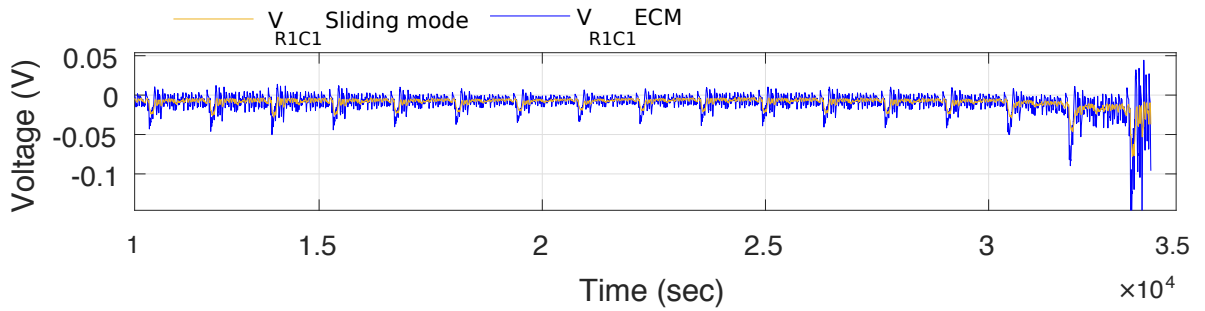


Figure 5.16: Estimated RC element voltage by the SMO and the ECM

The SMO has a certain limitation. Particularly, observer coefficients are a function of cell parameters (R_i , R_1 and C_1). This means that, by using the SMO for the SOC estimation, the observer requires the availability of all cell parameters. Then the cell parameters are used to compute the observer coefficients, which can be used later for SOC estimation. As the cell coefficients are coming from the ECM, the implementation of the SMO is dependent of the ECM. Alternatively, as the SMO implementation requires less effort than other methods, such as the Kalman filter, the parameter estimator method, introduced in Section 5.2, can be coupled with the SMO for fast and robust SOC estimation. In this case, the effort of extracting the aging parameters can be avoided.

5.4 Kalman filter

The linear and extended Kalman filters are introduced in Section 2.7.3.1. To develop the Extended Kalman filter algorithm for the cell, a state-space model was used for a 1RC battery model. The model input “ u ” is the measured cell current I ($u = I$), and the model output “ y_k ” is the cell terminal voltage V_t ($y_k = V_t$).

For the 1RC model, the voltage of the RC circuit is expressed as Equation 2.22. The discrete-time description of $V_{R_1C_1}$ is:

$$V_{R_1C_1,k+1} = e^{-\frac{t_s}{R_{1,k}C_{1,k}}} V_{R_1C_1,k} + R_{1,k} \left(1 - e^{-\frac{t_s}{R_{1,k}C_{1,k}}} \right) I_k + \mathbf{w}_k \quad (5.18)$$

where “ t_s ” is the fixed sample time, and “ k ” is the fixed step time. The discrete-time SOC equation shown in Equation 2.72 is:

$$\text{SOC}_{k+1} = \text{SOC}_k + \frac{t_s}{C_{\text{act}}} I_k + \mathbf{w}_k \quad (5.19)$$

Taking the SOC and the voltage of the RC element as the system states “ \mathbf{x} ”:

$$\mathbf{x} = \begin{bmatrix} V_{R_1C_1} & \text{SOC} \end{bmatrix}^T \quad (5.20)$$

The state-space representation of the 1RC model becomes:

$$\mathbf{A}_k = \begin{bmatrix} e^{-\frac{t_s}{R_{1,k}C_{1,k}}} & 0 \\ 0 & 1 \end{bmatrix} \quad \mathbf{B}_k = \begin{bmatrix} R_{1,k} \left(1 - e^{-\frac{t_s}{R_{1,k}C_{1,k}}} \right) \\ \frac{t_s}{C_N} \end{bmatrix} \quad (5.21)$$

$$\mathbf{C}_k = \begin{bmatrix} 1 & \frac{OCV(\text{SOC}_k)}{SOC_k} \end{bmatrix} \quad D_k = \begin{bmatrix} R_{i,k} \end{bmatrix} \quad (5.22)$$

The performance of the Kalman filter is also influenced by the process noise “ \mathbf{w} ” (with the covariance of “ \mathbf{Q} ”, as shown in Equation 5.23), and the measurement noise “ \mathbf{v} ” (with covariance of “ R ” as shown in Equation 5.24). The process noise represents the inaccuracies of the model, and the measurement noise represents the voltage measurement error. Both the measurement and the process noises are considered to have a Gaussian distribution.

$$E[\mathbf{w}_k] = 0 \quad E[\mathbf{w}_k \mathbf{w}_k^T] = \mathbf{Q} \quad \mathbf{w}_k \sim \mathcal{N}(0, \mathbf{Q}) \quad (5.23)$$

$$E[v_k] = 0 \quad E[v_k v_k^T] = R \quad v_k \sim \mathcal{N}(0, R) \quad (5.24)$$

R and \mathbf{Q} have an affect on the Kalman gain, as shown in Equation 2.81. A higher modeling error (higher \mathbf{Q}) leads to a higher Kalman gain, so the filter output obtains more correction. Having more trust in the measurement (lower measurement noise) leads to a lower R , hence a higher Kalman gain. By having a higher Kalman gain, the system output trusts the sensor measurements, and the states obtain more correction gain. \mathbf{Q} and R are the filter parameters and at the moment, there is no known reference that presents an optimal method for tuning the extended Kalman filter for battery SOC applications (no direct calculation method is available).

Standard deviation can be used to calculate the scalar covariance of the cell voltage output, as shown in Equation 5.25.

$$R = E[v_k v_k^T] = \sigma_m^2 \quad (5.25)$$

\mathbf{Q} is a two-dimensional matrix for the state-space system, and can be written as:

$$\mathbf{Q} = E[\mathbf{w}_k \mathbf{w}_k^T] = E \begin{bmatrix} v_{V_{R_1C_1}}^2 & v_{V_{R_1C_1}} v_{\text{SOC}} \\ v_{V_{R_1C_1}} v_{\text{SOC}} & v_{\text{SOC}}^2 \end{bmatrix} \quad (5.26)$$

$$= \begin{bmatrix} E[v_{V_{R_1C_1}}^2] & E[v_{V_{R_1C_1}} v_{\text{SOC}}] \\ E[v_{V_{R_1C_1}} v_{\text{SOC}}] & E[v_{\text{SOC}}^2] \end{bmatrix} \quad (5.27)$$

However, the tuning parameters (R and \mathbf{Q}) of the Extended Kalman filter are mainly adjusted man-

ually, and, depending on the experience of the programmer, the best result for the state variable estimation can be achieved.

The first step to implementing the EKF is to initialize the algorithm for the first iteration. The equations are evaluated at each time step “ k ” with a constant time step size, for example, $t = 1$ s, for the first iteration $k = 1$, and so on. As the common procedure for a two-state system, the algorithm can be initialized with:

$$\hat{\mathbf{x}}_{0|0} = \begin{bmatrix} 0 & 0 \end{bmatrix} \quad (5.28)$$

$$\mathbf{P}_{0|0} = \begin{bmatrix} 1 & 0 \\ 0 & 1 \end{bmatrix} \quad (5.29)$$

However, as explained in Figure 2.18, a proposed method for auto-initialization of the algorithm has been used. In general, filter-convergence speed and accuracy solely depend on \mathbf{Q} and \mathbf{R} .

In the previous section, the SMO was implemented, and its performance against an enhanced ECM-SOC model (combined ECM, and PI controller, as presented in Equation 2.91) was shown. In this section, Figure 5.17 compares the EKF algorithm to the SMO, and the ECM. The EKF algorithm had some advantages over the SMO. The modeling error of the EKF was less than that of the SMO, and, at the same time, the EKF convergence speed was faster. The results are magnified and shown in Figure 5.18.

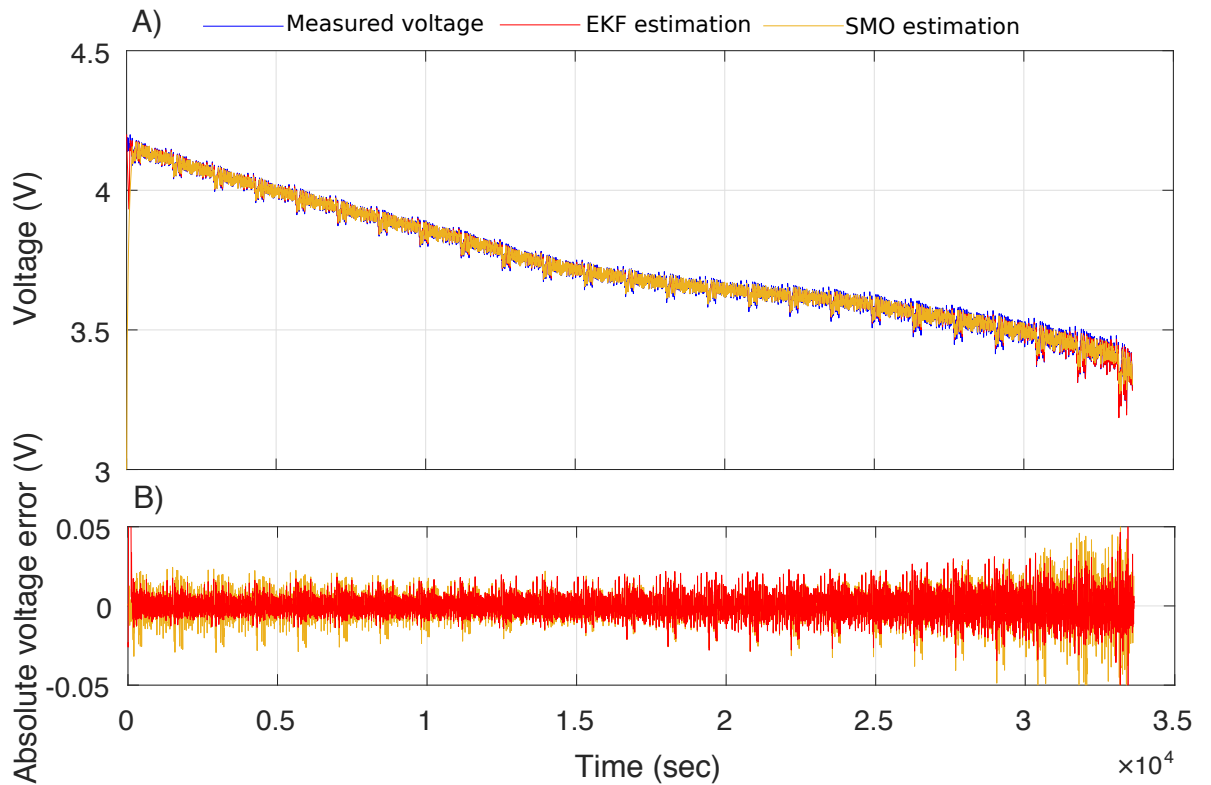


Figure 5.17: A) Estimation of the cell terminal voltage by the EKF and the SMO, B) Absolute error of the estimated terminal voltage

The next step is dedicated to the evaluation of the SOC estimation performance with the EKF method.

Figure 5.19 presents a comparison between the estimated SOC from the EKF algorithm and the other methods.

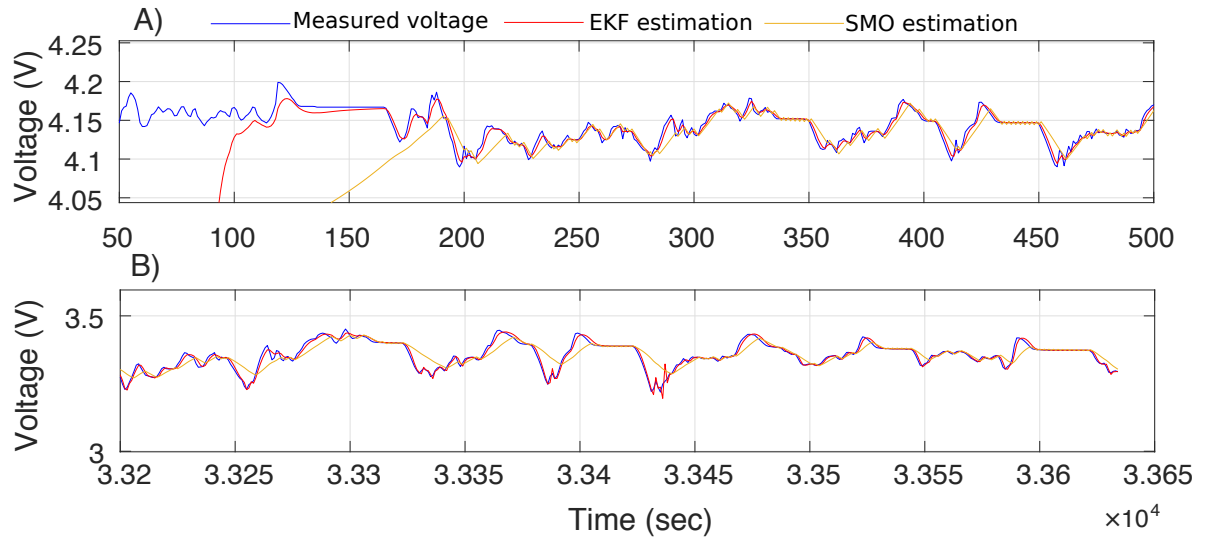


Figure 5.18: A) A comparison between the EKF and the SMO convergence speed at the beginning of the dynamic current profile, B) A comparison between the EKF and the SMO accuracy at the end of the dynamic current profile

Both the EKF and the SMO showed more accurate SOC estimation results than the improved ECM model with PI controller. Comparing the SOC estimation based on the EKF and the SMO, the SOC error from the EKF method is smaller than the SMO estimation for the majority of parts in the SOC region. Both algorithms are implementable in the HIL system or the BMS for successful estimation of the parameters and for SOC detection.

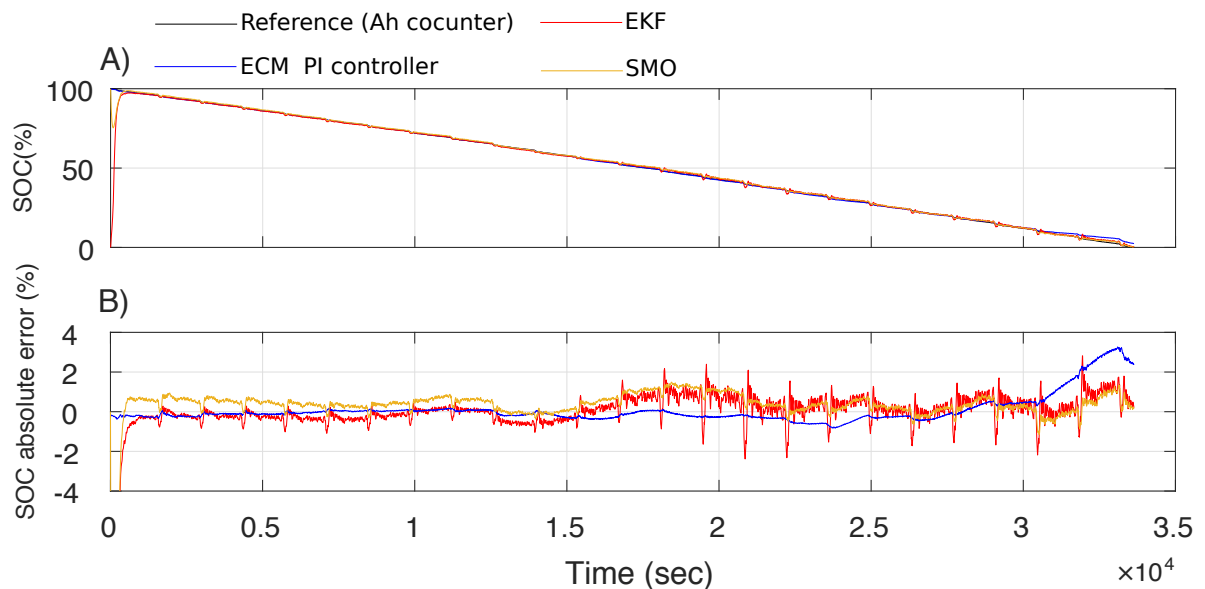


Figure 5.19: A) The SOC estimation performance of the EKF, SMO, filter-based technique, and enhanced combined ECM-PI controlled model; B) The error of the estimation

A PID controller is a constant gain observer. The drawback of constant gain observers is that, throughout the state trajectory, the output error is corrected with the same amplification. In the state-space

representation, the sensitivity of the output with respect to the states could be low. In this case, using only a constant gain tends to inject noise and disturbance into the system. Therefore, a variable gain observer such as the EKF, accordingly, performs more successfully.

This chapter introduced three algorithms for parameter and state detection. The first one was the filter-based parameter estimation. This method is a stand-alone technique which demonstrated good accuracy for dynamic loads such as drive-cycles. However, it is shown that its performance was unreliable under non-dynamic conditions. The sliding mode observer is a popular method; however, its performance was highly dependent on the ECM. This is because all the coefficients of the algorithms needs to be directly provided by the ECM. The extended Kalman filter is a popular technique for state and parameter estimation. The implementation of the EKF is more complicated than the SMO. The performance (convergence and accuracy) of the EKF is sensitive to its tuning parameters. With a good set of tuned parameters, EKF showed better convergence compared to the SMO. The SOC estimation performance of the EKF was better than the SMO as well. The tuning of the parameters are based on the try and error, and are mainly performed manually. Proving the robustness and practicality of the EKF for long term EV operation is a challenging task.

To cover all the dynamic and non-dynamic driving phases, a carefully parameterized ECM model combined with the improved Ah-counting method for SOC estimation controlled with a PI-controller has a reliable performance. To guarantee the performance of the model, the filter-based technique, and the EKF can be used in parallel with this ECM.

6 Implementation, Evaluation, Verification, and Upscaling

For the verification of the developed cell-level software, functions and algorithms have been implemented in a BMS and a HIL system. For testing, a load-current profile including several charging and discharging cycles with constant current phases, and dynamic drive-cycle profile has been selected. In this chapter, Section 6.1 presents a scaled BMS development platform. Section 6.2 presents a real-time battery monitoring developed with the HIL system. Finally, the battery pack simulation is presented in section 6.3

6.1 A scaled BMS development platform

In this section, a scaled BMS development-platform to test the cell-level developed functions and algorithms is explained. The BMS has several tasks; assuring safety is the most critical task of the BMS, which has to be ensured by detecting the pack's momentary and long-term conditions and states. This includes the observation of temperatures, voltages, and states. Other tasks, such as data acquisition (current, voltage, temperature, or even the external forces on the cells, module, or pack), monitoring and storing, data processing, secondary-data computation, and thermal and electrical management should be included in the EV's BMS as well.

In [212], a scaled BMS development platform to monitor a large number of cells containing microcontroller, sensors, and memory storage was developed. This BMS was used to evaluate the software in the application. For that, Kok-511 was selected to be monitored by the BMS and the HIL at the same time. The purpose of this test was to use the BMS for monitoring purposes, so additional hardware components such as relays, fuses, contactors, and emergency switches were ignored.

The BMS controller used for this setup was a Kinetis 60, based on an ARM Cortex 120 MHz M4 core from Freescale. The controller was integrated into a TWR-K60F120M, boarded to connect to the PC, managing power supply and providing storage slots and LEDs. The BMS was extendable to other peripherals as well. The preferred sampling time of 100 ms to capture the battery dynamics was ensured. Accuracy and precision of the measurements should be considered during data conversion as well. Two 16-bit Delta-Sigma ADCs were used for voltage measurement through a "LTC 6804-2" controller from Linear Technology, which was designed for multi-cell battery-stack monitoring. This controller was able to monitor up to 12 cells in series connection with a maximum total measurement error of 1.2 mV. To extend this controller, a maximum of sixteen other controllers can be connected, and each controller can be individually addressed. With this setup, a total number of 192 cells can be monitored.

For the EV's BMS, using both, a hall-effect sensor as an indirect method of current measurement and a shunt resistor as a direct method of current measurement simultaneously, can be beneficial. This would enhance the reliability of current measurement. A modular shunt sensor from Isabellenhütte

(IVT-MODULAR¹) was used for current measurement. The results of the current measurement were compared with the current measured from the battery cycler. A BMS can normally communicate with external devices, sensors, and actuators through standard interfaces such as LIN, I^2C , CAN, and two- or four-wire bus systems, known as SMBUS and SPI. The BMS communicates to the shunt sensor through a CAN interface was done at the speed of 500 kbit/s.

A few thermistors² and thermocouples have been used for temperature measurement of the battery cycler and the scaled BMS. The schematic of the cell with a mounted temperature sensor used for the experiment is shown in Figure 6.1. A RTD temperature sensor, type "TMP175" from Texas Instruments, which can read up to 150°C using a two-wire I^2C interface and a 5 V supply was used for this setup. It offered the configurable resolution of 9- and 12-bits. This allowed to measure a temperature change as small as 0.0625°C.

The sensor conversion time was between 28 ms, this would increase to 220 ms for up to 27 other devices on the same bus. In this figure, T1 and T2 are TMP175-type temperature sensors. PT100-type sensors have been connected to locations a and b. Five thermocouples have been used at locations marked with 1-5.

As it is shown in Chapter 5, the developed cell-level algorithms had acceptable accuracies for use in the BMS. For the pack-level, these algorithms can be implemented in a BMS. C language was used to implement the models and algorithms.

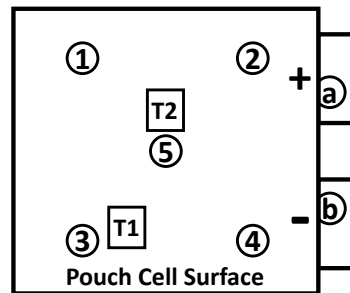


Figure 6.1: Location of the temperature sensors attached to the DUT

As illustrated in Figure 5.1, the method developed in this thesis was a combination of models and algorithms, which continuously estimate cell voltage, SOC, parameters, and cell surface and internal temperatures. For the pack-level, each cell had its own dedicated model. With this model, cell's SOC imbalance, and temperatures deviation can be monitored. Other safety functions can be further developed and implemented according to the requirement.

The accuracy of the BMS voltage and current measurement is not presented here; however, it was checked by comparing it to the battery cycler measurements, and the error was found to be less than 1% of full scale. The current profile in Figure 6.2 A was used to validate the robustness of the algorithms of the BMS. This current profile contained different phases via a combination of calibration phases, full cycles, pulses, and drive-cycles used for comprehensive evaluation. Figure 6.2 B presents the cell terminal voltage model simulated from the BMS calculation in comparison with the measurement. Except for low voltages at SOCs smaller than 5%, the mean error of the estimated voltage was $\pm 0.7\%$. The error peaks occurred at the locations where the cells were fully discharged, and the

¹ The shunt sensor was powered by a 12 V power supply. it is using 16 bit ADC and offers several current measurement ranges between ± 100 A to ± 2500 A

² A resistance based temperature detector (RTD) sensor

nonlinear behavior had a big influence on the model. OCV measurement inaccuracies were mainly contributing to this part of the modeling performance. Model simplification was another contributing aspect of the modeling error. Voltage modeling error is shown in Figure Figure 6.2 C.

Figure 6.3 A compares the reference SOC (Ah-counting method, without the PI controller) to the BM estimated SOC with the EKF method. The EKF SOC estimation error (Figure 6.3 B) remained in the $\pm 1\%$ bound full scale. The SOC error bound was valid when the cell was exposed to any type of current profile, including high current pulses (10 s), drive-cycles, full CCCV charge, and full CC discharge for a prolonged period of time. The course of the error showed no identifiable weakness in the model. However, the SOC was recalibrated during full charge or full discharge conditions by the BMS. The increasing error during the long drive-cycle intervals without reaching the full charge or full discharge conditions possibly led to an accumulated error of SOC during this long term intervals. So a worst case scenario are assumed to be the cases that no full cycles are performed.

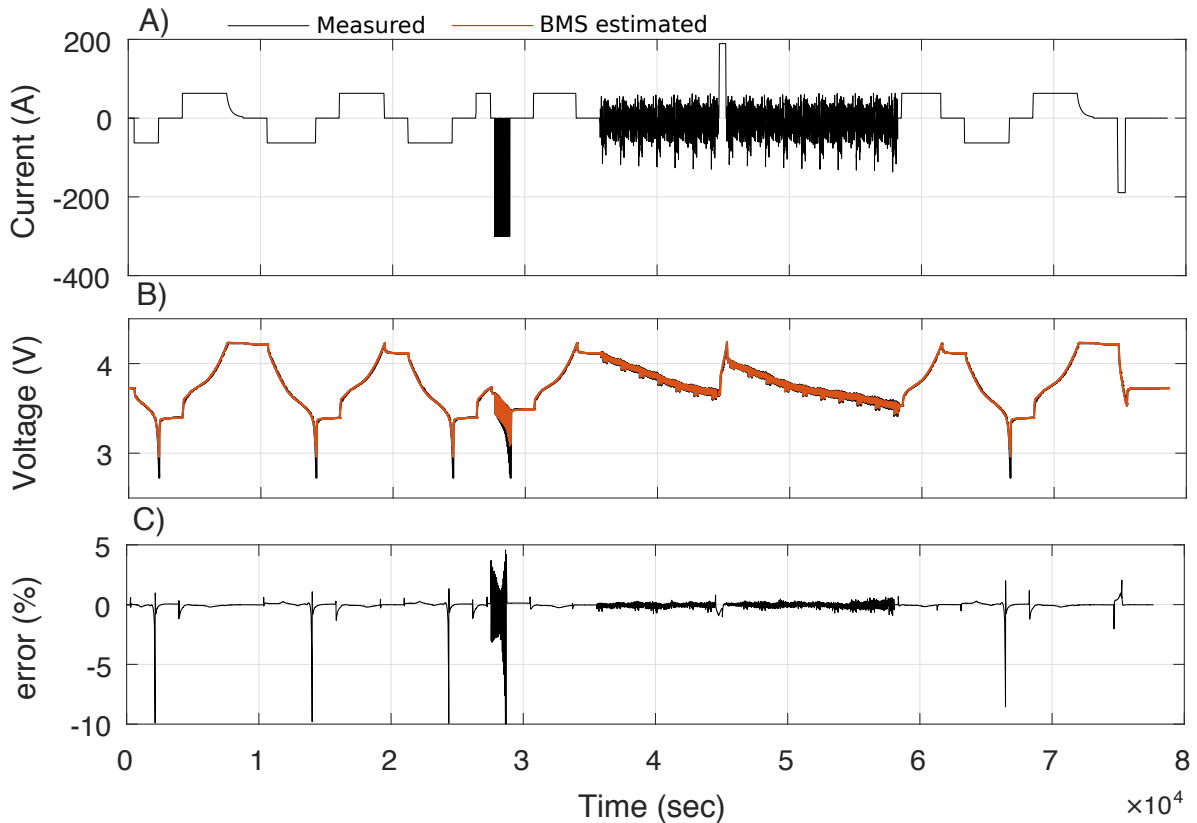


Figure 6.2: A) A current profile with different long term interval phases used to verify the BMS cell-level performance: a mixture of high current pulses, CC charges/discharges, CCCV charges, and dynamic drive-cycles, B) The BMS terminal voltage model in comparison with the measured voltage, C) The BMS voltage modeling error

Figure 6.3 C presents the results of the BMS temperature estimation. The TECM as introduced in Section 4.3.1 was implemented in the BMS. During the drive-cycle, the cell temperature became almost constant, and remained slightly above the ambient temperature. According to this measurement, the conditions contributing to the significant temperature increase (temperature peaks) were:

- Fast charging or fast discharging with 3C or higher

- A pulse train of 5C or higher
- Standard CC discharge (1C) when the SOC was lower than 10%

The modeling error of the estimated temperature was less than 0.5°C during normal operation but reached about 2°C during the extreme cases mentioned above. The reason for the higher temperature modeling error at the higher current rates was that the temperature inhomogeneity increased with higher currents, and the parameters of the TECM were also more inaccurate due to the nonlinear behavior of the cell at these currents and SOC levels.

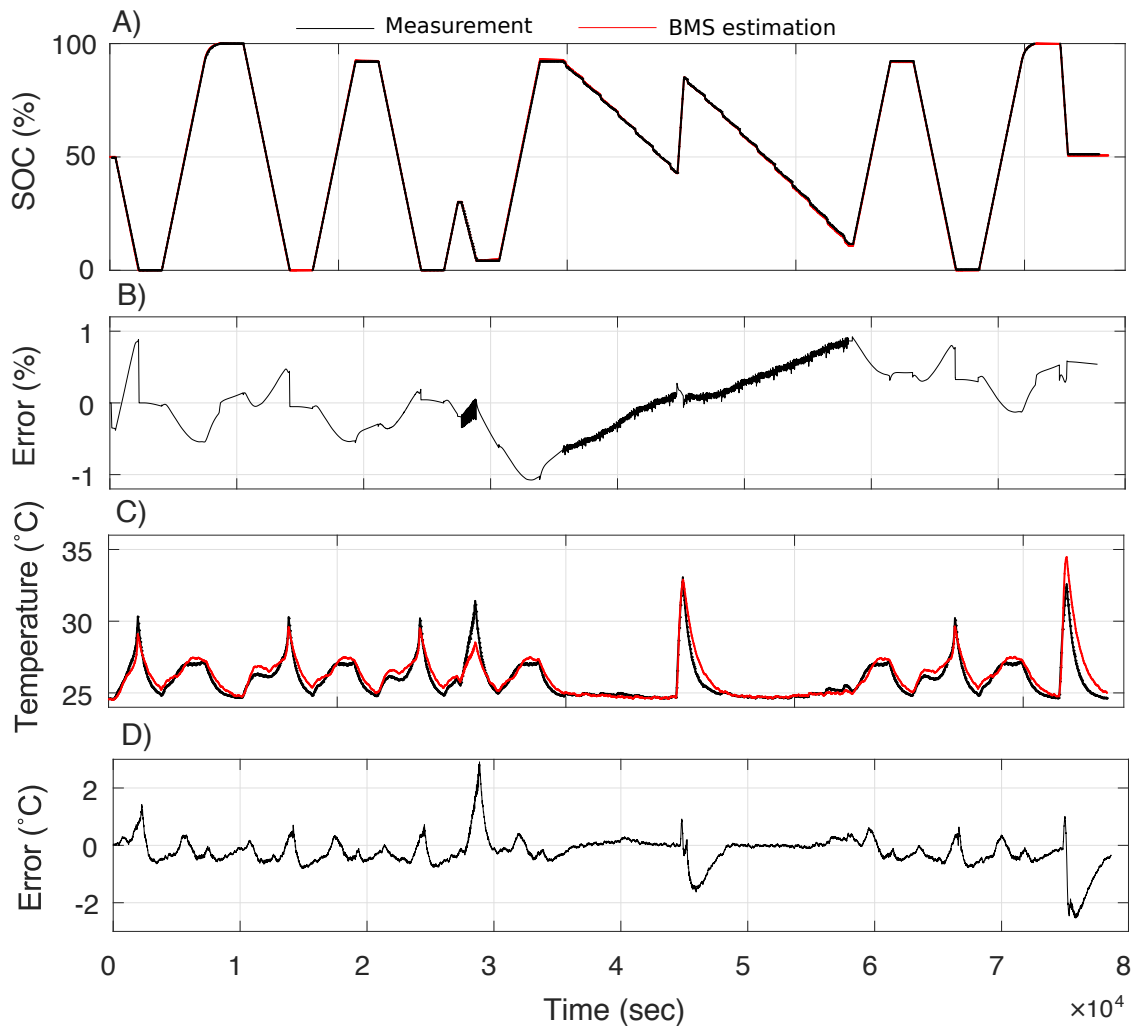


Figure 6.3: A) BMS SOC estimation with the EKF method vs. the reference SOC with the Ah-counting method, B) SOC estimation error, C) BMS estimated cell surface temperature vs. sensor measurement, D) Surface temperature estimation error

6.2 HIL: Real-time battery monitoring

This chapter includes the dSPACE setup including the PX10 housing, DS1006 processor board, and DS2202 Multi I/O board for the hardware parts. The experimental architecture of the HIL consists of three main components: the DUT, software (models/algorithms), and the HIL hardware. The communication between these three modules was realized with TCP/IP protocol. The dSPACE itself

had some interacting parts, including ControlDesk software as the graphical user interface (GUI), I/O boards, signal conditioning for automotive application, and the processor board for the HIL system. The dSPACE processor board was a DS2202, which was used to set up the HIL experiment. Simulink was used for online simulations. The real-time workshop (RTW) provided by dSPACE was used for C-code generation. Simulink was used with the HIL system via the real-time interface (RTI). RTI includes a block library for I/O hardware integration and automatic software implementation. Finally, ControlDesk can be used for experiment control and test automation. ControlDesk can be used for virtual ECU testing, rapid control prototyping, HIL simulation, ECU measurement, calibration, diagnostics, and access to the vehicle bus system. Of the aforementioned functions, the HIL simulation was used for models and algorithm implementation. Of the I/O boards, a P2B board was used for CAN communication, for example, for a shunt sensor CAN communication. A P1A board was used as the ADC for other battery analogue signals, such as temperature and voltages. CAN communication was established through CANoe from Vector Informatik for the shunt current sensor.

An EVT-A shunt sensor, manufactured by Isabellenhütte, with CAN communication capability, was used for current measurement. The reason for using CAN communication was the increasing amount of required communication data along with the development of automobile electronics, while the reliability requirements for data transmission are becoming stricter.

There were no boards available for direct temperature measurement, hence thermistor voltage readouts were converted into temperature data in Simulink via respective LUTs. Figure 6.4 presents the results of the scaled BMS setup and the HIL system setup in comparison with the measurements and reference data.

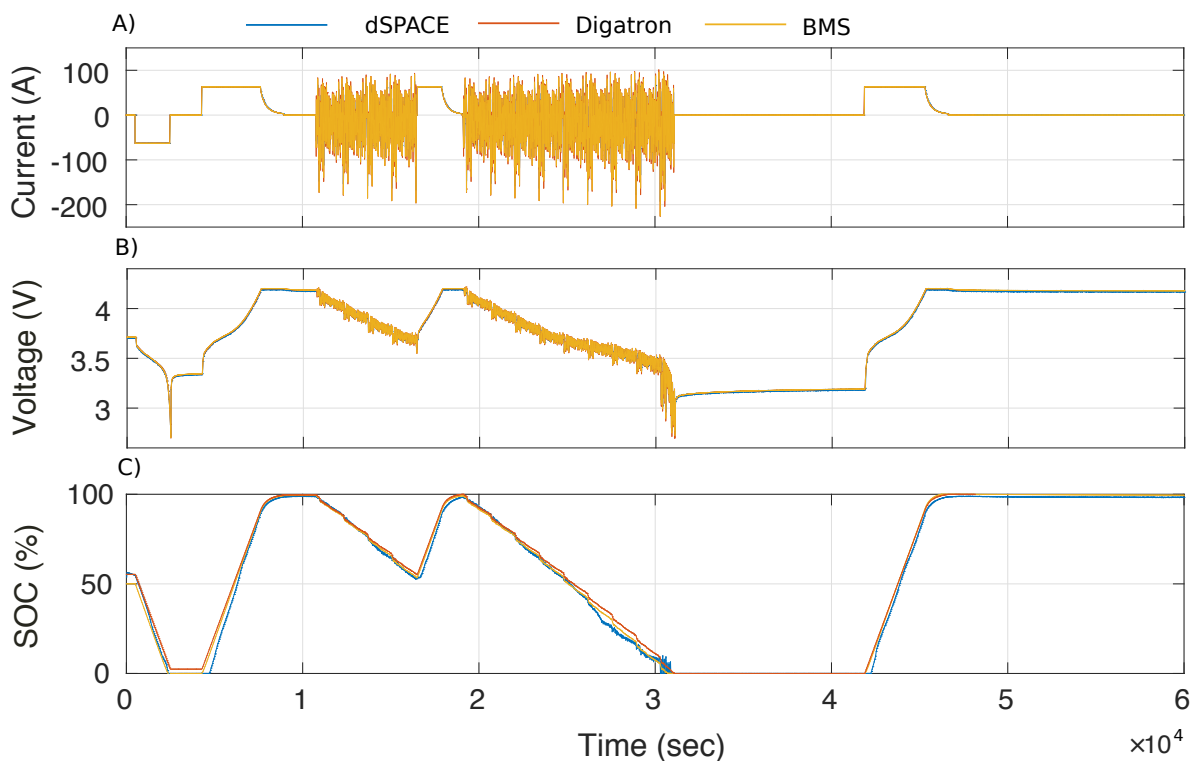


Figure 6.4: A) A comparison between the battery current measurement by the BMS, HIL system, and Digatron tester, B) Cell voltage simulation by the BMS, HIL system, and sensor measurement, C) A comparison between the estimated SOC by the BMS, HIL system and reference SOC (Ah counter of the Digatron battery tester)

In Figure 6.4 A, Digatron current was considered as the reference, and the current measurement from the BMS, and HIL system were evaluated. Figure 6.4 B, presents the real-time simulated cell terminal voltage for the BMS, and HIL system. The reference SOC in Figure 6.4 C was calculated via the Ah-counting method of the Digatron current measurement. Both BMS and HIL system used EKF for SOC estimation. Although both BMS and HIL system used EKF for the SOC estimation, to observe the effect of online EKF tuning during the experiment, the EKF tuning parameters for the HIL system were manually varied.

As was explained before, the model used for the BMS was similar to the model used for the HIL system, however, the BMS system used an approximated discretized model while the real-time HIL system directly used the compiled Simulink model. This could lead to some differences in the results between the two platforms. The developed algorithms were proved to be robust and accurate on both platforms. A closeup of the results is presented in Figure 6.5.

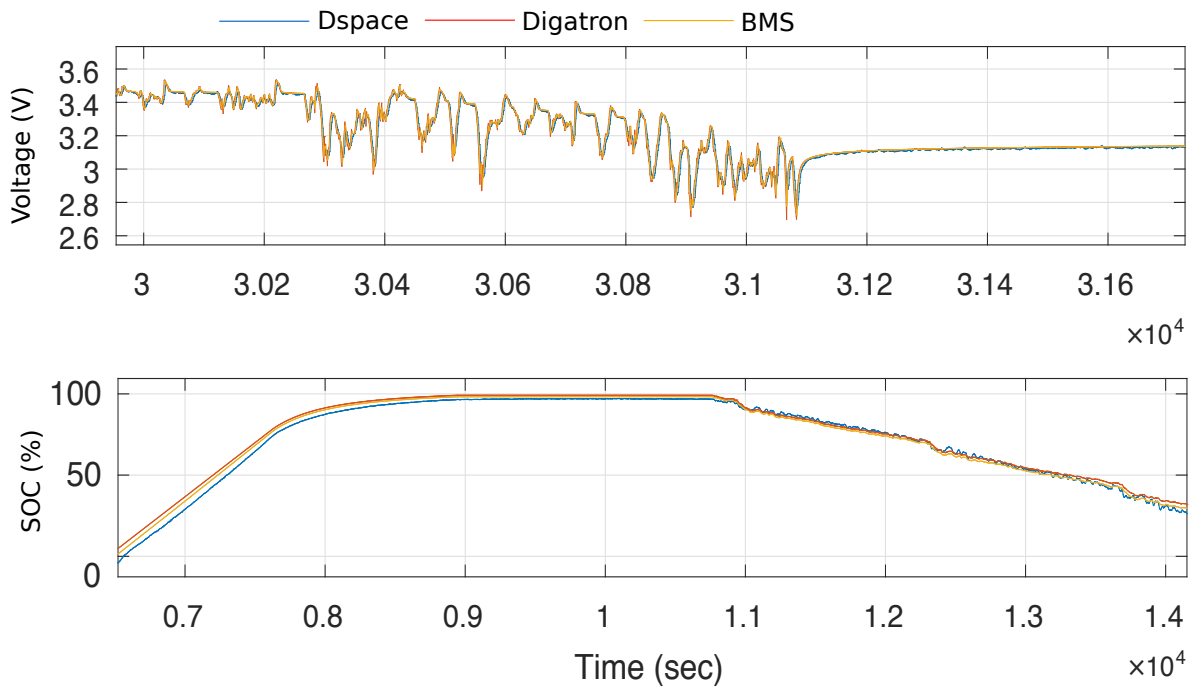


Figure 6.5: Results zoomed from Figure 6.4. A) Terminal voltage model estimated by the BMS vs. the HIL and was compared to the reference measured voltage by the Digatron battery tester voltage sensor, B) The estimated SOC comparison between the BMS, HIL and the reference SOC

The next section presents the cell-level upscaled modeling results to present the pack-level simulation.

6.3 Advanced battery pack simulation

There is not much literature available on monitoring the battery pack itself. In [239], an ECM model combined with an EKF has been proposed for monitoring the pack; however, the error of SOC estimation was about 4%, and no information about the pack parameters was available. In [203], an EKF has been introduced among the successful methods to be used for the (H)EV's BMS. At the moment, 2D and 3D models are rarely used for EV/HEV/PHEV (XEV) applications.

In [163], authors modeled a 21.3 kWh HEV LIB pack. The proposed model contains constant param-

eters. This simplified model provides only the simulated pack voltage and SOC. Authors verified the results by charging and discharging pulses at room temperature, while no aging-, and safety-related information can be obtained from this model.

Battery pack models can be used to serve several tasks. They are included in the overall simulation of the EV, which is composed of the gear system, AD/DC inverters, DC/DC converters, recuperation system, and E-motor. Another usage of the battery pack model is in monitoring of the individual cells, power prediction, state detection, and assuring the safety of the system. The third usage of the battery pack model is sizing and design optimization to avoid over-engineering. The simulated battery pack in this work was a 400 V pack with an energy content of 50.3 kWh provided by 216 high-power NMC Kokam cells (63 Ah capacity). The cells had a 10S2P configuration. Figure 6.6 demonstrates a general schematic of the pack's signal flow used for the modeling.

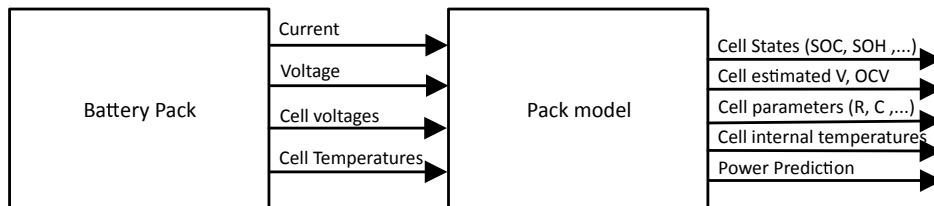


Figure 6.6: General schematic of the pack's signal flow used for the modeling

The LIB pack is the most expensive component of the EV. Therefore, instead of the aging investigation of the LIB pack, which demands a lot of resources, this investigation has been reduced to the cell-level investigation under various operational conditions. This helps to find the optimum operational conditions for the LIB pack. The pack had similar cells used for the cell-level aging investigation presented in Section 3.4.

The LIB pack with the help of the BMS must operate in an optimum range that satisfies all the required automotive safety standard (or the automotive safety integrity level (ASIL)). Desirable parameters to be obtained from the pack simulation are the individual cell SOCs, SOHs, temperatures, and other parameters like OCVs or resistances used for power calculations. The next section presents the cell-level upscaling results to model the LIB pack.

6.3.1 Upscaling and battery pack simulation

A battery pack without BMS is exposed to several issues such, as non-uniform cell aging and serious safety issues, which could lead to a critical hazard levels (HL). Most battery packs contain several cells in series to reach the desired voltage level as well as cells in parallel to reach the desired capacity. Big-cell (see Figure 6.9 A) in this thesis refers to a parallel connection of two cells. In a battery pack, there is a high possibilities that the cells become imbalanced (due to aging or other factors). Over-discharge or over-charge can occur due to the voltage difference of the imbalanced cells.

The currently available BMSs employ low-order ECMs or fractional models, which are parameterized using time-domain, frequency-domain, or in-situ experimental data [31]. At present, only a few off-the-shelf commercially available BMSs are fully programmable by the user, and the rest can not be fully adapted to the battery pack developed in-house. The BMS of the EVA was programmed by Sensortechnik Wiedemann (STW Germany). This BMS was responsible for supervision and safety control of 216 cells; however, it was not possible to flash the hardware with the in-house developed software, which posed significant limitations.

Models and algorithms introduced in this work can be adapted to any battery pack with different cells or form factors. For modeling and simulation, the inputs into the system model are the pack current, pack response-voltage, and the big-cells voltages in the series connection. A schematic of the pack and its BMS is shown in Figure 6.7.

The EVA BMS had a decentralized architecture of BMS master and slaves. Individual cell monitoring and balancing were performed by the BMS slave. Each slave was responsible for monitoring 2 stacks, each stack has a 6S2P configuration. This means, in total 24 cells were monitored by each slave; however, because of the big-cell configuration, only 12 voltages have been monitored.

The Master-slave communication was done through four CAN interfaces. The BMS master could receive preprocessed information from each slave. The preprocessed information from the BMS slave was used for monitoring LIB safety and other tasks, such as data logging or range estimation.

In this study, the battery pack was simulated by upscaling the cell model in Matlab/Simulink. The pack had 18 stacks in the high-level Simulation model, as shown in Figure 6.8 A. Figure 6.8 B, presents the top-layer stack simulation inputs/outputs.

In the mid-level simulation, there were six big-cells in each stack (a total number of 12 cells in each stack); each big-cell model block consisted of some sub-block models that were located in the low-level simulation model. Each big-cell had twice the single-cell capacity. To model the big-cell, half of the current was assumed to flow into each cell.

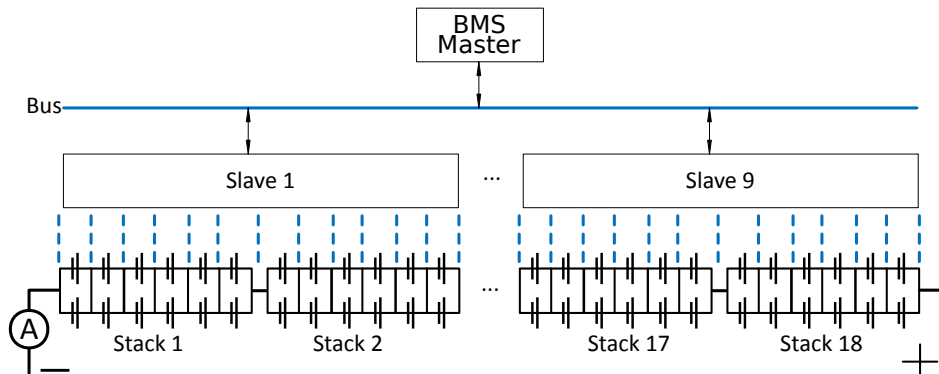


Figure 6.7: Battery pack configuration, including one BMS master and nine BMS slaves. There is one slave for every two stacks (a total of 18 stacks with a configuration of 6S2P)

Figure 6.9 B shows how the low-level simulation blocks interact with each other (in some cases, the blocks are coupled). For instance, the ECM model and the TECM have been coupled. With this modeling scheme, further development is also possible. For instance, by coupling the EKF with the ECM in such a way that the EKF calculates the SOC for the ECM, and at the same time, the ECM updated parameters are returned to the EKF.

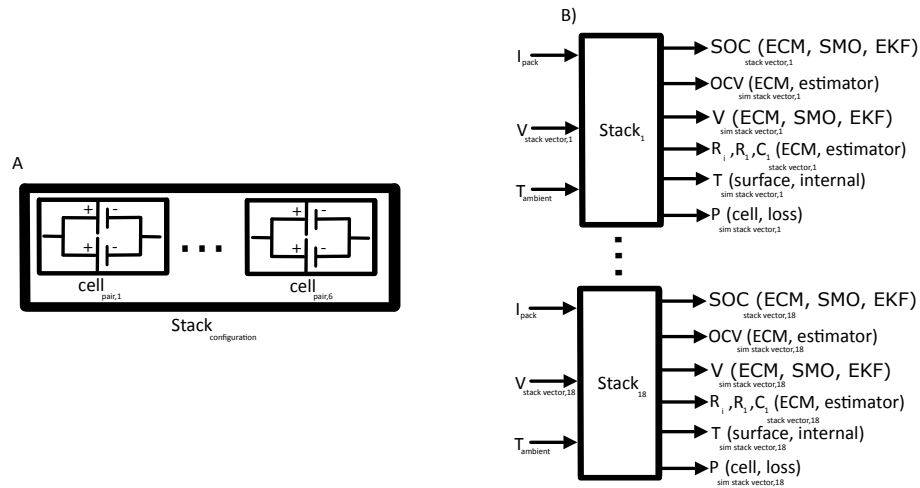


Figure 6.8: A) Stack simulation (high-level simulation) block configuration, B) Battery pack top-layer stack simulation inputs/outputs (the simulated pack voltage is the summation of all 18 stacks' simulated voltages)

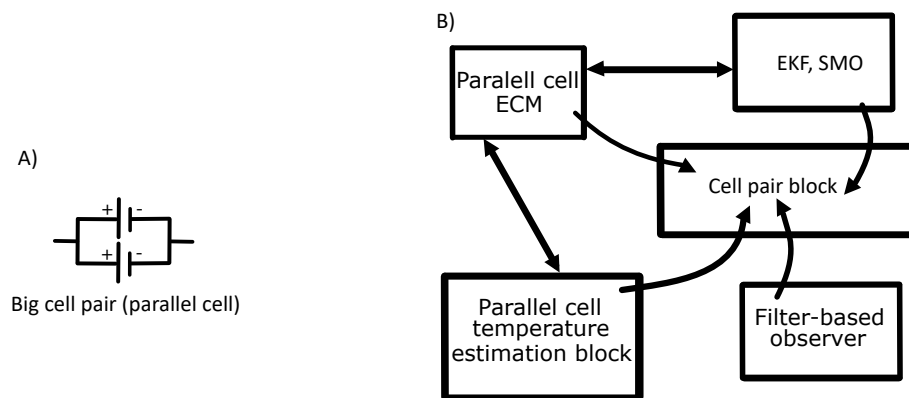


Figure 6.9: A) A big-cell (parallel cell) block used to simulate two parallel cells (mid-level simulation), B) In each big-cell block, there exists a big-cell enhanced ECM model, TECM for parallel cells, filter-based method block, SMO and EKF block (low level simulation)

Another advantage of the pack modeling is that a virtual fault can be examined and simulated on any cell, and the model response can be observed. Different types of faults can be simulated in the battery pack, for instance, short circuit or the drastic changes of the internal resistance due to accelerated aging, loose connections, or other failures. In fault case simulation, if the model assumption is based on the big-cell architecture, the fault location can only be found for the faulty big-cell, and the model is unable to predict, on which cell the fault has happened. Fault simulation has not been performed but can be considered for further development.

The cells in the battery pack are not identical; external/internal operating conditions lead to cell-to-cell discrepancies. Cell variations could result from the manufacturing process, or from the external hot spots affecting the certain cells in the pack. Sudden failures, among other influences, cause different behavior among the cells.

The battery pack measurement data were gathered from CAN interface. Two scenarios have been used to evaluate the battery pack model. The first scenario evaluated the pack modeling results under CC

load profile as presented in Section 6.3.2. The second scenario evaluated the battery pack modeling performance under dynamic drive-cycle current profile as presented in Section 6.3.3. In both cases, no temperature data were available from the measurement, so the pack temperature data shown in this part were sensor-less estimation (for both surface and core temperatures). This work demonstrates the simulation method for estimating the SOC for individual cells in the battery pack and the overall battery pack SOC, considering the cell-to-cell variations as well as the temperature differences between the cells. This method could lead to better utilization of the storage system and provide safe, optimized, and reliable operation of the cells.

6.3.2 Battery pack modeling under constant current profile

The battery pack model was composed of 108 ECMs, because the battery pack topology was 108S2P, each ECM representing a parallel connection of two cells (see Figure 6.7). Ideally, half of the total current flows into each cell in the parallel connection. This is true only, when the impedances of the cells in the parallel connection are equal. Because of the manufacturing inconsistencies and unique performance characteristics of individual cells in the battery pack, cells impedance behavior might not be identical. If due to the design requirements, a big-cell configuration is required, selecting similar cells is beneficial.

The EVA pack voltage range was 367.2 to 453.6 V, and the capacity was approximately 126 Ah. In the first scenario, the LIB pack was charged with the CCCV method and discharged with the CC method. In the second case, the pack was charge with CCCV method, but discharged under a real drive-cycle load profile to evaluate the pack in a more realistic condition.

In this section, models and algorithms have been used to simulate the pack under more realistic drive-cycles. However, most algorithms and observers may suffer from inaccuracy or slow converging speeds during non-dynamic conditions, such as during constant current charging and discharging.

In the EV case, the load profile during the city driving is mostly dynamic, so the algorithms work more precisely during the driving periods (dynamic discharging plus recuperation charging). In this test, the 400 V LIB pack was tested with a Digatron pack tester at room temperature (25°C). The current profile for the first test is shown in Figure 6.10. The battery pack was charged from an initial OCV of 389 V (ideally, 3.6 V per cell) with 60 A for the first 90 minutes in the CC mode ($1C \cong 126$ A); then the voltage was kept constant at 446.5 V for 20 minutes in the CV phase (ideally, 4.134 V per cell).

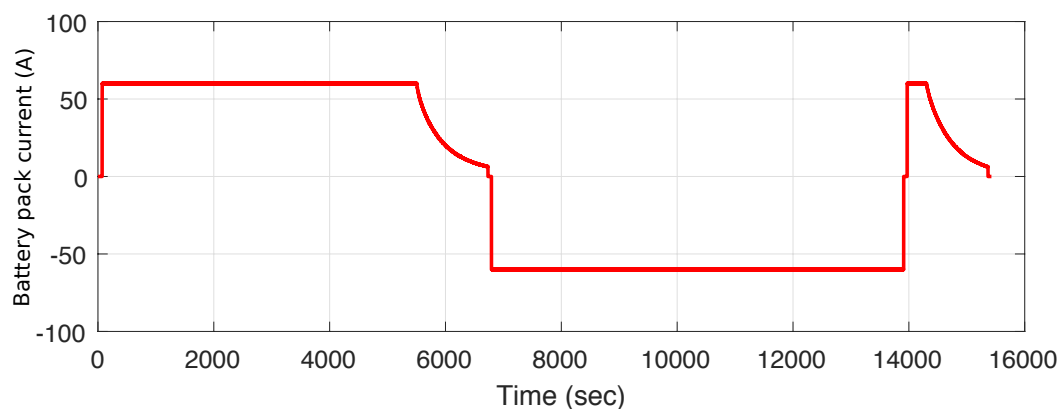


Figure 6.10: Battery pack current measured by the BMS

The voltage response of the weakest and the strongest cells have been measured and are shown in

Figure 6.11. A close look into the weakest and strongest big cell voltage during the CV phase revealed that, before the injection of the charging current, the weakest cell voltage was measured at 3.587 V and the strongest cell was measured at 3.609 V. So the cells have not been balanced properly. During the CV phase, the voltage difference between the strongest cell and the weakest cell was about 51 mV (4.156 V vs. 4.105 V). The voltage difference reached about 250 mV at the end of the discharge when the battery pack reached 356.3 V (the pack was considered fully discharged at 291.6 V). To avoid a deep discharge, the pack was charged for 5 minutes at 60 A. The resting voltage difference was measured at 25 mV between the weakest cell and the strongest cell.

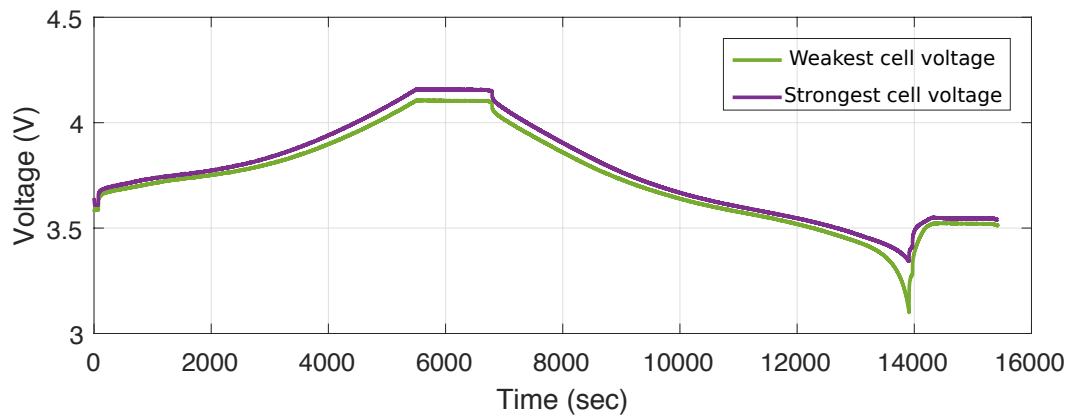


Figure 6.11: Battery pack weakest-cell voltage vs. strongest-cell voltage

Figure 6.12 presents the simulation results for the LIB pack. The upscaled ECM model was controlled with a P-controller. The simulation error for this scenario was less than 0.5% full range.

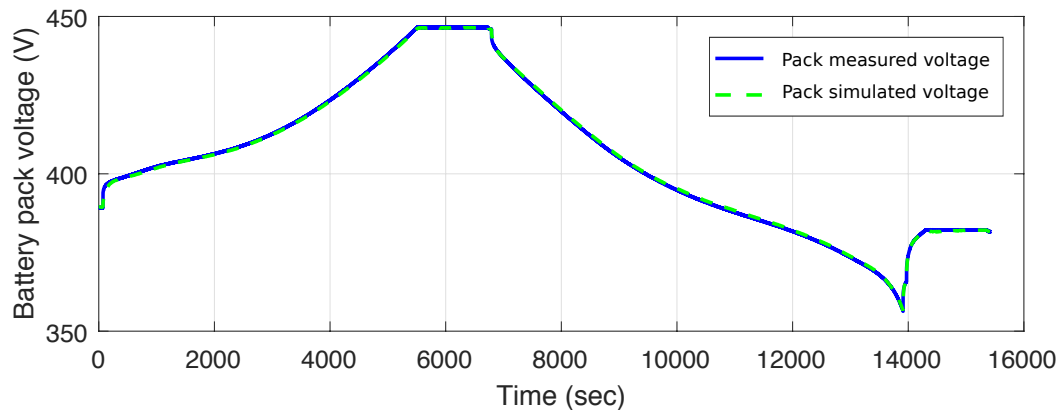


Figure 6.12: Battery pack measured voltage vs. battery pack simulated voltage as the sum of the simulation of 108 big-cells (two parallel cells)

The next section presents the second scenario for the LIB pack modeling.

6.3.3 Battery pack modeling under dynamic drive-cycle current profile

In the second scenario, the battery pack was tested with the dynamic profile known as the Sg taxi drive-cycle. At the beginning of the test, the battery pack had an initial SOC of about 5%. A big-cell level voltage was estimated by dividing the pack voltage by the total number of the cells in series (108s). Then, by using a cell OCV-SOC LUT, the initial SOC of the LIB pack was estimated. However, it is important to measure the pack OCV in a separate experiment.

The pack current is shown in Figure 6.13 A. At first, the battery pack was charged in CC mode with 60 A for about 118 minutes to 447 V and for 13.5 minutes in CV mode until the pack current dropped to 6.5 A at about 96% SOC. Then, the battery pack was given a rest for 1 minute, and the drive-cycle profile discharged the pack to below 380 V in about 10 hours and 42 minutes. For the cells of this LIB pack, the manufacturer recommended a discharge cut-off voltage of 2.7 V. This means that, for a series connection of 108 cells, the LIB pack voltage should not go below 291.6 V. One should always consider a safe operation region for the LIB pack. To consider this safe operating region, all additional system resistances should be taken into account. This includes the voltage drop because of the contact resistances, relays, busbars, and other wiring resistances. In addition to that, according to the development requirement, considering some safety margin is mandatory. In the last step of the test profile, the battery pack was CC-charged at 60 A for 63 minutes until 420 V.

Figure 6.13 B presents the battery pack voltage-response, and the simulated battery pack voltage (indicated by the green dashed line). The battery pack voltage model error is presented in Figure 6.13 C. The error is expressed as an absolute error between the measurement and the model. The peak of absolute error was as high as 2.3 V at the discharging current of 165A. This means that the error bound was $\pm 0.5\%$ or the error was kept within 1% during the CCCV charging and drive-cycle discharging.

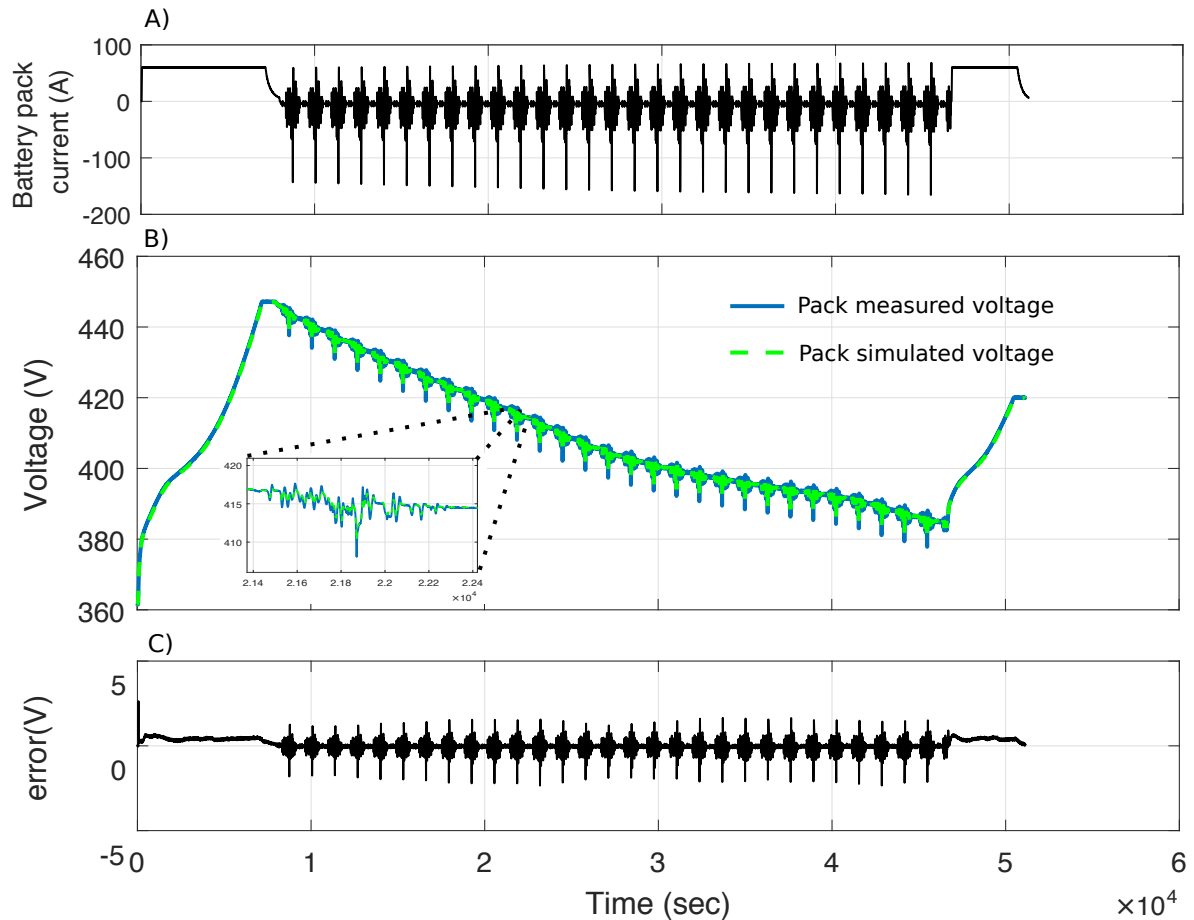


Figure 6.13: A) Battery pack dynamic current, B) Battery pack measured voltage vs. simulated voltage, C) Absolute error of the voltage simulation

The next section presents the results of battery pack thermal modeling (using TECM) and employment of algorithms such as the extended Kalman filter, filter-based method, and the SMO algorithm to compare the performance of each technique in the estimation of parameters and SOC. These algorithms and models were capable of the following:

- Voltage simulation of the cells and the pack
- Parameter estimation of the cells
- SOC estimation of the cells and the pack
- Sensor-less temperature estimation of the cells (surface and core)
- OCV estimation of the cells and the pack
- Power-loss calculation

6.3.4 Battery pack state, parameter, and temperature estimation

In addition to the upscaled ECM model for the LIB pack to model the pack terminal voltage, in order to estimate the temperatures of individual cells within the pack, sensor-less technique has been upscaled as well. The required parameters of the TECM were provided by the ECM model of that specific cell,

and, due to the internal resistance variations between the cells, the amount of heat generation was different for each cell. This led to temperature variations among the cells.

Figure 6.14 A shows the minimum and maximum of the total internal resistances of the cells in the pack due to the current profile shown in Figure 6.13 A. In this figure, the internal resistance value for the cells in the battery pack were in the range of $0.5 \text{ m}\Omega$.

The total cells' ohmic resistance of the battery pack with 108 cells (cell data from the manufacturer data sheet) was approximately $108 * 0.25 \text{ m}\Omega = 27 \text{ m}\Omega$. During the drive-cycle profile, the voltage drop was caused not only by the summation of the cells ohmic resistances, but also the charge transfer resistances, resistances with the longer time constants, and wiring resistance contribute in the total battery pack resistance. The total pack dynamic resistance ($R_{d,pack}$) is shown in Figure 6.14 B. In this figure, simulation results from the parameter estimator and the ECM model are in good agreement.

Figure 6.15 presents the simulation results of the estimated pack OCV. The filter-based OCV estimation returned acceptable and comparable results to the ECM model during the dynamic current range; however, it was unable to track the OCV precisely during CC phases when no dynamic changes were present. During the CC phases, the inputs of the R-observer (current and voltage) were first passed through the HPF, which resulted in the highly attenuated signal around zero. To fix this issue, the filter-based estimator should be combined with the ECM or other techniques. Only to have a comparison between the methods performance, the results of one method has been compared against the other method.

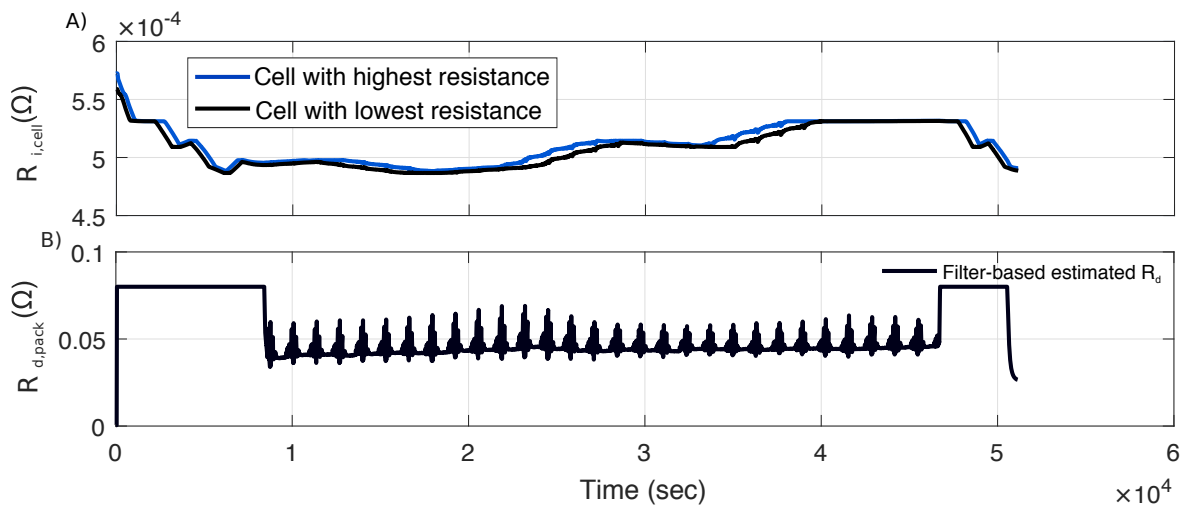


Figure 6.14: A) The cells with the highest and the lowest resistances calculated by the ECM, B) Battery pack's dynamic resistance ($R_{d,pack}$) including 108 cells in series estimated by the filter-based estimator

For BMS implementation, a signal qualifier can be used to evaluate the validity of the measurement, and the modeling performance.

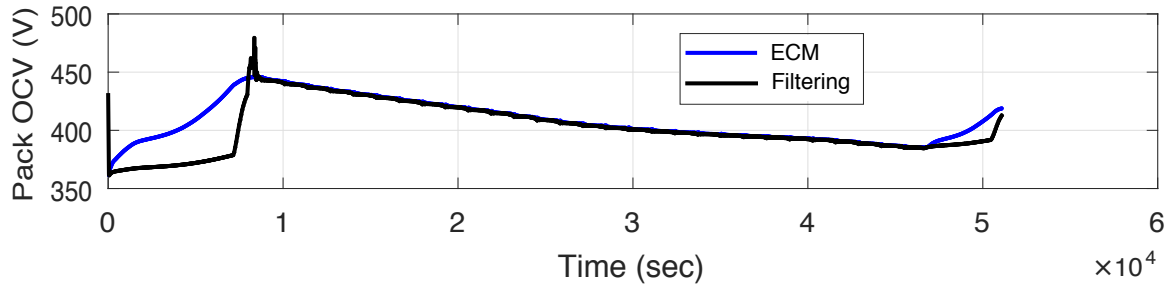


Figure 6.15: Battery pack OCV calculated by the ECM model and the filter-based estimator model (LPF with a time constant of 120 s) during the dynamic load profile presented in Figure 6.13 A

The technique and quality of connecting one cell to another, affects the pack's total resistance. In a battery pack, which contains hundreds up to thousands of cells, bad cell connections affect the efficiency and functionality of the whole system.

Connecting one cell to another, creates a contact resistance. The contact resistance is defined as the interface resistance between the current-carrying members of a device [266]. Cells in the pack can be physically connected to each other via simple screws, laser-beam welding, ultrasonic welding, or resistance spot welding [184]. Welding the cells would introduce contact resistance at the joint parts; this resistance contributes to the Joule heating at the cell terminals and increases the power loss.

Spot welding uses a melting technique. This technique is limited to the thickness of the metal sheets, which makes it impractical for high-current applications, i.e., more than 20 A. On the other hand, laser welding faces great challenges in connecting copper and aluminium (Cu-Al) materials [51].

Ultrasonic welding avoids the defects of spot welding or laser welding, such as brittle phases and porosities in the fusion zone, and it also reduces the formation of intermetallic compounds (IMCs) between dissimilar materials [175, 184]. However, it is reported in [37], the lowest electrical contact resistance and the highest joint strength can be obtained with laser-beam welding, although the difficulties in this process is reported in [51]. Cells in the EVA pack have been welded with ultrasonic technology. During the testing load current shown in Figure 6.13, no hot-spots or unexpected temperatures have been observed. Figure 6.16 presents the sensor-less estimated temperature of the cells. As is apparent in this figure, there was a difference of about 1°C between the cells' estimated core temperature and the estimated surface temperature during 0.5C charging of the battery pack. The surface temperature under the drive-cycle profile was slightly above room temperature. The effect of the driving-cycle test on the temperature profile of the single cell has already been discussed.

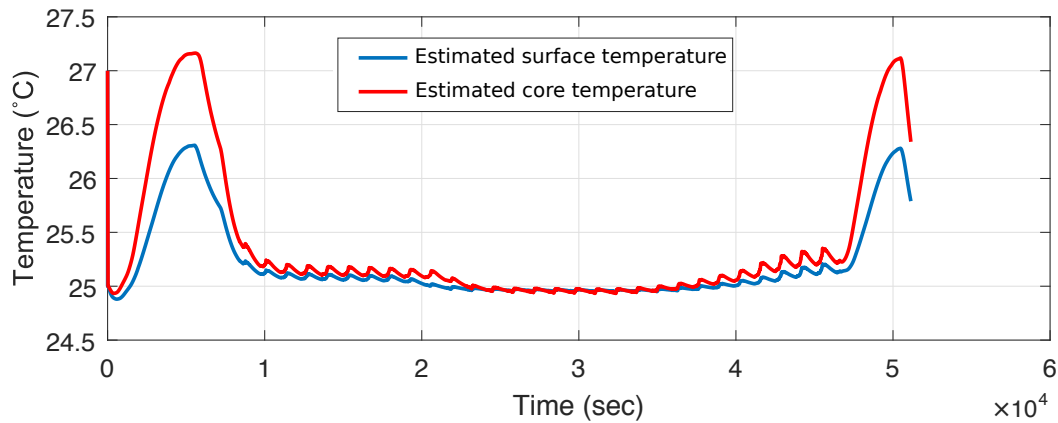


Figure 6.16: The cell-pair with the lowest surface temperature in the pack vs. the estimated core temperature of this cell-pair, resulting from the current profile as shown in Figure 6.13

The LIB pack reference SOC was calculated with the Ah-counting algorithm. This was used as a reference for evaluation of the methods implemented for individual-cell SOC estimation. Based on the current input shown in Figure 6.13 A, the battery pack SOC and the weakest and the strongest cell-pair SOC under the dynamic profile are shown in Figure 6.17. The SOC estimation method for the cell-pairs were based on the EKF in this figure.

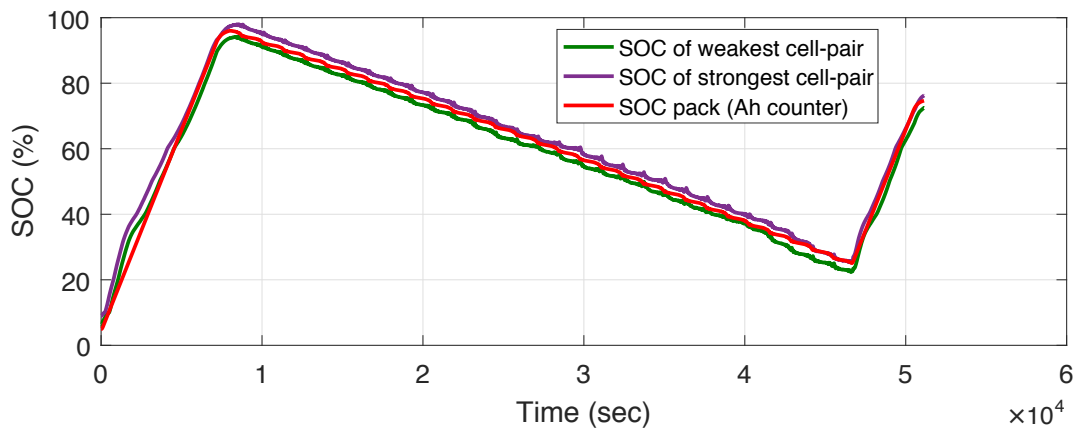


Figure 6.17: The battery pack SOC calculated with the Ah-counting method (reference method) vs. the estimated SOC of the weakest pair and the strongest pair (EKF estimation)

Usually there are SOC limits on the battery pack due to the energy restrictions. For the case of the battery pack, not only the actual cells' SOC are important, but the average and weighted average SOC of the cells should also be registered. Beside that, the minimum and maximum SOC of all cells and their differences should be registered as well. This is because the SOC limits (high and low) of the cells, and SOC distribution are key parameters of the overall performance of the system; hence, these limits are key parameters of the BMS and have to be addressed. Lower SOC limits are critical to ensuring the availability of minimum required discharge power, and higher SOC limits are critical to ensuring the availability of the minimum required charge power.

In this test, the initial SOC of the battery pack was 5%, but the algorithms were manually initialized to SOC = 100%. The reason for that was to observe the voltage and SOC modeling convergence speed and accuracy. It must be mentioned that the battery pack model was developed in such a way that

the model did not require manual initialization. This task was done in an automatic manner, and the model was auto-initialized, based on the OCV-SOC relation. However, to test the algorithms under the most extreme conditions, false initialization was examined. Figure 6.18 presents the minimum and maximum SOC of the cells in the pack, estimated with different techniques.

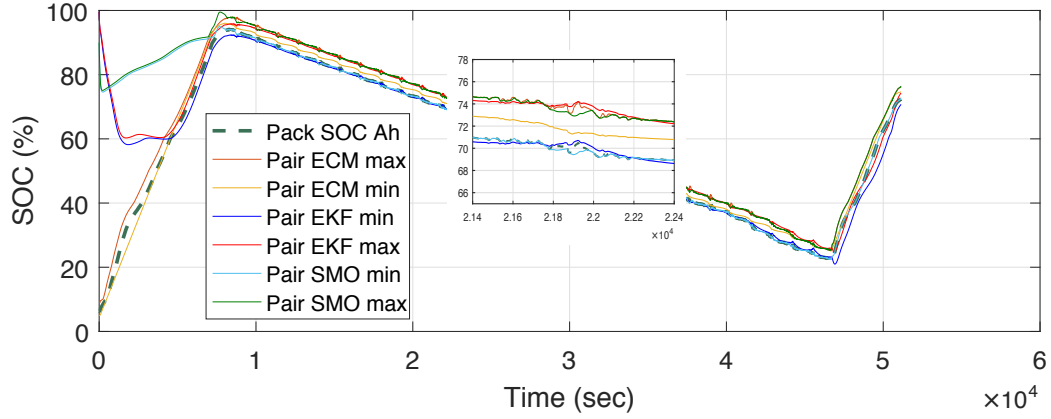


Figure 6.18: Battery pack estimated SOC vs. big-cells SOC estimated with various techniques and different initialization values

In this chapter ECM, TECM, EKF, SMO, and the filter-based algorithms have been implemented and evaluated for a holistic LIB pack model. Further design consideration and improvements have been discussed in depth.

- SOC accuracy in the LIB pack and BMS system:

At high SOC levels, the fast/pulse charging of the LIB pack with relatively high power could lead to high over-voltage. This affects the LIB pack charging capability with the required peak-power charging. The reason for this over-voltage lies in the fact that, during high current phases, the anode voltage might go below 0 V which could lead to Li-plating (in case of lower temperatures). On the other hand, when the LIB has a relatively low SOC, high discharge power for providing the required power for the EV application will violate the lower voltage limit. The reason for that is, at low SOC levels, the number of Li-ions in the anode are limited, and the required ions can not be transferred to the cathode. Hence, the anode-cathode voltage will be reduced sharply to below the lower cut-off voltage. This leads to the technical importance of the SOC for protecting the LIB pack against destructive behavior and accelerated aging.

Similarly to the cells, SOC_{max} is the maximum allowable SOC, if the pack is able to accept the required maximum charging power without the upper-limit violation. SOC_{min} is the minimum SOC that is able to deliver the required discharging power for the application. Considering this definition for maximum and minimum allowable SOC as the requirement for the EV application, the allowable SOC range for the pack lies between these two values and should be calibrated. Another fact that should be pointed out is that, when the pack limits are reached, the cells should still be operating inside the defined voltage and SOC windows, and the voltage and SOC limits of the cells should never be reached before the pack limits.

7 Summary, future work, and outlook

- Summary:

TUM CREATE Phase I, between April 2011 and March 2016 in Singapore, provided the opportunity to accomplish the present work. In Phase I, the focus was set on the field of electric taxi research and development. Over 120 scientists, researchers, and engineers and more than 12 chair professors conducted pioneering research across ten different fields. These included new battery materials and storage, innovative EV designs, low-energy air conditioning, transportation system optimization, and energy storage [1].

This thesis contributed to Research Project 2 (RP2), which dealt with cell-level battery research. Aside from the development and building up of a unique battery laboratory in the South East Asia region, the main scientific contribution of this work comprised of several parts. All these parts were arranged and explained in an orderly manner, covering most requirements and considerations from the cell-level (Li-ion cells) investigation up to the pack-level.

Extensive literature research on the methods for system classification, characterization, and monitoring techniques for both cells and the pack have been presented here. Different testing techniques and industry standards were reviewed, explained, and adjusted for system classification, and various methods for cell characterization were comprehensively described. They included time-domain characterization and frequency-domain characterization of the cells. Time-domain characterization had the advantage of collecting the OCV data together with other cell parameters. This required less data analysis and parameter-extraction effort than the frequency-domain technique. The frequency-domain technique based on EIS experiments provided deeper insight into the electrochemical storage system, while the simulation models based on this technique showed a higher accuracy level at the expense of the more complicated and time-consuming procedure for parameter extraction and model development.

The literature research section was also dedicated to the explanation of different modeling techniques and the state of the art in developing models and monitoring systems. The cell-modeling section includes an explanation of electrical, thermal, and aging models as well as coupling and model upscaling. For electrical models based on the frequency-domain technique, an accuracy of better than 10 mV was achieved, while the accuracy of the simpler time-domain technique was about 20 mV in absolute error. Whereas the frequency-domain models were more accurate, due to the modeling complexities, time-domain-models were selected for further investigation and algorithm development.

A thermal model considering the different heat sources, heat-generation mechanisms, and heat-transfer mechanisms with an absolute temperature error of $\pm 1^\circ C$ was coupled with the electrical model. The thermal model was able to estimate both, surface and core temperatures of the cell, and the temperature-dependent cell parameters were updated accordingly.

Furthermore, main battery states such as SOC and SOH were defined, and the algorithms were explained in detail. Extensive laboratory experiments required for the development of simulation models and monitoring algorithms were conducted in order to create reference data. The experimental section included both, a cycle-life and a calendar-life investigation of the cells at different temperature

levels from 0°C up to 60°C. Additionally, cells were cycled based on the drive-cycle profile to provide a clear understanding between the standard aging experiments based on constant charging and discharging profiles and the drive-cycle profile. Cell-aging data were analyzed, and relevant parameters were extracted. Cell parameters were used to develop the electrical and thermal models alongside the monitoring algorithms. In addition, the extracted parameters were used for state detection. Monitoring algorithms for parameter prediction and state detection are not new topics; however, there are not many consolidated or proven methods publicly available on this topic, and the research findings and publications are limited and case-specific. There are several research papers available on SOC detection and fewer publications on SOH estimation. Nonetheless, there is not a unique, universally-agreed-upon method for state detection. For industry solutions, the current integration technique is widely used for SOC calculation, while SOH detection is usually avoided and is limited to the number of cycles for which the battery is used.

In this work, for monitoring the states and parameter prediction, conventional methods (direct measurement and bookkeeping), learning algorithms (data driven), adaptive filter algorithms (model-based and non-model-based), controllers and observers (linear/nonlinear), and combined (hybrid) methods have been investigated, and the performance of different methods have been evaluated. Some selected algorithms have been developed, and the performance of the algorithms was evaluated and compared under different conditions. The selected methods took advantage of the developed ECM model in combination with conventional models. A hybrid combination of different methods for performance enhancement can be created. The extended Kalman filter, and the sliding mode observer in combination with various observers and controllers such as the PI controller and also the filter-based method have been developed and evaluated.

Models and algorithms have been verified by the real-time HIL system, and implemented in the BMS. These models aid in examining different operation conditions (including environmental and technical requirements). This is useful because real-life testing and measurement can be replaced, and the battery pack can be simulated with the desired current/power and temperature profiles.

In this thesis, similar cells to the EVA battery pack have been examined. The battery pack model included the single-cell models connected in series and parallel through upscaling. This enabled parameter estimation, temperature estimation, and state detection for the individual cell. The battery pack model was evaluated with real experimental data; however, the HIL system setup can be used further, together with the cell-voltage simulator (battery cycler with several channels), for further development and investigation of the pack behavior without the need of testing the real pack.

- Future work and outlook:

There are a few open topics for further discussion and improvement in continuation of this work:

1. Temperature: The work in this thesis was performed in order to address the challenges of monitoring the cells and the battery pack for tropical megacities such as Singapore; hence, harsh temperature conditions were simulated by injecting pulses with extreme amplitude at temperatures of 25°C and above, while low temperatures of 0°C and below should be considered for a comprehensive and detailed study on cell monitoring. At these low temperatures, the performance of the cells is further reduced - this requires further investigation.
2. Charging power: As has been discussed in this thesis, it is necessary that the charging power requirement is fulfilled within the usable SOC range. This requirement can be limited further by other causes, such as Li-plating. The study on development of the monitoring algorithms can be extended to the estimation of charging power and providing optimal maximum charge power to the cells and pack while minimizing the Li-plating.
3. System resistances: During the operation of the LIB pack, it is not sufficient to only consider the electrical characteristics of the cells, as has been shown in this thesis. The reason for this is the additional resistances of the system resulting from usage of other components such as fuses, relays, cell connectors, shunts, busbars, wirings, and other connections in the pack. Each of these components/connections reduces the electrical performance and the usable energy of the pack. These components increase the total electrical resistance. This additional resistance increase affects the monitoring of LIBs such as measured voltages and cell resistances. The BMS has to be programmed in a way so as to compensate for the additional resistance increase and voltage drops.
4. Thermal simulation: As has been described in this work, the heat mechanisms, including heat generation and heat transfer, were only considered for a single cell; however, it is possible to calculate the inner and outer housing temperature together with the cooling system as a source of forced cooling. The implementation of total-system thermal modeling is rather simple and can be implemented with Matlab/Simulink. As this topic was outside the scope of this work, it was not fully developed to represent the thermal model for the whole pack, including its housing and with the cooling system. This added feature could be developed and validated for future work.
5. Upscaling: As already discussed, the production spread for the cells has variations in resistive behavior and available discharge capacity. To compensate for the variations, either the worst-case scenario has to be considered or the production spread has to be defined in more detail, and some boundary conditions should be set for the cells regarding the maximum deviation from the nominal resistances and discharge capacity. The production spread can either be provided by the cell manufacturer or has to be done in-house by performance tests and sorting the cells to be used in the pack. This production spread can be defined by the ratio of measured to nominal resistance for the evaluation of each cell-resistance variation and similarly by the ratio of the measured to nominal discharge capacity of the cells. With this method, the desired boundary for pack design and development of the monitoring algorithms can be defined.

6. Gray box modeling: In this work, the application of the ECM model has been fully studied, and all application possibilities have been discussed. Gray-box models, which requires more detailed knowledge of cell fundamentals, could be the next generation of models to be developed and implemented in the BMS. Fractional models use simplified fundamental cell-governing equations while still being computationally efficient. They can possibly provide more detailed information on aging and safety of the cells to be used in the BMS.

Bibliography

- [1] *EVA by TUM CREATE - Electric Taxi for Tropical Megacities*. Available from: <https://www.nrf.gov.sg/innovation-enterprise/innovative-projects/urban-solutions-and-sustainability/eva-electric-taxi>
- [2] LOCKHEED IDAHO TECHNOLOGIES CO., IDAHO FALLS, ID (UNITED STATES): PNGV battery test manual. 10.2172/578702 DOI, Feb 2001 (Rev. 3). – Technical Report
- [3] Impedance in Electrochemistry—From Analytical Applications to Mechanistic Speculation 2. In: *Vanjsek, P and Hansen, D and Orazem, M* The Electrochemical Society, 2009
- [4] ACUÑA, D. E.; ORCHARD, M. E.: Particle-filtering-based failure prognosis via sigma-points: Application to Lithium-Ion battery State-of-Charge monitoring. In: *Mechanical Systems and Signal Processing* (2017), pp. 827–848
- [5] AFFANNI, A.; BELLINI, A.; CONCARI, C.; FRANCESCHINI, G.; LORENZANI, E.; TASSONI, C.: EV battery state of charge: neural network based estimation. In: *Electric Machines and Drives Conference, 2003. IEMDC'03. IEEE International Bd. 2* IEEE, 2003, pp. 684–688
- [6] ANAND, I.; MATHUR, B.: State of charge estimation of lead acid batteries using neural networks. In: *Circuits, Power and Computing Technologies (ICCPCT), 2013 International Conference on* IEEE, 2013, pp. 596–599
- [7] ANDRE, D.; MEILER, M.; STEINER, K.; WIMMER, C.; SOCZKA-GUTH, T.; SAUER, D.: Characterization of high-power lithium-ion batteries by electrochemical impedance spectroscopy. I. Experimental investigation. In: *Journal of Power Sources* 196 (2011), Nr. 12, 5334 - 5341. <http://dx.doi.org/http://dx.doi.org/10.1016/j.jpowsour.2010.12.102>. – DOI <http://dx.doi.org/10.1016/j.jpowsour.2010.12.102>. – ISSN 0378–7753
- [8] ANDRE, D.; NUHIC, A.; SOCZKA-GUTH, T.; SAUER, D.: Comparative study of a structured neural network and an extended Kalman filter for state of health determination of lithium-ion batteries in hybrid electricvehicles. In: *Engineering Applications of Artificial Intelligence* 26 (2013), Nr. 3, 951 - 961. <http://dx.doi.org/http://dx.doi.org/10.1016/j.engappai.2012.09.013>. – DOI <http://dx.doi.org/10.1016/j.engappai.2012.09.013>. – ISSN 0952–1976
- [9] ANDRE, D.; APPEL, C.; SOCZKA-GUTH, T.; SAUER, D. U.: Advanced mathematical methods of {SOC} and {SOH} estimation for lithium-ion batteries. In: *Journal of Power Sources* 224 (2013), 20 - 27. <http://dx.doi.org/http://dx.doi.org/10.1016/j.jpowsour.2012.10.001>. – DOI <http://dx.doi.org/10.1016/j.jpowsour.2012.10.001>. – ISSN 0378–7753
- [10] ANTON, J. A.; NIETO, P. G.; COS JUEZ, F. de; LASHERAS, F. S.; VEGA, M. G.; GUTIERREZ, M. R.: Battery state-of-charge estimator using the SVM technique. In: *Applied Mathematical Modelling* 37 (2013), Nr. 9, pp. 6244–6253

-
- [11] ANTON, J. C. A.; NIETO, P. J. G.; VIEJO, C. B.; VILÁN, J. A. V.: Support vector machines used to estimate the battery state of charge. In: *IEEE Transactions on Power Electronics* 28 (2013), Nr. 12, pp. 5919–5926
- [12] APPELBAUM, J.; WEISS, R.: An electrical model of the lead-acid battery. In: *Telecommunications Energy Conference, 1982. INTELEC 1982. International IEEE*, 1982, pp. 304–307
- [13] ARULAMPALAM, M. S.; MASKELL, S.; GORDON, N.; CLAPP, T.: A tutorial on particle filters for online nonlinear/non-Gaussian Bayesian tracking. In: *IEEE Transactions on signal processing* 50 (2002), Nr. 2, pp. 174–188
- [14] AUNG, H.; LOW, K. S.; GOH, S. T.: State-of-charge estimation of lithium-ion battery using square root spherical unscented Kalman filter (Sqrt-UKFST) in Nanosatellite. In: *IEEE Transactions on Power Electronics* 30 (2015), Nr. 9, pp. 4774–4783
- [15] AYLOR, J. H.; THIEME, A.; JOHNSO, B.: A battery state-of-charge indicator for electric wheelchairs. In: *IEEE transactions on industrial electronics* 39 (1992), Nr. 5, pp. 398–409
- [16] BAI, G.; WANG, P.; HU, C.; PECHT, M.: A generic model-free approach for lithium-ion battery health management. In: *Applied Energy* 135 (2014), 247 - 260. <http://dx.doi.org/http://dx.doi.org/10.1016/j.apenergy.2014.08.059>. – DOI <http://dx.doi.org/10.1016/j.apenergy.2014.08.059>. – ISSN 0306–2619
- [17] BAKER, D. R.; VERBRUGGE, M. W.: Temperature and Current Distribution in Thin-Film Batteries. In: *Journal of the Electrochemical Society* 146 (1999), Nr. 7, pp. 2413–2424
- [18] BALAGOPAL, B.; CHOW, M.-Y.: The state of the art approaches to estimate the state of health (SOH) and state of function (SOF) of lithium Ion batteries. In: *2015 IEEE 13th International Conference on Industrial Informatics (INDIN)* IEEE, 2015, pp. 1302–1307
- [19] BAO, H.; YU, Y.: State of Charge Estimation for Electric Vehicle Batteries Based on LS-SVM. In: *Intelligent Human-Machine Systems and Cybernetics (IHMSC), 2013 5th International Conference on IEEE*, 2013, pp. 442–445
- [20] BARD, A. J.; FAULKNER, L. R.; LEDDY, J.; ZOSKI, C. G.: *Electrochemical methods: fundamentals and applications*. Bd. 2. Wiley New York, 1980
- [21] BARLOW, T. J.; LATHAM, S.; MCCRAE, I. S.; BOULTER, P. G.: A Reference Book of Driving Cycles for Use in the Measurement of Road Vehicle emissions / TRL Limited. 2009 (Ver. 3). – Project Report
- [22] BARONTI, F.; FANTECHI, G.; FANUCCI, L.; LEONARDI, E.; RONCELLA, R.; SALETTI, R.; SAPONARA, S.: State-of-charge estimation enhancing of lithium batteries through a temperature-dependent cell model. In: *Applied Electronics (AE), 2011 International Conference on IEEE*, 2011, pp. 1–5
- [23] BARSOUKOV, E.; KIM, J. H.; YOON, C. O.; LEE, H.: Universal battery parameterization to yield a non-linear equivalent circuit valid for battery simulation at arbitrary load. In: *Journal of Power Sources* 83 (1999), Nr. 1–2, 61 - 70. [http://dx.doi.org/http://dx.doi.org/10.1016/S0378-7753\(99\)00257-8](http://dx.doi.org/http://dx.doi.org/10.1016/S0378-7753(99)00257-8). – DOI [http://dx.doi.org/10.1016/S0378-7753\(99\)00257-8](http://dx.doi.org/10.1016/S0378-7753(99)00257-8). – ISSN 0378–7753

- [24] BARSUKOV, E.; MACDONALD, J.: Impedance Spectroscopy: Theory, Experiment, and Application. In: *2nd edition Wiley-Interscience* (2005)
- [25] BELT, J. R.: Battery Test Manual For 12 Volt Start/Stop Hybrid Electric Vehicles / Idaho National Lab. (INL), Idaho Falls, ID (United States). 10.2172/1186741 DOI, May 2015 (Rev. 1). – Technical Report
- [26] BERECIBAR, M.; GANDIAGA, I.; VILLARREAL, I.; OMAR, N.; MIERLO, J. V.; BOSSCHE, P. V.: Critical review of state of health estimation methods of Li-ion batteries for real applications. In: *Renewable and Sustainable Energy Reviews* 56 (2016), 572 - 587. <http://dx.doi.org/http://dx.doi.org/10.1016/j.rser.2015.11.042>. – DOI <http://dx.doi.org/10.1016/j.rser.2015.11.042>. – ISSN 1364-0321
- [27] BERGVELD, H.: *Battery Management Systems, Design by Modeling*, University Twente, Diss., 2001
- [28] BERNARDI, D.; PAWLIKOWSKI, E.; NEWMAN, J.: A General Energy Balance for Battery Systems. In: *Journal of The Electrochemical Society* 132 (1985), Nr. 1, pp. 5
- [29] BERNARDI, D. M.; GU, H.; SCHOENE, A. Y.: Two-Dimensional Mathematical Model of a Lead-Acid Cell. In: *Journal of The Electrochemical Society* 140 (1993), Nr. 8, pp. 2250–2258
- [30] BHATIKAR, S.; MAHAJAN, R.; WIPKE, K.; JOHNSON, V.: Neural network based energy storage system modeling for hybrid electric vehicles. In: *National Renewable Energy Laboratory* (1999), pp. 1–43
- [31] BIZERAY, A.; ZHAO, S.; DUNCAN, S.; HOWEY, D.: Lithium-ion battery thermal-electrochemical model-based state estimation using orthogonal collocation and a modified extended Kalman filter. In: *Journal of Power Sources* 296 (2015), 400 - 412. <http://dx.doi.org/http://dx.doi.org/10.1016/j.jpowsour.2015.07.019>. – DOI <http://dx.doi.org/10.1016/j.jpowsour.2015.07.019>. – ISSN 0378-7753
- [32] BLAIFI, S.; MOULAHOU, S.; COLAK, I.; MERROUCHE, W.: An enhanced dynamic model of battery using genetic algorithm suitable for photovoltaic applications. In: *Applied Energy* 169 (2016), 888 - 898. <http://dx.doi.org/http://dx.doi.org/10.1016/j.apenergy.2016.02.062>. – DOI <http://dx.doi.org/10.1016/j.apenergy.2016.02.062>. – ISSN 0306-2619
- [33] BOHLEN, O.: *Impedance-based battery monitoring*, Ph. D. Dissertation, RWTH Aachen, Aachen, Germany, Diss., 2008
- [34] BOHLEN, O.; KOWAL, J.; SAUER, D. U.: Ageing behaviour of electrochemical double layer capacitors: Part II. Lifetime simulation model for dynamic applications. In: *Journal of Power Sources* 173 (2007), Nr. 1, 626 - 632. <http://dx.doi.org/http://dx.doi.org/10.1016/j.jpowsour.2007.07.059>. – DOI <http://dx.doi.org/10.1016/j.jpowsour.2007.07.059>. – ISSN 0378-7753
- [35] BONANNO, F.; CAPIZZI, G.; NAPOLI, C.: Hybrid neural networks architectures for soc and voltage prediction of new generation batteries storage. In: *IEEE international conference on clean electrical power (ICCEP)* IEEE, 2011, pp. 341–344

- [36] BOTTE, G. G.; WHITE, R. E.; ZHANG, Z.: Thermal stability of LiPF₆-EC:EMC electrolyte for lithium ion batteries. In: *Journal of Power Sources* 97–98 (2001), 570 - 575. [http://dx.doi.org/http://dx.doi.org/10.1016/S0378-7753\(01\)00746-7](http://dx.doi.org/http://dx.doi.org/10.1016/S0378-7753(01)00746-7). – DOI [http://dx.doi.org/10.1016/S0378-7753\(01\)00746-7](http://dx.doi.org/10.1016/S0378-7753(01)00746-7). – ISSN 0378-7753. – Proceedings of the 10th International Meeting on Lithium Batteries
- [37] BRAND, M. J.; SCHMIDT, P. A.; ZAEH, M. F.; JOSSEN, A.: Welding techniques for battery cells and resulting electrical contact resistances. In: *Journal of Energy Storage* 1 (2015), 7 - 14. <http://dx.doi.org/http://dx.doi.org/10.1016/j.est.2015.04.001>. – DOI <http://dx.doi.org/10.1016/j.est.2015.04.001>. – ISSN 2352-152X
- [38] BUCHMANN, I.: *Types of Lithium-ion*. https://batteryuniversity.com/learn/article/types_of_lithium_ion. Version: 2018, Abruf: 2019-03-13
- [39] BULLER, S.: *Impedance-based simulation models for energy storage devices in advanced automotive applications*, Ph. D. Dissertation, RWTH Aachen, Aachen, Germany, Diss., 2003
- [40] BULLER, S.: Impedance based simulation models for energy storage devices in advanced automotive power systems. Aachen : Shaker, 2003, pp. 138 S. : Ill., graph. Darst.
- [41] BURGOS, C.; SÁEZ, D.; ORCHARD, M. E.; CÁRDENAS, R.: Fuzzy modelling for the state-of-charge estimation of lead-acid batteries. In: *Journal of Power Sources* 274 (2015), 355 - 366. <http://dx.doi.org/http://dx.doi.org/10.1016/j.jpowsour.2014.10.036>. – DOI <http://dx.doi.org/10.1016/j.jpowsour.2014.10.036>. – ISSN 0378-7753
- [42] CAI, C. H.; DU, D.; LIU, Z. Y.: Battery state-of-charge (SOC) estimation using adaptive neuro-fuzzy inference system (ANFIS). In: *Fuzzy Systems, 2003. FUZZ '03. The 12th IEEE International Conference on* Bd. 2 IEEE, 2003, pp. 1068–1073
- [43] CAI, L.; WHITE, R. E.: Mathematical modeling of a lithium ion battery with thermal effects in {COMSOL} Inc. Multiphysics (MP) software. In: *Journal of Power Sources* 196 (2011), Nr. 14, 5985 - 5989. <http://dx.doi.org/http://dx.doi.org/10.1016/j.jpowsour.2011.03.017>. – DOI <http://dx.doi.org/10.1016/j.jpowsour.2011.03.017>. – ISSN 0378-7753
- [44] CANNARELLA, J.; ARNOLD, C. B.: State of health and charge measurements in lithium-ion batteries using mechanical stress. In: *Journal of Power Sources* 269 (2014), 7 - 14. <http://dx.doi.org/http://dx.doi.org/10.1016/j.jpowsour.2014.07.003>. – DOI <http://dx.doi.org/10.1016/j.jpowsour.2014.07.003>. – ISSN 0378-7753
- [45] CANNARELLA, J.; ARNOLD, C. B.: Stress evolution and capacity fade in constrained lithium-ion pouch cells. In: *Journal of Power Sources* 245 (2014), 745 - 751. <http://dx.doi.org/http://dx.doi.org/10.1016/j.jpowsour.2013.06.165>. – DOI <http://dx.doi.org/10.1016/j.jpowsour.2013.06.165>. – ISSN 0378-7753
- [46] CHANG, W.-Y.: The state of charge estimating methods for battery: a review. In: *ISRN Applied Mathematics* 2013 (2013)
- [47] CHARKHGARD, M.; FARROKHI, M.: State-of-charge estimation for lithium-ion batteries using neural networks and EKF. In: *IEEE transactions on industrial electronics* 57 (2010), Nr. 12, pp. 4178–4187

- [48] CHATURVEDI, N. A.; KLEIN, R.; CHRISTENSEN, J.; AHMED, J.; KOJIC, A.: Algorithms for advanced battery-management systems. In: *IEEE Control Systems* 30 (2010), Nr. 3, pp. 49–68
- [49] CHAU, K.; WU, K.; CHAN, C.; SHEN, W.: A new battery capacity indicator for nickel–metal hydride battery powered electric vehicles using adaptive neuro-fuzzy inference system. In: *Energy Conversion and Management* 44 (2003), Nr. 13, 2059 - 2071. [http://dx.doi.org/http://dx.doi.org/10.1016/S0196-8904\(02\)00249-2](http://dx.doi.org/http://dx.doi.org/10.1016/S0196-8904(02)00249-2). – DOI [http://dx.doi.org/10.1016/S0196-8904\(02\)00249-2](http://dx.doi.org/10.1016/S0196-8904(02)00249-2). – ISSN 0196–8904
- [50] CHEN, K.; UNSWORTH, G.; LI, X.: Measurements of heat generation in prismatic Li-ion batteries. In: *Journal of Power Sources* 261 (2014), 28 - 37. <http://dx.doi.org/http://dx.doi.org/10.1016/j.jpowsour.2014.03.037>. – DOI <http://dx.doi.org/10.1016/j.jpowsour.2014.03.037>. – ISSN 0378–7753
- [51] CHEN, K.; ZHANG, Y.: Mechanical analysis of ultrasonic welding considering knurl pattern of sonotrode tip. In: *Materials Design* 87 (2015), 393 - 404. <http://dx.doi.org/http://dx.doi.org/10.1016/j.matdes.2015.08.042>. – DOI <http://dx.doi.org/10.1016/j.matdes.2015.08.042>. – ISSN 0264–1275
- [52] CHEN, M.; RINCON-MORA, G. A.: Accurate electrical battery model capable of predicting runtime and IV performance. In: *IEEE transactions on energy conversion* 21 (2006), Nr. 2, pp. 504–511
- [53] CHEN, X.; SHEN, W.; CAO, Z.; KAPOOR, A.: Adaptive gain sliding mode observer for state of charge estimation based on combined battery equivalent circuit model. In: *Computers Chemical Engineering* 64 (2014), 114 - 123. <http://dx.doi.org/http://dx.doi.org/10.1016/j.compchemeng.2014.02.015>. – DOI <http://dx.doi.org/10.1016/j.compchemeng.2014.02.015>. – ISSN 0098–1354
- [54] CHEN, Y.; LONG, B.; LEI, X.: The battery state of charge estimation based weighted least squares support vector machine. In: *Power and Energy Engineering Conference (APPEEC), 2011 Asia-Pacific IEEE, 2011*, pp. 1–4
- [55] CHEN, Y.; EVANS, J. W.: Three-Dimensional Thermal Modeling of Lithium-Polymer Batteries under Galvanostatic Discharge and Dynamic Power Profile. In: *Journal of the Electrochemical Society* 141 (1994), Nr. 11, pp. 2947–2955
- [56] CHEN, Z. u. a.: Bayesian filtering: From Kalman filters to particle filters, and beyond. In: *Statistics* 182 (2003), Nr. 1, pp. 1–69
- [57] CHEN, Z.; QIU, S.; MASRUR, M. A.; MURPHEY, Y. L.: Battery state of charge estimation based on a combined model of extended Kalman filter and neural networks. In: *Neural Networks (IJCNN), The 2011 International Joint Conference on IEEE, 2011*, pp. 2156–2163
- [58] CHO, S.; JEONG, H.; HAN, C.; JIN, S.; LIM, J. H.; OH, J.: State-of-charge estimation for lithium-ion batteries under various operating conditions using an equivalent circuit model. In: *Computers Chemical Engineering* 41 (2012), 1 - 9. <http://dx.doi.org/http://dx.doi.org/10.1016/j.compchemeng.2012.02.003>. – DOI <http://dx.doi.org/10.1016/j.compchemeng.2012.02.003>. – ISSN 0098–1354

- [59] CHRISTOPHERSEN, J. P.: U.S. Department of Energy Vehicle Technologies Program: Battery Test Manual For Plug-In Hybrid Electric Vehicles / Idaho National Laboratory (INL). 10.2172/1169249 DOI, Sep 2014 (Rev. 3). – Technical Report
- [60] CHRISTOPHERSEN, J. P.: Battery Test Manual For Electric Vehicles / Idaho National Lab. (INL), Idaho Falls, ID (United States). 10.2172/1186745 DOI, June 2015 (Rev. 3). – Technical Report
- [61] CODECA, F.; SAVARESI, S. M.; RIZZONI, G.: On battery state of charge estimation: A new mixed algorithm. In: *2008 IEEE International Conference on Control Applications* IEEE, 2008, pp. 102–107
- [62] COLEMAN, M.; LEE, C. K.; ZHU, C.; HURLEY, W. G.: State-of-charge determination from EMF voltage estimation: Using impedance, terminal voltage, and current for lead-acid and lithium-ion batteries. In: *IEEE Transactions on industrial electronics* 54 (2007), Nr. 5, pp. 2550–2557
- [63] CUMA, M. U.; KOROGLU, T.: A comprehensive review on estimation strategies used in hybrid and battery electric vehicles. In: *Renewable and Sustainable Energy Reviews* 42 (2015), 517 - 531. <http://dx.doi.org/http://dx.doi.org/10.1016/j.rser.2014.10.047>. – DOI <http://dx.doi.org/10.1016/j.rser.2014.10.047>. – ISSN 1364–0321
- [64] DAI, H.; GUO, P.; WEI, X.; SUN, Z.; WANG, J.: ANFIS (adaptive neuro-fuzzy inference system) based online SOC (State of Charge) correction considering cell divergence for the EV (electric vehicle) traction batteries. In: *Energy* 80 (2015), 350 - 360. <http://dx.doi.org/http://dx.doi.org/10.1016/j.energy.2014.11.077>. – DOI <http://dx.doi.org/10.1016/j.energy.2014.11.077>. – ISSN 0360–5442
- [65] DAI, H.; WEI, X.; SUN, Z.; WANG, J.; GU, W.: Online cell {SOC} estimation of Li-ion battery packs using a dual time-scale Kalman filtering for {EV} applications. In: *Applied Energy* 95 (2012), 227 - 237. <http://dx.doi.org/http://dx.doi.org/10.1016/j.apenergy.2012.02.044>. – DOI <http://dx.doi.org/10.1016/j.apenergy.2012.02.044>. – ISSN 0306–2619
- [66] DAI, H.; ZHU, L.; ZHU, J.; WEI, X.; SUN, Z.: Adaptive Kalman filtering based internal temperature estimation with an equivalent electrical network thermal model for hard-cased batteries. In: *Journal of Power Sources* 293 (2015), 351 - 365. <http://dx.doi.org/http://dx.doi.org/10.1016/j.jpowsour.2015.05.087>. – DOI <http://dx.doi.org/10.1016/j.jpowsour.2015.05.087>. – ISSN 0378–7753
- [67] DAMAY, N.; FORGEZ, C.; BICHAT, M.-P.; FRIEDRICH, G.: Thermal modeling of large prismatic LiFePO₄/graphite battery. Coupled thermal and heat generation models for characterization and simulation. In: *Journal of Power Sources* 283 (2015), 37 - 45. <http://dx.doi.org/http://dx.doi.org/10.1016/j.jpowsour.2015.02.091>. – DOI <http://dx.doi.org/10.1016/j.jpowsour.2015.02.091>. – ISSN 0378–7753
- [68] DAMBROWSKI, J.: Review on Methods of State-of-Charge Estimation with Viewpoint to the Modern LiFePO₄/Li₄Ti₅O₁₂ Lithium-Ion Systems. In: *INTELEC 2013 - THE 35TH INTERNATIONAL TELECOMMUNICATION ENERGY CONFERENCE*, 2013, pp. 1–6
- [69] DANILOV, D.; NIESSEN, R.; NOTTEN, P.: Modeling all-solid-state Li-ion batteries. In: *Journal of the Electrochemical Society* 158 (2011), Nr. 3, pp. A215–A222

- [70] DEY, S.; AYALEW, B.; PISU, P.: Nonlinear robust observers for state-of-charge estimation of lithium-ion cells based on a reduced electrochemical model. In: *Control Systems Technology, IEEE Transactions on* 23 (2015), Nr. 5, pp. 1935–1942
- [71] DINGER, A.; MARTIN, R.; MOSQUET, X.; RABL, M.; RIZOULIS, D.; RUSSO, M.; STICHER, G.: Batteries for electric cars: Challenges, opportunities, and the outlook to 2020. In: *The Boston Consulting Group* 7 (2010), pp. 2017
- [72] DOYLE, M.; FULLER, T. F.; NEWMAN, J.: Modeling of galvanostatic charge and discharge of the lithium/polymer/insertion cell. In: *Journal of the Electrochemical Society* 140 (1993), Nr. 6, pp. 1526–1533
- [73] DREYER, W.; JAMNIK, J.; GUHLKE, C.; HUTH, R.; MOSKON, J.; GABERSCEK, M.: The thermodynamic origin of hysteresis in insertion batteries. In: *Nature Materials* 9 (2010), Apr., Nr. 5, 448–453. <http://dx.doi.org/10.1038/nmat2730>. – DOI 10.1038/nmat2730. – ISSN 1476–1122
- [74] DU, J.; LIU, Z.; WANG, Y.: State of charge estimation for Li-ion battery based on model from extreme learning machine. In: *Control Engineering Practice* 26 (2014), 11 - 19. <http://dx.doi.org/http://dx.doi.org/10.1016/j.conengprac.2013.12.014>. – DOI <http://dx.doi.org/10.1016/j.conengprac.2013.12.014>. – ISSN 0967–0661
- [75] DU, J.; LIU, Z.; WANG, Y.; WEN, C.: An adaptive sliding mode observer for lithium-ion battery state of charge and state of health estimation in electric vehicles. In: *Control Engineering Practice* 54 (2016), 81 - 90. <http://dx.doi.org/http://dx.doi.org/10.1016/j.conengprac.2016.05.014>. – DOI <http://dx.doi.org/10.1016/j.conengprac.2016.05.014>. – ISSN 0967–0661
- [76] EDDAHECH, A.; BRIAT, O.; BERTRAND, N.; DELÉTAGE, J.-Y.; VINASSA, J.-M.: Behavior and state-of-health monitoring of Li-ion batteries using impedance spectroscopy and recurrent neural networks. In: *International Journal of Electrical Power Energy Systems* 42 (2012), Nr. 1, 487 - 494. <http://dx.doi.org/http://dx.doi.org/10.1016/j.ijepes.2012.04.050>. – DOI <http://dx.doi.org/10.1016/j.ijepes.2012.04.050>. – ISSN 0142–0615
- [77] EDDAHECH, A.; BRIAT, O.; VINASSA, J.-M.: Adaptive voltage estimation for EV Li-ion cell based on artificial neural networks state-of-charge meter. In: *Industrial Electronics (ISIE), 2012 IEEE International Symposium on IEEE*, 2012, pp. 1318–1324
- [78] FANG, H.; WANG, Y.; SAHINOGLU, Z.; WADA, T.; HARA, S.: State of charge estimation for lithium-ion batteries: An adaptive approach. In: *Control Engineering Practice* 25 (2014), 45 - 54. <http://dx.doi.org/http://dx.doi.org/10.1016/j.conengprac.2013.12.006>. – DOI <http://dx.doi.org/10.1016/j.conengprac.2013.12.006>. – ISSN 0967–0661
- [79] FARMANN, A.; WAAG, W.; SAUER, D. U.: Adaptive approach for on-board impedance parameters and voltage estimation of lithium-ion batteries in electric vehicles. In: *Journal of Power Sources* 299 (2015), 176 - 188. <http://dx.doi.org/http://dx.doi.org/10.1016/j.jpowsour.2015.08.087>. – DOI <http://dx.doi.org/10.1016/j.jpowsour.2015.08.087>. – ISSN 0378–7753
- [80] FEKRY, H. M.; HASSAN, M. M.; EL AZIZ, M. A.: The state of charge estimation for rechargeable batteries using Adaptive Neuro Fuzzy Inference System (ANFIS). In: *Innovative Engineering Systems (ICIES), 2012 First International Conference on IEEE*, 2012, pp. 201–206

- [81] FLEISCHER, C.; WAAG, W.; BAI, Z.; SAUER, D. U.: Self-learning state-of-available-power prediction for lithium-ion batteries in electrical vehicles. In: *2012 IEEE Vehicle Power and Propulsion Conference IEEE*, 2012, pp. 370–375
- [82] FLEISCHHAMMER, M.; WALDMANN, T.; BISLE, G.; HOGG, B.-I.; WOHLFAHRT-MEHRENS, M.: Interaction of cyclic ageing at high-rate and low temperatures and safety in lithium-ion batteries. In: *Journal of Power Sources* 274 (2015), 432 - 439. <http://dx.doi.org/http://dx.doi.org/10.1016/j.jpowsour.2014.08.135>. – DOI <http://dx.doi.org/10.1016/j.jpowsour.2014.08.135>. – ISSN 0378-7753
- [83] FLETCHER, T.: Support vector machines explained. In: *Online*. <http://sutikno.blog.undip.ac.id/files/2011/11/SVM-Explained.pdf>. [Accessed 06 06 2013] (2009)
- [84] FORGEZ, C.; DO, D. V.; FRIEDRICH, G.; MORCRETTE, M.; DELACOURT, C.: Thermal modeling of a cylindrical LiFePO₄/graphite lithium-ion battery. In: *Journal of Power Sources* 195 (2010), Nr. 9, 2961 - 2968. <http://dx.doi.org/http://dx.doi.org/10.1016/j.jpowsour.2009.10.105>. – DOI <http://dx.doi.org/10.1016/j.jpowsour.2009.10.105>. – ISSN 0378-7753
- [85] FOTOUHI, A.; AUGER, D. J.; PROPP, K.; LONGO, S.; WILD, M.: A review on electric vehicle battery modelling: From Lithium-ion toward Lithium-Sulphur. In: *Renewable and Sustainable Energy Reviews* 56 (2016), 1008 - 1021. <http://dx.doi.org/http://dx.doi.org/10.1016/j.rser.2015.12.009>. – DOI <http://dx.doi.org/10.1016/j.rser.2015.12.009>. – ISSN 1364-0321
- [86] FRAZZOLI, E.: *6.241 Dynamic Systems and Control- MITOPENCOURSEWARE*. Available from: <http://ocw.mit.edu/courses/electrical-engineering-and-computer-science/6-241j-dynamic-systems-and-control-spring-2011/lecture-notes/>
- [87] FULLER, T. F.; DOYLE, M.; NEWMAN, J.: Simulation and optimization of the dual lithium ion insertion cell. In: *Journal of the Electrochemical Society* 141 (1994), Nr. 1, pp. 1–10
- [88] GAO, L.; LIU, S.; DOUGAL, R. A.: Dynamic lithium-ion battery model for system simulation. In: *Components and Packaging Technologies, IEEE Transactions on* 25 (2002), Nr. 3, pp. 495–505
- [89] GAO, M.; LIU, Y.; HE, Z.: Battery state of charge online estimation based on particle filter. In: *Image and Signal Processing (CISP), 2011 4th International Congress on Bd.* 4 IEEE, 2011, pp. 2233–2236
- [90] GARCHE, J.; JOSSEN, A.; DÖRING, H.: Proceedings of the Fifth European Lead Battery Conference The influence of different operating conditions, especially over-discharge, on the lifetime and performance of lead/acid batteries for photovoltaic systems. In: *Journal of Power Sources* 67 (1997), Nr. 1, 201 - 212. [http://dx.doi.org/http://dx.doi.org/10.1016/S0378-7753\(97\)02601-3](http://dx.doi.org/http://dx.doi.org/10.1016/S0378-7753(97)02601-3). – DOI [http://dx.doi.org/10.1016/S0378-7753\(97\)02601-3](http://dx.doi.org/10.1016/S0378-7753(97)02601-3). – ISSN 0378-7753
- [91] GARCHE, J.; DYER, C. K.; MOSELEY, P. T.; OGUMI, Z.; RAND, D. A.; SCROSATI, B.: *Encyclopedia of electrochemical power sources*. Newnes, 2013
- [92] GERVER, R. E.; MEYERS, J. P.: Three-dimensional modeling of electrochemical performance and heat generation of lithium-ion batteries in tabbed planar configurations. In: *Journal of The Electrochemical Society* 158 (2011), Nr. 7, pp. A835–A843

- [93] GIRISHKUMAR, G.; BAILEY, W. H.; PETERSON, B. K.; CASTEEL, W. J.: Electrochemical and Spectroscopic Investigations of the Overcharge Behavior of StabiLife Electrolyte Salts in Lithium-Ion Batteries. In: *Journal of The Electrochemical Society* 158 (2011), Nr. 2, pp. A146–A153
- [94] GLAIZE, C.; GENIES, S.: *Lithium batteries and other electrochemical storage systems*. John Wiley & Sons, 2013
- [95] GORTER, R. R. J.: *Grey-box identification of induction machines: on-line and off-line approaches*, Technische Universiteit Eindhoven, Diss., 1997
- [96] GUO, G.; LONG, B.; CHENG, B.; ZHOU, S.; XU, P.; CAO, B.: Three-dimensional thermal finite element modeling of lithium-ion battery in thermal abuse application. In: *Journal of Power Sources* 195 (2010), Nr. 8, 2393 - 2398. <http://dx.doi.org/http://dx.doi.org/10.1016/j.jpowsour.2009.10.090>. – DOI <http://dx.doi.org/10.1016/j.jpowsour.2009.10.090>. – ISSN 0378–7753
- [97] GUO, G.; WU, X.; ZHUO, S.; XU, P.; XU, G.; CAO, B.: Prediction state of charge of Ni-MH battery pack using support vector machines for hybrid electric vehicles. In: *2008 IEEE Vehicle Power and Propulsion Conference IEEE*, 2008, pp. 1–4
- [98] GYENES, B.; STEVENS, D.; CHEVRIER, V.; DAHN, J.: Understanding anomalous behavior in coulombic efficiency measurements on Li-ion batteries. In: *Journal of The Electrochemical Society* 162 (2015), Nr. 3, pp. A278–A283
- [99] HAMETNER, C.; JAKUBEK, S.: State of charge estimation for Lithium Ion cells: Design of experiments, nonlinear identification and fuzzy observer design. In: *Journal of Power Sources* 238 (2013), 413 - 421. <http://dx.doi.org/http://dx.doi.org/10.1016/j.jpowsour.2013.04.040>. – DOI <http://dx.doi.org/10.1016/j.jpowsour.2013.04.040>. – ISSN 0378–7753
- [100] HAMMOUCHE, A.; KARDEN, E.; DONCKER, R. W. D.: Monitoring state-of-charge of Ni–MH and Ni–Cd batteries using impedance spectroscopy. In: *Journal of Power Sources* 127 (2004), Nr. 1–2, 105 - 111. <http://dx.doi.org/http://dx.doi.org/10.1016/j.jpowsour.2003.09.012>. – DOI <http://dx.doi.org/10.1016/j.jpowsour.2003.09.012>. – ISSN 0378–7753. – Eighth Ulmer Electrochemische Tage
- [101] HAN, S.-s.; CHEN, W.-z.: The algorithm of dynamic battery SOC based on mamdani fuzzy reasoning. In: *Fuzzy Systems and Knowledge Discovery, 2008. FSKD'08. Fifth International Conference on Bd. 1 IEEE*, 2008, pp. 439–443
- [102] HANSEN, T.; WANG, C.-J.: Support vector based battery state of charge estimator. In: *Journal of Power Sources* 141 (2005), Nr. 2, 351 - 358. <http://dx.doi.org/http://dx.doi.org/10.1016/j.jpowsour.2004.09.020>. – DOI <http://dx.doi.org/10.1016/j.jpowsour.2004.09.020>. – ISSN 0378–7753
- [103] HAQ, I. N.; SAPUTRA, R. H.; EDISON, F.; KURNIADI, D.; LEKSONO, E.; YULIARTO, B.: State of Charge (SoC) Estimation of LiFePO₄ Battery Module Using Support Vector Regression. In: *Joint International Conference on Electric Vehicular Technology and Industrial Bd. 4*, 2015, pp. 4
- [104] HARB, J. N.; LAFOLLETTE, R. M.: Mathematical Model of the Discharge Behavior of a Spirally Wound Lead-Acid Cell. In: *Journal of The Electrochemical Society* 146 (1999), Nr. 3, pp. 809–818

- [105] HAYKIN, S. S. u. a.: *Kalman filtering and neural networks*. Wiley Online Library, 2001
- [106] HE, F.; SHEN, W.; KAPOOR, A.; HONNERY, D.; DAYAWANSA, D.: H infinity observer based state of charge estimation for battery packs in electric vehicles. In: *Industrial Electronics and Applications (ICIEA), 2016 IEEE 11th Conference on IEEE*, 2016
- [107] HE, H.; XIONG, R.; PENG, J.: Real-time estimation of battery state-of-charge with unscented Kalman filter and {RTOS} Î¼COS-II platform. In: *Applied Energy* 162 (2016), 1410 - 1418. <http://dx.doi.org/http://dx.doi.org/10.1016/j.apenergy.2015.01.120>. – DOI <http://dx.doi.org/10.1016/j.apenergy.2015.01.120>. – ISSN 0306–2619
- [108] HE, H.; XIONG, R.; ZHANG, X.; SUN, F.; FAN, J.: State-of-charge estimation of the lithium-ion battery using an adaptive extended Kalman filter based on an improved Thevenin model. In: *IEEE Transactions on Vehicular Technology* 60 (2011), Nr. 4, pp. 1461–1469
- [109] HE, W.; WILLIARD, N.; CHEN, C.; PECHT, M.: State of charge estimation for Li-ion batteries using neural network modeling and unscented Kalman filter-based error cancellation. In: *International Journal of Electrical Power Energy Systems* 62 (2014), 783 - 791. <http://dx.doi.org/http://dx.doi.org/10.1016/j.ijepes.2014.04.059>. – DOI <http://dx.doi.org/10.1016/j.ijepes.2014.04.059>. – ISSN 0142–0615
- [110] HE, Y.; LIU, X.; ZHANG, C.; CHEN, Z.: A new model for State-of-Charge (SOC) estimation for high-power Li-ion batteries. In: *Applied Energy* 101 (2013), 808 - 814. <http://dx.doi.org/http://dx.doi.org/10.1016/j.apenergy.2012.08.031>. – DOI <http://dx.doi.org/10.1016/j.apenergy.2012.08.031>. – ISSN 0306–2619. – Sustainable Development of Energy, Water and Environment Systems
- [111] HE, Z.; GAO, M.; XU, J.; LIU, Y.: Battery model parameters estimation with the sigma point kalman filter. In: *Artificial Intelligence and Computational Intelligence, 2009. AICI'09. International Conference on Bd. 3 IEEE*, 2009, pp. 303–306
- [112] HE, Z.; LIU, Y.; GAO, M.; WANG, C.: A joint model and SOC estimation method for lithium battery based on the sigma point KF. In: *2012 IEEE Transportation Electrification Conference and Expo (ITEC) IEEE*, 2012, pp. 1–5
- [113] HOL, J. D.; SCHON, T. B.; GUSTAFSSON, F.: On resampling algorithms for particle filters. In: *Nonlinear Statistical Signal Processing Workshop, 2006 IEEE IEEE*, 2006, pp. 79–82
- [114] HU, C.; YOUN, B. D.; CHUNG, J.: A multiscale framework with extended Kalman filter for lithium-ion battery {SOC} and capacity estimation. In: *Applied Energy* 92 (2012), 694 - 704. <http://dx.doi.org/http://dx.doi.org/10.1016/j.apenergy.2011.08.002>. – DOI <http://dx.doi.org/10.1016/j.apenergy.2011.08.002>. – ISSN 0306–2619
- [115] HU, X.; LI, S.; PENG, H.; SUN, F.: Robustness analysis of State-of-Charge estimation methods for two types of Li-ion batteries. In: *Journal of Power Sources* 217 (2012), 209 - 219. <http://dx.doi.org/http://dx.doi.org/10.1016/j.jpowsour.2012.06.005>. – DOI <http://dx.doi.org/10.1016/j.jpowsour.2012.06.005>. – ISSN 0378–7753
- [116] HU, X.; SUN, F.; ZOU, Y.: Estimation of state of charge of a lithium-ion battery pack for electric vehicles using an adaptive Luenberger observer. In: *Energies* 3 (2010), Nr. 9, pp. 1586–1603

- [117] HU, X.; SUN, F.; ZOU, Y.: Comparison between two model-based algorithms for Li-ion battery {SOC} estimation in electric vehicles. In: *Simulation Modelling Practice and Theory* 34 (2013), 1 - 11. <http://dx.doi.org/http://dx.doi.org/10.1016/j.simpat.2013.01.001>. – DOI <http://dx.doi.org/10.1016/j.simpat.2013.01.001>. – ISSN 1569–190X
- [118] HU, Y.; YURKOVICH, S.; GUEZENNEC, Y.; YURKOVICH, B.: Electro-thermal battery model identification for automotive applications. In: *Journal of Power Sources* 196 (2011), Nr. 1, 449 - 457. <http://dx.doi.org/http://dx.doi.org/10.1016/j.jpowsour.2010.06.037>. – DOI <http://dx.doi.org/10.1016/j.jpowsour.2010.06.037>. – ISSN 0378–7753
- [119] HU, Y.; YURKOVICH, S.: Battery state of charge estimation in automotive applications using LPV techniques. In: *Proceedings of the 2010 American Control Conference IEEE*, 2010, pp. 5043–5049
- [120] HU, Y.; YURKOVICH, S.; GUEZENNEC, Y.; BORNATICO, R.: Model-based calibration for battery characterization in HEV applications. In: IEEE (Ed.): *2008 American Control Conference*, 2008, pp. 318–325
- [121] HUANG, Q.-A.; SHEN, Y.; HUANG, Y.; ZHANG, L.; ZHANG, J.: Impedance Characteristics and Diagnoses of Automotive Lithium-Ion Batteries at 7.5 In: *Electrochimica Acta* 219 (2016), 751 - 765. <http://dx.doi.org/http://dx.doi.org/10.1016/j.electacta.2016.09.154>. – DOI <http://dx.doi.org/10.1016/j.electacta.2016.09.154>. – ISSN 0013–4686
- [122] HUBER, M. F.: Chebyshev polynomial Kalman filter. In: *Digital Signal Processing* 23 (2013), Nr. 5, 1620 - 1629. <http://dx.doi.org/http://dx.doi.org/10.1016/j.dsp.2013.06.005>. – DOI <http://dx.doi.org/10.1016/j.dsp.2013.06.005>. – ISSN 1051–2004
- [123] HUET, F.: A review of impedance measurements for determination of the state-of-charge or state-of-health of secondary batteries. In: *Journal of Power Sources* 70 (1998), Nr. 1, 59 - 69. [http://dx.doi.org/http://dx.doi.org/10.1016/S0378-7753\(97\)02665-7](http://dx.doi.org/http://dx.doi.org/10.1016/S0378-7753(97)02665-7). – DOI [http://dx.doi.org/10.1016/S0378-7753\(97\)02665-7](http://dx.doi.org/10.1016/S0378-7753(97)02665-7). – ISSN 0378–7753
- [124] HURIA, T.; CERAOLO, M.; GAZZARRI, J.; JACKY, R.: High fidelity electrical model with thermal dependence for characterization and simulation of high power lithium battery cells. In: *Electric Vehicle Conference (IEVC), 2012 IEEE International IEEE*, 2012, pp. 1–8
- [125] JACKY, R. A.; PLETT, G. L.; KLEIN, M. J.: Parameterization of a Battery Simulation Model Using Numerical Optimization Methods. In: *SAE Technical Paper* (2009), pp. 01–1381
- [126] JALKANEN, K.; KARPPINEN, J.; SKOGSTRÖM, L.; LAURILA, T.; NISULA, M.; VUORILEHTO, K.: Cycle aging of commercial NMC/graphite pouch cells at different temperatures. In: *Applied Energy* 154 (2015), 160 - 172. <http://dx.doi.org/http://dx.doi.org/10.1016/j.apenergy.2015.04.110>. – DOI <http://dx.doi.org/10.1016/j.apenergy.2015.04.110>. – ISSN 0306–2619
- [127] JAZWINSKI, A. H.: *Stochastic processes and filtering theory*. Courier Corporation, 2007
- [128] JEON, D. H.: Numerical modeling of lithium ion battery for predicting thermal behavior in a cylindrical cell. In: *Current Applied Physics* 14 (2014), Nr. 2, 196 - 205. <http://dx.doi.org/http://dx.doi.org/10.1016/j.cap.2013.11.006>. – DOI <http://dx.doi.org/10.1016/j.cap.2013.11.006>. – ISSN 1567–1739

- [129] JEON, S.; YUN, J.-J.; BAE, S.: Comparative Study on the Battery State-of-Charge Estimation Method. In: *Indian Journal of Science and Technology* 8 (2015), Nr. 26
- [130] JIAN, W.; JIANG, X.; ZHANG, J.; XIANG, Z.; JIAN, Y.: Comparison of SOC estimation performance with different training functions using neural network. In: *Computer Modelling and Simulation (UKSim), 2012 UKSim 14th International Conference on IEEE*, 2012, pp. 459–463
- [131] JIANG, J.; DAHN, J.: ARC studies of the thermal stability of three different cathode materials: LiCoO₂; Li[Ni_{0.1}Co_{0.8}Mn_{0.1}]O₂; and LiFePO₄, in LiPF₆ and LiBoB EC/DEC electrolytes. In: *Electrochemistry Communications* 6 (2004), Nr. 1, 39 - 43. <http://dx.doi.org/http://dx.doi.org/10.1016/j.elecom.2003.10.011>. – DOI <http://dx.doi.org/10.1016/j.elecom.2003.10.011>. – ISSN 1388–2481
- [132] JIANG, J.; ZHANG, C.: *Fundamentals and Application of Lithium-ion Batteries in Electric Drive Vehicles*. John Wiley & Sons, 2015
- [133] JOSSEN, A.: Fundamentals of battery dynamics. In: *Journal of Power Sources* 154 (2006), Nr. 2, 530 - 538. <http://dx.doi.org/http://dx.doi.org/10.1016/j.jpowsour.2005.10.041>. – DOI <http://dx.doi.org/10.1016/j.jpowsour.2005.10.041>. – ISSN 0378–7753. – Selected papers from the Ninth Ulm Electrochemical Days
- [134] JULIER, S. J.; UHLMANN, J. K.: Unscented filtering and nonlinear estimation. In: *Proceedings of the IEEE* 92 (2004), Nr. 3, pp. 401–422
- [135] JUNPING, W.; JINGANG, G.; LEI, D.: An adaptive Kalman filtering based State of Charge combined estimator for electric vehicle battery pack. In: *Energy Conversion and Management* 50 (2009), Nr. 12, 3182 - 3186. <http://dx.doi.org/http://dx.doi.org/10.1016/j.enconman.2009.08.015>. – DOI <http://dx.doi.org/10.1016/j.enconman.2009.08.015>. – ISSN 0196–8904
- [136] JUNPING, W.; QUANSHI, C.; BINGGANG, C.: Support vector machine based battery model for electric vehicles. In: *Energy Conversion and Management* 47 (2006), Nr. 7–8, 858 - 864. <http://dx.doi.org/http://dx.doi.org/10.1016/j.enconman.2005.06.013>. – DOI <http://dx.doi.org/10.1016/j.enconman.2005.06.013>. – ISSN 0196–8904
- [137] KALAWOUN, J.; BILETSKA, K.; SUARD, F.; MONTARU, M.: From a novel classification of the battery state of charge estimators toward a conception of an ideal one. In: *Journal of Power Sources* 279 (2015), 694 - 706. <http://dx.doi.org/http://dx.doi.org/10.1016/j.jpowsour.2015.01.038>. – DOI <http://dx.doi.org/10.1016/j.jpowsour.2015.01.038>. – ISSN 0378–7753. – 9th International Conference on Lead-Acid Batteries – {LABAT} 2014
- [138] KANG, L.; ZHAO, X.; MA, J.: A new neural network model for the state-of-charge estimation in the battery degradation process. In: *Applied Energy* 121 (2014), 20 - 27. <http://dx.doi.org/http://dx.doi.org/10.1016/j.apenergy.2014.01.066>. – DOI <http://dx.doi.org/10.1016/j.apenergy.2014.01.066>. – ISSN 0306–2619
- [139] KARDEN, E.; MAURACHER, P.; SCHÖPE, F.: Electrochemical modelling of lead/acid batteries under operating conditions of electric vehicles. In: *Journal of Power Sources* 64 (1997), Nr. 1, 175 - 180. [http://dx.doi.org/http://dx.doi.org/10.1016/S0378-7753\(96\)02518-9](http://dx.doi.org/http://dx.doi.org/10.1016/S0378-7753(96)02518-9). – DOI [http://dx.doi.org/10.1016/S0378-7753\(96\)02518-9](http://dx.doi.org/10.1016/S0378-7753(96)02518-9). – ISSN 0378–7753

- [140] KEIL, P.; SCHUSTER, S.; LUDERS, C. V.; JOSSEN, A.: Lifetime Analyses of Lithium-Ion EV Batteries 3rd Electromobility Challenging Issues Conference (ECI), 2015
- [141] KEIL, P.; JOSSEN, A.: Charging protocols for lithium-ion batteries and their impact on cycle life—An experimental study with different 18650 high-power cells. In: *Journal of Energy Storage* 6 (2016), 125 - 141. <http://dx.doi.org/http://dx.doi.org/10.1016/j.est.2016.02.005>. – DOI <http://dx.doi.org/10.1016/j.est.2016.02.005>. – ISSN 2352–152X
- [142] KIM, I.-S.: The novel state of charge estimation method for lithium battery using sliding mode observer. In: *Journal of Power Sources* 163 (2006), Nr. 1, 584 - 590. <http://dx.doi.org/http://dx.doi.org/10.1016/j.jpowsour.2006.09.006>. – DOI <http://dx.doi.org/10.1016/j.jpowsour.2006.09.006>. – ISSN 0378–7753. – Special issue including selected papers presented at the Second International Conference on Polymer Batteries and Fuel Cells together with regular papers
- [143] KIM, I.-S.: A technique for estimating the state of health of lithium batteries through a dual-sliding-mode observer. In: *IEEE Transactions on Power Electronics* 25 (2010), Nr. 4, pp. 1013–1022
- [144] KIM, J.; LEE, S.; CHO, B.: Complementary cooperation algorithm based on DEKF combined with pattern recognition for SOC/capacity estimation and SOH prediction. In: *IEEE Transactions on Power Electronics* 27 (2012), Nr. 1, pp. 436–451
- [145] KIM, T.; QIAO, W.: A hybrid battery model capable of capturing dynamic circuit characteristics and nonlinear capacity effects. In: *IEEE Transactions on Energy Conversion* 26 (2011), Nr. 4, pp. 1172–1180
- [146] KIM, T.; QIAO, W.; QU, L.: Online SOC and SOH estimation for multicell lithium-ion batteries based on an adaptive hybrid battery model and sliding-mode observer. In: *2013 IEEE Energy Conversion Congress and Exposition IEEE*, 2013, pp. 292–298
- [147] KIM, U. S.; YI, J.; SHIN, C. B.; HAN, T.; PARK, S.: Modelling the thermal behaviour of a lithium-ion battery during charge. In: *Journal of Power Sources* 196 (2011), Nr. 11, 5115 - 5121. <http://dx.doi.org/http://dx.doi.org/10.1016/j.jpowsour.2011.01.103>. – DOI <http://dx.doi.org/10.1016/j.jpowsour.2011.01.103>. – ISSN 0378–7753
- [148] KLEIN, M.; PLETT, G. L.: Advances in HEV Battery Management Systems. (2006)
- [149] KLEIN, R.; CHATURVEDI, N.; CHRISTENSEN, J.; AHMED, J.; FINDEISEN, R.; KOJIC, A.: Electrochemical Model Based Observer Design for a Lithium-Ion Battery. In: *Control Systems Technology, IEEE Transactions on* 21 (2013), March, Nr. 2, pp. 289–301
- [150] KNAUFF, M.; DAFIS, C. J.; NIEBUR, D.; KWATNY, H. G.; NWANKPA, C.: Simulink model for hybrid power system test-bed. In: *Electric Ship Technologies Symposium, 2007. ESTS'07. IEEE*, 2007, pp. 421–427
- [151] KÖTZ, R.; HAHN, M.; GALLAY, R.: Temperature behavior and impedance fundamentals of supercapacitors. In: *Journal of Power Sources* 154 (2006), Nr. 2, pp. 550–555
- [152] KOZÁK, Š.: State-of-the-art in control engineering. In: *Journal of Electrical Systems and Information Technology* 1 (2014), Nr. 1, pp. 1–9

-
- [153] KUO, T.-J.; LEE, K.-Y.; HUANG, C.-K.; CHEN, J.-H.; CHIU, W.-L.; HUANG, C.-F.; WU, S.-D.: State of charge modeling of lithium-ion batteries using dual exponential functions. In: *Journal of Power Sources* 315 (2016), 331 - 338. <http://dx.doi.org/http://dx.doi.org/10.1016/j.jpowsour.2016.03.021>. – DOI <http://dx.doi.org/10.1016/j.jpowsour.2016.03.021>. – ISSN 0378–7753
- [154] LEE, D.-J.: *Nonlinear Bayesian filtering with applications to estimation and navigation*, Texas A&M University, Diss., 2005
- [155] LEE, J.; NAM, O.; CHO, B.: Li-ion battery {SOC} estimation method based on the reduced order extended Kalman filtering. In: *Journal of Power Sources* 174 (2007), Nr. 1, 9 - 15. <http://dx.doi.org/http://dx.doi.org/10.1016/j.jpowsour.2007.03.072>. – DOI <http://dx.doi.org/10.1016/j.jpowsour.2007.03.072>. – ISSN 0378–7753. – Hybrid Electric Vehicles
- [156] LEE, J. L.; ALDRICH, L. L.; STETZEL, K. D.; PLETT, G. L.: Extended operating range for reduced-order model of lithium-ion cells. In: *Journal of Power Sources* 255 (2014), 85 - 100. <http://dx.doi.org/http://dx.doi.org/10.1016/j.jpowsour.2013.12.134>. – DOI <http://dx.doi.org/10.1016/j.jpowsour.2013.12.134>. – ISSN 0378–7753
- [157] LEE, K.: Methods and Optimization in Ohmic Resistance Measurement of Batteries. In: *Technical University of Munich, Master Thesis* (2013), Feb
- [158] LEE, S.; KIM, J.; LEE, J.; CHO, B.: State-of-charge and capacity estimation of lithium-ion battery using a new open-circuit voltage versus state-of-charge. In: *Journal of Power Sources* 185 (2008), Nr. 2, 1367 - 1373. <http://dx.doi.org/http://dx.doi.org/10.1016/j.jpowsour.2008.08.103>. – DOI <http://dx.doi.org/10.1016/j.jpowsour.2008.08.103>. – ISSN 0378–7753
- [159] LEE, Y.-S.; JAO, C.-W.: Fuzzy controlled lithium-ion battery equalization with state-of-charge estimator. In: *Systems, Man and Cybernetics, 2003. IEEE International Conference on* Bd. 5 IEEE, 2003, pp. 4431–4438
- [160] LEI, X.; CHAN, C.; LIU, K.; MA, L.: Pruning LS-SVM Based Battery Model for Electric Vehicles. In: *Third International Conference on Natural Computation (ICNC 2007)* Bd. 3 IEEE, 2007, pp. 333–337
- [161] LI, I.-H.; WANG, W.-Y.; SU, S.-F.; LEE, Y.-S.: A merged fuzzy neural network and its applications in battery state-of-charge estimation. In: *IEEE Transactions on Energy Conversion* 22 (2007), Nr. 3, pp. 697–708
- [162] LI, J.; BARILLAS, J. K.; GUENTHER, C.; DANZER, M. A.: A comparative study of state of charge estimation algorithms for LiFePO₄ batteries used in electric vehicles. In: *Journal of Power Sources* 230 (2013), 244 - 250. <http://dx.doi.org/http://dx.doi.org/10.1016/j.jpowsour.2012.12.057>. – DOI <http://dx.doi.org/10.1016/j.jpowsour.2012.12.057>. – ISSN 0378–7753
- [163] LI, J.; MAZZOLA, M. S.: Accurate battery pack modeling for automotive applications. In: *Journal of Power Sources* 237 (2013), pp. 215 – 228. <http://dx.doi.org/http://dx.doi.org/10.1016/j.jpowsour.2013.03.009>. – DOI <http://dx.doi.org/10.1016/j.jpowsour.2013.03.009>. – ISSN 0378–7753

- [164] LI, J.; LU, H.; YANG, Z.; PEI, F.: State-of-charge estimation and charge equalization for electric agricultural machinery using Square-Root Central Difference Kalman Filter. In: *Transportation, Mechanical, and Electrical Engineering (TMEE), 2011 International Conference on IEEE*, 2011, pp. 966–969
- [165] LI, J.; WANG, L.; LYU, C.; WANG, H.; LIU, X.: New method for parameter estimation of an electrochemical-thermal coupling model for LiCoO₂ battery. In: *Journal of Power Sources* 307 (2016), 220 - 230. <http://dx.doi.org/http://dx.doi.org/10.1016/j.jpowsour.2015.12.058>. – DOI <http://dx.doi.org/10.1016/j.jpowsour.2015.12.058>. – ISSN 0378–7753
- [166] LI, M.: Li-ion dynamics and state of charge estimation. In: *Renewable Energy* (2016), -. <http://dx.doi.org/http://dx.doi.org/10.1016/j.renene.2016.06.009>. – DOI <http://dx.doi.org/10.1016/j.renene.2016.06.009>. – ISSN 0960–1481
- [167] LI, X.; HUI, D.; WU, L.; LAI, X.: Control strategy of battery state of charge for wind/battery hybrid power system. In: *2010 IEEE International Symposium on Industrial Electronics IEEE*, 2010
- [168] LIN, C.; ZHANG, F.; XUE, H.; LU, X.: Estimation of battery state of charge using \hat{z} observer. In: *Power Electronics and Motion Control Conference (IPEMC), 2012 7th International Bd. 1 IEEE*, 2012, pp. 422–428
- [169] LIN, H.-T.; LIANG, T.-J.; CHEN, S.-M.: Estimation of battery state of health using probabilistic neural network. In: *IEEE Transactions on Industrial Informatics* 9 (2013), Nr. 2, pp. 679–685
- [170] LIN, X.; PEREZ, H. E.; MOHAN, S.; SIEGEL, J. B.; STEFANOPOULOU, A. G.; DING, Y.; CASTANIER, M. P.: A lumped-parameter electro-thermal model for cylindrical batteries. In: *Journal of Power Sources* 257 (2014), 1 - 11. <http://dx.doi.org/http://dx.doi.org/10.1016/j.jpowsour.2014.01.097>. – DOI <http://dx.doi.org/10.1016/j.jpowsour.2014.01.097>. – ISSN 0378–7753
- [171] LIU, Y.; ZHAO, K.; HUANG, X.; PEI, F.: A new method based on RBFNN in SOC estimation of HEV battery. In: *Proceedings of the 29th Chinese Control Conference IEEE*, 2010, pp. 4923–4927
- [172] LU, L.; HAN, X.; LI, J.; HUA, J.; OUYANG, M.: A review on the key issues for lithium-ion battery management in electric vehicles. In: *Journal of Power Sources* 226 (2013), 272 - 288. <http://www.sciencedirect.com/science/article/pii/S0378775312016163>. – ISSN 0378–7753
- [173] MA, Y.; LI, B.; XIE, Y.; CHEN, H.: Estimating the State of Charge of Lithium-ion Battery based on Sliding Mode Observer. In: *IFAC-PapersOnLine* 49 (2016), Nr. 11, 54 - 61. <http://dx.doi.org/http://dx.doi.org/10.1016/j.ifacol.2016.08.009>. – DOI <http://dx.doi.org/10.1016/j.ifacol.2016.08.009>. – ISSN 2405–8963. – 8th {IFAC} Symposium on Advances in Automotive Control {AAC} 2016Norrköping, Sweden, 20–23 June 2016
- [174] MACDONALD, D. D.: Reflections on the history of electrochemical impedance spectroscopy. In: *Electrochimica Acta* 51 (2006), Nr. 8–9, 1376 - 1388. <http://dx.doi.org/http://dx.doi.org/10.1016/j.electacta.2005.02.107>. – DOI <http://dx.doi.org/10.1016/j.electacta.2005.02.107>. – ISSN 0013–4686. – Electrochemical Impedance Spectroscopy Selection of papers from the 6th International Symposium (EIS 2004) 16–21 May 2004, Cocoa Beach, FL, {USA}

- [175] MACWAN, A.; PATEL, V.; JIANG, X.; LI, C.; BHOLE, S.; CHEN, D.: Ultrasonic spot welding of Al/Mg/Al tri-layered clad sheets. In: *Materials Design* 62 (2014), 344 - 351. <http://dx.doi.org/http://dx.doi.org/10.1016/j.matdes.2014.05.035>. – DOI <http://dx.doi.org/10.1016/j.matdes.2014.05.035>. – ISSN 0261–3069
- [176] MALEKI, H.; DENG, G.; ANANI, A.; HOWARD, J.: Thermal Stability Studies of Li ion Cells and Components. In: *Journal of The Electrochemical Society* 146 (1999), Nr. 9, 3224–3229. <http://dx.doi.org/10.1149/1.1392458>. – DOI 10.1149/1.1392458
- [177] MALKHANDI, S.: Fuzzy logic-based learning system and estimation of state-of-charge of lead-acid battery. In: *Engineering Applications of Artificial Intelligence* 19 (2006), Nr. 5, 479 - 485. <http://dx.doi.org/http://dx.doi.org/10.1016/j.engappai.2005.12.005>. – DOI <http://dx.doi.org/10.1016/j.engappai.2005.12.005>. – ISSN 0952–1976
- [178] MARIE-FRANCOISE, J.-N.; GUALOUS, H.; BERTHON, A.: Supercapacitor thermal-and electrical-behaviour modelling using ANN. In: *IEE Proceedings-Electric Power Applications* 153 (2006), Nr. 2, pp. 255–262
- [179] MARTÍN-MARTÍN, L.; GASTELURRUTIA, J.; NIETO, N.; RAMOS, J. C.; RIVAS, A.; GIL, I.: Modeling based on design of thermal management systems for vertical elevation applications powered by lithium-ion batteries. In: *Applied Thermal Engineering* 102 (2016), pp. 1081–1094
- [180] MARTINY, N.; RHEINFELD, A.; GEDER, J.; WANG, Y.; KRAUS, W.; JOSSEN, A.: Development of an all kapton-based thin-film thermocouple matrix for in situ temperature measurement in a lithium ion pouch cell. In: *IEEE Sensors Journal* 14 (2014), Nr. 10, pp. 3377–3384
- [181] MAURACHER, P.; KARDEN, E.: Proceedings of the Fifth European Lead Battery Conference Dynamic modelling of lead/acid batteries using impedance spectroscopy for parameter identification. In: *Journal of Power Sources* 67 (1997), Nr. 1, 69 - 84. [http://dx.doi.org/http://dx.doi.org/10.1016/S0378-7753\(97\)02498-1](http://dx.doi.org/http://dx.doi.org/10.1016/S0378-7753(97)02498-1). – DOI [http://dx.doi.org/10.1016/S0378-7753\(97\)02498-1](http://dx.doi.org/10.1016/S0378-7753(97)02498-1). – ISSN 0378–7753
- [182] MAYER, D.; BISCAGLIA, S.: Use of the modeling of lead-acid battery operation for the development of a state of charge meter. In: *Tenth EC Photovoltaic Solar Energy Conference* Springer, 1991, pp. 1209–1213
- [183] MCCLEARY, D. A.; MEYERS, J. P.; KIM, B.: Three-dimensional modeling of electrochemical performance and heat generation of spirally and prismatically wound lithium-ion batteries. In: *Journal of The Electrochemical Society* 160 (2013), Nr. 11, pp. A1931–A1943
- [184] MECO, S.; PARDAL, G.; GANGULY, S.; WILLIAMS, S.; MCPHERSON, N.: Application of laser in seam welding of dissimilar steel to aluminium joints for thick structural components. In: *Optics and Lasers in Engineering* 67 (2015), 22 - 30. <http://dx.doi.org/http://dx.doi.org/10.1016/j.optlaseng.2014.10.006>. – DOI <http://dx.doi.org/10.1016/j.optlaseng.2014.10.006>. – ISSN 0143–8166
- [185] MICHEL, P.-H.; HEIRIES, V.: An Adaptive Sigma Point Kalman Filter Hybridized by Support Vector Machine Algorithm for Battery SoC and SoH Estimation. In: *2015 IEEE 81st Vehicular Technology Conference (VTC Spring)* IEEE, 2015, pp. 1–7

- [186] MITTER, S. K.: Nonlinear Estimation / Massachusetts Institute of Technology. Department of Electrical Engineering and Computer Science, Laboratory for Information and Decision Systems, Cambridge, MA 02139, . – Forschungsbericht
- [187] MO, B.; YU, J.; TANG, D.; LIU, H.: A remaining useful life prediction approach for lithium-ion batteries using Kalman filter and an improved particle filter. In: *Prognostics and Health Management (ICPHM), 2016 IEEE International Conference on*, 2016, pp. 1–5
- [188] MONTALENTI, P.; STANGERUP, P.: Thermal simulation of NiCd batteries for spacecraft. In: *Journal of Power Sources* 2 (1977), Nr. 2, 147 - 162. [http://dx.doi.org/http://dx.doi.org/10.1016/0378-7753\(77\)80015-3](http://dx.doi.org/http://dx.doi.org/10.1016/0378-7753(77)80015-3). – DOI [http://dx.doi.org/10.1016/0378-7753\(77\)80015-3](http://dx.doi.org/10.1016/0378-7753(77)80015-3). – ISSN 0378–7753
- [189] NEWMAN, J.; TIEDEMANN, W.: Porous-electrode theory with battery applications. In: *AIChE Journal* 21 (1975), Nr. 1, pp. 25–41
- [190] NG, K. S.; MOO, C.-S.; CHEN, Y.-P.; HSIEH, Y.-C.: Enhanced coulomb counting method for estimating state-of-charge and state-of-health of lithium-ion batteries. In: *Applied Energy* 86 (2009), Nr. 9, 1506 - 1511. <http://dx.doi.org/http://dx.doi.org/10.1016/j.apenergy.2008.11.021>. – DOI <http://dx.doi.org/10.1016/j.apenergy.2008.11.021>. – ISSN 0306–2619
- [191] NING, B.; XU, J.; CAO, B.; WANG, B.; XU, G.: A Sliding Mode Observer {SOC} Estimation Method Based on Parameter Adaptive Battery Model. In: *Energy Procedia* 88 (2016), 619 - 626. <http://dx.doi.org/http://dx.doi.org/10.1016/j.egypro.2016.06.088>. – DOI <http://dx.doi.org/10.1016/j.egypro.2016.06.088>. – ISSN 1876–6102. – {CUE} 2015 - Applied Energy Symposium and Summit 2015: Low carbon cities and urban energy systems
- [192] NOTTEN, P.; BERGVELD, H.; KRUIJT, W.: Battery Management Systems: Design by modeling. In: *Kluwer Academic Publisher* (2002)
- [193] OUYANG, Q.; CHEN, J.; WANG, F.; SU, H.: Nonlinear Observer Design for the State of Charge of Lithium-Ion Batteries. In: *{IFAC} Proceedings Volumes* 47 (2014), Nr. 3, 2794 - 2799. <http://dx.doi.org/http://dx.doi.org/10.3182/20140824-6-ZA-1003.02115>. – DOI <http://dx.doi.org/10.3182/20140824-6-ZA-1003.02115>. – ISSN 1474–6670. – 19th {IFAC} World Congress
- [194] PANCHAL, S.; DINCER, I.; AGELIN-CHAAB, M.; FRASER, R.; FOWLER, M.: Thermal modeling and validation of temperature distributions in a prismatic lithium-ion battery at different discharge rates and varying boundary conditions. In: *Applied Thermal Engineering* 96 (2016), 190 - 199. <http://dx.doi.org/http://dx.doi.org/10.1016/j.applthermaleng.2015.11.019>. – DOI <http://dx.doi.org/10.1016/j.applthermaleng.2015.11.019>. – ISSN 1359–4311
- [195] PAPAZOGLU, A.; LONGO, S.; AUGER, D.; ASSADIAN, F.: Nonlinear Filtering Techniques Comparison for Battery State Estimation. In: *Journal of Sustainable Development of Energy, Water and Environment Systems* 2 (2014), Nr. 3, pp. 259–269
- [196] PARTOVIBAKHSH, M.; LIU, G.: An adaptive unscented Kalman filtering approach for online estimation of model parameters and state-of-charge of Lithium-ion batteries for autonomous mobile robots. In: *IEEE Transactions on Control Systems Technology* 23 (2015), Nr. 1, pp. 357–363

- [197] PELED, E.; YAMIN, H.; RESHEF, I.; KELRICH, D.; ROZEN, S.: *Method and apparatus for determining the state-of-charge of batteries particularly lithium batteries*. Google Patents, Feb 1988
- [198] PIAO, C.-h.; FU, W.-l.; LEI, G.-h.; CHO, C.-d. u. a.: Online parameter estimation of the Ni-MH batteries based on statistical methods. In: *Energies* 3 (2010), Nr. 2, pp. 206–215
- [199] PILLER, S.; PERRIN, M.; JOSSEN, A.: Methods for state-of-charge determination and their applications. In: *Journal of Power Sources* 96 (2001), Nr. 1, 113 - 120. [http://dx.doi.org/http://dx.doi.org/10.1016/S0378-7753\(01\)00560-2](http://dx.doi.org/http://dx.doi.org/10.1016/S0378-7753(01)00560-2). – DOI [http://dx.doi.org/10.1016/S0378-7753\(01\)00560-2](http://dx.doi.org/10.1016/S0378-7753(01)00560-2). – ISSN 0378-7753. – Proceedings of the 22nd International Power Sources Symposium
- [200] PLETT, G.: LiPB dynamic cell models for Kalman-filter SOC estimation. In: *The 19th international battery, hybrid and fuel electric vehicle symposium and exhibition* Citeseer, 2002, pp. 1–12
- [201] PLETT, G. L.: Extended Kalman filtering for battery management systems of LiPB-based {HEV} battery packs: Part 1. Background. In: *Journal of Power Sources* 134 (2004), Nr. 2, 252 - 261. <http://dx.doi.org/http://dx.doi.org/10.1016/j.jpowsour.2004.02.031>. – DOI <http://dx.doi.org/10.1016/j.jpowsour.2004.02.031>. – ISSN 0378-7753
- [202] PLETT, G. L.: Extended Kalman filtering for battery management systems of LiPB-based {HEV} battery packs: Part 2. Modeling and identification. In: *Journal of Power Sources* 134 (2004), Nr. 2, 262 - 276. <http://dx.doi.org/http://dx.doi.org/10.1016/j.jpowsour.2004.02.032>. – DOI <http://dx.doi.org/10.1016/j.jpowsour.2004.02.032>. – ISSN 0378-7753
- [203] PLETT, G. L.: Extended Kalman filtering for battery management systems of LiPB-based {HEV} battery packs: Part 3. State and parameter estimation. In: *Journal of Power Sources* 134 (2004), Nr. 2, 277 - 292. <http://dx.doi.org/http://dx.doi.org/10.1016/j.jpowsour.2004.02.033>. – DOI <http://dx.doi.org/10.1016/j.jpowsour.2004.02.033>. – ISSN 0378-7753
- [204] PLETT, G. L.: Sigma-point Kalman filtering for battery management systems of LiPB-based {HEV} battery packs: Part 1: Introduction and state estimation. In: *Journal of Power Sources* 161 (2006), Nr. 2, 1356 - 1368. <http://dx.doi.org/http://dx.doi.org/10.1016/j.jpowsour.2006.06.003>. – DOI <http://dx.doi.org/10.1016/j.jpowsour.2006.06.003>. – ISSN 0378-7753
- [205] PLETT, G. L.: Battery management system algorithms for HEV battery state-of-charge and state-of-health estimation. In: *Advanced Materials and Methods for Lithium-Ion Batteries*, 2007
- [206] POP, V.; BERGVELD, H.; REGTIEN, P.; VELD, J. O.; DANILOV, D.; NOTTEN, P.: Battery aging and its influence on the electromotive force. In: *Journal of The Electrochemical Society* 154 (2007), Nr. 8, pp. A744–A750
- [207] PRAJAPATI, V.; HESS, H.; WILLIAM, E. J.; GUPTA, V.; HUFF, M.; MANIC, M.; RUFUS, F.; THAKKER, A.; GOVAR, J.: A literature review of state of-charge estimation techniques applicable to lithium poly-carbon monofluoride (Li/CFx) battery. In: *India International Conference on Power Electronics 2010 (IICPE2010)* IEEE, 2011, pp. 1–8

- [208] RAHIMI-EICHI, H.; BARONTI, F.; CHOW, M.-Y.: Online adaptive parameter identification and state-of-charge coestimation for lithium-polymer battery cells. In: *IEEE Transactions on Industrial Electronics* 61 (2014), Nr. 4, pp. 2053–2061
- [209] RAIJMAKERS, L.; DANILOV, D.; LAMMEREN, J. van; LAMMERS, M.; NOTTEN, P.: Sensorless battery temperature measurements based on electrochemical impedance spectroscopy. In: *Journal of Power Sources* 247 (2014), 539 - 544. <http://dx.doi.org/http://dx.doi.org/10.1016/j.jpowsour.2013.09.005>. – DOI <http://dx.doi.org/10.1016/j.jpowsour.2013.09.005>. – ISSN 0378–7753
- [210] RAMADESIGAN, V.; NORTHROP, P. W. C.; DE, S.; SANTHANAGOPALAN, S.; BRAATZ, R. D.; SUBRAMANIAN, V. R.: Modeling and Simulation of Lithium-Ion Batteries from a Systems Engineering Perspective. In: *Journal of The Electrochemical Society* 159 (2012), Jan., Nr. 3, R31–R45. <http://dx.doi.org/10.1149/2.018203jes>. – DOI 10.1149/2.018203jes. – ISSN 1945–7111
- [211] RAO, L.; NEWMAN, J.: Heat-Generation Rate and General Energy Balance for Insertion Battery Systems. In: *Journal of the Electrochemical Society* 144 (1997), Nr. 8, pp. 2697–2704
- [212] RAUH, T.: Microcontroller-Based BMS to Monitor Battery Cells in EV Applications. In: *Technical University of Munich, Master Thesis* (2015), Sep
- [213] REDDY, V.; AREY, S.; SINGH, P.; FENNIE, C.; REISNER, D.: Preliminary design SOC meter for Li/SO₂ cells based on fuzzy logic methodology. In: *Battery Conference on Applications and Advances, 1999. The Fourteenth Annual IEEE, 1999*, pp. 237–239
- [214] REMMLINGER, J.; BUCHHOLZ, M.; SOCZKA-GUTH, T.; DIETMAYER, K.: On-board state-of-health monitoring of lithium-ion batteries using linear parameter-varying models. In: *Journal of Power Sources* 239 (2013), 689 - 695. <http://dx.doi.org/http://dx.doi.org/10.1016/j.jpowsour.2012.11.102>. – DOI <http://dx.doi.org/10.1016/j.jpowsour.2012.11.102>. – ISSN 0378–7753
- [215] REZVANIZANIANI, S. M.; LIU, Z.; CHEN, Y.; LEE, J.: Review and recent advances in battery health monitoring and prognostics technologies for electric vehicle (EV) safety and mobility. In: *Journal of Power Sources* 256 (2014), 110 - 124. <http://dx.doi.org/http://dx.doi.org/10.1016/j.jpowsour.2014.01.085>. – DOI <http://dx.doi.org/10.1016/j.jpowsour.2014.01.085>. – ISSN 0378–7753
- [216] RICHARDSON, R.; HOWEY, D. A.: Sensorless Battery Internal Temperature Estimation using a Kalman Filter with Impedance Measurement. In: *IEEE Transactions on Sustainable Energy* 6 (2015), Nr. 4, pp. 1190–1199
- [217] RICHARDSON, R. R.; IRELAND, P. T.; HOWEY, D. A.: Battery internal temperature estimation by combined impedance and surface temperature measurement. In: *Journal of Power Sources* 265 (2014), 254 - 261. <http://dx.doi.org/http://dx.doi.org/10.1016/j.jpowsour.2014.04.129>. – DOI <http://dx.doi.org/10.1016/j.jpowsour.2014.04.129>. – ISSN 0378–7753
- [218] RIEGEL, B.: Anforderungen an Batterien für den stationären Einsatz. In: *Handbuch Lithium-Ionen-Batterien*. Springer, 2013

- [219] ROBAT, A. R. P.; SALMASI, F. R.: State of charge estimation for batteries in HEV using locally linear model tree (LOLIMOT). In: *Electrical Machines and Systems, 2007. ICEMS. International Conference on IEEE*, 2007, pp. 2041–2045
- [220] RODRIGUES, S.; MUNICHANDRAIAH, N.; SHUKLA, A.: A review of state-of-charge indication of batteries by means of a.c. impedance measurements. In: *Journal of Power Sources* 87 (2000), Nr. 1–2, 12 - 20. [http://dx.doi.org/http://dx.doi.org/10.1016/S0378-7753\(99\)00351-1](http://dx.doi.org/http://dx.doi.org/10.1016/S0378-7753(99)00351-1). – DOI [http://dx.doi.org/10.1016/S0378-7753\(99\)00351-1](http://dx.doi.org/10.1016/S0378-7753(99)00351-1). – ISSN 0378–7753
- [221] ROJAS, R.: *Neural networks: a systematic introduction*. Springer Science & Business Media, 2013
- [222] ROTH, M.: *Kalman filters for nonlinear systems and heavy-tailed noise*, Linköping University Electronic Press, Diss., 2013
- [223] RUI-HAO, L.; YU-KUN, S.; XIAO-FU, J.: Battery state of charge estimation for electric vehicle based on neural network. In: *Communication Software and Networks (ICCSN), 2011 IEEE 3rd International Conference on IEEE*, 2011, pp. 493–496
- [224] SALAMEH, Z. M.; CASACCA, M. A.; LYNCH, W. A.: A mathematical model for lead-acid batteries. In: *IEEE Transactions on Energy Conversion* 7 (1992), Nr. 1, pp. 93–98
- [225] SALKIND, A. J.; FENNIE, C.; SINGH, P.; ATWATER, T.; REISNER, D. E.: Determination of state-of-charge and state-of-health of batteries by fuzzy logic methodology. In: *Journal of Power Sources* 80 (1999), Nr. 1–2, 293 - 300. [http://dx.doi.org/http://dx.doi.org/10.1016/S0378-7753\(99\)00079-8](http://dx.doi.org/http://dx.doi.org/10.1016/S0378-7753(99)00079-8). – DOI [http://dx.doi.org/10.1016/S0378-7753\(99\)00079-8](http://dx.doi.org/10.1016/S0378-7753(99)00079-8). – ISSN 0378–7753
- [226] SAMBA, A.; OMAR, N.; GUALOUS, H.; FIROUZ, Y.; BOSSCHE, P. V.; MIERLO, J. V.; BOUBEKEUR, T. I.: Development of an Advanced Two-Dimensional Thermal Model for Large size Lithium-ion Pouch Cells. In: *Electrochimica Acta* 117 (2014), 246 - 254. <http://dx.doi.org/http://dx.doi.org/10.1016/j.electacta.2013.11.113>. – DOI <http://dx.doi.org/10.1016/j.electacta.2013.11.113>. – ISSN 0013–4686
- [227] SAUER, D. U.; BOPP, G.; JOSSEN, A.; GARCHE, J.; ROTHERT, M.; WOLLNY, M.: State-of-charge—what do we really speak about? In: *The 21st international telecommunications energy conference*, 1999, pp. 6–9
- [228] SAUER, D. U.; BOHLEN, O.; SANDERS, T.; WAAG, W.; SCHMIDT, R.; GERSCHLER, J. B.: Batteriezustandserkennung: mögliche verfahrens-und algorithmenansätze, grenzen der batteriezustandserkennung. In: *Energiemanagement und Bordnetze II, Hrsg. Matthias Schöllmann, Expert-Verlag* (2007), pp. 1–30
- [229] SAUER, D. U.; WENZL, H.: Comparison of different approaches for lifetime prediction of electrochemical systems—Using lead-acid batteries as example. In: *Journal of Power Sources* 176 (2008), Nr. 2, 534 - 546. <http://dx.doi.org/http://dx.doi.org/10.1016/j.jpowsour.2007.08.057>. – DOI <http://dx.doi.org/10.1016/j.jpowsour.2007.08.057>. – ISSN 0378–7753. – Selected Papers presented at the 10th {ULM} ElectroChemical DaysW. Tillmetz, J. Lindenmayer 10th Ulm ElectroChemical Days

- [230] SCHEDULES, A. I. d.: *Environmental Protection Agency (EPA): 40 C.F.R.*, 2008
- [231] SCHMIDT, J. P.; ARNOLD, S.; LOGES, A.; WERNER, D.; WETZEL, T.; IVERS-TIFFÉE, E.: Measurement of the internal cell temperature via impedance: Evaluation and application of a new method. In: *Journal of Power Sources* 243 (2013), 110 - 117. <http://dx.doi.org/http://dx.doi.org/10.1016/j.jpowsour.2013.06.013>. – DOI <http://dx.doi.org/10.1016/j.jpowsour.2013.06.013>. – ISSN 0378-7753
- [232] SCHUSTER, E.; ZIEBERT, C.; MELCHER, A.; ROHDE, M.; SEIFERT, H. J.: Thermal behavior and electrochemical heat generation in a commercial 40 Ah lithium ion pouch cell. In: *Journal of Power Sources* 286 (2015), 580 - 589. <http://dx.doi.org/http://dx.doi.org/10.1016/j.jpowsour.2015.03.170>. – DOI <http://dx.doi.org/10.1016/j.jpowsour.2015.03.170>. – ISSN 0378-7753
- [233] SCHWEIGER, H.-G.; OBEIDI, O.; KOMESKER, O.; RASCHKE, A.; SCHIEMANN, M.; ZEHNER, C.; GEHNEN, M.; KELLER, M.; BIRKE, P.: Comparison of Several Methods for Determining the Internal Resistance of Lithium Ion Cells. In: *Sensors* 10 (2010), Nr. 6, 5604. <http://dx.doi.org/10.3390/s100605604>. – DOI [10.3390/s100605604](http://dx.doi.org/10.3390/s100605604). – ISSN 1424-8220
- [234] SCHWEIGHOFER, B.; RAAB, K. M.; BRASSEUR, G.: Modeling of high power automotive batteries by the use of an automated test system. In: *Instrumentation and Measurement, IEEE Transactions on* 52 (2003), Nr. 4, pp. 1087-1091
- [235] SCHWUNK, S.: *Partikelfilter zur Ladezustands-und Alterungsbestimmung bei Lithium-Ionen-Batterien auf Basis von Metalloxiden und Phosphorolvinen*, Hagen, Univ., Diss., 2013, Diss., 2013
- [236] SCHWUNK, S.; ARMBRUSTER, N.; STRAUB, S.; KEHL, J.; VETTER, M.: Particle filter for state of charge and state of health estimation for lithium-iron phosphate batteries. In: *Journal of Power Sources* 239 (2013), 705 - 710. <http://dx.doi.org/http://dx.doi.org/10.1016/j.jpowsour.2012.10.058>. – DOI <http://dx.doi.org/10.1016/j.jpowsour.2012.10.058>. – ISSN 0378-7753
- [237] SEAMAN, A.; DAO, T.-S.; MCPHEE, J.: A survey of mathematics-based equivalent-circuit and electrochemical battery models for hybrid and electric vehicle simulation. In: *Journal of Power Sources* 256 (2014), 410 - 423. <http://dx.doi.org/http://dx.doi.org/10.1016/j.jpowsour.2014.01.057>. – DOI <http://dx.doi.org/10.1016/j.jpowsour.2014.01.057>. – ISSN 0378-7753
- [238] SEPASI, S.; GHORBANI, R.; LIAW, B. Y.: SOC estimation for aged lithium-ion batteries using model adaptive extended Kalman filter. In: *Transportation Electrification Conference and Expo (ITEC), 2013 IEEE IEEE*, 2013, pp. 1-6
- [239] SEPASI, S.; GHORBANI, R.; LIAW, B. Y.: Improved extended Kalman filter for state of charge estimation of battery pack. In: *Journal of Power Sources* 255 (2014), 368 - 376. <http://dx.doi.org/http://dx.doi.org/10.1016/j.jpowsour.2013.12.093>. – DOI <http://dx.doi.org/10.1016/j.jpowsour.2013.12.093>. – ISSN 0378-7753
- [240] SHAHRIARI, M.; FARROKHI, M.: State of health estimation of VRLA batteries using fuzzy logic. In: *2010 18th Iranian Conference on Electrical Engineering IEEE*, 2010, pp. 629-634
- [241] SHAHRIARI, M.; FARROKHI, M.: Online state-of-health estimation of VRLA batteries using state of charge. In: *IEEE Transactions on Industrial Electronics* 60 (2013), Nr. 11, pp. 191-202

- [242] SHAO, S.; BI, J.; YANG, F.; GUAN, W.: On-line estimation of state-of-charge of Li-ion batteries in electric vehicle using the resampling particle filter. In: *Transportation Research Part D: Transport and Environment* 32 (2014), 207 - 217. <http://dx.doi.org/http://dx.doi.org/10.1016/j.trd.2014.07.013>. – DOI <http://dx.doi.org/10.1016/j.trd.2014.07.013>. – ISSN 1361–9209
- [243] SHARMA, P.; BHATTI, T.: A review on electrochemical double-layer capacitors. In: *Energy Conversion and Management* 51 (2010), Nr. 12, 2901 - 2912. <http://dx.doi.org/http://dx.doi.org/10.1016/j.enconman.2010.06.031>. – DOI <http://dx.doi.org/10.1016/j.enconman.2010.06.031>. – ISSN 0196–8904
- [244] SHEN, J.-N.; HE, Y.-J.; MA, Z.-F.; LUO, H.-B.; ZHANG, Z.-F.: Online state of charge estimation of lithium-ion batteries: A moving horizon estimation approach. In: *Chemical Engineering Science* 154 (2016), 42 - 53. <http://dx.doi.org/http://dx.doi.org/10.1016/j.ces.2016.06.061>. – DOI <http://dx.doi.org/10.1016/j.ces.2016.06.061>. – ISSN 0009–2509. – Recent Advances in Energy Conversion and Storage Devices
- [245] SHEN, W.; VO, T. T.; KAPOOR, A.: Charging algorithms of lithium-ion batteries: An overview. In: *Industrial Electronics and Applications (ICIEA), 2012 7th IEEE Conference on IEEE*, 2012
- [246] SHEN, Y.: Adaptive online state-of-charge determination based on neuro-controller and neural network. In: *Energy Conversion and Management* 51 (2010), Nr. 5, 1093 - 1098. <http://dx.doi.org/http://dx.doi.org/10.1016/j.enconman.2009.12.015>. – DOI <http://dx.doi.org/10.1016/j.enconman.2009.12.015>. – ISSN 0196–8904
- [247] SHEN, Y.; LI, G.; ZHOU, S.; HU, Y.; YU, X.: RBF neural network and modified pid controller based State of Charge determination for lead-acid batteries. In: *2008 IEEE International Conference on Automation and Logistics IEEE*, 2008, pp. 769–774
- [248] SHEPHERD, C.: Theoretical design of primary and secondary cells. part 3. battery discharge equation / DTIC Document. 1963. – Forschungsbericht
- [249] SHI, Q.-S.; ZHANG, C.-H.; CUI, N.-X.: Estimation of battery state-of-charge using ν -support vector regression algorithm. In: *International Journal of Automotive Technology* 9 (2008), Nr. 6, pp. 759–764
- [250] SHI, Q.; ZHANG, C.; CUI, N.; ZHANG, X.: Battery state-of-charge estimation in electric vehicle using elman neural network method. In: *Proceedings of the 29th Chinese Control Conference IEEE*, 2010, pp. 5999–6003
- [251] SIEG, J.; BANDLOW, J.; MITSCH, T.; DRAGICEVIC, D.; MATERNA, T.; SPIER, B.; WITZENHAUSEN, H.; ECKER, M.; SAUER, D. U.: Fast charging of an electric vehicle lithium-ion battery at the limit of the lithium deposition process. In: *Journal of Power Sources* 427 (2019), pp. 260–270
- [252] SINGH, P.; JR., C. F.; REISNER, D.: Fuzzy logic modelling of state-of-charge and available capacity of nickel/metal hydride batteries. In: *Journal of Power Sources* 136 (2004), Nr. 2, 322 - 333. <http://dx.doi.org/http://dx.doi.org/10.1016/j.jpowsour.2004.03.035>. – DOI <http://dx.doi.org/10.1016/j.jpowsour.2004.03.035>. – ISSN 0378–7753. – Selected papers presented at the International Power Sources Symposium

- [253] SINGH, P.; KANERIA, S.; BROADHEAD, J.; WANG, X.; BURDICK, J.: Fuzzy logic estimation of SOH of 125Ah VRLA batteries. In: *Telecommunications Energy Conference, 2004. INTELEC 2004. 26th Annual International IEEE*, 2004, pp. 524–531
- [254] SINGH, P.; REISNER, D.: Fuzzy logic-based state-of-health determination of lead acid batteries. In: *Telecommunications Energy Conference, 2002. INTELEC. 24th Annual International IEEE*, 2002, pp. 583–590
- [255] SINGH, P.; VINJAMURI, R.; WANG, X.; REISNER, D.: Design and implementation of a fuzzy logic-based state-of-charge meter for Li-ion batteries used in portable defibrillators. In: *Journal of Power Sources* 162 (2006), Nr. 2, 829 - 836. <http://dx.doi.org/http://dx.doi.org/10.1016/j.jpowsour.2005.04.039>. – DOI <http://dx.doi.org/10.1016/j.jpowsour.2005.04.039>. – ISSN 0378–7753. – Special issue including selected papers from the International Power Sources Symposium 2005 together with regular papers
- [256] SINGH, P.; VINJAMURI, R.; WANG, X.; REISNER, D.: Fuzzy logic modeling of {EIS} measurements on lithium-ion batteries. In: *Electrochimica Acta* 51 (2006), Nr. 8–9, 1673 - 1679. <http://dx.doi.org/http://dx.doi.org/10.1016/j.electacta.2005.02.143>. – DOI <http://dx.doi.org/10.1016/j.electacta.2005.02.143>. – ISSN 0013–4686. – Electrochemical Impedance Spectroscopy Selection of papers from the 6th International Symposium (EIS 2004) 16-21 May 2004, Cocoa Beach, FL, {USA}
- [257] SOMMER, L. W.; RAGHAVAN, A.; KIESEL, P.; SAHA, B.; STAUDT, T.; LOCHBAUM, A.; GANGULI, A.; BAE, C.-J.; ALAMGIR, M.: Embedded fiber optic sensing for accurate state estimation in advanced battery management systems. In: *MRS Online Proceedings Library Archive* 1681 (2014)
- [258] SONG, L.; EVANS, J. W.: Electrochemical-Thermal Model of Lithium Polymer Batteries. In: *Journal of the Electrochemical Society* 147 (2000), Nr. 6, pp. 2086–2095
- [259] SPAGNOL, P.; ROSSI, S.; SAVARESI, S. M.: Kalman filter SoC estimation for Li-ion batteries. In: *2011 IEEE International Conference on Control Applications (CCA) IEEE*, 2011, pp. 587–592
- [260] STETZEL, K. D.; ALDRICH, L. L.; TRIMBOLI, M. S.; PLETT, G. L.: Electrochemical state and internal variables estimation using a reduced-order physics-based model of a lithium-ion cell and an extended Kalman filter. In: *Journal of Power Sources* 278 (2015), 490 - 505. <http://dx.doi.org/http://dx.doi.org/10.1016/j.jpowsour.2014.11.135>. – DOI <http://dx.doi.org/10.1016/j.jpowsour.2014.11.135>. – ISSN 0378–7753
- [261] SU, L.; ZHANG, J.; WANG, C.; ZHANG, Y.; LI, Z.; SONG, Y.; JIN, T.; MA, Z.: Identifying main factors of capacity fading in lithium ion cells using orthogonal design of experiments. In: *Applied Energy* 163 (2016), 201 - 210. <http://dx.doi.org/http://dx.doi.org/10.1016/j.apenergy.2015.11.014>. – DOI <http://dx.doi.org/10.1016/j.apenergy.2015.11.014>. – ISSN 0306–2619
- [262] SUN, B.; WANG, L.: The SOC estimation of NIMH battery pack for HEV based on BP neural network. In: *Intelligent Systems and Applications, 2009. ISA 2009. International Workshop on IEEE*, 2009, pp. 1–4
- [263] SUN, B.; WANG, L.; LIAO, C.: SOC estimation of NiMH battery for HEV based on adaptive neuro-fuzzy inference system. In: *2008 IEEE Vehicle Power and Propulsion Conference IEEE*, 2008

- [264] SUN, F.; HU, X.; ZOU, Y.; LI, S.: Adaptive unscented Kalman filtering for state of charge estimation of a lithium-ion battery for electric vehicles. In: *Energy* 36 (2011), Nr. 5, 3531 - 3540. <http://dx.doi.org/http://dx.doi.org/10.1016/j.energy.2011.03.059>. – DOI <http://dx.doi.org/10.1016/j.energy.2011.03.059>. – ISSN 0360-5442
- [265] SUN, F.; XIONG, R.; HE, H.: Estimation of state-of-charge and state-of-power capability of lithium-ion battery considering varying health conditions. In: *Journal of Power Sources* 259 (2014), 166 - 176. <http://dx.doi.org/http://dx.doi.org/10.1016/j.jpowsour.2014.02.095>. – DOI <http://dx.doi.org/10.1016/j.jpowsour.2014.02.095>. – ISSN 0378-7753
- [266] TAHERI, P.; HSIEH, S.; BAHRAMI, M.: Investigating electrical contact resistance losses in lithium-ion battery assemblies for hybrid and electric vehicles. In: *Journal of Power Sources* 196 (2011), Nr. 15, 6525 - 6533. <http://dx.doi.org/http://dx.doi.org/10.1016/j.jpowsour.2011.03.056>. – DOI <http://dx.doi.org/10.1016/j.jpowsour.2011.03.056>. – ISSN 0378-7753
- [267] TAKANO, K.; SAITO, Y.; KANARI, K.; NOZAKI, K.; KATO, K.; NEGISHI, A.; KATO, T.: Entropy change in lithium ion cells on charge and discharge. In: *Journal of Applied Electrochemistry* 32 (2002), Nr. 3, 251-258. <http://dx.doi.org/10.1023/A:1015547504167>. – DOI [10.1023/A:1015547504167](http://dx.doi.org/10.1023/A:1015547504167). – ISSN 1572-8838
- [268] TANG, X.; WANG, Y.; CHEN, Z.: A method for state-of-charge estimation of LiFePO₄ batteries based on a dual-circuit state observer. In: *Journal of Power Sources* 296 (2015), 23 - 29. <http://dx.doi.org/http://dx.doi.org/10.1016/j.jpowsour.2015.07.028>. – DOI <http://dx.doi.org/10.1016/j.jpowsour.2015.07.028>. – ISSN 0378-7753
- [269] TEUTSCH, T.: *Methods for Lithium-ion Cell Characterization and Model-Based Approach for State of Charge Determination*, Technical University of Munich, Diplomarbeit, 2013
- [270] THOMAS, K. E.; BOGATU, C.; NEWMAN, J.: Measurement of the entropy of reaction as a function of state of charge in doped and undoped lithium manganese oxide. In: *Journal of the Electrochemical Society* 148 (2001), Nr. 6, pp. A570-A575
- [271] THOMAS, K. E.; NEWMAN, J.: Heats of mixing and of entropy in porous insertion electrodes. In: *Journal of Power Sources* 119-121 (2003), 844 - 849. [http://dx.doi.org/http://dx.doi.org/10.1016/S0378-7753\(03\)00283-0](http://dx.doi.org/http://dx.doi.org/10.1016/S0378-7753(03)00283-0). – DOI [http://dx.doi.org/10.1016/S0378-7753\(03\)00283-0](http://dx.doi.org/10.1016/S0378-7753(03)00283-0). – ISSN 0378-7753. – Selected papers presented at the 11th International Meeting on Lithium Batteries
- [272] TONG, S.; LACAP, J. H.; PARK, J. W.: Battery state of charge estimation using a load-classifying neural network. In: *Journal of Energy Storage* 7 (2016), 236 - 243. <http://dx.doi.org/http://dx.doi.org/10.1016/j.est.2016.07.002>. – DOI <http://dx.doi.org/10.1016/j.est.2016.07.002>. – ISSN 2352-152X
- [273] TÓTH, R.: *Modeling and identification of linear parameter-varying systems*, Springer, 2010
- [274] TROXLER, Y.; WU, B.; MARINESCU, M.; YUFIT, V.; PATEL, Y.; MARQUIS, A. J.; BRANDON, N. P.; OFFER, G. J.: The effect of thermal gradients on the performance of lithium-ion batteries. In: *Journal of Power Sources* 247 (2014), 1018 - 1025. <http://dx.doi.org/http://dx.doi.org/10.1016/j.jpowsour.2013.06.084>. – DOI <http://dx.doi.org/10.1016/j.jpowsour.2013.06.084>. – ISSN 0378-7753

- [275] TULSYAN, A.; TSAI, Y.; GOPALUNI, R. B.; BRAATZ, R. D.: State-of-charge estimation in lithium-ion batteries: A particle filter approach. In: *Journal of Power Sources* 331 (2016), 208 - 223. <http://dx.doi.org/http://dx.doi.org/10.1016/j.jpowsour.2016.08.113>. – DOI <http://dx.doi.org/10.1016/j.jpowsour.2016.08.113>. – ISSN 0378-7753
- [276] UCHIDA, I.; ISHIKAWA, H.; MOHAMEDI, M.; UMEDA, M.: AC-impedance measurements during thermal runaway process in several lithium/polymer batteries. In: *Journal of Power Sources* 119-121 (2003), pp. 821 - 825. [http://dx.doi.org/http://dx.doi.org/10.1016/S0378-7753\(03\)00248-9](http://dx.doi.org/http://dx.doi.org/10.1016/S0378-7753(03)00248-9). – DOI [http://dx.doi.org/10.1016/S0378-7753\(03\)00248-9](http://dx.doi.org/10.1016/S0378-7753(03)00248-9). – ISSN 0378-7753. – Selected papers presented at the 11th International Meeting on Lithium Batteries
- [277] UNTERRIEDER, C.; PRIEWASSER, R.; MARSILI, S.; HUEMER, M.: Battery State Estimation Using Mixed Kalman/Hinfinity, Adaptive Luenberger and Sliding Mode Observer. In: *2013 IEEE Vehicle Power and Propulsion Conference (VPPC)* IEEE, 2013, pp. 1-6
- [278] VISWANATHAN, V. V.; CHOI, D.; WANG, D.; XU, W.; TOWNE, S.; WILLIFORD, R. E.; ZHANG, J.-G.; LIU, J.; YANG, Z.: Effect of entropy change of lithium intercalation in cathodes and anodes on Li-ion battery thermal management. In: *Journal of Power Sources* 195 (2010), Nr. 11, 3720 - 3729. <http://dx.doi.org/http://dx.doi.org/10.1016/j.jpowsour.2009.11.103>. – DOI <http://dx.doi.org/10.1016/j.jpowsour.2009.11.103>. – ISSN 0378-7753
- [279] VLADIMÍR, K.: Control theory and forty years of IFAC: A personal view. In: *IFAC Newsletter* (1997), pp. 4
- [280] VO, T. T.; CHEN, X.; SHEN, W.; KAPOOR, A.: New charging strategy for lithium-ion batteries based on the integration of Taguchi method and state of charge estimation. In: *Journal of Power Sources* 273 (2015), 413 - 422. <http://dx.doi.org/http://dx.doi.org/10.1016/j.jpowsour.2014.09.108>. – DOI <http://dx.doi.org/10.1016/j.jpowsour.2014.09.108>. – ISSN 0378-7753
- [281] WAAG, W.; FLEISCHER, C.; SAUER, D. U.: On-line estimation of lithium-ion battery impedance parameters using a novel varied-parameters approach. In: *Journal of Power Sources* 237 (2013), 260 - 269. <http://dx.doi.org/http://dx.doi.org/10.1016/j.jpowsour.2013.03.034>. – DOI <http://dx.doi.org/10.1016/j.jpowsour.2013.03.034>. – ISSN 0378-7753
- [282] WAAG, W.; KÄBITZ, S.; SAUER, D. U.: Experimental investigation of the lithium-ion battery impedance characteristic at various conditions and aging states and its influence on the application. In: *Applied Energy* 102 (2013), 885 - 897. <http://dx.doi.org/http://dx.doi.org/10.1016/j.apenergy.2012.09.030>. – DOI <http://dx.doi.org/10.1016/j.apenergy.2012.09.030>. – ISSN 0306-2619. – Special Issue on Advances in sustainable biofuel production and use - {XIX} International Symposium on Alcohol Fuels - {ISAF}
- [283] WAHLSTROM, M.: Design of a Battery State Estimator Using a Dual Extended Kalman Filter. In: *University of Waterloo* (2011)
- [284] WALDMANN, T.; KASPER, M.; WOHLFAHRT-MEHRENS, M.: Optimization of Charging Strategy by Prevention of Lithium Deposition on Anodes in high-energy Lithium-ion Batteries – Electrochemical Experiments. In: *Electrochimica Acta* 178 (2015), 525 - 532. <http://dx.doi.org/http://dx.doi.org/10.1016/j.electacta.2015.08.056>. – DOI <http://dx.doi.org/10.1016/j.electacta.2015.08.056>. – ISSN 0013-4686

- [285] WALKER, E.; RAYMAN, S.; WHITE, R. E.: Comparison of a particle filter and other state estimation methods for prognostics of lithium-ion batteries. In: *Journal of Power Sources* 287 (2015), 1 - 12. <http://dx.doi.org/http://dx.doi.org/10.1016/j.jpowsour.2015.04.020>. – DOI <http://dx.doi.org/10.1016/j.jpowsour.2015.04.020>. – ISSN 0378–7753
- [286] WANG, C.-W.; SASTRY, A. M.: Mesoscale modeling of a Li-ion polymer cell. In: *Journal of the Electrochemical Society* 154 (2007), Nr. 11, pp. A1035–A1047
- [287] WANG, C.; SRINIVASAN, V.: Computational battery dynamics (CBD)—electrochemical/thermal coupled modeling and multi-scale modeling. In: *Journal of Power Sources* 110 (2002), Nr. 2, 364 - 376. [http://dx.doi.org/http://dx.doi.org/10.1016/S0378-7753\(02\)00199-4](http://dx.doi.org/http://dx.doi.org/10.1016/S0378-7753(02)00199-4). – DOI [http://dx.doi.org/10.1016/S0378-7753\(02\)00199-4](http://dx.doi.org/10.1016/S0378-7753(02)00199-4). – ISSN 0378–7753
- [288] WANG, H.; HU, D.: Comparison of SVM and LS-SVM for regression. In: *2005 International Conference on Neural Networks and Brain* Bd. 1 IEEE, 2005, pp. 279–283
- [289] WANG, J.; CAO, B.; CHEN, Q.; WANG, F.: Combined state of charge estimator for electric vehicle battery pack. In: *Control Engineering Practice* 15 (2007), Nr. 12, 1569 - 1576. <http://dx.doi.org/http://dx.doi.org/10.1016/j.conengprac.2007.03.004>. – DOI <http://dx.doi.org/10.1016/j.conengprac.2007.03.004>. – ISSN 0967–0661
- [290] WANG, N.; QIN, Y.: Research on State of Charge Estimation of Batteries Used in Electric Vehicle. In: *Power and Energy Engineering Conference (APPEEC), 2011 Asia-Pacific*, 2011, pp. 1–4
- [291] WANG, T.-W.; YANG, M.-J.; SHYU, K.-K.; LAI, C.-M.: Design fuzzy SOC estimation for sealed lead-acid batteries of electric vehicles in Reflex TM. In: *2007 IEEE International Symposium on Industrial Electronics* IEEE, 2007, pp. 95–99
- [292] WANG, W.; GAO, Z.: A comparison study of advanced state observer design techniques. In: *American Control Conference, 2003. Proceedings of the 2003* Bd. 6 IEEE, 2003, pp. 4754–4759
- [293] WANG, W.; WANG, D.; WANG, X.; LI, T.; AHMED, R.; HABIBI, S.; EMADI, A.: Comparison of Kalman Filter-based state of charge estimation strategies for Li-Ion batteries. In: *Transportation Electrification Conference and Expo (ITEC), 2016 IEEE* IEEE, 2016, pp. 1–6
- [294] WANG, Y.; ZHANG, C.; CHEN, Z.: A method for state-of-charge estimation of LiFePO₄ batteries at dynamic currents and temperatures using particle filter. In: *Journal of Power Sources* 279 (2015), 306 - 311. <http://dx.doi.org/http://dx.doi.org/10.1016/j.jpowsour.2015.01.005>. – DOI <http://dx.doi.org/10.1016/j.jpowsour.2015.01.005>. – ISSN 0378–7753. – 9th International Conference on Lead-Acid Batteries – {LABAT} 2014
- [295] WANG, Y.; ZHANG, C.; CHEN, Z.: An adaptive remaining energy prediction approach for lithium-ion batteries in electric vehicles. In: *Journal of Power Sources* 305 (2016), 80 - 88. <http://dx.doi.org/http://dx.doi.org/10.1016/j.jpowsour.2015.11.087>. – DOI <http://dx.doi.org/10.1016/j.jpowsour.2015.11.087>. – ISSN 0378–7753
- [296] WATRIN, N.; BLUNIER, B.; MIRAOU, A.: Review of adaptive systems for lithium batteries State-of-Charge and State-of-Health estimation. In: *2012 IEEE Transportation Electrification Conference and Expo (ITEC)* IEEE, 2012, pp. 1–6

- [297] WEIGERT, T.; TIAN, Q.; LIAN, K.: State-of-charge prediction of batteries and battery-supercapacitor hybrids using artificial neural networks. In: *Journal of Power Sources* 196 (2011), Nr. 8, 4061 - 4066. <http://dx.doi.org/http://dx.doi.org/10.1016/j.jpowsour.2010.10.075>. – DOI <http://dx.doi.org/10.1016/j.jpowsour.2010.10.075>. – ISSN 0378-7753
- [298] WENG, C.; CUI, Y.; SUN, J.; PENG, H.: On-board state of health monitoring of lithium-ion batteries using incremental capacity analysis with support vector regression. In: *Journal of Power Sources* 235 (2013), 36 - 44. <http://dx.doi.org/http://dx.doi.org/10.1016/j.jpowsour.2013.02.012>. – DOI <http://dx.doi.org/10.1016/j.jpowsour.2013.02.012>. – ISSN 0378-7753
- [299] WENG, C.; SUN, J.; PENG, H.: A unified open-circuit-voltage model of lithium-ion batteries for state-of-charge estimation and state-of-health monitoring. In: *Journal of Power Sources* 258 (2014), 228 - 237. <http://dx.doi.org/http://dx.doi.org/10.1016/j.jpowsour.2014.02.026>. – DOI <http://dx.doi.org/10.1016/j.jpowsour.2014.02.026>. – ISSN 0378-7753
- [300] WIEGMAN, H. L.; LORENZ, R. D.: *Battery state estimation and control for power buffering applications*, University of Wisconsin-Madison, Diss., 1999
- [301] WILHELM, J.; SEIDLMAYER, S.; KEIL, P.; SCHUSTER, J.; KRIELE, A.; GILLES, R.; JOSSEN, A.: Cycling capacity recovery effect: A coulombic efficiency and post-mortem study. In: *Journal of Power Sources* 365 (2017), pp. 327-338
- [302] WU, G.; ZHU, C.; CHAN, C.: Comparison of the first order and the second order equivalent circuit model applied in state of charge estimation for battery used in electric vehicles. In: *Journal of Asian Electric Vehicles* 8 (2010), Nr. 1, pp. 1357-1362
- [303] WU, T.; WANG, M.; XIAO, Q.; WANG, X.: The SOC estimation of power Li-ion battery based on ANFIS model. In: *Smart Grid and Renewable Energy* 3 (2012), Nr. 01, pp. 51
- [304] XIA, B.; CHEN, C.; TIAN, Y.; SUN, W.; XU, Z.; ZHENG, W.: A novel method for state of charge estimation of lithium-ion batteries using a nonlinear observer. In: *Journal of Power Sources* 270 (2014), 359 - 366. <http://dx.doi.org/http://dx.doi.org/10.1016/j.jpowsour.2014.07.103>. – DOI <http://dx.doi.org/10.1016/j.jpowsour.2014.07.103>. – ISSN 0378-7753
- [305] XIONG, R.; HE, H.; SUN, F.; ZHAO, K.: Evaluation on state of charge estimation of batteries with adaptive extended Kalman filter by experiment approach. In: *IEEE Transactions on Vehicular Technology* 62 (2013), Nr. 1, pp. 108-117
- [306] XIONG, R.; SUN, F.; CHEN, Z.; HE, H.: A data-driven multi-scale extended Kalman filtering based parameter and state estimation approach of lithium-ion polymer battery in electric vehicles. In: *Applied Energy* 113 (2014), 463 - 476. <http://dx.doi.org/http://dx.doi.org/10.1016/j.apenergy.2013.07.061>. – DOI <http://dx.doi.org/10.1016/j.apenergy.2013.07.061>. – ISSN 0306-2619
- [307] XU, J.; DESHPANDE, R. D.; PAN, J.; CHENG, Y.-T.; BATTAGLIA, V. S.: Electrode Side Reactions, Capacity Loss and Mechanical Degradation in Lithium-Ion Batteries. In: *Journal of The Electrochemical Society* 162 (2015), Nr. 10, pp. A2026-A2035
- [308] XU, J.; MI, C. C.; CAO, B.; DENG, J.; CHEN, Z.; LI, S.: The state of charge estimation of lithium-ion batteries based on a proportional-integral observer. In: *IEEE Transactions on Vehicular Technology* 63 (2014), Nr. 4, pp. 1614-1621

- [309] XU, L.; WANG, J.; CHEN, Q.: Kalman filtering state of charge estimation for battery management system based on a stochastic fuzzy neural network battery model. In: *Energy Conversion and Management* 53 (2012), Nr. 1, 33 - 39. <http://dx.doi.org/http://dx.doi.org/10.1016/j.enconman.2011.06.003>. – DOI <http://dx.doi.org/10.1016/j.enconman.2011.06.003>. – ISSN 0196–8904
- [310] XU, M.; ZHANG, Z.; WANG, X.; JIA, L.; YANG, L.: A pseudo three-dimensional electrochemical–thermal model of a prismatic LiFePO₄ battery during discharge process. In: *Energy* 80 (2015), 303 - 317. <http://dx.doi.org/http://dx.doi.org/10.1016/j.energy.2014.11.073>. – DOI <http://dx.doi.org/10.1016/j.energy.2014.11.073>. – ISSN 0360–5442
- [311] XUE, L.; JIUCHUN, J.; CAIPING, Z.; WEIGE, Z.; BINGXIANG, S.: Effects analysis of model parameters uncertainties on battery SOC estimation using H-infinity observer. In: *2014 IEEE 23rd International Symposium on Industrial Electronics (ISIE)* IEEE, 2014, pp. 1647–1653
- [312] XUN, J.; LIU, R.; JIAO, K.: Numerical and analytical modeling of lithium ion battery thermal behaviors with different cooling designs. In: *Journal of Power Sources* 233 (2013), 47 - 61. <http://dx.doi.org/http://dx.doi.org/10.1016/j.jpowsour.2013.01.095>. – DOI <http://dx.doi.org/10.1016/j.jpowsour.2013.01.095>. – ISSN 0378–7753
- [313] YAN, J.; CHENG, Z.; XU, G.; QIAN, H.; XU, Y.: Fuzzy control for battery equalization based on state of charge. In: *Vehicular Technology Conference Fall (VTC 2010-Fall), 2010 IEEE 72nd* IEEE, 2010, pp. 1–7
- [314] YAN, J.; LI, C.; XU, G.; XU, Y.: A novel on-line self-learning state-of-charge estimation of battery management system for hybrid electric vehicle. In: *Intelligent Vehicles Symposium, 2009 IEEE* IEEE, 2009, pp. 1161–1166
- [315] YANHUI, Z.; WENJI, S.; SHILI, L.; ZIPING, F.; OTHER: A critical review on state of charge of batteries. In: *Journal of Renewable and Sustainable Energy* 5 (2013), Nr. 2, pp. 021403
- [316] YATSUI, M. W.; BAI, H.: Kalman filter based state-of-charge estimation for lithium-ion batteries in hybrid electric vehicles using pulse charging. In: *2011 IEEE Vehicle Power and Propulsion Conference* IEEE, 2011, pp. 1–5
- [317] YE, Y.; SAW, L. H.; SHI, Y.; SOMASUNDARAM, K.; TAY, A. A.: Effect of thermal contact resistances on fast charging of large format lithium ion batteries. In: *Electrochimica Acta* 134 (2014), 327 - 337. <http://dx.doi.org/http://dx.doi.org/10.1016/j.electacta.2014.04.134>. – DOI <http://dx.doi.org/10.1016/j.electacta.2014.04.134>. – ISSN 0013–4686
- [318] YE, Y.; SHI, Y.; CAI, N.; LEE, J.; HE, X.: Electro-thermal modeling and experimental validation for lithium ion battery. In: *Journal of Power Sources* 199 (2012), 227 - 238. <http://dx.doi.org/http://dx.doi.org/10.1016/j.jpowsour.2011.10.027>. – DOI <http://dx.doi.org/10.1016/j.jpowsour.2011.10.027>. – ISSN 0378–7753
- [319] YE, Y.; SHI, Y.; SAW, L. H.; TAY, A. A.: An electro-thermal model and its application on a spiral-wound lithium ion battery with porous current collectors. In: *Electrochimica Acta* 121 (2014), 143 - 153. <http://dx.doi.org/http://dx.doi.org/10.1016/j.electacta.2013.12.122>. – DOI <http://dx.doi.org/10.1016/j.electacta.2013.12.122>. – ISSN 0013–4686

- [320] YE, Y.; SHI, Y.; TAY, A. A.: Electro-thermal cycle life model for lithium iron phosphate battery. In: *Journal of Power Sources* 217 (2012), 509 - 518. <http://dx.doi.org/http://dx.doi.org/10.1016/j.jpowsour.2012.06.055>. – DOI <http://dx.doi.org/10.1016/j.jpowsour.2012.06.055>. – ISSN 0378-7753
- [321] YI, J.; KOO, B.; SHIN, C. B.: Three-dimensional modeling of the thermal behavior of a lithium-ion battery module for hybrid electric vehicle applications. In: *Energies* 7 (2014), Nr. 11, pp. 7586-7601
- [322] ZENATI, A.; DESPREZ, P.; RAZIK, H.: Estimation of the SOC and the SOH of Li-ion Batteries, by combining Impedance Measurements with the Fuzzy Logic Inference. In: *IECON 2010-36th Annual Conference on IEEE Industrial Electronics Society IEEE*, 2010, pp. 1773-1778
- [323] ZENATI, A.; DESPREZ, P.; RAZIK, H.; RAEL, S.: Impedance measurements combined with the fuzzy logic methodology to assess the SOC and SOH of lithium-ion cells. In: *2010 IEEE Vehicle Power and Propulsion Conference IEEE*, 2010, pp. 1-6
- [324] ZHANG, C.; LI, K.; DENG, J.: Real-time estimation of battery internal temperature based on a simplified thermoelectric model. In: *Journal of Power Sources* 302 (2016), 146 - 154. <http://dx.doi.org/http://dx.doi.org/10.1016/j.jpowsour.2015.10.052>. – DOI <http://dx.doi.org/10.1016/j.jpowsour.2015.10.052>. – ISSN 0378-7753
- [325] ZHANG, D.; POPOV, B. N.; WHITE, R. E.: Modeling lithium intercalation of a single spinel particle under potentiodynamic control. In: *Journal of The Electrochemical Society* 147 (2000), Nr. 3, pp. 831-838
- [326] ZHANG, F.; REHMAN, M. M. U.; WANG, H.; LEVRON, Y.; PLETT, G.; ZANE, R.; MAKSIMOVIĆ, D.: State-of-charge estimation based on microcontroller-implemented sigma-point Kalman filter in a modular cell balancing system for Lithium-Ion battery packs. In: *2015 IEEE 16th Workshop on Control and Modeling for Power Electronics (COMPEL) IEEE*, 2015, pp. 1-7
- [327] ZHANG, N.; LIU, K.: The prediction of SOC based on multiple dimensioned Support Vector Machine. In: *Mechanic Automation and Control Engineering (MACE), 2011 Second International Conference on*, 2011, pp. 1786-1788
- [328] ZHANG, S.; YANG, L.; ZHAO, X.; QIANG, J.: A {GA} optimization for lithium-ion battery equalization based on {SOC} estimation by {NN} and {FLC}. In: *International Journal of Electrical Power Energy Systems* 73 (2015), 318 - 328. <http://dx.doi.org/http://dx.doi.org/10.1016/j.ijepes.2015.05.018>. – DOI <http://dx.doi.org/10.1016/j.ijepes.2015.05.018>. – ISSN 0142-0615
- [329] ZHANG, W.; SHI, W.; MA, Z.: Adaptive unscented Kalman filter based state of energy and power capability estimation approach for lithium-ion battery. In: *Journal of Power Sources* 289 (2015), 50 - 62. <http://dx.doi.org/http://dx.doi.org/10.1016/j.jpowsour.2015.04.148>. – DOI <http://dx.doi.org/10.1016/j.jpowsour.2015.04.148>. – ISSN 0378-7753
- [330] ZHANG, X.: Thermal analysis of a cylindrical lithium-ion battery. In: *Electrochimica Acta* 56 (2011), Nr. 3, 1246 - 1255. <http://dx.doi.org/http://dx.doi.org/10.1016/j.electacta.2010.10.054>. – DOI <http://dx.doi.org/10.1016/j.electacta.2010.10.054>. – ISSN 0013-4686

- [331] ZHONG, F.; LI, H.; ZHONG, S.; ZHONG, Q.; YIN, C.: An {SOC} estimation approach based on adaptive sliding mode observer and fractional order equivalent circuit model for lithium-ion batteries. In: *Communications in Nonlinear Science and Numerical Simulation* 24 (2015), Nr. 1–3, 127 - 144. <http://dx.doi.org/http://dx.doi.org/10.1016/j.cnsns.2014.12.015>. – DOI <http://dx.doi.org/10.1016/j.cnsns.2014.12.015>. – ISSN 1007–5704
- [332] ZHOU, F.; WANG, L.; LIN, H.; LV, Z.: High accuracy state-of-charge online estimation of EV/HEV lithium batteries based on Adaptive Wavelet Neural Network. In: *ECCE Asia Dunder (ECCE Asia), 2013 IEEE IEEE*, 2013, pp. 513–517

List of Figures

2.1	Comparison of the specific energy of lead-, nickel-, and lithium-based cells [38].	5
2.2	Summerized details of current commercial LIBs normalized to the scale of 0 to 5, where 5 is the best scenario and 0 is the worst scenario. The figure is based on the data of [38, 71].	5
2.3	A) DUT under load, B) Transfer function representation of the DUT under load	6
2.4	Overview of the interaction between the models in this thesis	14
2.5	A) A simple ECM representing a cell with a resistor, and OCV source, B) ECM with 1RC element to capture the cell dynamics, C) ECM with 2RC elements for a better physical interpretation, D) ECM with three or more RCs (the physical interpretation of the parameters can be challenging), may produce a better fit, E) ECM used for LABs, including surface and bulk capacitor, F) A fractional model (CPE: constant phase element)	15
2.6	Modified HPPC profile used to parameterize the LIB in the time-domain	17
2.7	A) LIB typical voltage response to the current pulses, respective voltage points are marked (“P”), B) No load, ohmic, and dynamic behavior of the LIB ($I(t)$: load current, and $V_t(t)$: terminal voltage response)	18
2.8	Time-domain LIB model (LIB-ECM) used to reproduce the LIB terminal voltage, OCV reproduces the no-load behavior of the cell, which is represented either by analytical, or empiric expressions. All parameters and OCV are a function of SOC, temperature, and SOH	19
2.9	A) Impedance path at high frequencies dominated by R_i and current flows through C_1 , B) Impedance path at low frequencies dominated by $R_i + R_1$	22
2.10	A) General Nyquist impedance diagram of a LIB, where the high frequency depressed semicircle represents the SEI layer, and the second depressed semicircle, represents the charge transfer, and electrochemical double-layer. Effects caused by the mass transport are represented by the Warburg impedance, B) A simple RC model represented on the Nyquist diagram	23
2.11	Schematic explanation of BOL, EOL, SOH, and RUL	31
2.12	Chart showing the schematic of the test procedure used to periodically extract the cell parameters	32
2.13	Dynamic process represented by discrete state-space model [201]	33
2.14	Graphical illustration of the sequential Bayesian interface	34
2.15	Schematic illustration of various estimation problems; dashed lines represent the available measurements up to the time “m”	35
2.16	A) A representation of a dynamic system and its open-loop model, B) Closed-loop system model for state filtering including adaption scheme (for signal descriptions see Section 2.7.3.1). The adaption part can be a PID controller (see Figure 2.19, how SOC (x_k) as a state gets corrected, and Figure 2.20 the PID controller for the adaption part)	35
2.17	Voltage based method SOC estimation	38

2.18	Parameter/state initialization scheme	40
2.19	Implementation of the enhanced SOC estimator based on the Ah-counting method (Equation 2.72), combined with the OCV-based SOC detection technique used for algorithm initialization. The adaption part is a PI controller as shown in Figure 2.20	40
2.20	PI controller Simulink schematic	50
2.21	Series connection of two LIB-ECMs: A) 1RC, B) 2RC	53
2.22	Parallel connection of two LIB-ECMs: A) 1RC, B) 2RC	54
3.1	DUT mounted on the in-house custom-made cell holder	56
3.2	Complete test setup used in this work. Cell models and state detection algorithms were implemented in the HIL system and the BMS for evaluation purposes	58
3.3	Various in-house custom-made cell holders with gold-plated Kelvin probes and nickel-plated copper bars providing a four-wire measurement capability	59
3.4	Testing flowcharts containing calendar-life and cycle-life aging experiments	59
3.5	Comparison of CCCV vs. CC charging of a new cell	60
3.6	A) US EPA urban dynamometer driving schedule “UDDS” (also known as FTP), B) EV battery pack power output, C) Cell-level power data used for drive-cycle implementation	63
3.7	Usable capacity evolution over the cycle number: A) at 15°C, B) at 25°C, C) at 40°C, and D) at 60°C	64
3.8	Averaged R_i during cycle-life aging at A) 15°C, B) 25°C, C) 40°C, and D) 60°C	65
3.9	Averaged R_1 during cycle-life aging at A) 15°C, B) 25°C, C) 40°C, and D) 60°C	65
3.10	Averaged C_1 during cycle-life aging at A) 15°C, B) 25°C, C) 40°C, and D) 60°C	66
3.11	Averaged OCV measured at 25°C for cycle-life aging at A) 15°C, B) 25°C, C) 40°C, D) 60°C	66
3.12	Cycle-life aging (FTP-based) investigation of the cell’s usable capacity at A) 25°C and B) 40°C	67
3.13	Temperature effect on the EIS measurements, results for Kok-505 at 60% SOC: A) BOL, B) After 200 FTP cycles, C) After 400 FTP cycles, and D) After 600 FTP cycles	68
3.14	A) R_i from EIS measurement of the Kok-505 (FTP cycle at 25°C) and 60% SOC, B) R_i from EIS measurement of the Kok-529 (FTP cycle at 40°C) and 60% SOC, C) Normalized averaged R_i (Kok-502, Kok-504, Kok-505) from EIS measurement (FTP cycle at 25°C) and 60% SOC, D) Normalized averaged R_i (Kok-527, Kok-528, Kok-529) from EIS measurement (FTP cycle at 40°C) and 60% SOC	68
3.15	A) R_{ct} from EIS measurements of the Kok-505 (FTP cycle at 25°C) and 60% SOC, B) R_{ct} from EIS measurements of the Kok-529 (FTP cycle at 40°C) and 60% SOC	69
3.16	A) Kok-505 R_i frequencies, B) Kok-505 R_{ct} frequencies, C) Kok-529 R_i frequencies, D) Kok-529 R_{ct} frequencies	69
3.17	Normalized discharge capacity during calendar-aging at A) 10°C, B) 25°C, and C) 60°C. Normalized ohmic resistance at 60% SOC during calendar-aging at D) 10°C, E) 25°C, and F) 60°C	71
4.1	Time-domain representation of the cell voltage model with 1RC, used as LIB model (LIB-ECM) in this thesis	72
4.2	100 hr discharge with 0.01 C to approximate the OCV vs. 11 points OCV measurement vs. 41 points OCV measurement	73

4.3	A) OCV curve over the full range of SOC vs. the OCV-fit via polynomial function (9 th order, B) First derivative of the OCV with respect to SOC	73
4.4	A) A parallel RC circuit, B) Simulink implementation of a parallel RC circuit	74
4.5	A) OCV in series with the cell's ohmic resistance B) Simulink implementation of OCV in series with the cell's ohmic resistance	74
4.6	A) 1C discharge current implemented on the fresh cell at the controlled temperature of 25°C, B) SOC calculated with Ah-counting method (open-loop), C) Comparison between the measured terminal voltage, and the open-loop ECM voltage (no model correction), D) The relative error of the ECM voltage	75
4.7	3RC Ladder to approximate the ZARC element (approximation of the depressed semi-circle in the EIS Nyquist diagram)	76
4.8	Approximation of the Warburg element with N ladders of RC circuits	76
4.9	Voltage model of the cell based on the EIS measurement (for simulation, inductor "L" was neglected)	76
4.10	Kok-014 measurement and simulation from the Sg taxi drive-cycle at the BOL, and the FTP at the EOL. Frequency-domain model was parameterized from the EIS data. The model used Ah-counting method for SOC estimation and a P-controller	77
4.11	Temperature development of a new cell at different discharge currents of 0.5C, 1C (For 1C full charge and discharge temperature development, refer to figure 3.5), 2C, and 3C	78
4.12	Interaction between the ECM, and the TECM	79
4.13	1D TECM used to estimate the cell's core and surface temperature in the z coordinate	80
4.14	A) Test current profile including 20 pulses each 600A discharge for 10 s, B) Verification of the enhanced ECM voltage with the measurement, C) Absolute error of the ECM voltage	80
4.15	A) ECM ohmic resistance as a function of SOC B) ECM 10 s resistance as a function of SOC	81
4.16	A) Entropy change measurement as a function of SOC, B) Cell entropy change under the load profile shown in Figure 4.14 A	82
4.17	A) Ohmic irreversible heat loss, B) Entropic reversible heat loss	82
4.18	A) Measurement and simulation results for both core and surface temperature estimations using TECM and RLS methods, B) Error of TECM and RLS temperature estimation	83
4.19	A) TECM temperature difference between the cell's simulated core temperature, and the cell's surface temperature, B) Temperature rise, partially zoomed from Figure 4.18 A	84
4.20	A) Current profile containing 15C discharge pulses, FTP drive-cycle, and the reversed FTP drive-cycle profile for charging of the cell, B) Voltage response of the cell, C) Measured and simulated temperature, RLS optimization was used to enhance the TECM accuracy	84
5.1	Software architecture of the combined cell models and algorithms	86
5.2	Principle of digital signal filtering, the filter can be a HPF, a LPF or a BPF	87
5.3	The principle of HPF and LPF Simulink implementation. With the initial input, each filter can be initialized independently, and the time constant defines the corner frequency	87
5.4	The FTP drive-cycle implemented on the cell at 25°C and at BOL	88
5.5	A) The voltage response of the cell to the FTP drive-cycle, B) Dynamic part of the voltage response (V_z)	88

5.6	Block diagram of the proposed method to extract the current flowing into the RC-branch. For that, the HPF time constant should be equal to the time constant of the ECM model (10 s)	89
5.7	A) ECM- I_{C1} vs. I_{C1} extracted from the filter-based method, B) ECM- I_{R1} vs. I_{R1} extracted from the filter-based method, C) I_{C1} zoomed for 1000 s for a better visualization of I_{C1} , D) I_{R1} zoomed for 1000 for a better visualization of I_{R1}	89
5.8	A) OCV estimated from the low-pass filtering of the terminal voltage (see Figure 5.3 for the LPF design), OCV estimated from the filter-based method was evaluated with the OCV calculated by the ECM	90
5.9	Schematic of the filter-based method; including the filters, and R-observer. Time constant of HPF1, and HPF2 were set to 30 s. Time constant of the LPF was set to 120 s	90
5.10	Schematic of the R-observer design	91
5.11	The comparison between the dynamic resistance estimated from the filter-based method, and the total resistance ($R_i + R_1$) calculated from the ECM	91
5.12	A) Measured voltage vs. estimated voltage based on the filter-based method, B) The relative error of estimated voltage based on the filter-based method	92
5.13	A) The current profile containing CCCV charge, and the FTP drive-cycle for aged cell (2000 cycle), B) A comparison between the estimated total resistance between the ECM model and the filter-based method, C) Filter-based estimated voltage in comparison with the measured voltage	92
5.14	A) Estimated cell terminal voltage by SMO, B) Absolute error of the estimated terminal voltage by SMO	95
5.15	A) Cell SOC estimation performance: a comparison between the combined ECM-PI controller, the SMO vs. the reference SOC, B) SOC estimation error	96
5.16	Estimated RC element voltage by the SMO and the ECM	96
5.17	A) Estimation of the cell terminal voltage by the EKF and the SMO, B) Absolute error of the estimated terminal voltage	98
5.18	A) A comparison between the EKF and the SMO convergence speed at the beginning of the dynamic current profile, B) A comparison between the EKF and the SMO accuracy at the end of the dynamic current profile	99
5.19	A) The SOC estimation performance of the EKF, SMO, filter-based technique, and enhanced combined ECM-PI controlled model; B) The error of the estimation	99
6.1	Location of the temperature sensors attached to the DUT	102
6.2	A) A current profile with different long term interval phases used to verify the BMS cell-level performance: a mixture of high current pulses, CC charges/discharges, CCCV charges, and dynamic drive-cycles, B) The BMS terminal voltage model in comparison with the measured voltage, C) The BMS voltage modeling error	103
6.3	A) BMS SOC estimation with the EKF method vs. the reference SOC with the Ah-counting method, B) SOC estimation error, C) BMS estimated cell surface temperature vs. sensor measurement, D) Surface temperature estimation error	104

6.4	A) A comparison between the battery current measurement by the BMS, HIL system, and Digatron tester, B) Cell voltage simulation by the BMS, HIL system, and sensor measurement, C) A comparison between the estimated SOC by the BMS, HIL system and reference SOC (Ah counter of the Digatron battery tester)	105
6.5	Results zoomed from Figure 6.4. A) Terminal voltage model estimated by the BMS vs. the HIL and was compared to the reference measured voltage by the Digatron battery tester voltage sensor, B) The estimated SOC comparison between the BMS, HIL and the reference SOC	106
6.6	General schematic of the pack's signal flow used for the modeling	107
6.7	Battery pack configuration, including one BMS master and nine BMS slaves. There is one slave for every two stacks (a total of 18 stacks with a configuration of 6S2P)	108
6.8	A) Stack simulation (high-level simulation) block configuration, B) Battery pack top-layer stack simulation inputs/outputs (the simulated pack voltage is the summation of all 18 stacks' simulated voltages)	109
6.9	A) A big-cell (parallel cell) block used to simulate two parallel cells (mid-level simulation), B) In each big-cell block, there exists a big-cell enhanced ECM model, TECM for parallel cells, filter-based method block, SMO and EKF block (low level simulation) . .	109
6.10	Battery pack current measured by the BMS	110
6.11	Battery pack weakest-cell voltage vs. strongest-cell voltage	111
6.12	Battery pack measured voltage vs. battery pack simulated voltage as the sum of the simulation of 108 big-cells (two parallel cells)	111
6.13	A) Battery pack dynamic current, B) Battery pack measured voltage vs. simulated voltage, C) Absolute error of the voltage simulation	113
6.14	A) The cells with the highest and the lowest resistances calculated by the ECM, B) Battery pack's dynamic resistance ($R_{d,pack}$) including 108 cells in series estimated by the filter-based estimator	114
6.15	Battery pack OCV calculated by the ECM model and the filter-based estimator model (LPF with a time constant of 120 s) during the dynamic load profile presented in Figure 6.13 A	115
6.16	The cell-pair with the lowest surface temperature in the pack vs. the estimated core temperature of this cell-pair, resulting from the current profile as shown in Figure 6.13 .	116
6.17	The battery pack SOC calculated with the Ah-counting method (reference method) vs. the estimated SOCs of the weakest pair and the strongest pair (EKF estimation)	116
6.18	Battery pack estimated SOC vs. big-cells SOCs estimated with various techniques and different initialization values	117
A.1	Density function of normal standard Gaussian distribution with zero mean and covariance equal to one: $P(0,1)$	160
B.2	The sliding mode observer design	162
C.3	Laboratory test setup	164
C.4	Schematic of the laboratory test chambers	164
C.5	Laboratory abuse chamber	164
C.6	EVA pack	164

List of Tables

2.1	A summary of electrochemical models from literature	13
2.2	Summary of ECMs used for terminal voltage simulation	16
2.3	Battery testing manuals used for EVs, PHEVs, and 12 V start/stop vehicles	16
2.4	A summary of a thermal LIB modeling, sorted based on the modeling technique, cell type, and cell chemistry	26
2.5	Reviews of SOC detection techniques available in the literature	30
2.6	State detection categorizes	37
2.7	SOC detection techniques based on the conventional methods	37
2.8	Advantages and disadvantages of SOC detection methods based on the voltage-based methods	38
2.9	Advantages and disadvantages of SOC detection methods based on the current-based methods	39
2.10	Advantages and disadvantages of SOC detection methods based on the impedance-based methods	41
2.11	Learning algorithms used for battery state detection	42
2.12	Available literature on different neural network methods used for battery state detection	42
2.13	Advantages and disadvantages of neural network algorithms for state, and parameter estimation gathered from the literature presented in Table 2.12	43
2.14	Available literature on the neuro-fuzzy combined method used for battery state detection	43
2.15	Available literature on the fuzzy logic method used for battery state detection	44
2.16	Available literature on other learning algorithm techniques used for battery state detection	45
2.17	Available literature on the variation of Kalman filter methods used for battery state detection	46
2.18	Available literature on the particle filter technique used for battery state detection	49
2.19	Available literature on observer algorithm techniques used for battery state detection	49
2.20	Literatures on hybrid techniques (a combination of the Kalman filter with other techniques) used for SOC detection	52
3.1	The DUT specification (manufactured by Kokam). Cell data sheet can be found in Appendix D.1	55
3.2	An overview of the cells used for the calendar-aging experiment	57
3.3	An overview of the cells used for the cycle-life experiments based on the accelerated aging profile with the SOC range of 0%-100%	57
3.4	Overview of the cells used for cycle-life experiments based on the FTP drive-cycle in order to simulate a real case scenario with the SOC range of 0%-100%	57
3.5	Testing equipment	58
3.6	1C (63 A) CCCV vs. CC charging comparison between a new cell and an aged cell at 25°C (for both charge protocols, the same cell was used)	61

3.7	1C (126 A) CCCV vs. CC charging comparison of two new parallel cells at 25°C	62
4.1	A comparison between the time-domain, and frequency-domain voltage modeling techniques	77
4.2	DUT thermal parameters	81
4.3	DUT physical parameters	82
5.1	The SMO coefficients calculation taken from Equations 5.10 to 5.12	94

Appendix

A.1 Discrete-time approximation

A continuous transfer function $H(s)$ can be discretized by some approximations. Bilinear transform is a first-order approximation of the natural logarithm function that is an exact mapping of the z -plane to the s -plane where z is the discretization operator. The inverse of this mapping ($H(z) \rightarrow H_p(s) |_{s=\frac{1}{T_s} \ln(z)}$) is called discretization, where T_s is the numerical integration with the step size of the sample time. The Laurent series expansion for $\ln(z)$ is:

$$\ln(z) = 2\left[\frac{z-1}{z+1} + \frac{1}{3}\left(\frac{z-1}{z+1}\right)^3 + \frac{1}{5}\left(\frac{z-1}{z+1}\right)^5 + \dots\right] \quad \text{for } \Re \geq 0 \quad \& \quad z \neq 0$$

The bilinear transform method uses the truncated series approximation:

$$s = \frac{1}{T_s} \ln(z) \approx \frac{2}{T_s} \left(\frac{z-1}{z+1}\right) = \frac{2}{T_s} \left(\frac{1-z^{-1}}{1+z^{-1}}\right) \quad (\text{A.1})$$

Equation A.1 is a general form of Tustin's method. The bilinear transform maps the left half of the s -plane to the interior of the unit circle, and thus preserves stability and avoids aliasing in the frequency response.

The right-sided z -transform while $z = e^{\sigma + j\omega T_s}$ holds is defined by:

$$X(z) = \sum_{n=0}^{\infty} x_n z^{-n} \quad (\text{A.2})$$

where T is the sampling time. If $\sigma = 0$, z transform is similar to the FFT described in Appendix A.4.

A.2 Gaussian (normal) distribution

Gaussian distribution is one of the most widely used distributions. This distribution has been used throughout this thesis to represent the standard process and measurement noise distribution. This type of probability distribution is used in solving estimation problems, machine learning, and filtering algorithms. In fact, in algorithms such as the KF family, the distribution of measurement and process noise does not have to be strictly zero-mean white Gaussian noise, while the filter is still able to track the parameter with an acceptable degree of performance.

Taking μ as the mean or expected value of \mathbf{x} and Σ as the covariance operator, we have:

$$\mu = \mathbb{E}\{\mathbf{x}\} = \int_{\mathbf{S}} \mathbf{x} P_{\mathbf{x}}(\mu, \Sigma) d\mathbf{x} \quad (\text{A.3})$$

$$\Sigma = \text{Cov}\{\mathbf{x}\} = \mathbb{E}\{(\mathbf{x} - \mu)(\mathbf{x} - \mu)^T\} \quad (\text{A.4})$$

where \mathbf{S} is the sample space with the dimension of the state vector \mathbf{x} . $P(\mathbf{x})$ is the probability density

function defined by:

$$P_{\mathbf{x}}(\boldsymbol{\mu}, \boldsymbol{\Sigma}) \triangleq \frac{1}{\sqrt{|\mathbf{2}\pi\boldsymbol{\Sigma}|}} e^{-\frac{1}{2}(\mathbf{x}-\boldsymbol{\mu})^T\boldsymbol{\Sigma}^{-1}(\mathbf{x}-\boldsymbol{\mu})} \quad (\text{A.5})$$

$P(\boldsymbol{\mu}, \boldsymbol{\Sigma})$ is the cumulative Gaussian distribution function, and, for a mean value of “zero” ($\boldsymbol{\mu} = \mathbf{0}$) and covariance of “one” ($\boldsymbol{\Sigma} = 1$), the distribution is based on the standard Gaussian distribution.

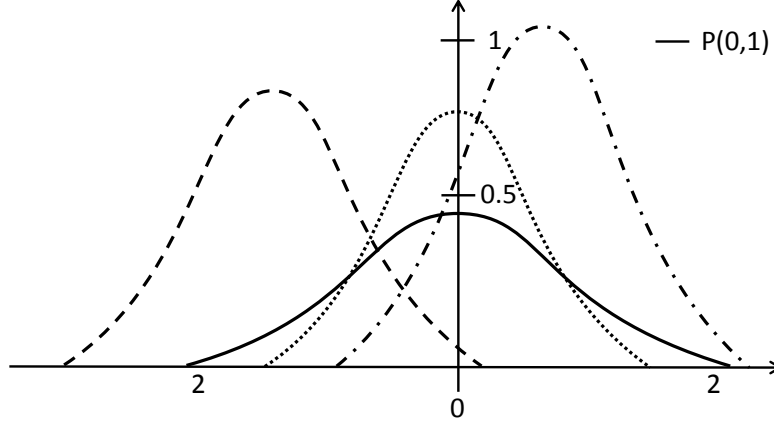


Figure A.1: Density function of normal standard Gaussian distribution with zero mean and covariance equal to one: $P(0,1)$

A.3 Matrix-operations

Computer processor speed is defined by operating-point operations per second ($\frac{Flops}{sec}$) and the Program execution time depends on the number of operating-point (N_{FLOPs}) operations, so the program execution time ($t_{execution}(sec)$) is defined by:

$$t_{execution}(sec) = \frac{N_{FLOPs}}{\frac{Flops}{sec}} \quad (\text{A.6})$$

In case of matrix operations, for instance in the Kalman filter algorithm if $A = \begin{pmatrix} a_{11} & a_{12} \\ a_{21} & a_{22} \end{pmatrix}$ is a

2×2 matrix, using Gauss-Jordan method $A^{-1} = \frac{1}{DET(A)} \begin{pmatrix} a_{22} & -a_{12} \\ -a_{21} & a_{11} \end{pmatrix}$ where determinant of A ($DET(A) = a_{11}a_{22} - a_{12}a_{21}$) must be non-zero.

If $B = \begin{pmatrix} b_{11} & b_{12} & b_{13} \\ b_{21} & b_{22} & b_{23} \\ b_{31} & b_{32} & b_{33} \end{pmatrix}$ and $DET(B) = b_{11}(b_{33}b_{22} - b_{32}b_{23}) - b_{21}(b_{33}b_{12} - b_{32}b_{13}) + b_{31}(b_{23}b_{12} - b_{22}b_{13})$

then the B inverse can be calculated as $B^{-1} = \frac{1}{DET(B)} \begin{pmatrix} b_{22}b_{33} - b_{23}b_{32} & b_{13}b_{32} - b_{12}b_{33} & b_{12}b_{23} - b_{13}b_{22} \\ b_{23}b_{31} - b_{21}b_{33} & b_{11}b_{33} - b_{13}b_{31} & b_{13}b_{21} - b_{11}b_{23} \\ b_{21}b_{32} - b_{22}b_{31} & b_{12}b_{31} - b_{11}b_{32} & b_{11}b_{22} - b_{12}b_{21} \end{pmatrix}$

Gauss-Jordan method is not recommended to calculate inverse matrix of $N \times N$ with $N \geq 4$. This is because the calculation time and programming effort increases considerably.

Controllability and observability of the system also introduced by R. Kalman. For the state space system representation, the system is controllable, if the controllability matrix:

$ctrb = [B \ AB \ A^2B \ \dots \ A^{N-1}B]$ is full rank:

$$\Gamma(ctrb) = N \quad (A.7)$$

The system is observable, if the observability matrix: $obsv = \begin{bmatrix} C \\ CA \\ CA^2 \\ \dots \\ CA^{N-1} \end{bmatrix}$ is full rank:

$$\Gamma(obsv) = N \quad (A.8)$$

A.4 FFT algorithm

A faster version of the discrete Fourier transform (DFF) is FFT. FFT is used for the frequency-domain representation of the time-domain signal. In this thesis, the FFT function has been written with the Matlab function. Compared to the z-transform for the discrete transfer function, the FFT operation does a similar job for continuous signals.

$$NFFT = 2^{nextpow2(\text{length}(InputSignal))} \quad (A.9)$$

$$y = \frac{fft(InputSignal, NFFT)}{N} \quad (A.10)$$

$$f = \frac{Fs}{2} \text{linspace}(0, 1, \frac{NFFT}{2} + 1) \quad (A.11)$$

$$output = (f, 2 \text{abs}(y(1 : \frac{NFFT}{2} + 1))) \quad (A.12)$$

A.5 Moving average filter (MAF) algorithm

For time-domain signals, MAF is the finite response impulse (FIR) optimal linear filter. MAF is used in digital signal processing (DSP) for reduction of random noise. The functional algorithm with “w” moving average (window of $2w+1$) with Matlab is written as:

$$WMA = \text{repmat}(\frac{1}{2w+1}, 2w+1, 1) \quad (A.13)$$

$$FilteredSignal = \text{conv}(InputSignal, WMA, 'valid') \quad (A.14)$$

where, in Equation A.13, WMA is the weighted moving-average matrix, and, in Equation A.14, “conv” is the convolution operator.

B.1 Sliding mode observer Simulink diagram

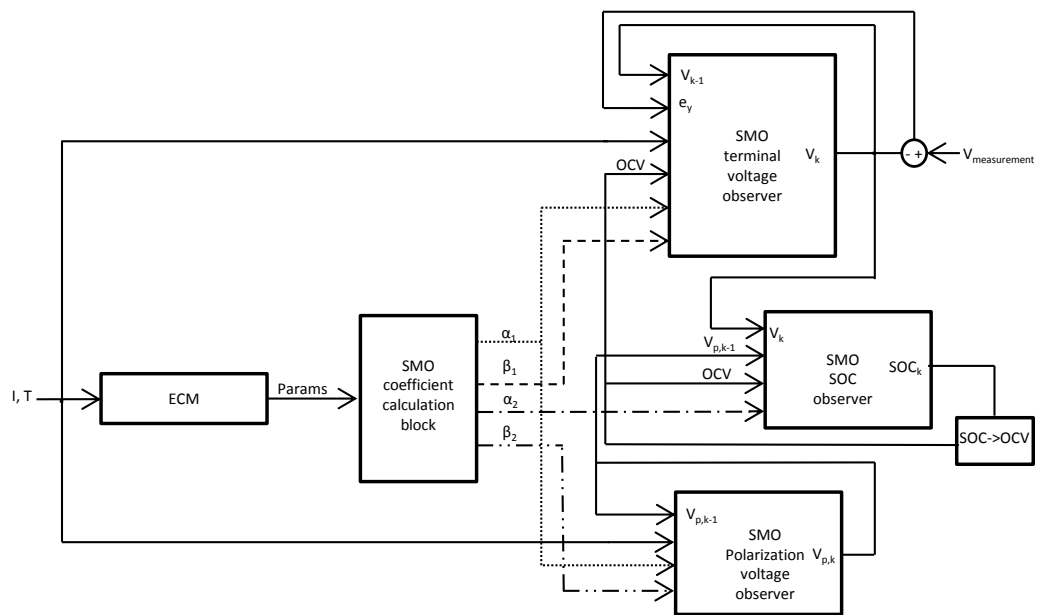


Figure B.2: The sliding mode observer design

C.1 Lab design and visits

During the laboratory design phase, several companies, suppliers, and research institutes were visited and good contacts were made. The first visit was to Memmert GmbH, a climate-chamber supplier located in Schwabach, Germany. The host was Ms. Andrea Weiss. The visit started with basic discussion about our general requirements, and it continued with a production line visit, from the general body construction to the insulations and electronics. Limitations and options for producing custom-made climate chambers were discussed. A technical discussion with expert engineers cleared our doubts and gave those engineers a clear understating of our requirements. Several custom-made chambers were ordered.

Two visits to BaSyTec GmbH in Asselfingen were paid for. The first one was to discuss about the products and visit the production line, and the second visit was meant for training. A visit to the Zentrum für Sonnenenergie und Wasserstoff (ZSW), or the Center for Solar Energy and Hydrogen came next. The host was Dr. Harry Doering sub-devision of the electrochemical energy technologies, Accumulators. At ZSW, they mainly test the cells, modules, and battery packs from different clients. Another visit was in Pfaffenhofen, Germany, to dSPACE GbmH. It also included a training for the dSPACE real-time system, which included the main features of dSPACE prototyping and simulator systems.

Besides participating in the dSPACE training, an official visit was also made to the dSPACE company in Paderborn, Germany. A two day trip to Aachen, Germany, including a visit to Digatron GmbH and the Institut für Stromrichtertechnik und Elektrische Antriebe (ISEA) at RWTH Aachen University, was next. Visiting ISEA provided a good impression of their activities and different projects. These trips made me confident in making a final decision on how to equip a battery laboratory with the most suitable combination of the battery test equipment to cover all the requirements for battery research and testing. During the lab operation, several researchers, students, and industry projects profited from it.

The chair of technical electrochemistry, Professor Hubert Gasteiger and Fraunhofer ICT Karlsruhe were also visited. Another visit was paid to Fraunhofer ICT in Garching, hosted by Dr. Kai C. Moeller. I also visited Dr. Peter Spies, head of “Integrated Energy Supplies” at Fraunhofer IIS; he was active in BMS design and development. Other visit included Fraunhofer ITWM, the host was Dr. Jochen Zausch from, who was active in 3D numerical simulations of batteries. Another visit was paid to the Fraunhofer IWM, the host was Dr. Leonhard Mayrhofer, who was active in the battery multi-scale modeling field.

C.2 Selected photos of the TUM CREATE battery laboratory, and test setup



Figure C.3: Laboratory test setup

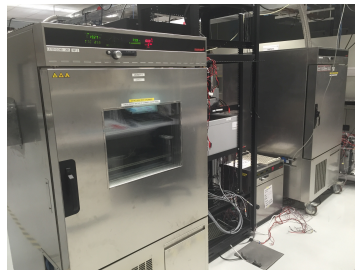


Figure C.4: Schematic of the laboratory test chambers



Figure C.5: Laboratory abuse chamber

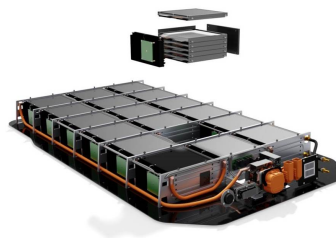


Figure C.6: EVA pack

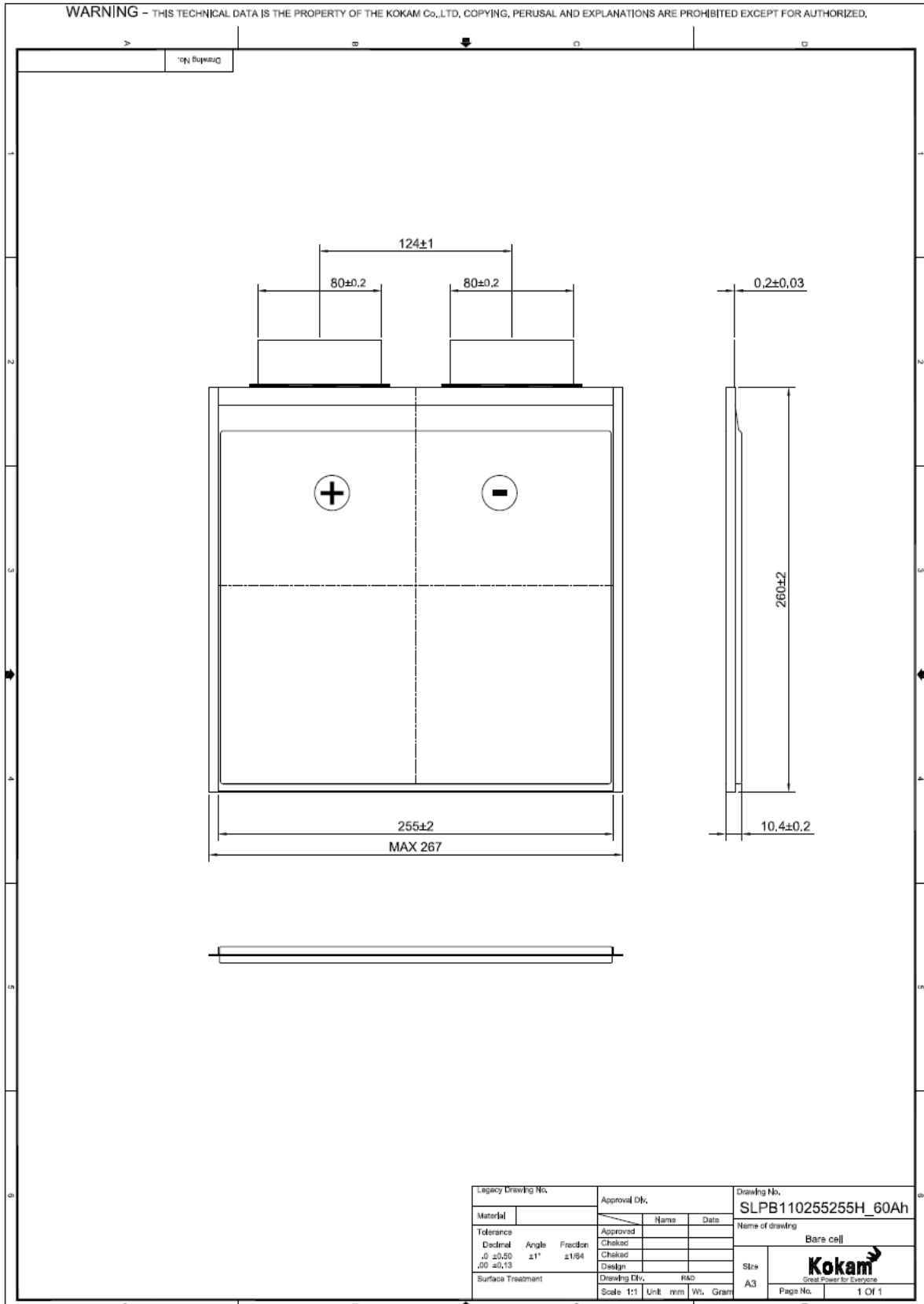
D.1 DUT datasheet

2. Technical Specification

2.1 General Information

No.	ITEM	VALUE	REMARK
1	Rated Capacity	Typ. 64.0Ah Min. 63.0Ah	Charge@0.2C(12A) Discharge@0.5C(30A)
2	Nominal Voltage	3.7V	
	Lower limit voltage	2.7V	
	Upper limit voltage	4.2 ±0.03V	
3	Max. Conti. Charge Current	180A	CC-CV charging is required End Condition: 0.05C(3A) or 5Hr Temperature: 23±3°C
4	Max. Conti. Discharge Current	480A	
	Peak Discharge Current	720A	Less than 10sec
5	Operation Temperature Range	Charge: 0 ~ 45°C	@60±25% R.H.
		Discharge: -20 ~ 60°C	
6	Storage Temperature Range	less than 1 year -20 ~ 25 °C	@60±25% R.H. SOC 50 ±5%
		less than 3 months 25 ~ 40 °C	
		less than 1 week 40 ~ 60 °C	
7	Weight	Max. 1.52kg	
8	Cell Dimension	Length : Max.262.0mm	Except for tab length
		Width : Max.257.0mm	
		Thickness : Max.10.6mm	Initial full charge

2.2 Drawing



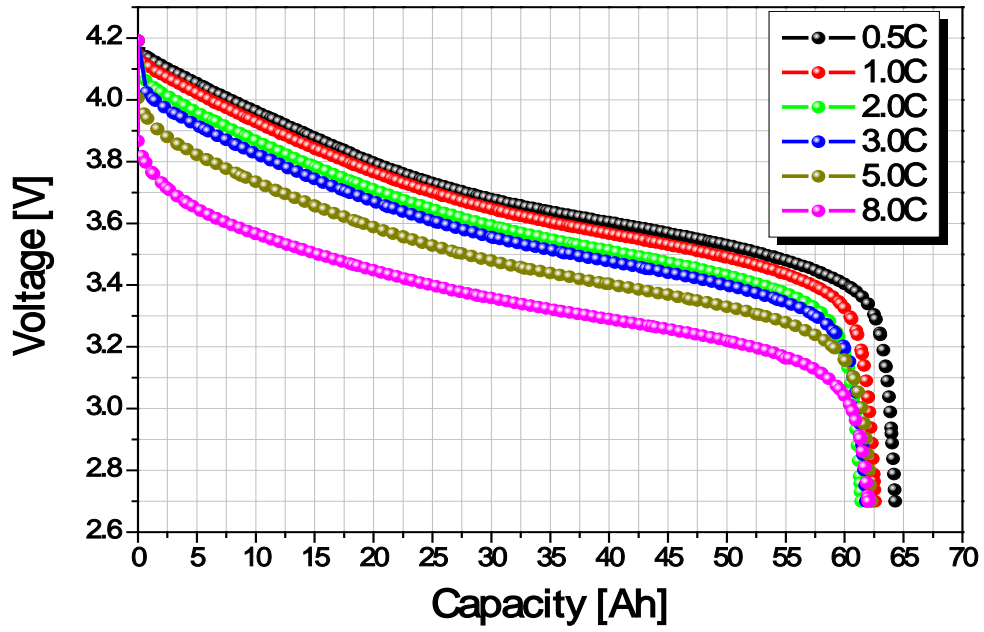
2.3 Electrical Performance

.No	ITEM	CRITERIA				TESTING CONDITIONS		
1	Outside Appearance	No abnormal strain, Deformation nor damage				Visual check		
2	External Dimension	According to the attached drawing				Use caliper (0.05mm a division) specified in ISO 3599		
3	Discharge Time	More than the time Mentioned hereunder				Measure capacity by holding at various temperatures for 1Hr after standard charging.		
	Discharge Rate	0.5C	1.0C	2.0C	3.0C	5.0C	8.0C	
	Capacity (%)	100%	> 95%	> 92%	> 92%	> 90%	> 85%	
	Discharge Temperature	-20°C	-10°C	0°C	25°C	40°C	60°C	
	Capacity (%)	>70%	>75%	> 85%	100%	> 97%	> 97%	
4	Charge Current	Less than 5.0 hrs			0.5C			
		Less than 2.0 hrs			1.0C			
5	Initial Internal Impedance	Less than 0.6mΩ				Measure by alternate current (1kHz) within 6hr after charge. (23±3°C)		
6	Cycle Life	Above 48.0Ah				Carry out 1400cycles charging/discharging in the below condition. ■ Charge : CC/CV, 1.0C(60A), 4.2V, 0.05C(3A)(5Hr)-END ■ Discharge : 1.0C(60A) to 3.0V ■ Rest Time between charge/discharge : 10min. ■ Temperature : 23±3°C		
7	Storage Performance	Above 54.0Ah				After full charge at 60±3°C, then leave 1 week. After storage, measure discharge capacity at 23±3°C		
8	Leakage-Proof	No leakage [visual inspection]				After full charge, stand at 60±3°C, 60±10%RH for 1month.		

◆ Discharge profiles at RT

❖ Charge : CC-CV, 1.0C, 4.2V, 0.05C cut-off @23°C±3°C

❖ Discharge : CC, 0.5 ~ 8.0C, 2.7V cut-off @23°C±3°C

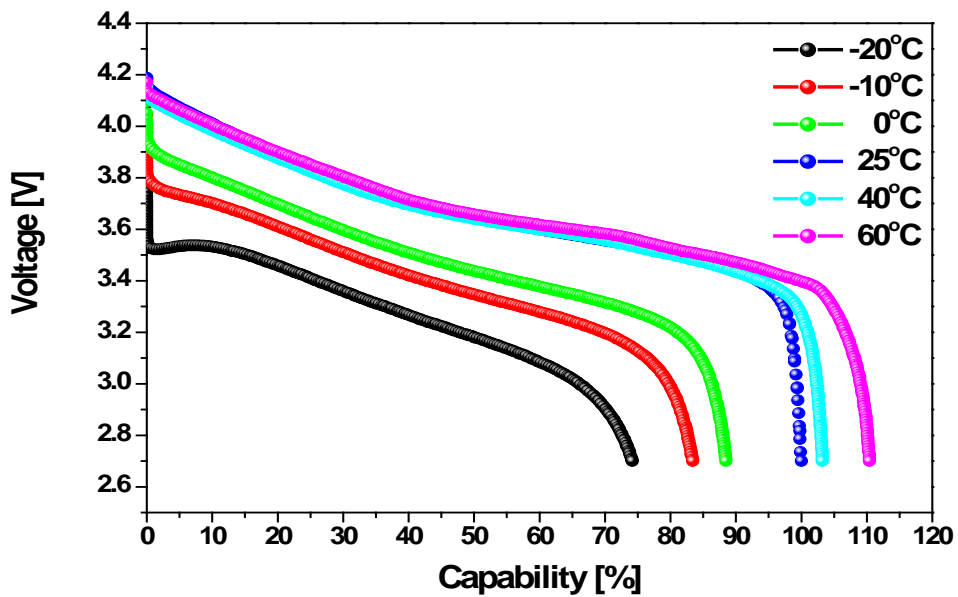


◆ Temperature characteristics

❖ Charge : CC-CV, 0.5C, 4.2V, 0.05C cut-off @23°C±3°C

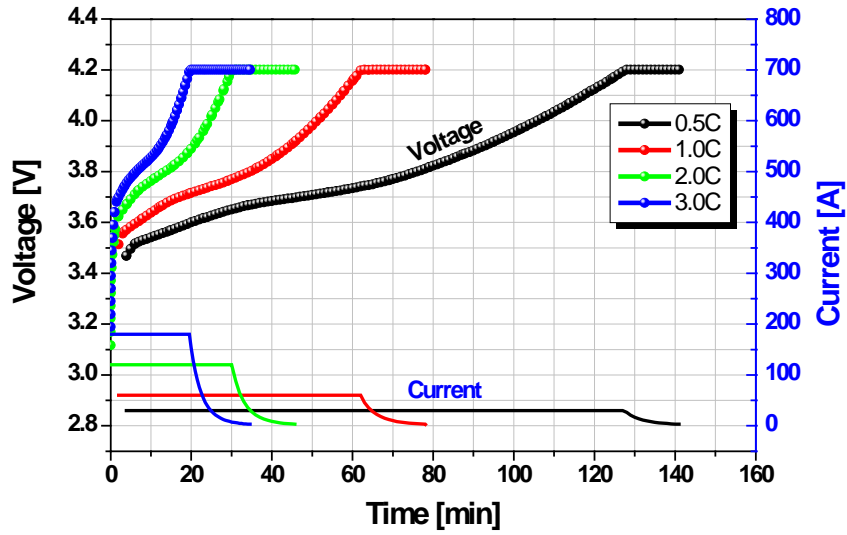
❖ Discharge : CC, 0.5C, 2.7V cut-off @ each temperature

❖ Soaking time : 2hr



◆ Charge profiles at RT

❖ Charge : CC-CV, 0.5C ~ 3.0C, 4.2V, 0.05C cut off @23°C ±3°C



2.4 Environmental Performance

- Operating condition

Charging : 0~45°C

Discharging : -20~60°C

- Storage condition

SOC 40~60% at -20~60°C

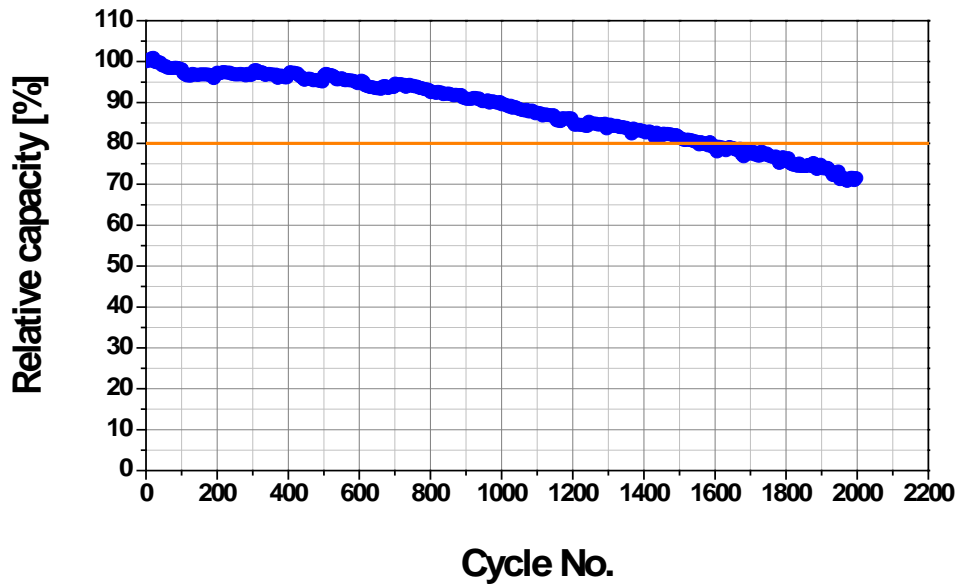
- Self discharging rate

< 1% for Month at Room temperature

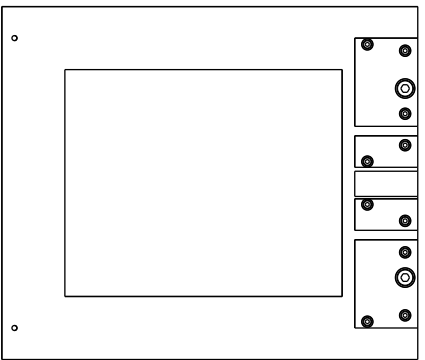
2.5 Life Performance

◆ Cycle characteristics at RT

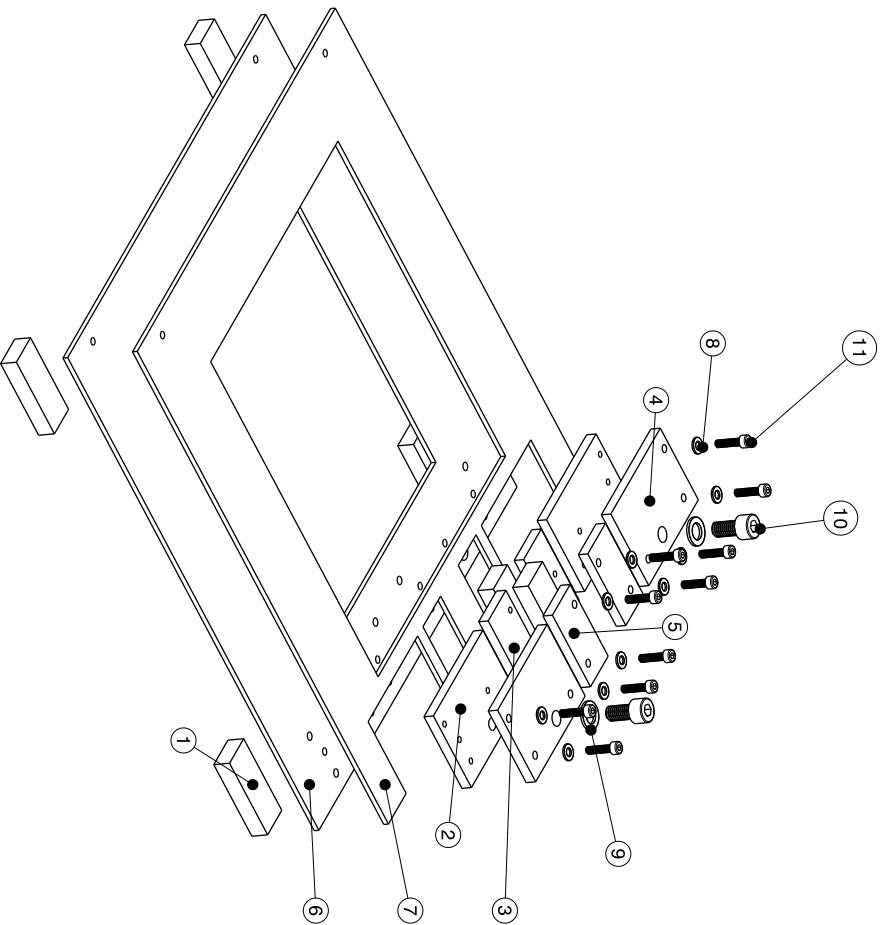
- ❖ Charge : CC-CV, 1.0C, 4.2V, 0.05C cut-off @23°C ±3°C
- ❖ Discharge : CC, 1.0C, 3.0V cut-off @23°C ±3°C



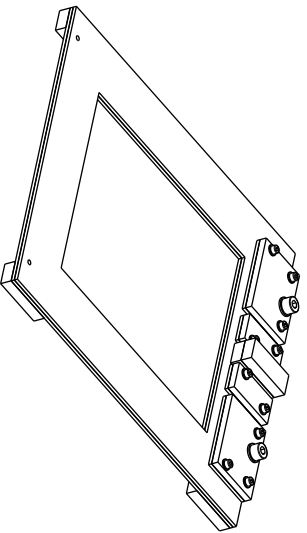
D.2 Cell holder design and construction



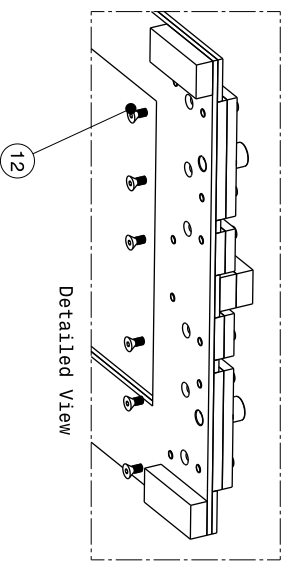
Front view



Isometric view



Isometric view



Detailed View

Bill of Material: 65Ah / 75Ah Cell Holder

Number	Part Number	Quantity
1	Rubber Stopper	6
2	Big Plate Bottom	2
3	Small Plate Bottom	2
4	Big Plate Top	2
5	Small Plate Top	2
6	Bottom Board	1
7	Top Board	1
8	M4 Washer	10
9	M8 Washer	2
10	M8X16 Hex Screw	2
11	M4X16 Hex Screw	10
12	M4X8 Hex Screw	6

DESIGNED BY:
Lemuel.moraleja

DATE:
12/15/2015

CHECKED BY:
XXX

DATE:
XXX

65Ah/7Ah Cell Holder

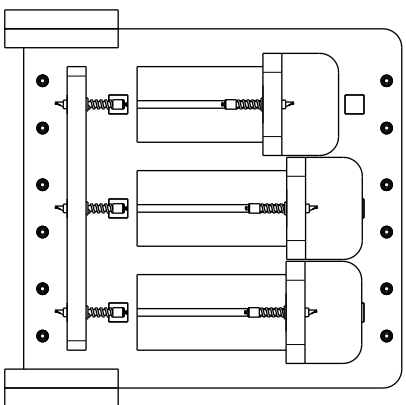
DASSAULT SYSTEMES

SCALE:
1:1

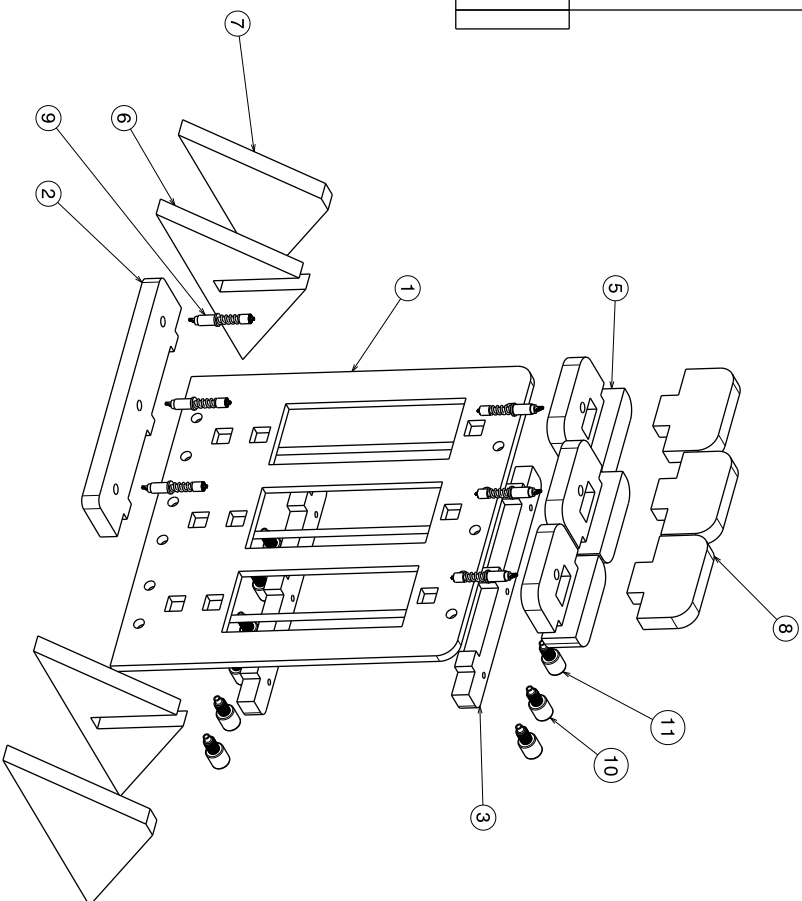
SIZE:
A2

SHEET:
1/1

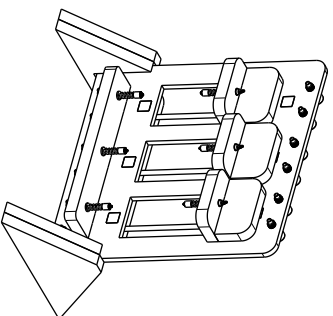
THIS DRAWING IS OUR PROPERTY. IT CAN'T BE REPRODUCED OR COMMUNICATED WITHOUT OUR WRITTEN AGREEMENT.



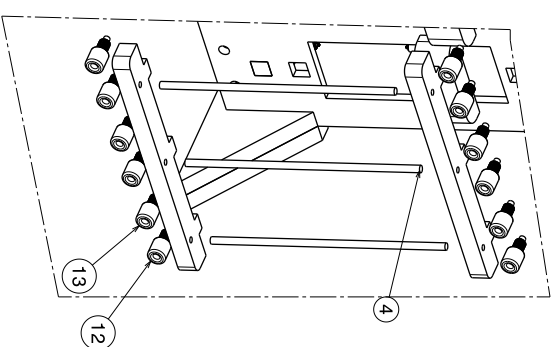
Front View



Isometric view



Isometric view



Detailed View

Bill of Material: Cylindrical Cell Holder

Number	Part Number	Quantity
1	Main Board	1
2	Fixed Probe Holder	1
3	Rod Holder	2
4	Studding	3
5	Adjustable Probe Holder	3
6	Stand	2
7	Stand Cover	2
8	Probe Guide	3
9	Kelvin Probe	6
10	Banana Red	3
11	Banana Blue	3
12	Banana Black	3
13	Banana Socket	5

DESIGNED BY:
Lemuel.moraleja

DATE:
5/6/2016

CHECKED BY:
XXX

DATE:
XXX

Cylindrical Cell Holder

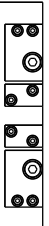
DASSAULT SYSTEMES

SCALE:
1:1

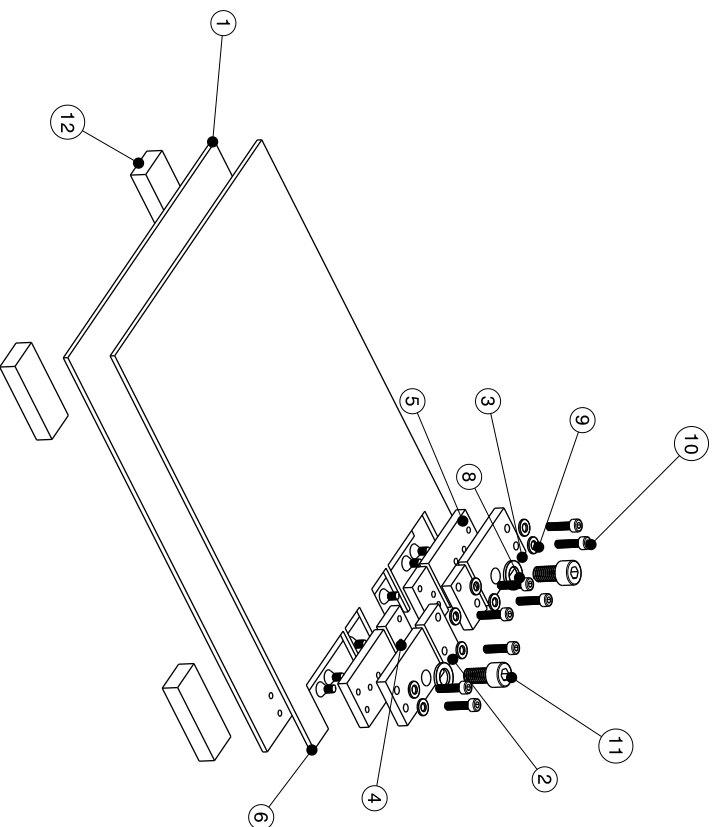
XXX

1/1

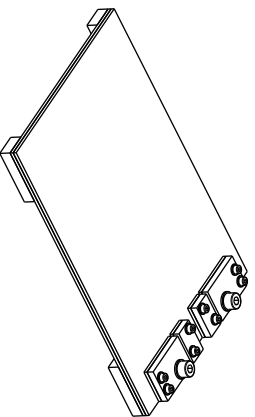
THIS DRAWING IS OUR PROPERTY. IT CAN'T BE REPRODUCED OR COMMUNICATED WITHOUT OUR WRITTEN AGREEMENT.



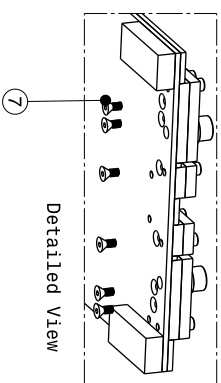
Front view



Isometric view



Isometric view



Detailed View

Bill of Material: 20Ah Cell Holder

Number	Part Number	Quantity
1	Top Board	1
2	Small Plate Top	2
3	Big Plate Top	2
4	Small Plate Bottom	2
5	Big Plate Bottom	2
6	Bottom Board	1
7	M4x8 Hex Screw	6
8	M8 Washer	2
9	M4 Washer	8
10	M4x16 Hex Screw	8
11	M8x16 Hex Screw	2
12	Rubber Stopper	4

DESIGNED BY:
Lemuel.moraleja

DATE:
5/6/2016

CHECKED BY:
XXX

DATE:
XXX

20Ah Cell Holder

DASSAULT SYSTEMES

SCALE:
1:1

SIZE:
A2

DRIVING NUMBER:
XXX

SHEET:
1/1

THIS DRAWING IS OUR PROPERTY. IT CAN'T BE REPRODUCED OR COMMUNICATED WITHOUT OUR WRITTEN AGREEMENT.